
Superconductivity in metallic glasses ($\text{Fe}_x\text{Ni}_{1-x}\text{Zr}_2$):
from transport and magnetization properties to
vortex dynamics

Josianne Lefebvre

Centre for the Physics of Materials

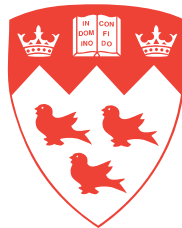
Department of Physics

McGill University

Montréal, Québec

Canada

May 2008



A Thesis submitted to

McGill University

in partial fulfillment of the requirements for the degree of

Doctor of Philosophy

CONTENTS

| | |
|--|-----------|
| Abstract | xii |
| Résumé | xiii |
| Acknowledgments | xv |
| Statement of Original Contributions | xvi |
| List of Symbols | xvii |
| 1 Introduction | 1 |
| 2 Theory of superconductivity | 8 |
| 2.1 Superconductivity in a nutshell | 9 |
| 2.2 The London equations | 11 |
| 2.3 Ginzburg-Landau theory: Main ideas | 12 |
| 2.3.1 The GL equations | 13 |
| 2.3.2 Consequences of the GL theory | 14 |
| 2.3.3 Flux quantization | 14 |
| 2.4 Type I and type II superconductivity | 15 |
| 2.5 Vortices | 16 |
| 2.5.1 Vortex matter | 18 |
| 2.6 Results from the BCS theory | 20 |
| 2.7 Bean critical state model | 23 |
| 2.7.1 Low-field limit | 24 |
| 2.7.2 High-field limit | 25 |
| 2.8 Amorphous metals | 26 |
| 2.8.1 Superconductivity in amorphous metals | 27 |
| 2.8.2 The McMillan equation | 29 |
| 2.9 Experimental probes of the superconducting state | 29 |
| 2.9.1 Specific heat | 30 |
| 2.9.2 Magnetization | 30 |
| 2.10 Note on the theories of superconductivity | 34 |
| 3 Experimental Techniques | 35 |
| 3.1 Samples | 35 |
| 3.1.1 Superconducting metal glasses preparation method | 35 |
| 3.1.2 Superconducting sample properties | 37 |
| 3.1.3 GaAs/AlGaAs samples for magnetization measurements | 40 |
| 3.2 Experimental setup | 43 |
| 3.2.1 Components and operation of the ^3He refrigerator | 43 |
| 3.2.2 Components and operation of the dilution refrigerator | 45 |

| | | |
|----------|--|------------|
| 3.2.3 | Data acquisition methods | 47 |
| 3.3 | Sources of systematic error | 49 |
| 3.3.1 | Current Distribution | 49 |
| 3.3.2 | Magnetic field offset | 49 |
| 3.3.3 | Temperature stability | 50 |
| 3.4 | Measuring superconducting properties using a 2-dimensional electron gas | 51 |
| 3.4.1 | Magnetic field of a vortex lattice | 52 |
| 3.4.2 | Experimental determination of the magnetization | 58 |
| 3.4.3 | Hall resistance results | 60 |
| 4 | Superconducting properties of the amorphous Fe-Ni-Zr alloys | 63 |
| 4.1 | Expressions for superconductors in the dirty limit | 66 |
| 4.1.1 | What is the dirty limit? | 66 |
| 4.1.2 | Dirty limit expressions | 67 |
| 4.1.3 | Calculated dirty limit parameters | 68 |
| 4.2 | Magnetization results | 73 |
| 4.2.1 | Experimental determination of the magnetization | 73 |
| 4.3 | The lower critical field | 75 |
| 4.3.1 | Theoretical predictions of B_{c1} | 76 |
| 4.3.2 | Experimental determination of B_{c1} | 80 |
| 4.4 | Upper critical field | 83 |
| 4.4.1 | Origin of limiting effects on B_{c2} | 88 |
| 4.4.2 | Discussion on critical fields results | 89 |
| 4.4.3 | The WHHM theory | 91 |
| 4.5 | Summary | 100 |
| 5 | Local structure dependence on x in the a-Fe$_x$Ni$_{1-x}$Zr$_2$ alloys | 102 |
| 5.1 | Fluctuations in magnetization | 103 |
| 5.2 | Anomalous hysteresis loops in $x = 0.5$ and $x = 0.6$ | 107 |
| 5.2.1 | Experimental results: Evidence for a dynamical effect | 108 |
| 5.2.2 | Effect of driving current | 112 |
| 5.2.3 | Temperature dependence of hysteresis | 114 |
| 5.2.4 | Magnetic field dependence of hysteresis | 114 |
| 5.3 | Analysis of results | 116 |
| 5.3.1 | Proposed model | 117 |
| 5.3.2 | The experimental results explained | 119 |
| 5.3.3 | The two-level critical state model | 123 |
| 5.3.4 | Origin of inhomogeneities in the $x = 0.5$ and $x = 0.6$ alloys | 130 |
| 5.4 | Summary | 132 |
| 6 | Transverse dynamics of the vortex state | 134 |
| 6.1 | Vortex phases | 135 |
| 6.1.1 | Static phase diagram | 135 |
| 6.1.2 | Dynamic phase diagram | 136 |
| 6.2 | Experimental measurements of vortex phases | 139 |
| 6.2.1 | Hall effect in type II superconductors | 139 |

| | | |
|----------|---|------------|
| 6.2.2 | Critical transverse depinning | 150 |
| 6.3 | Summary | 169 |
| 7 | Conclusions | 171 |
| A | Estimation of the magnetization | 176 |
| B | Magnetoresistance results | 178 |
| B.1 | Weak localisation | 178 |
| C | Hall resistance results | 183 |
| | References | 186 |

LIST OF FIGURES

| | | |
|-----|--|----|
| 2.1 | Schematic representation of a vortex with core size ξ and size λ showing the magnitude of the magnetic field and the circulating supercurrent. | 16 |
| 2.2 | Schematic representation of the field B and the order parameter ψ at the interface between a normal region and a superconducting region for a type I superconductor (left) and a type II superconductor (right). In red: properties pertaining to the magnetic field. In blue: properties pertaining to ψ . (Inspired from Fig.(4.3) of Ref.[1]) | 17 |
| 2.3 | Representation of the triangular vortex lattice, or Abrikosov lattice. . | 18 |
| 2.4 | Superconducting density of states $D_s(E)$ in the neighborhood of the energy gap. (Adapted from Fig.(6.4) of Ref.[2]. | 22 |
| 2.5 | Representation of a) the field distribution b) the current density distribution c) the pinning force density in a superconductor according to the Bean critical state model for increasing applied field. | 25 |
| 2.6 | Magnetic field distribution in the Bean critical state for decreasing applied field. | 26 |
| 2.7 | a) Magnetization vs applied magnetic field for an ideal type I superconductor ($\kappa < \frac{1}{\sqrt{2}}$) and for ideal type II superconductors with $\kappa \approx 0.8$ and $\kappa \approx 2$. Picture adapted from Fig.(5.2) of Ref.[1]. b) Representation of typical magnetization curves for an ideal (dotted line) and a nonideal (solid line) type II superconductor. | 32 |
| 2.8 | Representation of a typical magnetization hysteresis loop for different temperatures below T_c | 33 |
| 3.1 | Schematic representation of the sample preparation process by the melt-spinning technique. | 36 |
| 3.2 | X-ray diffraction pattern obtained with Cu K_α radiation from a sample of the alloy $\text{Fe}_{0.3}\text{Ni}_{0.7}\text{Zr}_2$ (left) and a sample of the alloy $\text{Fe}_{0.6}\text{Ni}_{0.4}\text{Zr}_2$ (right) demonstrating the absence of crystallinity by the absence of constructive diffraction Bragg peaks. | 37 |
| 3.3 | Representation of the layered structure of the GaAs/AlGaAs heterostructure containing the 2DEG. The energy bands resulting from the layered structure are also shown. | 41 |
| 3.4 | Representation of the 2DEG Hall bar pattern with the superconducting sample. | 41 |
| 3.5 | a) 2DEG sample with Hall bar pattern. b) Patterned 2DEG sample with superconductor fixed on the Hall bar with vacuum grease. | 42 |
| 3.6 | Schematic representation of the ^3He refrigerator showing the main components as described in the text. | 44 |
| 3.7 | Schematic representation of the dilution refrigerator showing the main components described in the text. | 46 |

| | | |
|------|--|----|
| 3.8 | Contact configuration according to the four-probe technique. | 48 |
| 3.9 | a) Ideal contact geometry for Hall resistance measurements. b) Contact configuration used for Hall resistance measurement on our superconductors. | 50 |
| 3.10 | Magnetic flux density induced by: black line: a single vortex at the surface of the superconductor, red line: a vortex lattice 100 nm away from the surface, and blue line: a vortex lattice 1000 nm away from the surface of the superconductor. The applied B field is 1 mT for these three curves. | 55 |
| 3.11 | Schematic representation of the 2DEG/superconductor arrangement for the magnetization measurements. | 59 |
| 3.12 | Hall resistance vs magnetic field up to 30 mT for the sample $\text{Fe}_{0.1}\text{Ni}_{0.9}\text{Zr}_2$. The results confirm the linearity of R_H at fields much larger than B_{c1} and highlight the small size of the Meissner phase in these samples. | 60 |
| 3.13 | Hall resistance vs applied magnetic field for a) a 2DEG only b) a 2DEG with a sample of $\text{Fe}_{0.2}\text{Ni}_{0.8}\text{Zr}_2$ on top, for different temperatures below T_c | 62 |
| 4.1 | Magnetization vs applied field at different temperatures below T_c for different alloys of $\text{Fe}_x\text{Ni}_{1-x}\text{Zr}_2$. The $M = 0$ line represents data above T_c | 75 |
| 4.2 | Representation of an isolated vortex using superconducting parameters for NiZr_2 , with $\kappa = 83$. $B(r)$ is the spatial dependence of the magnetic flux density of the vortex, and $\psi(r)$ is the superconducting order parameter. | 77 |
| 4.3 | B_{c1} vs T for $\text{Fe}_x\text{Ni}_{1-x}\text{Zr}_2$ alloys with $x = 0, 0.1, 0.2, 0.3, 0.4$, and 0.5 . The data points represent experimental data while the lines are fits to equation (4.17) performed using T_c and $B_{c1}(0)$ as fit parameters. The $B_{c1}(0)$ values shown in the graphs are the best-fit values obtained for B_{c1} at $T = 0$ | 84 |
| 4.4 | Representation of the density of vortices for different magnetic fields. | 85 |
| 4.5 | B_{c2} vs T for our different alloys. The data points represent experimental data, with error bars on T determined from temperature fluctuations during data acquisition, and experimental errors on B_{c2} smaller than the size of the dot. Blue curves: Fits to the full WHHM theory (equation (4.32)). Black curves: Plot of equation (4.38) including our experimental T_c and $\frac{dB_{c2}}{dT} _{T_c}$. Red curves: Plot of equation (4.39) using our experimental T_c and $\frac{dB_{c2}}{dT} _{T_c}$. Magenta curves: Fit to equation (4.32) using α^{e-ph} which includes a correction to account for electron-phonon coupling. | 97 |

| | | |
|------|--|-----|
| 4.6 | B_{c2} vs T for our different alloys. The data points represent experimental data, with error bars on T determined from temperature fluctuations during data acquisition, and experimental errors on B_{c2} smaller than the size of the dot. Blue curves: Fits to the full WHHM theory (equation (4.32)). Black curves: Plot of equation (4.38) including our experimental T_c and $\frac{dB_{c2}}{dT} _{T_c}$. Red curves: Plot of equation (4.39) using our experimental T_c and $\frac{dB_{c2}}{dT} _{T_c}$. Magenta curves: Fit to equation (4.32) using α^{e-ph} which includes a correction to account for electron-phonon coupling. | 98 |
| 5.1 | Standard error on the mean of the statistical distribution of the ratio of the fluctuations in magnetization to the mean magnetization for different $\text{Fe}_x\text{Ni}_{1-x}\text{Zr}_2$ alloys. | 104 |
| 5.2 | Standard deviation as a function of magnetic field increment $f(\varepsilon)$ used to determine the characteristic field of fluctuations B_0 at $\delta^2/2$. (The line is just a guide for the eye.) | 106 |
| 5.3 | Characteristic field of fluctuations B_0 and characteristic magnetic flux Φ threading grains in units of Φ_0 as a function of the Fe content x in the $\text{Fe}_x\text{Ni}_{1-x}\text{Zr}_2$ metallic glasses. | 107 |
| 5.4 | Normalized resistance vs applied magnetic field for different samples of the alloys $\text{Fe}_x\text{Ni}_{1-x}\text{Zr}_2$. Solid lines are for increasing B sweeps and dotted lines are for decreasing B sweeps. $T \simeq 0.35$ K | 108 |
| 5.5 | Width of hysteresis loop as a function of magnetic field sweep rate for a) $\text{Fe}_{0.5}\text{Ni}_{0.5}\text{Zr}_2$ at $T = 0.34$ K and b) $\text{Fe}_{0.6}\text{Ni}_{0.4}\text{Zr}_2$ at $T \simeq 50$ mK. The lines are guides to the eye. | 109 |
| 5.6 | Resistance as a function of time after pausing the external magnetic field in the B_{c2} transition during a) an increasing B sweep and b) a decreasing B sweep. | 110 |
| 5.7 | Resistance vs magnetic field from sweeping the magnetic field at 11 mT/s over a single field polarity without pausing at $B = 0$ (black curves), pausing at $B = 0$ for 5 min, and from sweeping over the two field polarities (green curves). | 111 |
| 5.8 | a) Resistance vs magnetic field for different driving currents for an alloy of $\text{Fe}_{0.5}\text{Ni}_{0.5}\text{Zr}_2$. Solid lines are for increasing magnetic field and dotted lines are for decreasing magnetic field. The B sweep rate is 15 mT/s. b) Width of the hysteresis loops observed in a). | 113 |
| 5.9 | a) Resistance vs magnetic field for different driving currents for an alloy of $\text{Fe}_{0.6}\text{Ni}_{0.4}\text{Zr}_2$. Solid lines are for increasing magnetic field and dotted lines are for decreasing magnetic field. The B sweep rate is 10 mT/s. b) Width of the hysteresis loops observed in a). | 113 |
| 5.10 | a) Resistance vs magnetic field at different temperatures for $\text{Fe}_{0.5}\text{Ni}_{0.5}\text{Zr}_2$. The B sweep rate is 15 mT/s. b) Width of the hysteresis loops normalized by the mean value of B_{c2} for increasing and decreasing B sweeps vs temperature. c) Width of the B_{c2} transition for increasing and decreasing magnetic field sweeps as a function of temperature. | 115 |

| | | |
|------|---|-----|
| 5.11 | a) Resistance vs temperature data at different magnetic fields for a sample of $\text{Fe}_{0.5}\text{Ni}_{0.5}\text{Zr}_2$. b) Width of hysteresis loops extracted from the data in a). c) Width of the transitions shown in a) determined from the temperature difference between the 90 % and 10 % of R_n criteria. | 116 |
| 5.12 | Schematic representation of the flux distribution upon increasing and decreasing the external magnetic field in inhomogeneous superconductors. The gray areas represent the inclusions with strong pinning properties. | 119 |
| 5.13 | Schematic representation of an inhomogeneous superconductor composed of inclusions with transition temperature $T_{c, B}$ and a majority phase with transition temperature $T_{c, A}$. | 119 |
| 5.14 | Side view of a superconducting flat slab in a perpendicular magnetic field with regions of large pinning properties represented by a lattice of squares. (Inspired from Ref. [3].) | 124 |
| 5.15 | Schematic representation of the average flux profile (dotted line) and local flux profile (solid line) in an inhomogeneous superconductor containing strongly-pinned regions (denoted by B) and weak pinning regions (A). Picture inspired by Fig.3 of Ref.[3]. | 125 |
| 5.16 | Total magnetic flux in percolating phase A as a function of the applied magnetic field determined according to the 2-level critical state model. The results are calculated for different characteristic fields B^* , with $s_p = 0.19$, $B_{\max} = 4$ T and $L_B = 20$ μm . Inset: Enlargement of the low field region. | 128 |
| 5.17 | Total magnetic flux in percolating phase A as a function of the applied magnetic field determined according to the 2-level critical state model. The results are calculated for different cross-sectional fractions of the strongly-pinned phase B s_p , with $B^* = 1.98$, $B_{\max} = 4$ T and $L_B = 20$ μm . | 129 |
| 6.1 | Representation of the magnetic field-temperature vortex phase diagram in the absence of a driving force. The peaks in structure factor $S(q)$ as a function of reciprocal lattice vector q (Bragg peaks) are also depicted in the Bragg phase. (Inspired from Ref.[4]). | 136 |
| 6.2 | Representation of the dynamic vortex phase diagram in temperature, disorder and driving force. Schematic vortex flow patterns are also shown for the moving phases. (Inspired from Ref.[5]). | 138 |
| 6.3 | Schematic representation of the direction of vortex motion due to the Lorentz force resulting from the action of the applied current and magnetic field. | 140 |
| 6.4 | Schematic drawing representing the direction of vortex flow and resulting Hall voltage from different combinations of driving current and magnetic field. | 142 |
| 6.5 | Comparison between the Hall resistance obtained using an AC current and $R_{\text{odd}}^- = [R_{xy}(-B, I) - R_{xy}(B, -I)]/2$ and $R_{\text{even}}^- = [R_{xy}(-B, I) + R_{xy}(B, -I)]/2$ obtained with a DC current. | 144 |

| | | |
|------|---|-----|
| 6.6 | Sample longitudinal resistance curve as a function of magnetic field showing the boundaries of the different vortex phases. | 144 |
| 6.7 | Upper panel: The lines represent the phase diagram obtained from the longitudinal resistance. The colour map as a function of B and I represents the value of the Hall resistance according to the colour scale shown in the lower panel. It is important to note that a line accounting for the contact misalignment was subtracted from the Hall curves in the graph. Lower panel: Hall resistance as a function of magnetic field for the following driving currents: 0.1, 1, 2.5, 3.33, 4.16, 5, 6.66, 7.5, 8.3, 9.5, and 10 mA. | 146 |
| 6.8 | Longitudinal resistance and Hall resistance as a function of magnetic field for up (solid lines) and down (dotted lines) B sweeps with $I = 0.5$ mA (purple curves) and $I = 5$ mA (green curves). Inset: Enlargement of the peak effect region. The nonzero Hall resistance above the critical field is due to the small unavoidable misalignment of the Hall contacts. | 147 |
| 6.9 | Longitudinal resistance and Hall resistance as a function of magnetic field for B sweeps with $I = 0.05$ mA. | 150 |
| 6.10 | a) Drawing showing the contact configuration and resulting directions of vortex motion due to the combination of ac and dc currents. b) Representation of the directions of applied currents and resulting forces with the contact misalignment as discussed in the text. | 151 |
| 6.11 | a) Schematic representation of the trajectory followed by vortices in the three regimes of vortex motion described in the text. b) Resistance vs magnetic field measured with different ac and dc currents. | 152 |
| 6.12 | Transverse ac voltage as a function of the applied ac force normalized by the critical force in the static case. The data for different longitudinal driving currents is shown. | 154 |
| 6.13 | Ratio of the critical force in the transverse case to that in the static case as a function of the choice of transverse voltage cutoff criteria. | 156 |
| 6.14 | Ratio of the critical force in the driven and the static case vs the longitudinal dc force determined using different cutoff voltages for a) a sample of NiZr_2 at $B = 0.95$ T b) a sample of $\text{Fe}_{0.3}\text{Ni}_{0.7}\text{Zr}_2$ at $B = 1.05$ T. | 158 |
| 6.15 | Longitudinal driving force vs magnetic field phase diagram showing the different vortex phases observed in the weakly-pinned amorphous metallic glass NiZr_2 and determined from longitudinal resistance measurements performed using an ac driving current. Also shown are regions for which a critical transverse depinning force was found (filled squares) with the magnitude $I_{y,c}/I_{x,c}$ given according to the colour scale on the right. Open squares represent regions for which transverse depinning was investigated but was not found to be critical. | 161 |

| | | |
|------|---|-----|
| 6.16 | Transverse voltage vs transverse driving force for $B = 0.95$ T for longitudinal driving current $I_{dc} = 0$ (dotted lines with triangular data points) and $I_{dc} = 1.0$ mA (solid lines with round data points). The lines are guides to the eye. The colours correspond to different temperatures. | 165 |
| 6.17 | a) Ratio of the critical transverse current determined with a 10 nV criterion in the driven and the static case vs the longitudinal current for a sample of NiZr ₂ at $B = 0.95$ T and for different temperatures. b) Map of the critical current ratio in the driven and static case according to the colour scale shown, as a function of longitudinal drive and magnetic field. The open squares represent data which do not exhibit <i>critical</i> transverse depinning. The solid line represents the longitudinal depinning line. | 167 |
| 6.18 | Transverse voltage as a function of transverse current at $B = 0.95$ T for different longitudinal driving currents at a) $T = 0.41$ K b) $T = 1.04$ K. The solid lines with square data points were acquired for increasing I_y , while the dotted lines with triangular data points were acquired from decreasing I_y | 168 |
| A.1 | B_z as a function of the distance away from the sample for $a = 0.5$ mm, $r = 0$, and $I = 10$ mA. Inset: Enlargement of the low z region. | 177 |
| B.1 | R_{xx} and R_H vs B_{app} for a) $T = 0.35$ K. Inset: schematic representation of the evolution of the magnetic field direction as it flips from positive to negative. b) $T = 2.31$ K, which is above T_c | 179 |
| B.2 | Magnetoconductivity at different temperatures obtained for our 2DEG sample with a Fe _{0.2} Ni _{0.8} Zr ₂ on top. | 179 |
| B.3 | Magnetoconductivity at different temperatures obtained for our 2DEG sample with a Fe _{0.5} Ni _{0.5} Zr ₂ on top. | 180 |
| B.4 | Log-log plot of the inelastic electron scattering time τ_i vs temperature obtained from a unique 2DEG, but with different superconductors on top. The difference between the results obtained is not attributed to the superconductor which is expected to have no effect here, but rather to the rate of cooldown of the sample which has a marked effect on the electron density. | 182 |
| C.1 | Hall resistance vs applied magnetic field for Fe _{x} Ni _{1-x} Zr ₂ with $x = 0$ and $x = 0.1$ | 183 |
| C.2 | Hall resistance vs applied magnetic field for Fe _{x} Ni _{1-x} Zr ₂ with $x = 0.2$ and $x = 0.3$ | 184 |
| C.3 | Hall resistance vs applied magnetic field for Fe _{x} Ni _{1-x} Zr ₂ with $x = 0.4$ and $x = 0.5$ | 185 |

LIST OF TABLES

| | | |
|-----|--|----|
| 4.1 | Details on the number of measurements of T_c performed for each alloy | 69 |
| 4.2 | Experimental superconducting parameters. | 71 |
| 4.3 | Some superconducting properties derived from experimental measurements. | 72 |
| 4.4 | Theoretical and experimental values of B_{c1} | 82 |
| 4.5 | Maki parameter and various critical fields | 87 |
| 4.6 | Some superconducting and electronic properties | 94 |
| 5.1 | Some parameters pertaining to phases A and B of the alloy $\text{Fe}_{0.6}\text{Ni}_{0.4}\text{Zr}_2$. 127 | |

Abstract

Properties of the superconducting state of the series of pseudo-binary metallic glasses $\text{Fe}_x\text{Ni}_{1-x}\text{Zr}_2$ have been studied from electrical transport and magnetization measurements performed using a nearby 2-dimensional electron gas (2DEG) as a magnetic flux detector. This series of alloys offers a variety of enviable qualities for the systematic study of superconducting properties amid which lies the alleged constant amorphous structure of alloys with different stoichiometry imparted by the similar atomic volume of the Fe and Ni atoms, which permits the determination of the dependence of superconducting parameters on chemical composition uniquely by eliminating structure-dependent contributions. Such a study aims at verifying how superconductivity is affected by the presence of iron which is known to induce pair-breaking spin fluctuations. The temperature dependence of B_{c1} and B_{c2} , and the T_c dependence on the iron content x in the alloys are determined and found to decrease with increasing x as expected from the increase of spin fluctuations.

Unexpected findings are also revealed: For instance, fluctuations in magnetization and anomalous hysteresis loops at the B_{c2} transition in alloys containing a large amount of Fe challenge the veracity of the assumption that the amorphous structure of the alloys $\text{Fe}_x\text{Ni}_{1-x}\text{Zr}_2$ remains constant with x . These results even bring the first evidence for the existence of a structural transition at some x value.

The absence of long-range order in amorphous alloys confers them weak vortex pinning character and makes the vortex state in the $\text{Fe}_x\text{Ni}_{1-x}\text{Zr}_2$ alloys ideal for the study of correlated systems since the density of vortices and the driving force can be tuned externally such as to measure their effects on correlations. For these reasons, dynamic vortex phases in these alloys were also studied. In particular, the transverse dynamics of vortex phases are investigated from Hall resistance measurements; large features are observed which can be attributed to long-range inhomogeneous vortex flow. The transverse vortex depinning transition is also investigated from measurements performed using crossed ac and dc currents. The existence of a large critical transverse force and the first order nature of the transverse depinning transition are proved experimentally for the first time in a system of vortices and confirm theoretical predictions.

Résumé

Les propriétés supraconductrices des verres métalliques pseudo-binaire $\text{Fe}_x\text{Ni}_{1-x}\text{Zr}_2$ sont étudiées à partir de mesures de transport électrique, ainsi qu'à partir de mesures d'aimantation prises en utilisant un gaz d'électrons bidimensionnel comme détecteur de champ magnétique. Cette série d'alliages démontre une variété de qualités enviables pour l'étude systématique de propriétés supraconductrices parmi lesquelles figure la présomption que la structure amorphe des alliages constante pour différentes stoechiométries conférée par le volume atomique similaire des atomes de Fe et de Ni, qui permet la définition de la dépendance des paramètres supraconducteurs sur la composition chimique uniquement et élimine les dépendances structurelles. Cette étude a donc pour but de vérifier comment la supraconductivité est affectée par la présence de fer dans le matériel, ce qui est reconnu pour causer des fluctuations de spin et tend à briser les paires de Cooper. La dépendance en température de B_{c1} et B_{c2} , et la dépendance de T_c sur la quantité de fer x dans les alliages sont déterminées et montrent une régression avec la croissance de x comme prévue due à l'augmentation des fluctuations de spin.

Des résultats non attendus sont aussi révélés: Par exemple, des fluctuations dans l'aimantation et des boucles d'hystérèse anormales à la transition B_{c2} dans les alliages contenant une grande quantité de fer mettent en doute la véracité de la supposition que la structure amorphe des alliages $\text{Fe}_x\text{Ni}_{1-x}\text{Zr}_2$ reste constante. Ces résultats constituent même la première preuve de l'existence d'une transition de phase structurelle pour une certaine valeur de x .

L'absence d'ordre à longue portée confère aux supraconducteurs amorphes leurs faibles propriétés d'ancrages des vortex, ce qui rend l'état mixte des alliages de $\text{Fe}_x\text{Ni}_{1-x}\text{Zr}_2$ idéal pour l'étude de systèmes corrélés puisque la densité de vortex ainsi que la force sur ceux-ci peuvent être ajustés de façon externe dans le but de mesurer leurs effets sur les corrélations. Pour ces raisons, les phases dynamiques de vortex dans ces alliages ont aussi été étudiées. En particulier, les phases transverses ont été examinées à partir de mesures de la résistance de Hall. De grands pics y sont observés qui sont attribuables au mouvement moins ordonné des vortex sur une longue distance. La dynamique transverse de l'état de vortex dans le régime de désancrage est aussi examinée à partir de mesures acquises en utilisant un courant ac et dc dans une configuration croisée. L'existence d'une grande force transverse critique et la

nature de premier ordre de la transition de désancrage transverse sont démontrées expérimentalement pour la première fois dans un système de vortex et apportent une confirmation à des prédictions théoriques.

Acknowledgments

The work presented in this thesis is the result of over three years of hard work and long nights spent in the lab. It was not easy, but fortunately some people were there to help along the way. So, I want to take this opportunity to thank them and express my gratitude.

First, I want to thank most importantly my supervisors Michael Hilke and Zaven Altounian; their enlightening suggestions throughout these years has made this work possible. I feel extremely fortunate to have had the chance to work on such an exciting subject with them. I am also very grateful that their enthusiasm toward this research was as high as mine.

I am also indebted to Robert Gagnon, John Smeros and Richard Talbot who have repaired pumps, soldering irons, and various equipment in the lab, and without whom this work would not be complete yet.

Finally, I specially thank my boyfriend Luis whose constant support and understanding in times of crisis has been invaluable. For many reasons, this work would not be complete yet without his suggestions. In fact, it might even not have started in the first place, but he helped me believe that I could do it. Last but not least, other special thanks go to my friend Anne-Sophie who never stopped telling me that I could complete this work, and to my parents, who, even though they still do not understand what I do exactly, have always been supportive with their unparalleled love. I also thank past and current group members for helpful discussion, and Olivier Landry for the fabrication of the scribing machine used to pattern 2DEGs. Other thank yous go to my brother and all my friends for understanding that I did not always have much time for them, but who remained nevertheless supportive. I also want to acknowledge the FQRNT agency for providing the funding that made this research possible.

Statement of Original Contributions

All the results presented in this thesis are the original work of the author. The author has however benefited from suggestions made by M. Hilke and Z. Altounian for the research topics and the analysis of the experimental results.

- In chapter 4, we present experimental results for the critical temperature and temperature dependence of the lower and upper critical field of the superconducting metallic glasses $\text{Fe}_x\text{Ni}_{1-x}\text{Zr}_2$ with $0 \leq x \leq 0.6$. We find that the alloys with $x = 0.5$ and $x = 0.6$ do become superconducting at attainable temperatures. Also, we unexpectedly find that the critical temperature and upper critical field of the alloy with $x = 0.1$ are larger than those for the alloy with $x = 0$, which contradicts what is anticipated from the addition of iron to a superconducting material. The expected dependence is observed in the other alloys.
- In chapter 5, we determine from the analysis of fluctuations in magnetization and anomalous superconducting properties the existence of a transition in amorphous structural order with x in the alloys $\text{Fe}_x\text{Ni}_{1-x}\text{Zr}_2$. Such a change in the amorphous structure of these alloys was not observed before from analysis performed using high resolution electron microscopy [6] and Mössbauer spectroscopy [7].
- In chapter 6, we present Hall resistance data in the superconducting state of the metallic glasses $\text{Fe}_x\text{Ni}_{1-x}\text{Zr}_2$ which reveal the existence of a vortex phase having long-range smectic-like order at high magnetic field just below the transition to the normal state. This phase is also revealed to exist for very low driving current, in opposition to what is suggested in [5]. These findings were also previously published in a peer-reviewed journal [8]. In this same chapter, resistance measurements performed using crossed ac and dc currents are also presented; the combination of ac and dc current proves to be effective and renders the decoupling of the longitudinal and transverse contributions of vortex motion possible. The results thus obtained bring experimental proof for the existence of a critical transverse depinning force; it is also confirmed that the transverse depinning transition is of first-order nature.

List of Symbols

| | | |
|--------------------|---|-----|
| \vec{A} | Magnetic vector potential | 13 |
| $\alpha^2(\omega)$ | Electron-phonon coupling strength | 28 |
| α | Maki parameter | 86 |
| α | Expansion coefficient of GL theory | 13 |
| β | Expansion coefficient of GL theory | 13 |
| \vec{B} | Magnetic field, in general | 11 |
| B_{app} | External magnetic field | 24 |
| B^* | Characteristic magnetic field in the Bean critical state model | 24 |
| B_c | Thermodynamic critical field | 67 |
| B_{c1} | Lower critical field | 17 |
| B_{c2} | Upper critical field | 17 |
| C_{en} | Electronic specific heat in the normal state | 30 |
| C_{es} | Electronic specific heat in the superconducting state | 30 |
| ΔC | Electronic specific heat discontinuity at T_c | 30 |
| D | Electron diffusion coefficient | 67 |
| Δ | Half energy gap | 21 |
| E_g | $E_g = 2\Delta$ Energy gap | 21 |
| $D_n(E)$ | Normal density of states | 23 |
| $D_s(E)$ | Superconducting density of states | 23 |
| $D_{ph}(\omega)$ | Phonon density of states | 28 |
| \vec{E} | Electric field, in general | 11 |
| e | Electronic charge | 11 |
| e^* | Effective electronic charge | 13 |
| ϵ_1 | Vortex line energy | 78 |
| f_n | Free energy per unit volume of the normal state | 31 |
| f_s | Free energy per unit volume of the superconducting state | 31 |
| f_0 | Force per unit length between two vortices separated by a distance λ 157 | |
| f_p | Pinning force per unit length | 159 |
| F_p | Pinning force | 19 |
| f_L | Lorentz force per unit length | 20 |
| F_L | Lorentz force | ?? |
| G_n | Gibbs free energy in the normal state | 33 |
| G_s | Gibbs free energy in the superconducting state | 33 |
| γ | Sommerfeld constant | 30 |
| h | Planck's constant = $6.6260755 \times 10^{-34}$ J s | 15 |
| \hbar | Reduced Planck constant = $\frac{h}{2\pi} = 1.05457266 \times 10^{-34}$ J s | 13 |
| \vec{J} | Current density, in general | 11 |
| J_{dep} | Depinning current density | 37 |
| κ | GL parameter | 14 |

| | | |
|------------------|--|-----|
| k_B | Boltzmann constant = $1.3806568 \times 10^{-23} \text{ J K}^{-1}$ | 21 |
| l | Mean free path | 92 |
| λ | Penetration depth, in general | 14 |
| λ_L | London penetration depth | 11 |
| λ_{e-ph} | electron-phonon coupling parameter | 28 |
| λ_{sf} | Spin fluctuation parameter | 29 |
| λ_{so} | Spin-orbit coupling parameter | 95 |
| l_B | Magnetic length. Average distance between vortices. | 53 |
| M | Magnetization | 31 |
| m_e | Electronic mass | 11 |
| m^* | Effective electronic mass | 13 |
| μ_0 | Permeability of free space = $4\pi \times 10^{-7} \text{ N / A}^2$ | 11 |
| μ^* | Coulomb interaction parameter | 28 |
| n_e | Electron density | 92 |
| $N(E_F)$ | Electronic density of states at the Fermi level | 28 |
| n_s | Number density of superconducting electrons | 11 |
| n_φ | Magnetic flux number density | 18 |
| ν_φ | Vortex velocity | 20 |
| Φ_0 | Flux quantum = $2.06783461 \times 10^{-15} \text{ Wb}$ | 15 |
| ψ | Digamma function | 95 |
| R_{xy} | Hall resistance | 141 |
| R_{xx} | Longitudinal resistance | 141 |
| ρ_n | Normal state resistivity | 67 |
| S_s | Entropy of the superconducting state | 33 |
| S_n | Entropy of the normal state | 33 |
| σ_{ns} | Surface energy between a normal-superconductor interface | 15 |
| σ_{xx} | Magnetoconductivity | 180 |
| t | Reduced temperature T/T_c | 95 |
| T_g | Glass transition temperature | 35 |
| Θ_D | Debye temperature | 29 |
| V | Electron-electron interaction potential | 28 |
| v_F | Fermi velocity | 22 |
| ξ | Coherence length, in general | 14 |
| ξ_0 | BCS coherence length | 22 |
| ξ_{GL} | GL coherence length | 14 |

Superconductivity in metallic glasses ($\text{Fe}_x\text{Ni}_{1-x}\text{Zr}_2$):
from transport and magnetization properties to
vortex dynamics

Introduction

Superconductivity can be described as a quantum state of matter in which a material loses all electrical resistance and can thus carry a current without any energy dissipation, and which also manifests peculiar magnetic properties in that it prevents an external magnetic field from penetrating inside the material. Although a fundamental and microscopic description of the state exposes a multiplicity of other intriguing physical phenomena, the aforementioned characteristics constitute the principal manifestations of the superconducting state that have been exploited in the development of superconductor-based technologies. The major, and often only, attribute of superconductivity which prevents its large scale usage is its appearance at extremely low temperatures: The first superconductor ever discovered in 1911 was mercury, which was found to be superconducting only below a temperature (called the critical temperature T_c) of 4.2 K. Fortunately, the past century has literally seen a race for the development of new superconducting materials which would exhibit this peculiar state of matter at higher and higher temperatures. This quest was quite successful since, by the 1970s, the critical temperature of various niobium intermetallic compounds was found to be above 20 K. The critical temperature then reached a new summit with $T_c=35$ K in 1986 with the advent of a new class of superconducting materials discovered by Bednorz and Müller [9]: the cuprates, in which CuO_2 layers assume most of the electrical conduction and amazing superconducting properties and which, for obvious reasons, are often called the high- T_c superconductors [10]. This jump in T_c was closely followed by another impressive one to T_c over 90 K during the following year in the same class of material. More recently, the observation of

superconductivity in organic materials still gave more impetus to the search for ever higher critical temperatures: In 1993, superconductivity has been reported to set in at temperatures between 60 K and 70 K in C_{60} doped with interhalogen compounds. Organic superconductors have been suggested to be a promising avenue for the chase of high- T_c materials because these molecules can be tailored almost at will and can thus be designed according to structures which will most likely favor superconductivity. However, the all time record T_c is still held by a cuprate superconductor with $T_c = 181$ K reported in January 2008 on a Pb-doped Sn-In-Tm interlayer [11].

The low critical temperature of superconductors is not the only impediment to the development of superconductor-based technologies, as the superconducting state has also been found to be limited by a critical magnetic field B_c and critical current density J_c which, if exceeded ensues destruction of the superconducting state. Indeed, the first projected applied usage of superconductors was in high magnetic field magnets: from winding a superconducting wire into a coil and applying a current to the wire, it was proposed that the absence of electrical resistance in the wire with resulting absence of energy loss to heat would allow enormous magnetic fields to be attained. The use of a solenoid composed of normal metal for the generation of magnetic field, even of a few Tesla, requires a huge amount of energy equivalent to a substantial fraction of the energy consumed by a small city [10]. This is because the resistance of the material infers an energy loss such that continuous supply of a large current is necessary; this energy loss is dissipated as heat and is highly undesirable, especially in cryogenic applications as it causes a large augmentation of the evaporation rate of the cryogenic liquid. Using a superconducting magnet, this problem would easily be circumvented as the absence of dissipation not only means no heat loss, but also that the external current does not need to be continually supplied as once the current is set up, it can flow without any measurable decrease for over 10^5 years [1]. The first tentatives at fabricating such magnets were however not very fruitful as it was observed that only a low magnetic field could be generated before the superconducting state was destroyed. Of course, at the time that these first attempts were made, the

peculiar magnetic properties of superconductors were not known and these observations remained puzzling until the discovery in 1933 that the superconducting state can be destroyed by a magnetic field; the destruction of superconductivity by a very low magnetic field was originally thought to arise because of the presence of impurities in the material [12]. Since then, a number of superconducting materials with desirable magnetic properties have been designed and found to be suitable for the production of high magnetic fields: for instance, widely-used NbTi magnets typically have a critical field as high as 10 T, while 45 T fields can be generated by hybrid magnets composed of NbTi and Nb₃Sn coils. Although the superconducting cuprates mentioned above have been shown to exhibit highly desirable properties as regard to their high critical temperature, they are however plagued by the fact that they often exhibit very low critical currents preventing their use in superconducting coils for the generation of large magnetic fields.

Another technological application of superconductivity is in electrical power distribution networks in which the benefits are obvious and can be substantial. Superconducting power transmission cables are expensive, but even accounting for the energetic cost of the cooling technology, it has been evaluated that the energy waste is halved [13] compared to the waste in regular copper transmission lines in which an enormous amount of energy is lost as heat. Superconducting power transmission lines are already in use in some densely populated regions of Mexico, Denmark and in the United States where the energy demand is high and the distances are short; it has also been estimated that the projected use of superconductor technology in Japan in 2010 could lead to an annual energy saving equivalent to 100 terawatt hours of power and result in a reduction of CO₂ emissions of 100 million tons per year [14]. Other technological applications of superconductors relying mostly on their magnetic properties are SQUIDS (superconducting quantum interference devices) which are used to measure small magnetic fields with an extreme sensitivity of about 10^{-15} T / Hz [14]. The famous Maglev (for magnetic levitation) trains also use superconductivity and electromagnetic forces to suspend the train, guide it and propel it at incredi-

ble speeds; the record speed being 581 km/h was attained in Japan in 2003 [15]. Superconductors can also be used in current limiting devices, resonators and filters, electrical transformers and as energy storage devices [14].

Considering all these applications of superconductivity and with the growing energy demand worldwide, it is indubitable that superconductor-based technologies will see a growing interest in the near future. However, there remains important issues that need to be solved for their more widespread use, and those do not lie only in the problem of the low operating temperatures. It has become evident now that beyond a high T_c , other material properties are important for applications, such as a large critical current density and critical magnetic field. Unfortunately, notwithstanding their desirable high critical temperature, high- T_c superconductors have shown disappointing properties with respect to their critical current density, and are also problematic because of the difficulty in producing large, robust and homogeneous samples with the right stoichiometry (which is highly important in these materials for the obtaining of high- T_c s) [10]. This is one of the reasons why the use of niobium-based alloys prevails for many applications which, despite their lower critical temperatures, offer more advantageous electrical properties and are easier to produce.

Setting aside the issues related to technological applications, other fundamental properties related to the superconducting state remain unsolved and constitute highly interesting problems from a physical standpoint. Indeed, the study of particle interaction and of highly correlated systems in the framework of superconductivity becomes less intuitive. For instance, as will be discussed in the next chapter, superconductivity essentially results from a positive interaction between two electrons; this is quite an uncanny concept as we are used to think in a context in which two electrons repel each other due to the Coulomb force. Therefore, in such a context, it is not surprising that many of our ideas about physical phenomena and interaction processes need to be revised. For instance, as will also be discussed in the next chapter, there exists a class of superconductors which allows the penetration of magnetic flux in its interior, but only in a quantized fashion; these quantized units of magnetic flux

are called vortices. The interaction between vortices in the superconducting state remains a puzzling problem today and its understanding is essential for the development of better superconductors. This is motivated by the fact that as a vortex moves in a superconductor, it dissipates energy which is seen in the development of a resistance across the superconductor; even though it remains in the superconducting state, this superconductor no longer exhibits the desirable property of perfect conductivity. Superconducting materials can be designed such that vortex motion does not result unless an enormous driving current is applied. This is the case in the NbTi and Nb₃Sn superconducting wires used to make the high-field superconducting magnets discussed above. On the other hand, superconducting materials in which vortex motion is easily induced by a low driving current are also interesting because they offer a unique setting for the study of moving vortex interaction which is now known to result in a variety of vortex phases. These vortex phases, much like phases found in ordinary matter such as the solid and liquid phases, can be governed by external variables such as magnetic field (which controls density) and temperature. The subject of vortex phases will be more extensively discussed in chapter (6).

The experiments presented in this thesis were all performed on amorphous superconducting alloys of Fe_xNi_{1-x}Zr₂ with $0 \leq x \leq 0.6$. Although these materials exhibit a low critical temperature of about 2 K depending on the iron content, they exhibit many interesting properties for the study of fundamental superconducting properties related to the purity and structure of the alloys, and also for the study of dynamic vortex phases. Indeed, in the first place, the amorphous nature of these alloys confers them a low critical current which eases vortex motion and permits the study of dynamic vortex phases. Similarly, material purity also affects the critical current density and vortex motion. The chemical composition of these alloys is also highly interesting as the presence of the ferromagnetic Fe and Ni atoms greatly influences the superconducting state. Knowing that (ideal) superconductors completely prevent the penetration of magnetic flux in their interior, it is not surprising that a superconductor in which ferromagnetic atoms are present would see its properties altered.

Although the presence of the Fe atoms does not completely destroy the superconducting state, it is seen that it greatly affects it by lowering superconducting critical parameters such as T_c , B_c and J_c .

The general organization of this thesis will be as follows: An introduction to the general and basic theories of superconductivity and related phenomena will first be introduced to familiarize the reader with the concepts of superconductivity and to explain its origin. Then, a more thorough description of the particularities of the $\text{Fe}_x\text{Ni}_{1-x}\text{Zr}_2$ amorphous alloys will be presented, along with the experimental methods employed for the measurements. Finally, the experimental data and analysis will be presented along with theoretical background relevant to that specific topic of superconductivity. The presentation of the experimental data will be divided into three chapters, each investigating a different aspect of superconductivity in the $\text{Fe}_x\text{Ni}_{1-x}\text{Zr}_2$ amorphous alloys. The first data analysis chapter will present the general superconducting parameters of the alloys such as their critical temperature and fields as obtained from resistance measurements as a function of magnetic field and temperature, and from magnetization measurements. Theoretical predictions pertaining to the measured parameters will also be described and compared to experimental values. The purpose of this is to determine how the $\text{Fe}_x\text{Ni}_{1-x}\text{Zr}_2$ alloys compare to other superconductors and also to establish the dependence of superconducting parameters on the relative amount of iron in the alloys. The second data analysis chapter will concentrate on the x -dependence in the $\text{Fe}_x\text{Ni}_{1-x}\text{Zr}_2$ alloys as regard to physical structure and chemical composition probed by observations in the superconducting state. It will be demonstrated that the observation of fluctuations in the magnetization can be correlated with the Fe content in the superconducting material. It will also be established that a structural transition with x exists in this series of alloys; this conclusion will be reached from the analysis of anomalous hysteresis loops observed at the B_{c2} transition in some of the alloys. The third of these chapters will complete the presentation of experimental results with a study of dynamic vortex phases in the $\text{Fe}_x\text{Ni}_{1-x}\text{Zr}_2$ superconducting alloys probed by lon-

gitudinal and transverse (Hall) resistance measurements performed using ac and dc currents. The results will confirm theoretical predictions about transversely-ordered dynamic vortex phases. For instance, it has been predicted theoretically that in the weak-pinning regime, the moving vortex lattice orders into a phase called the moving Bragg glass (MBG) [5, 16] characterized by vortex motion in coupled channels. As a consequence of the existence of these channels, transverse vortex motion would be seriously inhibited; this would also result in the existence of a transverse critical force [5, 17, 18, 19, 20, 21] which would also be the order parameter of the MBG [5]. For larger disorder strength and driving force, vortex motion would still proceed in channels in a phase having smectic order called the moving transverse glass (MTG) [5]; in this phase, a decoupling of the channels is however predicted [22] which we show results in large-scale channel reorientation.

Theory of superconductivity

The number of new discoveries and applications stemming from the phenomenon of superconductivity has not ceased growing since its first observation by Kamerlingh Onnes in his Leiden laboratory in 1911 [23]. At the time, he observed one of the two main characteristics of the superconducting state, that is the loss of any resistivity of a material below a certain temperature, subsequently called the critical temperature T_c , above which the superconductor is simply called “normal”. It was only in 1933 that the second main characteristic of the superconducting state, which differentiates superconductors from merely perfect conductors, was observed by Meissner and Ochsenfeld [24]. This characteristic is perfect diamagnetism, according to which a superconductor does not allow an external magnetic field to penetrate in its interior. Not content with simply being a perfect diamagnet, superconductors also have the property to expel an external magnetic field which would be present in their interior when they undergo the transition from the normal to the superconducting state: this property is what is now known as the Meissner effect. Shortly after the first observation of this effect, the London brothers, Fritz and Heinz, expressed this magnetic behaviour of superconductors into electromagnetic equations [25]; that was in 1935. Fifteen years passed before the next theoretical milestone: Named the Ginzburg-Landau (GL) theory after the names of its authors [26], this relatively simple phenomenological approach describes superconductivity in terms of an order parameter. The London predictions were found to arise as a natural consequence of this theory. Unfortunately, the GL theory was not very well accepted outside the Soviet Union until Gor’kov showed, in 1959, that it is derivable from the widely accepted microscopic

BCS theory published in 1957 [1]. The advent of the BCS theory, elaborated by J. Bardeen, L. Cooper, and J. R. Schrieffer [27], really marks the takeoff of this field of research and still reflects our understanding of the superconducting phenomenon today. This microscopic theory describes the superconducting state as being composed of bound electron pairs, called the Cooper pairs, which carry the supercurrent; it also describes the superconducting state as being separated from the normal state by an energy gap, proportional to the critical temperature of the superconducting material. These theories, which have forged our present knowledge of superconductivity, will be described in the next chapter in order to acquaint the reader with the basic ideas necessary to understand the results presented in subsequent chapters.

2.1 Superconductivity in a nutshell

In order to ease the introduction of the reader to the subject of superconductivity, we present in this section an overview of superconducting phenomena without going into the mathematical details, and delay the presentation of those to the following sections.

There exist two main types of superconductors, both characterised by the vanishing of their electrical resistance below a critical temperature T_c in a second order phase transition in the absence of a magnetic field. The transition at T_c is first order in the presence of a magnetic field, because then, as we will see later, the thermodynamic state changes discontinuously and a latent heat is associated with the transition. The first type of superconductors, called type I, comprises the pure elements: for instance, mercury (Hg), indium (In), zirconium (Zr), etc. As a rule of thumb, superconductors are generally not very good conductors in their normal state, and good conductors do not exhibit superconductivity (for instance copper (Cu), silver (Ag) and gold (Au)), or do only at extremely low temperature [2]. The reason for this will be discussed later in the text. The other type of superconductors, not surprisingly called type II, is a vast class which comprises all the alloys, heavy-fermions, perovskites, organic, and high- T_c copper oxide superconductors, and with the addition of niobium (Nb) which

is the only element to exhibit type-II superconductivity. The difference between the superconducting properties of type I and type II superconductors lies in their magnetic properties: Whereas type I superconductors show perfect diamagnetism, i.e. they exclude and expel an external magnetic field up to some critical field B_c above which the superconducting state is destroyed in a first order transition, type II superconductors do permit some magnetic field to penetrate in their interior without destroying the superconducting state and they can still carry electrical current without dissipation. The magnetic properties of type II superconductors are characterized by three critical fields, B_{c1} , B_c , and B_{c2} : for external fields below the lower critical field B_{c1} , they exhibit perfect diamagnetism and the Meissner effect just like type I superconductors. However, for fields larger than B_{c1} , it becomes energetically more favorable to allow the field to enter the superconductor in the form of quantized flux tubes: in this state, diamagnetism is no longer perfect, but the superconducting state nevertheless survives [1]. The number of flux tubes in the superconductor increases proportionally to the applied magnetic field until the upper critical field B_{c2} is reached, at which point superconductivity is destroyed in a second order transition. In type II superconductors, the thermodynamic critical field B_c is larger than B_{c1} but lower than B_{c2} ; as it does for type I superconductors, it still describes important properties of the superconducting state, but as regard to magnetic properties it does not directly appear in the observables.

Just as there exists a limit to the magnitude of an external magnetic field which will not destroy the superconducting state, there also exists a limit to the amount of current that a superconductor can carry without the superconducting state being destroyed. This limiting current is called the critical current density J_c and is a direct result of the existence of a critical field. Indeed, a circulating current itself produces a magnetic field proportional to the magnitude of the current; when the current is sufficiently large to generate a self-field which exceeds the critical field, superconductivity is destroyed [2]. J_c can also be the current density necessary to break a sufficient amount of Cooper pairs to destroy superconductivity.

The critical temperature, magnetic field and current density are the main external variables that can influence the superconducting state; these depend mainly on the composition of the superconducting material, but can also depend on the structural phase of the material and on its preparation conditions.

2.2 The London equations

The London equations provide a simple mathematical model of the superconducting state including a description of one of the most important parameters describing the superconducting state: the London penetration depth λ_L . As we will see, λ_L provides the length scale over which an external magnetic field penetrates into the superconductor and over which the screening current flows; it is given by [2, 1]

$$\lambda_L = \left(\frac{m_e}{\mu_0 n_s e^2} \right)^{1/2}, \quad (2.1)$$

where μ_0 is the permeability of free space, m_e and e are respectively the electron mass and charge, and n_s represents the number density of superconducting electrons. n_s is expected to be zero at $T = T_c$ (for continuity at the normal to superconducting state transition), and increases progressively as the temperature is lowered to a value close to the normal state electron density as T approaches zero. The first London equation,

$$\vec{E} = \mu_0 \lambda_L^2 \frac{d\vec{J}}{dt} \quad (2.2)$$

where \vec{E} is an electric field, and \vec{J} a current density, portrays perfect conductivity as it describes how any electric field accelerates the electrons rather than sustains their velocity as it does for a normal conductor described by Ohm's law ($\vec{J} = \sigma \vec{E}$, where σ is the conductivity). The second London equation,

$$\vec{B} = -\mu_0 \lambda_L^2 \vec{\nabla} \times \vec{J} \quad (2.3)$$

where \vec{B} denotes the magnetic field, explains the Meissner effect as it describes the existence of a screening current even for a magnetic field constant in time. Combining equation (2.3) with Ampère's law (in the absence of displacement currents)

$$\vec{\nabla} \times \vec{B} = \mu_0 \vec{J} \quad (2.4)$$

one obtains

$$\nabla^2 \vec{B} = \frac{\vec{B}}{\lambda_L^2} \quad (2.5)$$

from which it is deduced that the magnetic field is exponentially screened from the interior of a superconductor over a distance λ_L . Moreover, from Ampère's law and the London equations, one sees the relation between the magnetic field and current density in a superconductor: if one is present in a region, then so must be the other. Empirically, the temperature dependence of the penetration depth is given approximately by

$$\lambda_L(T) \approx \lambda_L(0) \left[1 - \left(\frac{T}{T_c} \right)^4 \right]^{-1/2} \quad (2.6)$$

i.e. it has a finite minimal value $\lambda_L(0)$ at $T = 0$ and increases with increasing temperature to vanish at T_c .

2.3 Ginzburg-Landau theory: Main ideas

As mentioned above, the Ginzburg-Landau theory [26] was not well recognized in the decade following its publication, especially in Western literature; however, after it was shown that it could be derived from the BCS theory [27] and that it correctly predicted many observable properties of superconductivity, it received more recognition. The theory introduces a complex pseudowavefunction $\psi(x)$ as an order parameter which describes the local density of superconducting electrons. This $\psi(x)$ relates to the density of superconducting electrons of the London theory according to $n_s = |\psi(x)|^2$. The GL theory is however much more powerful than the simple London theory because it can handle nonlinear effects due to the change of n_s brought by strong magnetic fields and spatial variation of n_s [1].

Order parameters are used to describe transitions between ordered and disordered states; these are common in nature, and can represent, for instance, a ferromagnetic transition for which the order parameter is the magnetization. In this case, the mag-

netization assumes a value in the high-temperature disordered state and another value in the low-temperature ordered state. In this respect, one can see the order parameter as providing an indication for the degree of alignment in the system. Returning to superconductors, the order parameter $\psi(x)$ proposed in the GL theory and which is related to the number of superconducting electrons assumes a null value in the normal state, as there are no superconducting electrons there except possibly close to T_c due to fluctuations. At T just below T_c , $\psi(x)$ assumes a finite but small value which increases as the temperature is decreased. In this manner, $\psi(x)$ provides a measure of the order that exists in the superconducting state [2, 1].

2.3.1 The GL equations

To formulate their theory, Ginzburg and Landau presumed a local functional of the order parameter expansion of the Gibbs free energy valid close to T_c . Then, assuming that the free energy must be a minimum with respect to variation of the order parameter and taking the variational derivative with respect to ψ of the series expansion of the free energy, they derived the first GL equation, with expansion coefficients α and β [2]

$$\frac{1}{2m^*} \left(i\hbar\vec{\nabla} + e^*\vec{A} \right)^2 \psi + \beta |\psi|^2 \psi + \alpha(T) \psi = 0, \quad (2.7)$$

in which m^* and e^* are respectively the effective mass and charge of the super electrons, \hbar is Planck's constant and \vec{A} is the magnetic vector potential. Taking the variational derivative of the Gibbs energy series expansion with respect to \vec{A} instead of ψ yields the second GL equation which gives an expression for the supercurrent density

$$\mu_0 \vec{J} = \frac{i\hbar e^*}{2m^*} \left(\psi^* \vec{\nabla} \psi - \vec{\nabla} \psi^* \psi \right) - \frac{e^{*2}}{m^*} \vec{A} |\psi|^2. \quad (2.8)$$

The two GL equations are coupled differential equations which, except for simple limiting cases, need to be solved numerically to obtain information on the superconducting state. Example limiting cases which can be solved in closed form are the zero field case, deep inside the superconductor, or near the boundary [2]. For instance, in the absence of a magnetic field, deep inside the superconductor, it is determined that

the order parameter assumes the value

$$\psi_\infty = \sqrt{\frac{|\alpha|}{\beta}}. \quad (2.9)$$

We will not present the details of these solutions because this would unduly extend the length of this section and thorough knowledge of these derivations is not necessary for the understanding of the data that will be presented in the body of this work. However, we felt it necessary to introduce the basic ideas of the GL theory because it is recognized now as a milestone in the development of our present understanding of the theory of superconductivity, and is a *chef d'oeuvre* of physical intuition.

2.3.2 Consequences of the GL theory

One of the main achievements of the GL theory is the introduction of a coherence length ξ , which we will subsequently refer to as the GL coherence length ξ_{GL} , which represents the distance over which ψ can vary without significant energy increase [1]. It turns out that

$$\xi_{GL}(T) = \frac{\hbar}{|2m^*\alpha(T)|^{1/2}}; \quad (2.10)$$

this length scale, and similar length scales issuing from other theories of superconductivity, will emerge continually in discussing superconducting properties. Take note that $\xi_{GL}(T)$ diverges close to T_c (since α vanishes at T_c) and decreases with temperature to reach the value of the BCS coherence length ξ_0 far below T_c (see section (2.6)). Another important consequence of the GL theory is the establishment of a new parameter composed of the ratio of the two characteristic superconducting lengths encountered so far: the penetration depth λ and the coherence length. As will be shown later, this GL parameter

$$\kappa = \frac{\lambda}{\xi} \quad (2.11)$$

plays an important role in the determination of the type (I or II) of a superconductor.

2.3.3 Flux quantization

As briefly introduced above, one of the strengths of the GL theory is the possible treatment of superconductors in a finite magnetic field. Indeed, writing the order

parameter as the product of a modulus and a phase factor, i.e. $\psi(x) \rightarrow |\psi(x)| e^{i\theta}$, inserting this into equation (2.8) and taking the line integral around a closed contour, one is led to the conclusion that, in order for the order parameter to be single valued, the amount of flux within the path integration must be quantized, with flux quantum

$$\Phi_0 = \frac{h}{e^*} = \frac{h}{2e}. \quad (2.12)$$

As will be established later, Φ_0 is the amount of magnetic flux held by single vortices, or flux tubes allowed to penetrate in type II superconductors when the applied field is between B_{c1} and B_{c2} .

2.4 Type I and type II superconductivity

As noted by London, by excluding an external magnetic field in the Meissner state, a superconductor increases its energy by an amount $\frac{B^2}{2\mu_0}$ per unit volume, such that unless a boundary energy exists, the superconductor cannot lower its energy sufficiently to enter a state of equilibrium. The calculation of this interface surface energy σ_{ns} constitutes one of the cases in which the value of the GL parameter κ exhibits a special value which allows the GL equations to be solved relatively easily [2]. And the result is worth the work because it leads to the establishment of the criteria leading to the definition of type I and type II superconductivity. Indeed, depending on the superconducting parameters ξ and λ , it is found that a state composed of alternating superconducting and normal regions, called the mixed state, is energetically more favorable if the contribution due to the surface energy exceeds the extra magnetic energy.

Defining the surface energy as the free energy per unit area between a homogeneous phase (fully normal or superconducting) and a mixed phase, one finds that if $\sigma_{ns} > 0$, the homogeneous phase has lower energy than the mixed phase, such that the superconductor will completely exclude an external magnetic field until it reaches a magnitude B_c above which the superconducting state is destroyed. These superconductors are called type I superconductors. On the contrary, if the surface energy

between homogeneous phase and mixed phase is negative, i.e. $\sigma_{ns} < 0$, then the superconductor is unstable to the formation of normal-superconducting interfaces and flux entry in the superconductor will be allowed, not destroying the superconducting state until a field B_{c2} is exceeded. These superconductors are type II superconductors [2]. It is found that the value of the GL parameter which leads to zero surface energy is $\kappa = \frac{1}{\sqrt{2}}$, thereby establishing that superconductors with $\kappa < \frac{1}{\sqrt{2}}$ are type I superconductors, and superconductors with $\kappa > \frac{1}{\sqrt{2}}$ are type II superconductors.

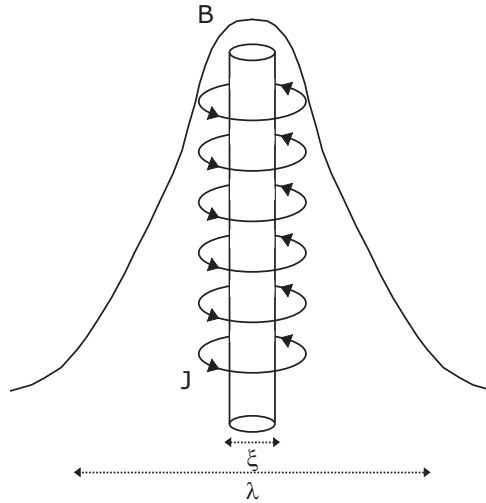


Figure 2.1: Schematic representation of a vortex with core size ξ and size λ showing the magnitude of the magnetic field and the circulating supercurrent.

2.5 Vortices

In the mixed state, or vortex state of type II superconductors, flux entry is allowed in a quantized fashion with single vortices carrying an amount of flux Φ_0 . As a sound approximation, a vortex is composed of a normal core of size ξ in which most of the flux is confined, and such that the superelectron density n_s varies from 0 inside the core to its bulk value at distance ξ at the core boundary. A supercurrent circulates around the core, over a distance λ to screen the magnetic flux [2]. Accordingly, vortices are generally depicted as having size λ ; a schematic representation of a vortex is shown in Fig.(2.1). As can be deduced from Fig.(2.2) which shows the variation of the order

parameter and the field inside low and high- κ superconductors, a large value of ξ , such as found in type I superconductors, can be seen as preventing n_s from increasing fast enough to provide the screening current necessary to shield the magnetic flux.

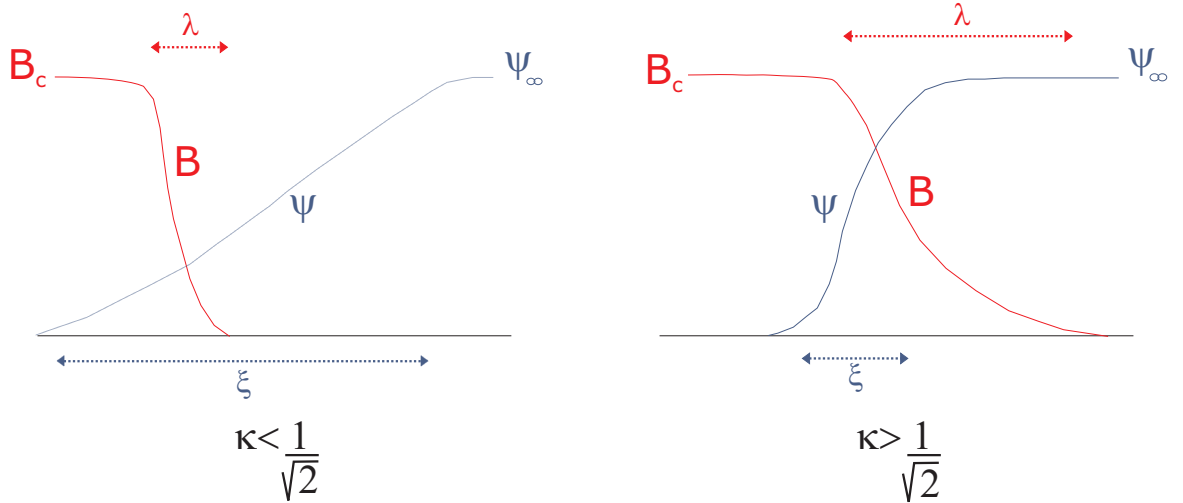


Figure 2.2: Schematic representation of the field B and the order parameter ψ at the interface between a normal region and a superconducting region for a type I superconductor (left) and a type II superconductor (right). In red: properties pertaining to the magnetic field. In blue: properties pertaining to ψ . (Inspired from Fig.(4.3) of Ref.[1])

The appellation of type I and type II superconductors is due to Abrikosov [28] who, in 1957, was the first to consider the case $\xi < \lambda$ leading to negative surface energy between a normal and a superconducting region. He also predicted that at low vortex density, close to the flux entry field B_{c1} , the vortices arrange in an array such as to lower their energy. Because vortex-vortex interaction is repulsive, it can be deduced that the configuration which will result in the state of minimal energy is that which will maximize the distance between them. This optimal configuration is that of a triangular lattice, such as shown in Fig.(2.3) and which bears the name Abrikosov lattice. Ironically, because of a numerical error, Abrikosov initially predicted that the vortices should arrange in a square array. As will be discussed in more detail later, the vortices assume the perfect arrangement of the Abrikosov lattice only at low density and in an ideal superconductor without impurities nor inhomogeneities.

An estimate for the upper critical field B_{c2} can be obtained by considering the

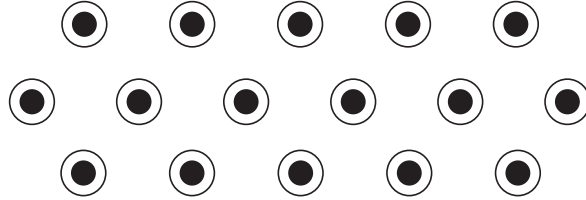


Figure 2.3: Representation of the triangular vortex lattice, or Abrikosov lattice.

following appealing simplification: Assuming that the superconducting state is destroyed when the superconductor is completely filled with vortices and such that the vortex cores nearly overlap, then

$$B_{c2} \approx \frac{\Phi_0}{\pi\xi^2} \quad (2.13)$$

because each vortex carries a flux quantum Φ_0 and the vortex cores have a radius of ξ . From this, it can also be deduced that the density of vortices in a superconductor is directly related to the applied field according to

$$n_\varphi \approx \frac{B_{app}}{\Phi_0}. \quad (2.14)$$

2.5.1 Vortex matter

As introduced above, under ideal conditions, i.e. in the absence of inhomogeneities or impurities, and of a driving force sufficiently large to induce vortex motion, the flux line lattice (FLL) assumes a triangular arrangement as dictated by the vortex repulsive force. Numerous conditions can alter this perfect arrangement: the presence of impurities or material defects provides pinning centers for the vortices which can distort the triangular lattice, but which can also prevent the vortices from moving under the action of an external force. Vortex motion and pinning will be overviewed in the next sections and will be discussed to a deeper extent in chapter (6) when we presents results from experiments on the dynamics of the vortex state.

Flux pinning

Pinning centers, which refer to locations in the superconductor through which the vortices can pass in order to lower their energy, arise at almost any material imperfection: impurities, point defects, structural inhomogeneities, columnar defects,

inclusions, oxygen vacancies, grain boundaries, etc. All these types of material imperfections have in common that they induce local variations of superconducting parameters such as ξ , λ , B_c , or ψ , which in turn induce local variations of the vortex line energy, thereby creating locations in the material where it is energetically favorable for flux lines to pin [1]. The strength of pinning centers is defined as the pinning force F_p , which is simply given by the Lorentz force necessary to depin the vortices (see next section for a definition of the Lorentz force). Inhomogeneities about the size of ξ or λ are found to be most effective at pinning because these length scales are respectively about the size of the vortex core and the size of the whole vortex, such that they really allow the vortex line to lower its energy. On the contrary, inhomogeneities on the atomic scale do not alter the pinning potential and only favor electronic scattering, thus diminishing the electron mean free path [1]. A large pinning force in superconductors is often desirable for practical applications; indeed, even in the presence of a large magnetic field, type II superconductors having a high degree of pinning are as good as a perfect superconductor and do not dissipate energy from vortex motion. Furthermore, for many applications, type II superconductors are more appropriate than type I superconductors because the latter often exhibit a very low critical field compared to the former.

Flux creep

Even in the presence of strong pinning centers, some amount of vortex motion is unavoidable at finite temperature because of thermal energy which allows a type of vortex motion called flux creep. Flux creep refers to the thermally activated hopping of vortices from one pinning site to another. This type of motion is typically unobservably slow – creep velocities of the order of 10^{-7} cm/s have been measured [1]– and dissipates a small but finite amount of energy. The time dependence of flux creeping is logarithmic, meaning that as a result of any flux creep motion, the creep rate gets slower and slower; this is because any creep that occurs relieves the flux density gradient. This type of vortex motion is obviously much more important in high- T_c superconductors, simply because of the high operating temperature which

often exceeds 77 K in the copper oxides.

Flux flow

Flux flow refers to a regime of vortex motion with velocity larger than that of flux creep and for which the Lorentz force exceeds the pinning force. The Lorentz force per unit length

$$\vec{F}_L = -\vec{J} \times \vec{B} \quad (2.15)$$

is provided by the combination of a driving current and a magnetic field, and results in vortex motion once it exceeds the pinning force. For many applications, vortex motion is undesirable because it leads to energy dissipation according to which a measurable electric field

$$\vec{E} = \vec{B} \times \vec{v}_\varphi \quad (2.16)$$

is induced in the sample (\vec{v}_φ refers to vortex velocity), which means that even though the sample is still in the superconducting state, it no longer exhibits zero resistivity. Despite its disadvantages for practical purposes, vortex motion is a flourishing research subject, as the interplay between vortex elastic interaction, density (as dictated by an external field), and driving force have been shown to yield a variety of vortex phases. In very clean superconductors exhibiting weak-pinning properties, flux flow is induced by very small driving currents which makes them ideal for the study of vortex phases since it circumvents all the inconveniences related to the use of a large driving current such as the augmentation of sample temperature. Flux motion and resulting dynamic vortex phases in weakly-pinned superconductors will be discussed in more detail in chapter (6).

2.6 Results from the BCS theory

The GL theory presented above explains to a sufficient extent the phenomenological properties of superconductivity, but it lacks an explanation for the microscopic origin of superconductivity. Fortunately, the BCS theory [27], which focuses on the microscopic phenomena of superconductivity and its origins fills all these gaps and

still constitutes today the most complete and exact description of the superconducting state. Interestingly, the GL theory can be derived from the BCS theory, as was shown by Gor'kov in 1959 [29], with the values for the effective electronic mass and charge, which were left unspecified in the GL theory, now embedded in the BCS theory as $m^* = 2m_e$ and $e^* = 2e$. The high level of the mathematical formalism used in the BCS theory makes it very difficult to grasp without the language of second quantization. We will therefore only introduce here the main ideas and results of the theory.

Whereas the treatment of superconductivity by Ginzburg and Landau focused on superconducting electrons, the BCS theory describes quasi-particle excitations. In this picture, the particles composing the superconducting state are the Cooper pairs, a bound pair of electrons; hence the determination of $m^* = 2m_e$ and $e^* = 2e$ mentioned above. In 1956, before the publication of the theory which revolutionized our understanding of superconductivity, Cooper showed that the electron gas is unstable against the formation of bound electron pairs, and that even a weak interaction between two electrons, such as that caused to second order by the electron-phonon interaction could be sufficient to bind them: The Cooper pair was born. The two electrons composing a Cooper pair generally have opposite momentum wavevectors and spins as required for symmetry of the orbital part of the wavefunction describing the superconductor. A Cooper pair can be broken apart if it receives a sufficient amount of energy 2Δ which also defines the size of the energy gap E_g between the superconducting ground state and the quasi-particle excitations. The theory yields that the critical temperature of a particular superconductor is directly proportional to the size of this energy gap according to

$$E_g = 2\Delta(0) = 3.528k_B T_c \quad (2.17)$$

where k_B is Boltzmann constant, $\Delta(0)$ defines the size of the energy gap at $T = 0$, and E_g is the energy gap and is the minimum energy required to break a Cooper pair, i.e. an amount of energy Δ is required to excite each electron composing the pair above the energy gap. The size of the energy gap is null at T_c and increases with

decreasing temperature to reach the value $\Delta(0) = 1.764k_B T_c$ at $T = 0$; the numerical factor has been corroborated in many experiments.

It is determined that the spatial extent of the Cooper pair is given by the so-called BCS coherence length ξ_0 ,

$$\xi_0 \equiv \frac{\hbar v_F}{\pi \Delta(0)} \quad (2.18)$$

where v_F is the Fermi velocity. Incidentally, ξ_0 is nearly temperature-independent, and reduces to about the size of the mean free path l for small l [14]. In contrast, the GL coherence length introduced previously depends on temperature, and represents the smallest length over which the Cooper pair density can vary. According to this, many Cooper pairs exist over the length ξ_{GL} , such that it is always larger than ξ_{BCS} which represents the average extension of a single Cooper pair.

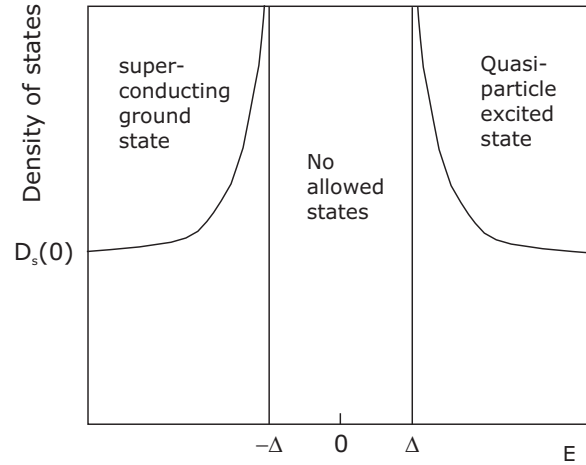


Figure 2.4: Superconducting density of states $D_s(E)$ in the neighborhood of the energy gap. (Adapted from Fig.(6.4) of Ref.[2].

Because of the existence of the energy gap between the superconducting ground state and the quasi-particle excited state, it can be shown that the density of states assumes the behavior shown in Fig.(2.4), and which obeys the following dependencies:

$$D_s(E) = \begin{cases} \frac{D_n(0)E}{\sqrt{E^2 - \Delta^2}} & E > \Delta \\ 0 & -\Delta < E < \Delta \\ \frac{-D_n(0)E}{\sqrt{E^2 - \Delta^2}} & E < -\Delta \end{cases} . \quad (2.19)$$

These equations make it obvious that no states with energy inside the gap are allowed, and that the density of superconducting states $D_s(E)$ is proportional to the normal density of states $D_n(0)$ and approaches its value in the neighborhood of the gap. Also, close to the gap energy, the superconducting density of states is greatly enhanced.

2.7 Bean critical state model

Leaving the rigorous framework of the BCS treatment of superconductivity, we present here a critical state model which treats the presence of currents and magnetic fields in a superconductor based on electrodynamic expressions. The critical state refers to a state in which a critical current flows in a superconductor in order to shield its interior from an external magnetic field [2]. As discussed in section (2.2), and according to Maxwell's equation (2.4), such shielding currents flow in a superconductor only where a magnetic field is present; for weak magnetic fields, both the current and field only occupy a thin layer at the edges of the superconducting material and the internal field remains zero. As the magnetic field is increased, both the field and the current present in the superconductor penetrate more deeply into the material to eventually invade the material completely. Various models have been proposed to describe the current and field distribution in the critical state, the most popular of which is unarguably the one proposed by Bean in 1962 [30, 31], which also shines by its simplicity. The Kim model [32, 33], according to which the current flowing in a superconductor depends on both the critical current density and the magnitude of the magnetic field in the sample, has also been extensively used; incidentally, it reduces to the Bean model for weak applied magnetic fields. Another model, by Ji *et al* [34]. and Le Blanc and Le Blanc [35], makes the assumption of constant pinning to describe the current distribution in the critical state and resembles the Kim model for high external fields. We will introduce here only the Bean critical state model because it is by far the most widely applied, and because we will discuss a model closely related to the Bean model in the analysis of data that will be presented in chapter (5).

The Bean critical state model assumes that, whatever the external field is, the current flowing within a superconductor is the critical current, such that for low applied fields the shielding current has magnitude $|J_c|$ and flows in a thin layer on the surface of the superconductor; the size of the layer over which the current flows then increases as the magnitude of the external field increases while the current density remains J_c . The Bean critical state model considers two cases, the low-field and the high-field cases, and describes the current and field distribution according to the Bean model in these two limits. The high and low field limits are defined in terms of a characteristic field $B^* = \mu_0 J_c a$ where a is the half width of a superconducting slab: the low field limit obeys $B_{app} < B^*$ while the high field limit obeys $B_{app} > B^*$. B^* represents the value of the applied field for which the internal field of the superconductor just reaches the middle of the slab, as shown by the red line in Fig.(2.5a).

2.7.1 Low-field limit

Assuming the geometry depicted in Fig.(2.5b) according to which the critical current flows in a superconducting slab over a layer from the boundary at point $|a|$ to a point $|a'|$ in the superconductor, the current density in the superconductor is given by

$$\begin{aligned} J_y(x) &= J_c & -a \leq x \leq -a' \\ J_y(x) &= 0 & -a' \leq x \leq a' \\ J_y(x) &= -J_c & a' \leq x \leq a \end{aligned} \quad (2.20)$$

as depicted by the black line in Fig.(2.5b). From equation (2.4), it can be deduced that the internal magnetic field $B_z(x)$ must have a linear dependence on x in regions where a current flows such that the magnetic field in the superconductor distributes according to

$$\begin{aligned} B_z(x) &= B_{app} \left(\frac{a'+x}{a'-a} \right) & -a \leq x \leq -a' \\ B_z(x) &= 0 & -a' \leq x \leq a' \\ B_z(x) &= B_{app} \left(\frac{x-a'}{a-a'} \right) & a' \leq x \leq a \end{aligned} \quad (2.21)$$

and the critical current density is

$$J_c = \frac{B_{app}}{\mu_0 (a - a')}. \quad (2.22)$$

The resulting pinning force, which equals the Lorentz force (equation (2.15)) necessary to depin the vortices is thus obtained from

$$\begin{aligned} F_p(x) &= J_c B_{app} \left(\frac{a'+x}{a'-a} \right) & -a \leq x \leq -a' \\ F_p &= 0 & -a' \leq x \leq a' \quad , \\ F_p &= J_c B_{app} \left(\frac{x-a'}{a-a'} \right) & a' \leq x \leq a \end{aligned} \quad (2.23)$$

from which it is deduced that the pinning force is larger for larger critical current densities. The critical current, field and pinning force distribution for the low-field case are shown as the black lines in Fig.(2.5).

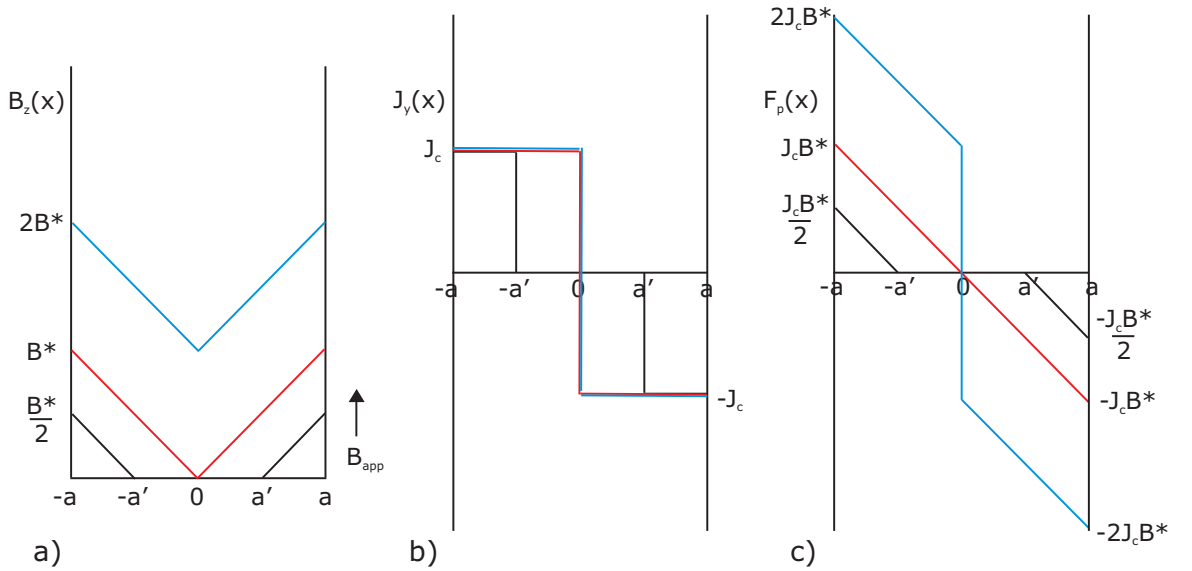


Figure 2.5: Representation of a) the field distribution b) the current density distribution c) the pinning force density in a superconductor according to the Bean critical state model for increasing applied field.

2.7.2 High-field limit

In the high field case, field penetration has reached the middle of the width of the superconducting slab at $B_{app} = B^*$ and upon further increase of the external field, the magnitude of the field inside the superconductor simply increases, as can be seen from the blue line in Fig.(2.5a). In this case, only two regions exist in the superconductor,

both traversed by a current and a field according to

$$\begin{aligned}
 J_y(x) &= J_c & -a \leq x \leq 0 \\
 J_y(x) &= -J_c & 0 \leq x \leq a \\
 B_z(x) &= B_{app} - B^* \left(\frac{a+x}{a}\right) & -a \leq x \leq 0 \\
 B_z(x) &= B_{app} + B^* \left(\frac{a+x}{a}\right) & 0 \leq x \leq a.
 \end{aligned}
 \tag{2.24}$$

These currents and field distributions are depicted by red and blue lines in Fig.(2.5).

As can be readily seen from Fig.(2.6), the flux distribution described above can lead to a significant amount of trapped flux and hysteresis when the external field is cycled back to zero after it has penetrated the superconductor. We will describe in chapter (5) how trapped flux can lead to anomalous behavior in superconductors.

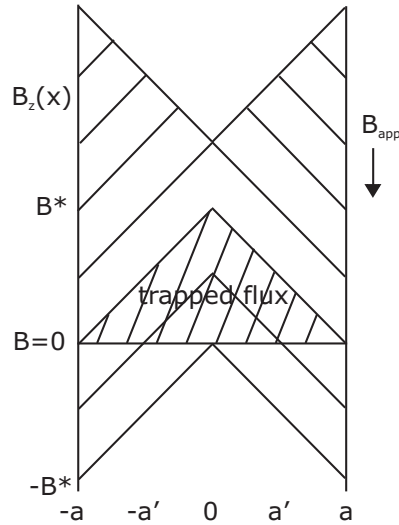


Figure 2.6: Magnetic field distribution in the Bean critical state for decreasing applied field.

2.8 Amorphous metals

It is relatively common knowledge that many of the physical and chemical properties of crystalline materials are determined by their structure; although it might seem less obvious, this is also true for amorphous materials or glasses. Indeed, amorphous materials do exhibit a structure which is not random nor chaotic, but which, much like it is the case in crystals, exhibits a high degree of short range order (SRO)

[36, 37]. In fact, the main difference between glasses and crystals is that the former lack the long range order and translational periodicity which characterize crystalline materials. In other words, glass structure is characterized by randomness, but only at large distances. The appellation SRO in metallic amorphous systems designates a length scale of $1-5 \text{ \AA}$ [36], which is basically the range of nearest-neighbour distances. Another range of order often used to characterize amorphous metals on larger scales is called medium range order (MRO), which, depending on the definition, refers to order on length scale $5-20 \text{ \AA}$ [36], and which relates to the existence of domains in the metallic system. Although ideal amorphous metals should not exhibit order on macroscopic length scales, they often show inhomogeneities of such range; more common in vapor deposited amorphous films, these are defects in morphology which can take the form of growth defects or voids [36]. Another form of macroscopic defect occurring even in amorphous metals fabricated by melt-quenching is phase separation. A common example of phase separation is the formation of crystallites in the glass; however, it can also arise as compositional glass-glass phase segregation due to the immiscibility of the melt [36]. We will discuss further in chapter (5) how order on these various length scales can affect superconducting properties.

2.8.1 Superconductivity in amorphous metals

Superconducting properties such as the critical temperature are very different in amorphous metals as compared to in their crystalline counterpart; this is because the absence of long range order in the amorphous phase modifies the electron-phonon coupling parameter λ_{e-ph} upon which T_c directly depends. Indeed, in most superconductor, whether amorphous or crystalline, the electron-electron (e-e) interaction is mediated by the exchange of virtual phonons such that if the electron-phonon (e-ph) coupling increases, so does the interaction potential between the two electrons forming a Cooper pair, and a larger T_c results [2, 38]. This is readily seen in the BCS theory equation:

$$k_B T_c = 1.14 \hbar \omega_c \exp(-1/N(E_F) V) \quad (2.25)$$

where $N(E_F)$ is the electron density of states at the Fermi level, and ω_c is a cutoff frequency of lattice vibrations defined in the BCS theory and which basically defines the range of energies away from the Fermi energy over which the electron-electron interaction is given by $-V$ (for energies outside of this range, the e-e interaction is taken as zero). While in amorphous materials the frequency of lattice vibrations is lowered, which according to equation (2.25) should lower T_c (because ω_c is lower), the increase of λ_{e-ph} (and thus of V) due to diffuse electron scattering leads to an increase in T_c [38, 14]. However, the e-e interaction does not uniquely depend on the e-ph interaction but also still depends on a residual repulsive screened Coulomb interaction represented by the parameter μ^* , and the net e-e interaction is given by the sum of these two contributions, i.e.

$$N(E_F)V = \lambda_{e-ph} - \mu^*. \quad (2.26)$$

The electron-phonon coupling constant was defined by Eliashberg [39, 40]:

$$\lambda_{e-ph} = 2 \int_0^\infty \frac{\alpha^2(\omega) D_{ph}(\omega)}{\omega} d\omega, \quad (2.27)$$

where $D_{ph}(\omega)$ is the phonon density of states and $\alpha^2(\omega)$ is the electron-phonon coupling strength. Among amorphous superconductors, λ_{e-ph} (and thus T_c) can vary significantly from one material to the other because it depends critically on the size of SRO, such that T_c can decrease very sharply with increasing SRO [38].

Superconductors can be classified in three categories based on the magnitude of their electron-phonon coupling constant, such that

$$\begin{aligned} \lambda_{e-ph} \ll 1 & \quad \text{weak coupling} \\ \lambda_{e-ph} \sim 1 & \quad \text{intermediate coupling} \\ \lambda_{e-ph} \gg 1 & \quad \text{strong coupling.} \end{aligned} \quad (2.28)$$

Various theories of superconductivity often apply to only one of these categories in order to make some simplifying assumption, for instance the expression for T_c given by equation (2.25) above and according to the BCS theory is only valid in the weak coupling limit [1]. In the intermediate to strong coupling limit ($\lambda \lesssim 2$), a prediction of T_c is available from McMillan's formula (see section below).

2.8.2 The McMillan equation

McMillan [41] derived equations that relate the maximum observable T_c to the strength of electron-phonon coupling. For intermediate coupling superconductors, one evaluates the electron-phonon coupling constant from experimentally measured values of T_c from

$$\lambda_{e-ph} = \frac{1.04 + \mu^* \ln(\Theta_D/1.45T_c)}{(1 - 0.62\mu^*) \ln(\Theta_D/1.45T_c) - 1.04}, \quad (2.29)$$

where μ^* is evaluated to $\mu^* = 0.13$ in Ref.[41] for polyvalent transition metals, and Θ_D is the Debye temperature.

A modification of the McMillan equation which includes effects of spin fluctuations has been suggested by various authors [42, 43], and reads

$$T_c = \frac{\Theta_D}{1.45} \exp\left(\frac{1 + \lambda_{e-ph} + \lambda_{sf}}{\lambda_{e-ph} - \lambda_{sf} - \mu^*}\right). \quad (2.30)$$

The parameter λ_{sf} is the spin-fluctuation mass enhancement parameter which is obtained from knowledge of the valence magnetic susceptibility. As will be discussed in chapter (4), the presence of spin fluctuations is expected to play a significant role in the superconducting properties of the alloys studied in this thesis.

2.9 Experimental probes of the superconducting state

There exists a variety of different experimental techniques that can probe the properties of the superconducting state. For instance, values of different parameters such as B_c and T_c can be determined from true thermodynamic variables, namely the magnetization and the specific heat. The resistivity of a superconductor can also be measured to determine T_c , B_{c2} and J_c , and many other properties related to vortex motion and pinning. On its part, the size of the energy gap can be determined from specific heat data and spectroscopic properties such as microwave absorption studies, appropriate for low- T_c superconductors, and infrared absorption studies, for which the energy scale is best-suited for energy gaps in high- T_c superconductors [2].

2.9.1 Specific heat

The electronic specific heat is a good thermodynamic probe of the superconducting state from which information on the bulk of a sample can be obtained. Above T_c , the electronic specific heat assumes the normal state value [1]

$$C_{en} = \gamma T = \frac{2\pi^2}{3} N(0) k_B^2 T \quad (2.31)$$

where γ is the Sommerfeld constant. Well below T_c , the BCS theory predicts that the specific heat contribution has an exponential dependence on temperature according to

$$C_{es} \sim \exp\left(\frac{-\Delta}{k_B T}\right), \quad (2.32)$$

from which it is readily seen that the size of the energy gap can be evaluated. The normal state contribution to the electronic specific heat is continuous at T_c , but the superconducting state contribution, while large below T_c is zero above T_c , which gives rise to a discontinuity in the specific heat at T_c . In experimental measurements, this discontinuity, given by

$$\Delta C = C_{es} - C_{en} = N(0) \left(-\frac{d\Delta^2}{dT} \right) \Big|_{T_c} = 9.4 N(0) k_B^2 T_c, \quad (2.33)$$

using the BCS prediction (equation (2.17)) for the size of the energy gap at T_c , reveals itself as a jump in the specific heat with normalized magnitude

$$\frac{\Delta C}{C_{en}} = \frac{9.4}{2\pi^2/3} = 1.43. \quad (2.34)$$

2.9.2 Magnetization

Magnetization data and related superconducting properties will be presented in chapters (4.2.1) and (5), so we introduce here the basic equations relating the magnetization of superconductors to known properties of the state such as the thermodynamic critical field, and discuss the differences in the behavior of the magnetization in type I and type II superconductors. The Gibbs free energy of the superconducting state can be related to the magnetization according to $dF = -M \cdot dB$, which is true under

isothermal conditions. Then, the difference in free energy density between the normal and the superconducting state can be written

$$f_n(T) - f_s(T)|_{B=0} = - \int_0^{B_c} [M_s(B) - M_n(B)] dB. \quad (2.35)$$

This equation reflects the fact that for an applied magnetic field larger than B_c (B_{c2} for type II superconductors) the superconducting state becomes unfavorable because the added magnetic energy associated with the diamagnetic response of the superconductor becomes greater than its energy benefit in zero field. Also, the difference in free energy between the normal and the superconducting state can be equated to the magnetic-energy density associated with the thermodynamic critical field (or condensation energy of the superconducting state)

$$f_n(T) - f_s(T) = \frac{B_c(T)^2}{2\mu_0}. \quad (2.36)$$

Combining equations (2.35) and (2.36) one is left with the relation between the magnetization dependence on B and the critical field B_c

$$\frac{B_c(T)^2}{2\mu_0} = - \int_0^{B_c} [M_s(B) - M_n(B)] dB, \quad (2.37)$$

i.e. given the complete magnetization loop from $B = 0$ to B_c (or B_{c2}), one can determine the thermodynamic critical field from the area of the loop. An ideal magnetization curve for both type I and type II superconductors is shown in Fig.(2.7a), from which we extract the following information: From an external magnetic field $B_{app} = 0$ to B_c (or B_{c1}) the magnetization reflects the perfect diamagnetism of the superconductor in the Meissner state: flux cancellation by shielding currents is complete and the magnitude of the magnetization $\mu_0 M$ equals B_{app} . For type I superconductors, the superconducting state is destroyed at B_c , whereas for type II superconductors the superconducting state remains until B_{c2} . However, between B_{c1} and B_{c2} the penetration of vortices in the superconductor is reflected in the magnetization which decreases as the sample no longer exhibits perfect diamagnetism. From Fig.(2.7a), it is also apparent that the magnetization of a type II superconductor starts decreasing rather abruptly at B_{c1} , even though this transition is second order. This initial sharp

decrease arises because as the first vortices start entering the superconductor at B_{c1} , a large distance separates them such that there is virtually no interaction between them, and there is therefore no mechanism to inhibit a large number of vortices to penetrate quickly. When a sufficient number of vortices has penetrated the sample and the distance between them is within $\sim \lambda$, they start interacting and the repulsive force between them slows down their entry. Close to B_{c2} the relation between magnetization and applied field is linear.

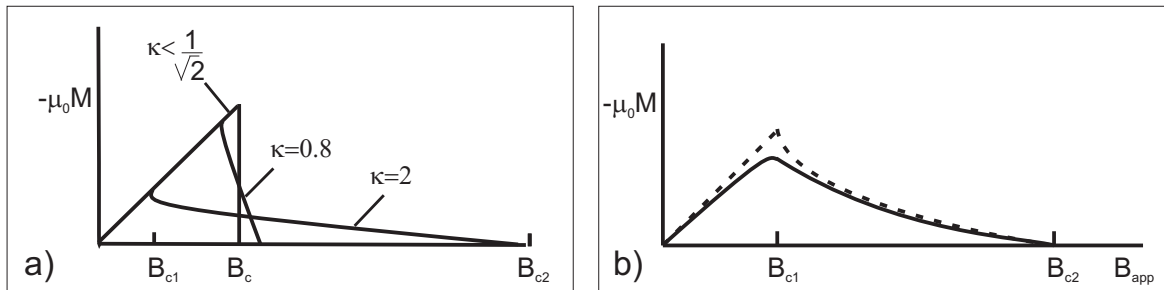


Figure 2.7: a) Magnetization vs applied magnetic field for an ideal type I superconductor ($\kappa < \frac{1}{\sqrt{2}}$) and for ideal type II superconductors with $\kappa \approx 0.8$ and $\kappa \approx 2$. Picture adapted from Fig.(5.2) of Ref.[1]. b) Representation of typical magnetization curves for an ideal (dotted line) and a nonideal (solid line) type II superconductor.

For non-idealized samples, the magnetization curves are more rounded at the critical fields, as depicted by the solid line in Fig.(2.7b). Also, in real systems, the magnetization below B_{c1} is often lower than that predicted by perfect diamagnetic shielding because, even if in theory no flux should penetrate the sample below B_{c1} , in practice some does and contributes to lowering the magnetization. This is due to flux pinning and trapping, which, in real type II superconductors almost always takes place, and results in the presence of remaining flux in the superconductor in zero applied field. Flux pinning and trapping also causes irreversible magnetization curves. A typical magnetization hysteresis loop is shown in Fig.(2.8) in which $B_{coercive}$ indicates the coercive field, i.e. the value of the external field for which the magnetization is reduced to zero; in type II superconductors, $B_{coercive} = B_{c2}$, the field at which superconductivity is destroyed. Also shown is $M_{remanent}$, the magnitude of the remanent magnetization when the external field is zero. At low temperature (T_1 in

Fig.(2.8)), the hysteresis loop is very broad and elongated over the applied field axis, but as the temperature increases the loops narrow and the ratio of the coercive field to the remanent magnetization diminishes.

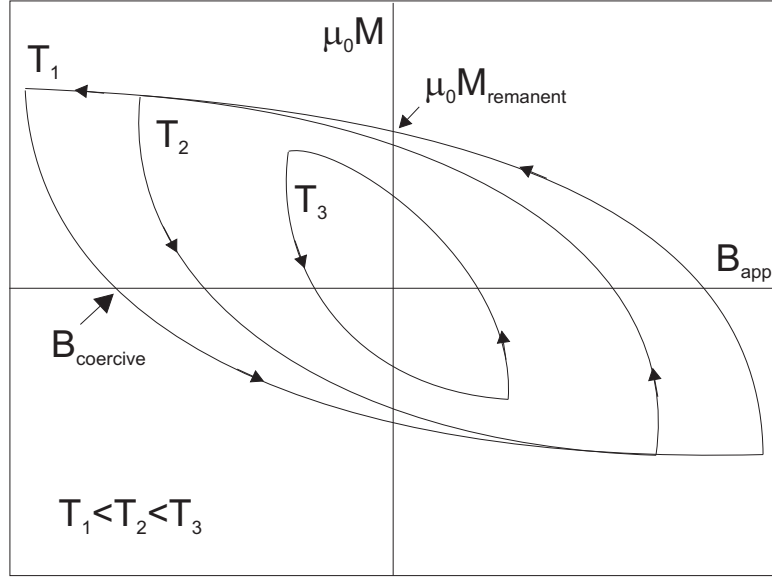


Figure 2.8: Representation of a typical magnetization hysteresis loop for different temperatures below T_c .

In passing, in the absence of an external magnetic field, the electronic specific heat in the superconducting state can be related to B_c from consideration of the relation between C_{es} and the entropy S_s of the superconducting state

$$C_{es} = T \left(\frac{dS_s}{dT} \right), \quad (2.38)$$

and from the relation between the entropy and the Gibbs free energy

$$S_s - S_n = -\frac{d}{dT} [G_s - G_n] \quad (2.39)$$

such that simply stating the result [2]:

$$C_{es}(T) = \gamma T + AT^3 + 2 \frac{B_c(0)^2}{\mu_0} \left(\frac{T}{T_c^2} \right) \left(3 \frac{T^2}{T_c^2} - 1 \right). \quad (2.40)$$

In this equation, γT is the normal state contribution to the specific heat from the conduction electrons, AT^3 is the normal state phonon contribution, and the rest is the contribution from the superconducting state.

2.10 Note on the theories of superconductivity

The basic concepts of superconductivity and the theories presented in this section only constitute an overview of all the phenomena and properties related to superconductivity that have been expressed so far since its discovery in the beginning of the 20th century. We chose to present those theories specifically either because they really constitute the milestones which have molded our understanding of superconductivity today, or because some of the concepts expressed will be necessary to understand the work that will be presented in this thesis. In this respect, the theories described so far are very general to the field of superconductivity and the more specific theories necessary for the understanding of the data presented will be introduced together with the data in later chapters.

3

Experimental Techniques

In the following chapters, results from measurements of various superconductivity-related phenomena on metallic glasses of the alloy $\text{Fe}_x\text{Ni}_{1-x}\text{Zr}_2$ with iron content x from 0 to 0.6 will be presented. In these amorphous alloys, superconductivity settles in at temperatures below 2.5 K. The critical temperature generally decreases with increasing iron content such that a ^3He refrigerator with a base temperature of 0.3 K could be used to perform measurements on the alloys with $0 \leq x \leq 0.5$, but measurement of the alloy with $x = 0.6$ in the superconducting state required the use of a dilution refrigerator with a base temperature of 5 mK. In this chapter, we present detailed information on the superconducting alloys' preparation method, characteristics and properties, in addition to a description of the experimental techniques used to perform the measurements. Potential sources of error will also be discussed. The chapter will end with a thorough presentation of the necessary conditions for the measurement of magnetic superconducting properties using a 2-dimensional electron gas as a detector of magnetic flux. This technique was used to acquire the magnetization curves of our superconducting alloys.

3.1 Samples

3.1.1 Superconducting metal glasses preparation method

The $\text{Fe}_x\text{Ni}_{1-x}\text{Zr}_2$ alloys used in this study have an amorphous structure. The preparation of such alloys requires a rapid cooling of the melt below the glass transition temperature T_g , since a too slow cooling rate leaves enough time to the atomic constituents of the alloy to find an energetically favorable position on crystal nodes and

leads to the formation of a crystalline material. These amorphous alloys are often called metallic glasses, because just like regular glass, they retain some of the random structure of the liquid state upon rapid solidification.

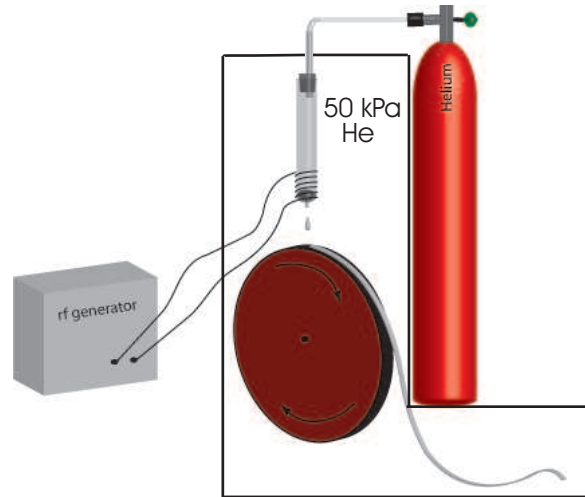


Figure 3.1: Schematic representation of the sample preparation process by the melt-spinning technique.

The alloys were prepared by melting appropriate amounts of high-purity starting materials (99.95 % pure Zr, 99.999 % pure Ni and 99.99 % pure Fe) under titanium-gettered argon atmosphere to avoid any possible oxidation during the melting process. The alloy buttons thus formed were re-melted several times to ensure homogeneous mixing of the constituents. A technique called melt-spinning was then used to fabricate the glassy alloys. This technique basically involves the rapid cooling of the melted alloy by its propulsion on a rapidly spinning copper wheel. In more detail, the alloy buttons are placed in a quartz tube with a small orifice at the bottom and maintained in a helium atmosphere at a pressure of 15 kPa to avoid oxidation, as schematically represented in Fig.(3.1). The alloy buttons are melted by radio frequency induction heating and heated to a temperature no higher than 150 K above their fusion temperature. Once liquefied, the alloy is propelled through the orifice at the bottom of the quartz tube and onto the cool rim of a copper wheel spinning at a tangential velocity of 55 m/s, thereby cooling the alloy at the desired rapid rate of $10^5 - 10^6$ K/s. The resulting metal glass samples take the form of long ribbons

with an approximate width of 1 mm and thickness of 20 μm . Typical lengths of samples measured is from 10 to 15 mm. The amorphous nature of the samples was confirmed by the absence of Bragg peaks in x-ray diffraction measurements, as shown for samples with $x = 0.3$ and $x = 0.6$ in Fig.(3.2), which are representative of the diffraction pattern obtained from all the alloys. The first noisy peak observed at low angle is due to diffraction from the regular glass support for the alloy samples, while the other two visible peaks are attributable to the alloys.

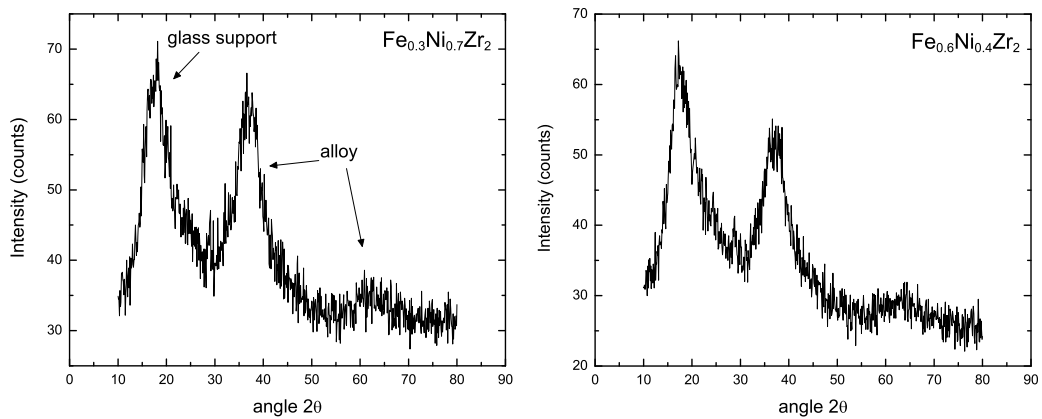


Figure 3.2: X-ray diffraction pattern obtained with Cu K_α radiation from a sample of the alloy $\text{Fe}_{0.3}\text{Ni}_{0.7}\text{Zr}_2$ (left) and a sample of the alloy $\text{Fe}_{0.6}\text{Ni}_{0.4}\text{Zr}_2$ (right) demonstrating the absence of crystallinity by the absence of constructive diffraction Bragg peaks.

3.1.2 Superconducting sample properties

The amorphous nature of the Fe-Ni-Zr-based alloys defines most of their interesting properties in the superconducting state. Indeed, whereas crystalline superconductors exhibit strong pinning properties due to their long-range order which translate into large critical currents, amorphous alloys are characterized by weak collective pinning as per the absence of long range order. The main sources of pinning in these metallic glasses are then rare structural defects, vacancies and grain boundaries. As a result, amorphous alloys also have a low depinning current density J_{dep} (not to be confused with the critical current density J_c which destroys the superconducting state), that is the minimum current density required to depin the vortices. This property makes

them ideal candidates for the study of various vortex phases which have been predicted to exist in the vortex state of superconductors because the necessary use of only a small driving current to induce vortex motion avoids undue heating of the sample related to the necessary use of a large driving current for the measurement of strongly-pinned vortices in superconductors. The depinning current of the $\text{Fe}_x\text{Ni}_{1-x}\text{Zr}_2$ alloys is $J_{dep} \leq 0.4 \text{ A/cm}^2$, which is found to be very low even among materials exhibiting the amorphous structure; this property is attributable to the purity of the alloy starting material and the careful preparation process. This J_{dep} is about 100 to 1000 times smaller than that measured from superconducting samples used in other studies of the moving vortex state [44, 45, 46, 47, 48], and still about an order of magnitude smaller than the depinning current found in other amorphous films [49, 50, 51, 52]. Moreover, the series of the metal glasses $\text{Fe}_x\text{Ni}_{1-x}\text{Zr}_2$ with $0 \leq x \leq 0.6$ is ideally-suited for the study of spin-fluctuation-dependent effects in the superconducting state since the sizes of the Fe and Ni atoms are very similar, such that the structure of the alloys should not change upon replacement of Ni with Fe, thereby avoiding structure-dependent effects in the superconducting properties across the series of alloys¹ [53]. More sample properties pertaining to the superconducting state will be presented in chapter (4).

Structural relaxation

As-made amorphous samples inevitably contain strain fields and voids in their structure as a result of the rapid cooling process which prevents their atomic constituents from arranging in the most compact fashion. As a result, important discrepancies between the superconducting properties measured on different parts of the ribbon may arise if they have attained a different degree of structural relaxation. It is possible to induce structural relaxation by heating the samples to a temperature about 40 K below their glass transition temperature to ensure that they do not crystallize. This process, called thermal annealing, must be performed under vacuum or in an

¹It will be shown in chapter (5) that this is not necessarily true for alloys containing a large amount of Fe.

inert gas atmosphere to prevent oxidation of the samples, which has been shown to result in a depression of T_c values in some alloys [54]. Thermal relaxation itself has also been shown to yield T_c values about 10 % lower than the typical T_c found in the unfully-relaxed counterpart samples [54], but it ensures that all samples have a comparable structure.

Some of the data presented in this thesis come from samples which were heated to 633 K[†] under vacuum in order to remove internal stresses and induce structural relaxation, but this process was not performed on other samples. The differences observed in the superconducting properties in non-relaxed and relaxed samples were found to be insignificant; in fact, the differences were as important as they were observed to be in different relaxed samples. Moreover, it has been determined that, even at room temperature and over a period of some months, amorphous samples will thermally anneal to some extent [55]. Therefore, because the thermal annealing process can sometimes make the sample brittle, causing them to break easily during attachment of the electrical contacts or during cool down, such that we prefer to avoid this step.

Contacts

Most of the results presented in this thesis come from electrical measurements of the transport properties in the superconducting state of the samples. In order to perform this type of measurement, electrical contacts must be attached to the samples; ideally, these contacts must be ohmic. We used the conventional method of soldering indium (In) (99.99 % purity) contacts to the sample. Because In melts at the relatively low temperature 430 K [56], it can safely be used to make the contacts without crystallizing parts of the sample surrounding the contact. 20 μm -diameter silver wire is then used to connect the contacts on the sample to the sample holder.

[†]This temperature is chosen because the glass transition temperature of these alloys is about 688 K, as was determined from differential scanning calorimetry (DCS).

3.1.3 GaAs/AlGaAs samples for magnetization measurements

In chapter (4), magnetization data in the superconducting state of the $\text{Fe}_x\text{Ni}_{1-x}\text{Zr}_2$ alloys will be presented. The measurements were performed using the 2-dimensional electron gas (2DEG) at the interface of a GaAs/AlGaAs heterostructure as a probe of magnetic field. In this section, we describe the structural characteristics of the GaAs/AlGaAs samples and describe how the $\text{Fe}_x\text{Ni}_{1-x}\text{Zr}_2/2\text{DEG}$ structures were made. Later in section (3.4) of this chapter, we will describe all the conditions which make these measurements possible.

GaAs/AlGaAs samples

The layered structure of the GaAs/AlGaAs heterostructures used for the magnetization measurements is shown in Fig.(3.3) along with resulting energy bands. The structure is fabricated by growing alternate layers of GaAs and $\text{Al}_{0.33}\text{Ga}_{0.67}\text{As}$ by molecular beam epitaxy (MBE) of thickness as shown. The Si doping serves to provide free electrons which can move relatively freely in the conducting 2DEG formed at low temperature at the interface between successive layers of $\text{Al}_{0.33}\text{Ga}_{0.67}\text{As}$ and GaAs. The dip in the energy bands at this interface is the cause for the creation of the 2DEG, as in this region, a single state is allowed in the z direction, but the electrons are free to move in the x-y plane.

Hall bar pattern The Hall bar pattern shown in Fig.(3.4) was scribed onto the GaAs/AlGaAs heterostructures using a home-made apparatus composed of a diamond scribe which can be moved by two motors horizontally and vertically as controlled by a Labview program. An actual picture of a 2DEG sample with the Hall bar pattern is also shown in Fig.(3.5a). The purpose of patterning the 2DEG is to confine its active area to the desired geometry; by scratching the surface of the GaAs/AlGaAs heterostructures, even superficially, the 2DEG is depleted thus creating a barrier for electrons within the 2DEG.

Contacting the 2DEG After the realization of the Hall bar pattern, indium solder (99.99 % pure) is deposited in the contact pads of the Hall bar. Because the

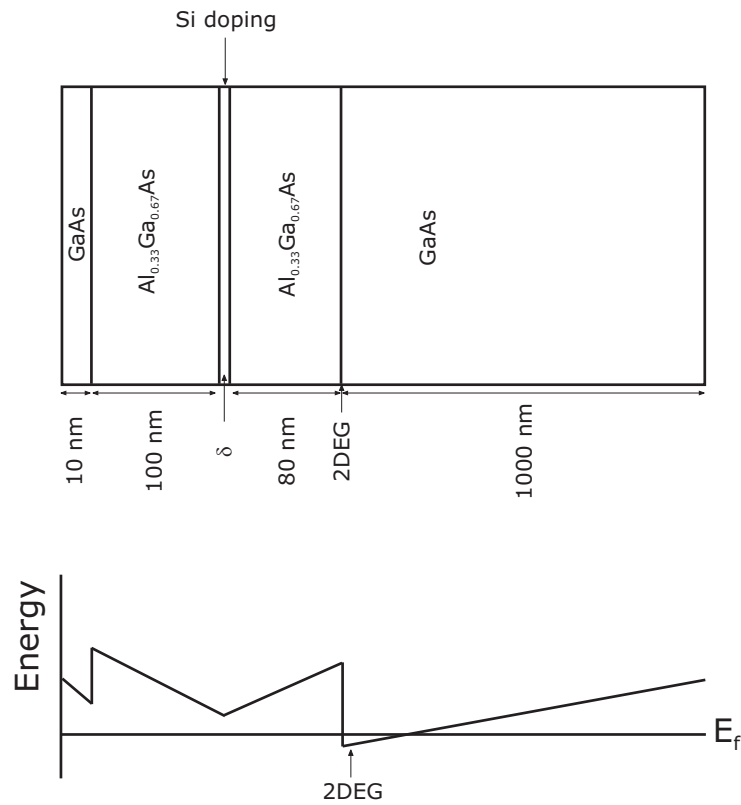


Figure 3.3: Representation of the layered structure of the GaAs/AlGaAs heterostructure containing the 2DEG. The energy bands resulting from the layered structure are also shown.

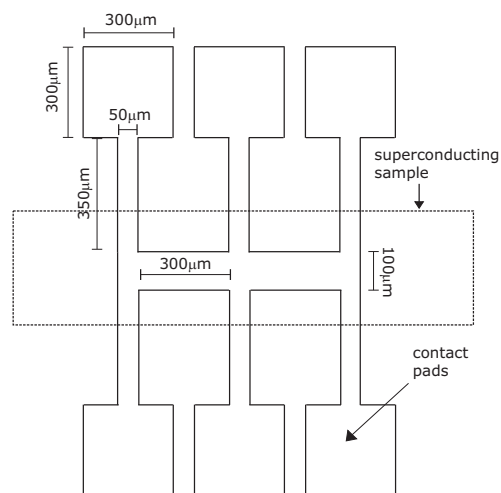


Figure 3.4: Representation of the 2DEG Hall bar pattern with the superconducting sample.

GaAs/AlGaAs heterostructure's surface is insulating and the 2DEG lies 200 nm below the surface, it is not sufficient to simply solder indium contacts to contact the 2DEG as we did for the superconducting samples. Instead, the GaAs/AlGaAs samples with the deposited In are placed in a quartz tube evacuated to a pressure of about 1×10^{-5} mbar and heated at a temperature of 673 K for 25 min to allow the indium to diffuse and reach the 2DEG. The samples are then left under vacuum until they are cooled back to room temperature in order to avoid oxidation. Voltage-current measurement are then performed to confirm the ohmicity of the contacts.

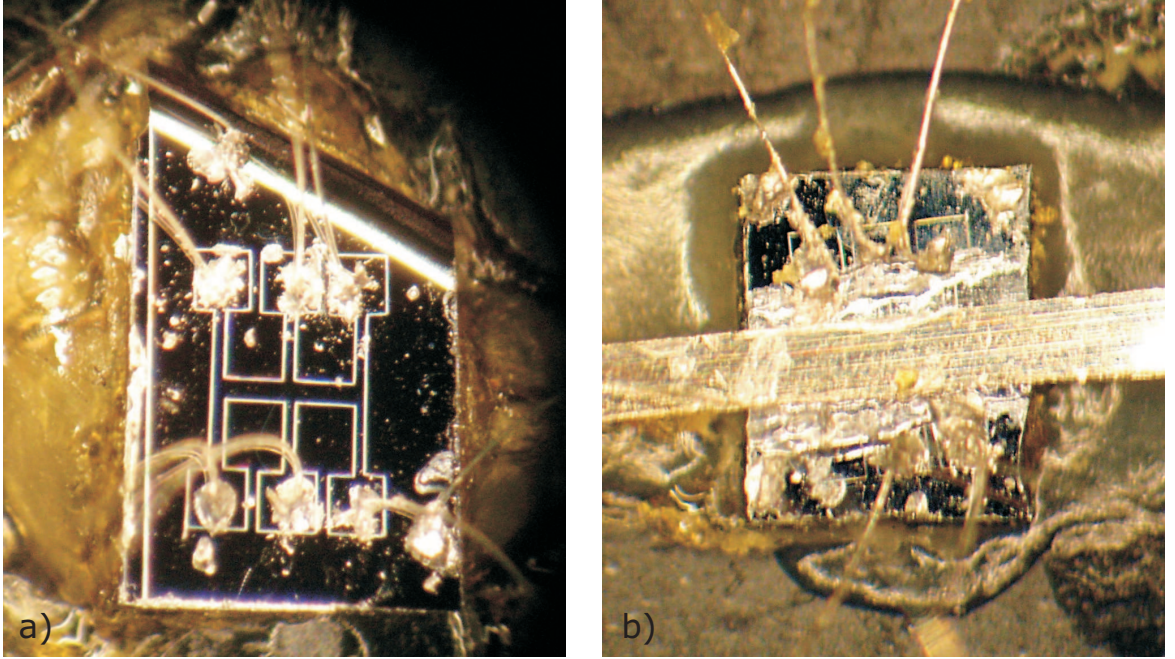


Figure 3.5: a) 2DEG sample with Hall bar pattern. b) Patterned 2DEG sample with superconductor fixed on the Hall bar with vacuum grease.

$\text{Fe}_x\text{Ni}_{1-x}\text{Zr}_2/2\text{DEG}$ structures

The superconductor/2DEG structures are realized by simply fixing the superconductor on top of the active area of the GaAs/AlGaAs defined by the Hall bar pattern with Dow Corning® silicone-based vacuum grease. A picture of a 2DEG sample with a superconductor on top of the Hall bar pattern is shown in Fig.(3.5b). The Hall bar pattern is hardly distinguishable because the vacuum grease has spread around the

superconductor and produces a lot of reflection. We find the use of vacuum grease very convenient because it permits the superconductor to be changed without affecting the 2DEG sample, and although vacuum grease is sufficiently viscous at room temperature to just maintain the superconductor in place, it contracts and hardens as it cools and really maintains the superconductor in close contact with the surface of the GaAs/AlGaAs sample. Moreover, even if vacuum grease is slightly conducting at room temperature which could be problematic for electrical measurements of the 2DEG samples, it becomes insulating at low temperature.

3.2 Experimental setup

The measurements that will be presented in this thesis were almost all performed in a ^3He refrigerator with a base temperature of 0.3 K, in which the sample sits in an evacuated chamber typically at a pressure under 1×10^{-6} mbar, located in the middle of a NbTi superconducting magnet with $T_c \simeq 10\text{K}$ and 9 T-field capability. Only measurements on the alloy $\text{Fe}_{0.6}\text{Ni}_{0.4}\text{Zr}_2$ with $T_c < 0.3$ K necessitated the use of a dilution refrigerator, in which the sample chamber is also held under vacuum and a superconducting magnet provides a magnetic field up to 9 T.

3.2.1 Components and operation of the ^3He refrigerator

The schematics of the main components of the ^3He refrigerator are shown in Fig.(3.6). In order to initiate cool down of the system, the ^3He refrigerator is lowered into the cryostat filled with liquid ^4He which has a temperature of 4.2 K. At this stage, it is necessary to introduce a small amount of gaseous ^4He in the sample chamber to permit thermal exchange between the chamber and the He bath and allow it to cool to 4.2 K. Otherwise, with the sample chamber under high vacuum, almost only radiative heat transport can take place and the sample is thermally isolated from the liquid ^4He bath and would thus never cool down. As the sample is slowly brought to liquid- ^4He temperature, liquid ^4He is drawn from the bath through the needle valve and into a small chamber called the 1-K pot by pumping on the 1-K line as shown in Fig.(3.6).

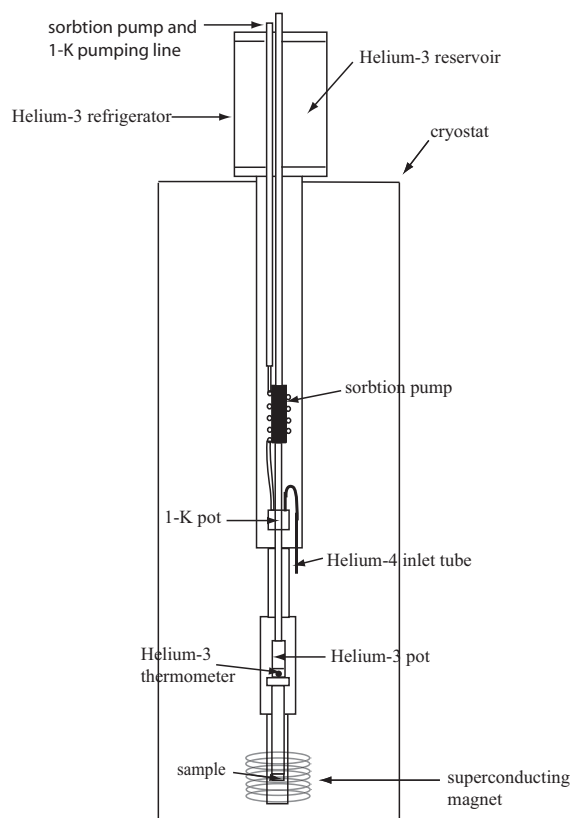


Figure 3.6: Schematic representation of the ^3He refrigerator showing the main components as described in the text.

By pumping on it, the vapor pressure in the 1-K pot is lowered which allows the more energetic molecules of the liquid ^4He in the 1-K pot to turn into the vapor phase and be pumped out; this process, called evaporative cooling, permits the temperature of the 1-K pot to be lowered to about 1.5 K. The cool 1-K pot then cools the sorbtion pump (a piece of charcoal) and the gaseous ^3He present in the head reservoir condenses. ^3He liquefies at a temperature of 3.2 K. The condensed ^3He gathers in the ^3He pot; and from the pumping action of the sorbtion pump which lowers the vapor pressure in the ^3He pot and removes the more energetic ^3He molecules, the temperature of the ^3He pot can be brought to 0.3 K. The ^3He pot is thermally connected to the sample holder via thin copper sheets; copper wires also assume the electrical connection to the sample holder to ensure efficient cooling of the sample. The temperature of the ^3He pot and sample holder is monitored by a calibrated Cernox temperature sensor, while the sorbtion pump temperature is obtained from a Si diode thermometer, and the temperature of the 1-K pot from a RuO_x thermometer. The ^3He refrigerator can remain at its base temperature for as long as 16 hours or more if there is a sufficient amount of liquid ^4He in the cryostat, but once the ^3He in the ^3He pot is all evaporated, the temperature at the sample will rise rapidly. The temperature can be brought down again by simply heating the sorbtion pump to desorb the ^3He which will condense again as the sorbtion pump is let to cool. ^3He is a very expensive and rare isotope of He, but is conveniently used in a closed cycle in this system.

3.2.2 Components and operation of the dilution refrigerator

A single set of data was acquired using a dilution refrigerator (for the $\text{Fe}_{0.6}\text{Ni}_{0.4}\text{Zr}_2$), nevertheless we introduce here the basic working principles of such a system to reach a temperature as low as 5 *m* K. Note that the schematic representation of the dilution refrigerator in Fig.(3.7) and the representation of the ^3He refrigerator of Fig.(3.6) are really not to scale: for instance, the total length of the ^3He refrigerator is about 1.8 m, while that of the dilution refrigerator is about 3 m. A dilution refrigerator also uses ^3He and ^4He as cooling liquids, but whereas both of these elements are kept in isolated cycles in the ^3He refrigerator described above, they are present in a mixture

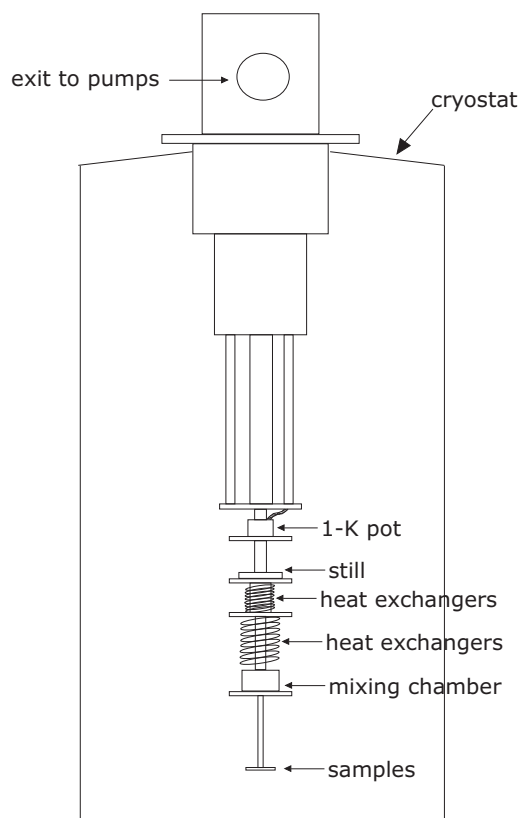


Figure 3.7: Schematic representation of the dilution refrigerator showing the main components described in the text.

in a dilution refrigerator. Also similarly to the case in the ^3He refrigerator, a 1-K pot condenses the $^3\text{He}/^4\text{He}$ mixture which can thereby reach a temperature around 1.2 K by evaporative cooling. Further cooling is provided by a still, upon which the He thus cooled goes through a series of heat exchangers and finally reaches the mixing chamber. It is necessary that the relative amounts of ^3He and ^4He be well-balanced for the phase separation which occurs at the tricritical point of ^3He at $T = 0.86$ K to take place in the mixing chamber. Cooling below the tricritical point is ensured by the transition across the phase boundary of ^3He atoms from a ^3He -rich phase in which the ^3He is mostly liquid to a ^3He -poor phase, in which the ^3He is mostly in the gas phase; this second phase is also composed of the ^4He which is inert and does not participate in the energy exchange process across the phase boundary. As ^3He atoms from the ^3He -rich phase undergo a transition to the ^3He -poor phase, effective cooling of the mixture in the mixing chamber takes place by a process similar to that of evaporative cooling which cools the 1-K pot. On continuous operation, the liquid ^3He present in the ^3He -poor phase is evaporated in the still and removed from the system to an outside reservoir where it is purified and recycled to be fed into the ^3He -rich phase.

3.2.3 Data acquisition methods

The measurement of small electrical signals from samples in cryogenic systems needs to be performed very carefully. One of the reasons for this is that the signals to be measured are often extremely small. For instance, the magnetization data that will be presented in chapter (4.15) requires a precision of about 10 nV. Another reason is that thermoelectric phenomena such as the Seebeck effect or the Thomson effect [57], by which a temperature gradient along an electrical circuit can cause a potential difference across it, or can cause different heat dissipation upon current direction reversal, can produce voltages of the order of a μV . For these reasons, for most of the measurements, an alternating current (ac) was used because it minimizes thermoelectric effects and filters an important part of the random noise. On the contrary, the use of a direct current (dc) can be problematic because it introduces noise volt-

age mainly due to the above-mentioned thermal effects in the sample and the wires. Nevertheless, the use of a dc current was required for some of the measurements and was provided by Keithley 2400-LV source meters. For the measurements of the Hall resistance in superconductors with a dc current that will be presented in chapter (6), a Keithley source meter was used, while a low-noise nanovoltmeter pre-amplifier (HMS elektronik, model 566) was used to amplify the measured voltage signal before measurement by another Keithley source meter. The ac measurements of the superconductor were performed using a resistance bridge (LR-400 from Linear Research Inc.) at a frequency of 15.9 Hz with variable source current up to 10 mA and 0.05 m Ω resolution. The sample temperature was provided by measurement of the resistance of a calibrated Cernox temperature sensor with another resistance bridge (AVS-47) at a frequency of 17 Hz and voltage excitation of 100 μ V. Some measurements of the Hall resistance and magnetoresistance of the 2DEG that will be presented in chapter (3.4) and appendix (B) were performed using SR830 and SR850 DSP lock-in amplifiers from Stanford Research Systems at a frequency of 17.777 Hz and a current of 1 μ A. The resistance measurements were all performed using a four-probe circuit, thereby eliminating the effect of lead resistance on the results; unless specified otherwise, the contact configuration used is as shown in Fig.(3.8). The current to the superconducting magnet was provided by a SMS-120C superconducting magnet controller, except for the measurements presented in chapter (4.15) for which the low-field required necessitated the use of a Keithley source meter since the usual magnet power supply, best-suited to source large currents, was found to be too unstable to supply the low currents required for such low magnetic field (< 2 mT). All measurement equipment were connected to a computer via GPIB interface and Labview programs controlled the instruments and data acquisition.



Figure 3.8: Contact configuration according to the four-probe technique.

3.3 Sources of systematic error

3.3.1 Current Distribution

The conventional and ideal electrical contact geometry that should be used for Hall resistance measurements is shown in Fig.(3.9a). However, the contact geometry used here for the measurements of the Hall resistance of the superconductors and for the measurements performed using crossed ac and dc currents that will be presented in chapter (6) resembles more that shown in Fig.(3.9b). The problem with this geometry is that the current lines threading the Hall probes, here denoted as $V+$ and $V-$, will be really warped and irregular, and not all current lines will flow between the Hall probes. On the contrary, the geometry shown in Fig.(3.9a) limits contact-dependent effects, since even if the length of the sample is much larger than the width, the current lines threading the sample can still be very parallel to the sample sides and all current lines can flow between the Hall probes. However, due to the geometry of our samples with a width of about 1 mm, such an ideal contact configuration could not be realized. To a first approximation, omitting effects due to the warping of current lines, the real current flowing between the Hall contacts will be reduced by a factor given by the ratio of the distance between the Hall probes (L_v) to the width (L_w) of the sample:

$$I_{\text{real}} = \frac{L_v}{L_w} I_{\text{applied}}. \quad (3.1)$$

3.3.2 Magnetic field offset

Upon sweeping the magnetic field provided by the superconducting magnet up and down, some magnetic flux always remains trapped in the magnet such that even when the source current to the magnet is zero, there is always some residual field present. Depending on the maximum field used, the trapped flux will be more or less important. For instance, we determined that the flux which remains trapped in the magnet is about 0.3 T when the field is swept to about 5 T, while if the field is swept only to about 3 mT the trapped flux only attains about 0.1 mT. The only way to eliminate this trapped flux is to let the magnet warm up to a temperature above

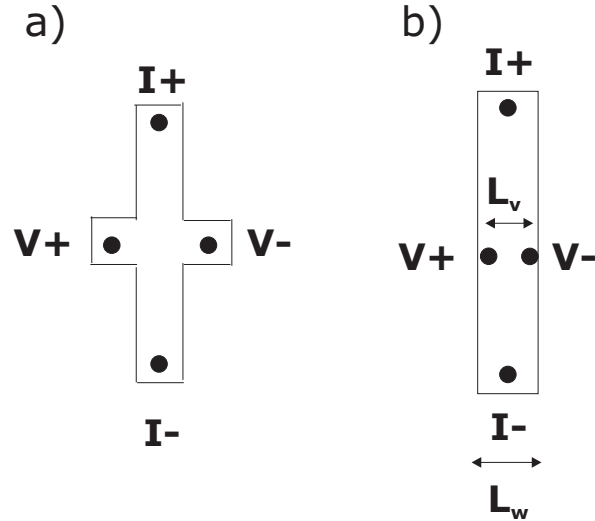


Figure 3.9: a) Ideal contact geometry for Hall resistance measurements. b) Contact configuration used for Hall resistance measurement on our superconductors.

its own T_c , which is about 10 K. This trapped flux causes a field offset in the raw data. Luckily, this field offset can be corrected using measurements such as the Hall resistivity which is null at zero field.

Another type of magnetic field offset arises from sweeping the field up and down which is due to the physical size of the magnet. Indeed, there exists a delay between the time it takes the magnetic field to reach the desired value and the moment the current was applied, such that upon supplying a current to the magnet or simply reversing the sweeping direction, the real value of the magnetic field lags the value it should have according to the current source. This lag becomes larger for faster magnetic field sweeps.

3.3.3 Temperature stability

In the range of temperature between 0.3 K and about 1.5 K in the ^3He refrigerator, the temperature of the sample is very easy to control and can remain stable to within 1 mK during the measurements. However, it becomes much more troublesome to maintain temperatures above 1.5 K stable while measurements are performed, and it becomes just impossible for temperature between about 2.8 K and 4.2 K; fortunately, stabilization of the temperature in this last range was not required for our measure-

ments. The difficulty in stabilizing the temperature above 1.5 K lies in the fact that in the ^3He refrigerator, this is the temperature of the 1-K pot. Temperatures lower than 1.5 K can easily be controlled from heating of the ^3He pot, which evaporates a portion of the liquid ^3He , but above this temperature, the ^3He pot is almost empty. Moreover, the inevitable higher temperature of the sorption pump at these temperatures makes it desorb the ^3He trapped in it such that it also starts to re-condense into the ^3He pot. In addition to these competing processes, the 1-K pot at a temperature of 1.5 K tends to keep the sample temperature at 1.5 K such that a lot of heat needs to be supplied to the ^3He pot heater to warm up the sample. However, the need to supply a lot of current to the ^3He pot heater is cumbersome because at this stage, not much ^3He is present in the pot which can all be evaporated easily by the use of a large current. Therefore, the competition between these processes renders the control of temperatures above 1.5 K very difficult, but by being very careful while heating the ^3He pot, it is possible to stabilize the temperature in this range to within about 0.05 K.

3.4 Measuring superconducting properties using a 2-dimensional electron gas

Since its discovery in 1980 by Klaus von Klitzing [58], the integer quantum Hall effect has triggered the development of many new areas of research which somehow rely on its properties. One of those is the use of Hall probes, simply composed of a 2-dimensional electron gas (2DEG) at the interface of two semiconductors (for instance GaAs/AlGaAs), to measure the local magnetic field at the surface of superconductors. Although semiconductor Hall probes had been used for many years to measure fairly uniform magnetic fields, the first proposal for an experiment in which the sample would be composed of a 2DEG and a superconductor in close proximity, and such that the inhomogeneous magnetic field of the vortices in the superconductor would extend intact into the 2DEG, was presented in 1987 by Rammer and Shelankov [59]. In their paper, they introduce a theoretical analysis for weak localisation corrections in an

inhomogeneous magnetic field and suggest to use a 2DEG/superconductor composite sample to test their predictions experimentally. However, an experimental realization of this technique, with measurements of the Hall resistance and magnetoresistance in the presence of an inhomogeneous magnetic field distribution, awaited until 1990, when it was performed by Bending, von Klitzing and Ploog [60]. Effects due to the superconductor on the 2DEG are not the only phenomena that can be investigated in 2DEG/superconductor hybrid structures: Enhanced vortex motion damping due to eddy currents generated in the 2DEG by the motion of the flux lines has also been observed in these structures [61]. In view of this, we intended to use a similar assembly, i.e. a 2DEG and superconductor composite structure, to measure signs of the different vortex phases in the $B - T$ phase diagram of the superconducting metallic glasses $\text{Fe}_x\text{Ni}_{1-x}\text{Zr}_2$, either through effects on the Hall resistance and/or magnetoresistance of the 2DEG, or through effects on the 2DEG which would be reflected in the electric transport properties of the superconductor. Indeed, the Hall resistance of a 2DEG is very sensitive to magnetic fields such that it can be used as an incredibly sensitive magnetic flux detector to probe the magnetic properties of the superconducting state. Various conditions pertaining to the 2DEG/superconductor assembly need to be considered for the possible measurement of effects due to single vortices or vortex phases in the 2DEG; most concern the 2DEG-superconductor separation. Throughout the remainder of this chapter, we will present these conditions and how they were evaluated. It will be determined that our 2DEG/superconductor system does not show the necessary qualities to permit observation of effects due to the vortex lattice on the 2DEG, so instead of these measurements, the macroscopic magnetization of the superconductors will be measured. We will therefore also present in this section how the magnetization of the superconductors is obtained from Hall resistance curves of the 2DEG.

3.4.1 Magnetic field of a vortex lattice

Even though we determine that our 2DEG/superconductor system does not render the measurement of single vortex effects possible, we still find it interesting to include

here the details of the computations leading to this conclusion, as this work might constitute the starting point for future work on a similar subject. Furthermore, it also explains why we decided to simply measure the magnetization instead; being a more macroscopic property, its measurement was possible with our system.

In principle, the realization of a 2DEG/superconductor system allowing the measurement of vortex effects on the 2DEG is relatively simple: The superconductor can be deposited on the semiconductor's surface, such that the distance (z) between the superconductor and 2DEG is really just the distance between the 2DEG and the surface, which can be easily made smaller than 200 nm, and which ensures that the vortex distribution in the superconductor is projected intact onto the 2DEG. Indeed, as a rough approximation, the non-uniformity of the magnetic field outside the superconductor exists over a distance of the order of the period of the magnetic flux structure. In type II superconductors, as the magnetic field determines the density of vortices (see section (4.4)), the distance between vortices, or magnetic length l_B , can be estimated from $l_B = \sqrt{\frac{\Phi_0}{B_{app}}}$. From this, it is apparent that for very low applied magnetic fields, the condition $z \ll l_B$ is relatively easily satisfied.

In practice however, things are not so simple: the distance over which the magnetic field is nonuniform is also affected by the size of vortices, and if the superconductor is not to be deposited onto the semiconductor heterostructure's surface, a distance between the 2DEG and superconductor of less than 1 μm is hardly attainable. We recall that our goal is to use our $\text{Fe}_x\text{Ni}_{1-x}\text{Zr}_2$ ribbons as the superconductors in these hybrid structures, and not to deposit new superconductors on the 2DEG, so bringing the 2DEG and superconductor in close enough contact will be an enormous challenge. In order to verify the possibility of measuring effects due to an inhomogeneous magnetic field in our 2DEG/superconductor system, we have computed the magnetic flux density induced by a vortex lattice at the surface of a superconductor and its dependence on the distance from the surface. In order to do so, we use the magnetic flux density of an isolated vortex centered on the z axis; as described by Clem [62]

$$B_z = \frac{\Phi_0}{2\pi\lambda\xi} \frac{K_0(R/\lambda)}{K_1(\xi/\lambda)}, \quad (3.2)$$

where the K_n s are Bessel functions of the second kind, and $R = \sqrt{r^2 + \xi^2}$, with $r = [x, y]$ the radial coordinate. Then, assuming that the vortices are ordered in a lattice, the magnetic flux density in a plane parallel to the surface of the superconductor, and at a perpendicular distance z is expanded in a Fourier series, and given by [59]

$$B_z(\vec{r}, z) = \sum_{\vec{q}} B_z(\vec{q}, z = 0) \exp(-|\vec{q}| z) \exp(i\vec{q} \cdot \vec{r}), \quad (3.3)$$

where the \vec{q} s are the reciprocal vortex lattice wavevectors. Assuming a triangular lattice; and $\lambda = 0.6 \mu\text{m}$, $\xi = 80 \text{ nm}$, and $B_{app} = 1 \text{ mT}$, and summing over 5 lattice sites, we obtain the magnetic flux profile shown in Fig.(3.10) for different distances away from the surface of the superconductor. As can be deduced from equation (3.3), the magnetic flux density due to vortices decreases exponentially with increasing distance from the superconductor's surface, and as can be seen in Fig.(3.10), this dramatically influences the distant magnetic flux profile. While the field inhomogeneity ΔB_z has a magnitude of about 0.32 mT at $z = 100 \text{ nm}$, it rapidly reduces to $\Delta B_z = 2.6 \mu\text{T}$ at $z = 1 \mu\text{m}$, and $\Delta B_z = 0.016 \mu\text{T} = 16 \text{ nT}$ at $z = 2 \mu\text{m}$. So the distance between the superconductor and 2DEG will be critical in determining whether or not we can expect to see effects due to the magnetic field inhomogeneity in the 2DEG. Moreover the disappearance of magnetic field inhomogeneity with distance in our Fe-Ni-Zr-based metal glasses turns out to be very dramatic because of the large size of our vortices, which overlap at very low applied magnetic field and rapidly make the vortex lattice appear homogeneous.

2DEG detector resolution

2DEG-superconductor distance considerations As argued in the previous section, the 2DEG-superconductor distance is the most influential factor in determining our detector's (the 2DEG) sensitivity to the vortex lattice. We described in section (3.1.3) how the superconducting samples were maintained over the Hall bar on the AlGaAs/GaAs heterostructure with vacuum grease, which, as it freezes, contracts and firmly holds the superconductor in place; even though this layer of vacuum grease can be made very thin, it is an additional medium between the 2DEG and superconductor

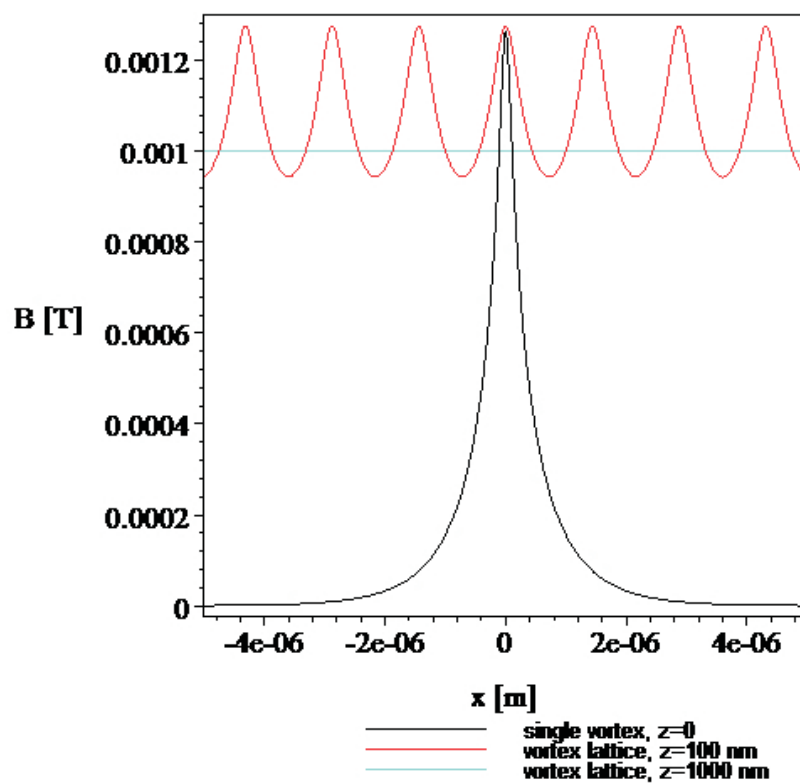


Figure 3.10: Magnetic flux density induced by: black line: a single vortex at the surface of the superconductor, red line: a vortex lattice 100 nm away from the surface, and blue line: a vortex lattice 1000 nm away from the surface of the superconductor. The applied B field is 1 mT for these three curves.

which contributes to increasing their separation. Another agent which can cause a large 2DEG-superconductor distance is the roughness of the superconductor's surface which was evaluated to be of the order of 100 nm from atomic force microscopy (AFM) imaging. The AlGaAs/GaAs heterostructure's surface is however very smooth.

The distance between the superconductor and 2DEG can be evaluated from the determination of the capacitance between them: Using the superconductor as a gate, the potential difference between the superconductor and the 2DEG ($V_{2DEG-sup}$) is varied and the Hall resistance of the 2DEG is measured. The Hall resistance can be related to the electron density in the 2D channel, which can in turn be related to the capacitance according to

$$C = |e| \frac{dn_e}{dV_{2DEG-sup}}. \quad (3.4)$$

Then the distance between the 2DEG and superconductor is computed from

$$d = \frac{\xi_d A}{C}, \quad (3.5)$$

where ξ_d is the dielectric permittivity and A is the area of the active region of the 2DEG defined by the Hall bar pattern; $\xi_d \simeq 1 \times 10^{-10}$ F / m for AlGaAs. To be more exact, the spacing between the 2DEG and superconductor is composed of AlGaAs, GaAs, vacuum, and vacuum grease, and so a dielectric permittivity from these combined media should be considered. However, because it is not known how much of the space is filled with vacuum grease, and how much is simply vacuum this cannot be determined. So we consider only the dielectric permittivity of AlGaAs and keep in mind that this is just an approximation. Performing these calculations, we generally obtain $1 \mu\text{m} < d < 10 \mu\text{m}$.

Experimental techniques and electronics considerations A typical Hall resistance (R_H) curve of a 2DEG is shown in Fig.(3.13a). As can be seen, the Hall resistance is linear at low magnetic field, and the slope of the relation between R_H and B_{app} is governed by the electron density in the 2D channel n_e according to

$$\frac{dR_H}{dB} = \frac{1}{|e| n_e}. \quad (3.6)$$

We generally obtain $\frac{dR_H}{dB}$ between $3800 \text{ } \Omega/\text{T}$ and $4200 \text{ } \Omega/\text{T}$. The Hall resistance in 2DEGs is independent of temperature such that the changes in R_H observed as a function of temperature while it is used as a magnetization detector can be solely attributed to the superconductor. Complications can arise if the electrical contacts to the 2DEG are non-ohmic: in this case a variation of R_H as a function of temperature can be seen, which is the temperature dependence of the contacts only, and not that of the 2DEG. Therefore, before using our 2DEG for the magnetization measurements, we have confirmed that our contacts are indeed ohmic by verifying the linearity of the current-voltage characteristic at liquid helium temperature. Also, for a stand-alone 2DEG, and over the timescale of the experiment, $\frac{dR_H}{dB}$ should not change because n_e should be constant. However, the superconductor on top of the 2DEG could act as a gate and inject (withdraw) electrons in (from) the 2DEG channel if it is not at the same electric potential as the 2DEG. Therefore, in order to ensure constant electron density, we short the 2DEG and superconductor during the experiment.

For $R_H < 15 \text{ } \Omega$ (or $B \lesssim 4 \text{ mT}$) the resistance bridge used to measure R_H ensures a resolution of $5 \text{ m}\Omega$, equivalent to about $1 \text{ } \mu\text{T}$. However, for $R_H > 1.5 \text{ k}\Omega$ (or $B \gtrsim 0.4 \text{ T}$), our resolution becomes about $50 \text{ m}\Omega$, or about $10 \text{ } \mu\text{T}$. Therefore, for $B_{app} = 1 \text{ mT}$ and $z = 1 \text{ } \mu\text{m}$, the magnetic field inhomogeneity ($\Delta B_z \simeq 2.6 \text{ } \mu\text{T}$) is just the same magnitude as our resolution, while for $z > 2 \text{ } \mu\text{m}$ the magnitude of the field inhomogeneity definitely becomes too small to be measured. We recall that we obtain $d = z > 1 \text{ } \mu\text{m}$. In the light of this information and according to our resolution, we conclude that the distances between the 2DEG and superconductor obtained here are much too large for any effects due to single vortices to be observed on the 2DEG. However, a resolution of $1 \text{ } \mu\text{T}$ is non-negligible, and more macroscopic properties of the superconducting state, such as the low-field magnetization, could easily be measured using this technique. So, we proceed with a description of how the magnetization is determined in this manner.

3.4.2 Experimental determination of the magnetization

Various techniques can be used to perform magnetization measurements of superconductors. For instance, neutron diffraction and nuclear magnetic resonance can both be used to detect the periodic flux structure of type II superconductors and hence determine the magnetization [63]. Several other types of magnetometers are also widely used: coil magnetometers, SQUID (superconducting quantum interference devices) magnetometers, vibrating sample magnetometers, etc. We performed our magnetization measurements using the Hall effect of a two-dimensional electron gas; as introduced in section (3.4.1), this technique is practical and very sensitive. Positioned in close proximity to the superconductor, the 2DEG can be used to measure the superconductor's magnetization through measurement of the demagnetizing field present at the superconductor's surface due to the Meissner effect. This situation is illustrated in Fig.(3.11). The picture shows a superconductor in the Meissner state in an externally applied magnetic field; accordingly, shielding currents circulate on the superconductor's surface and cancel the external field. The canceling magnetic field established by the shielding currents extends over some distance outside the superconductor and cancels part of the applied magnetic field by superposition. Therefore, the magnetic field (B_{tot}) traversing the 2DEG positioned close to the superconductor's surface is now composed of the externally applied field and the demagnetizing field of the superconductor, i.e. $B_{tot} = B_{app} - \mu_0 M$.

In order to confirm that the magnetization signal is large enough to be measured with our Hall probe technique, we estimated the magnitude of $\mu_0 M$ and its dependence on the distance away from the superconductor from a simple calculation of the magnetic field created by a ring of circulating current. The details of this calculation and the results are presented in Appendix (A). We obtained that the demagnetizing field right at the surface and in the middle of the superconductor should be about 0.16 mT, and that this field should decrease by less than 0.06 % over a distance of 10 μm from the surface of the superconductor, which is about the distance we obtain between the superconductor and the 2DEG, and which should easily be discernible

according to the resolution of our 2DEG probe. Since this 2DEG-superconductor distance is easily achieved and the magnetic field attenuation is minimal so close to the surface of the superconductor, we will consider no effects due to this distance in our measurements of $\mu_0 M$.

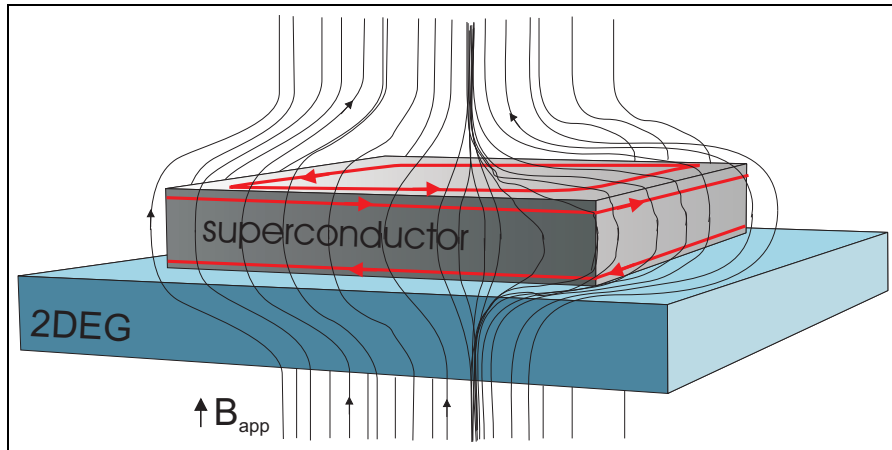


Figure 3.11: Schematic representation of the 2DEG/superconductor arrangement for the magnetization measurements.

Magnetization measurement procedure

The measurements are performed in the following manner: We first cool the samples down to $T \simeq 0.35 \text{ K}$ in zero external field. Moreover, no external current is passed through neither the superconductor nor the 2DEG during cool down to insure a uniform electron density in the 2DEG. Then, keeping the temperature constant, we sweep the magnetic field from 0 to some maximum value above B_{c1} , then back down to negative fields and up again to complete the loop, at a rate of 0.0105 mT/s . This very slow rate is necessary to obtain a high enough resolution to determine the detailed shape of the magnetization curve in the vicinity of B_{c1} , but it is also fast enough to allow full coverage of the temperature range below T_c over a reasonable time scale for the experiment. Also, we have restrained our magnetization measurements to a very low field range, not only because a single sweep to $B > B_{c2}$ would take over 130 hours at this sweep rate, but also because our detector becomes less sensitive as the magnetic field increases (see section (3.4.1)) since R_H increases and becomes

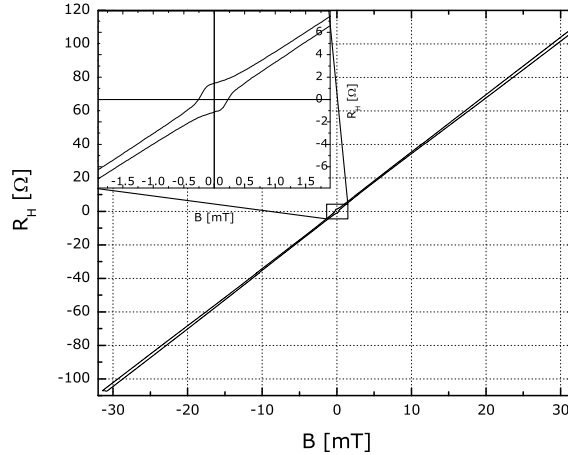


Figure 3.12: Hall resistance vs magnetic field up to 30 mT for the sample $\text{Fe}_{0.1}\text{Ni}_{0.9}\text{Zr}_2$. The results confirm the linearity of R_H at fields much larger than B_{c1} and highlight the small size of the Meissner phase in these samples.

less linear (it also shows step at high field because of the quantum Hall effect), and the magnitude of the magnetization decreases dramatically as B_{app} approaches B_{c2} . A resolution of 10 μT above $B = 0.4$ T is definitely insufficient to measure the magnetization signal at such high magnetic field: Indeed, from our measurements (see Fig.(4.1)), we observe that the magnitude of $\mu_0 M$ is already of the order of this resolution at fields slightly above 2 mT. The Hall resistance of the 2DEG in the presence of a sample of $\text{Fe}_{0.1}\text{Ni}_{0.9}\text{Zr}_2$ up to 30 mT shown in Fig.(3.12) confirms that no important sign of the presence of the nearby superconductor on the R_H curve at higher field can be seen except for a slight mismatch of R_H from up and down field sweeps.

3.4.3 Hall resistance results

In this section, we present the Hall resistance of the 2DEG in the presence of the demagnetizing field of the superconductors from which the magnetization will be deduced. Magnetoresistance measurements of the 2DEG/superconductor composite structures were also performed simultaneously with the Hall resistance measurements,

but as the results do not yield information on the superconducting state, but only interesting results about the 2DEG and weak localization effects at low temperature, these results are only shown and discussed in Appendix (B) for completeness.

A set of Hall resistance curves at different temperatures is shown in Fig.(3.13b), for which a sample of $\text{Fe}_{0.2}\text{Ni}_{0.8}\text{Zr}_2$ was present on the 2DEG. The entirety of the Hall resistance measurements for our different alloys can be found in Appendix (C). The deviations from linearity in these curves are all attributed to the demagnetizing field of the superconductor. The presence of hysteresis and the narrowing of the magnetization loop with increasing temperature are evident. For $T > T_c$, the Hall resistance is found to be very linear again, just like in the absence of the superconductor. The hysteresis results from trapped flux in the sample: as the field is swept down to negative field from positive field, or vice versa, some vortices that were pinned by inhomogeneities or defects remain pinned upon application of a field of opposite polarity. The total magnetic flux in the sample is really zero only when $R_H = 0$; at this point there is an equal number of positive and negative vortices present in the sample. The information about the superconducting state that could be extracted from these R_H curves will be presented in chapters (4) and (5).

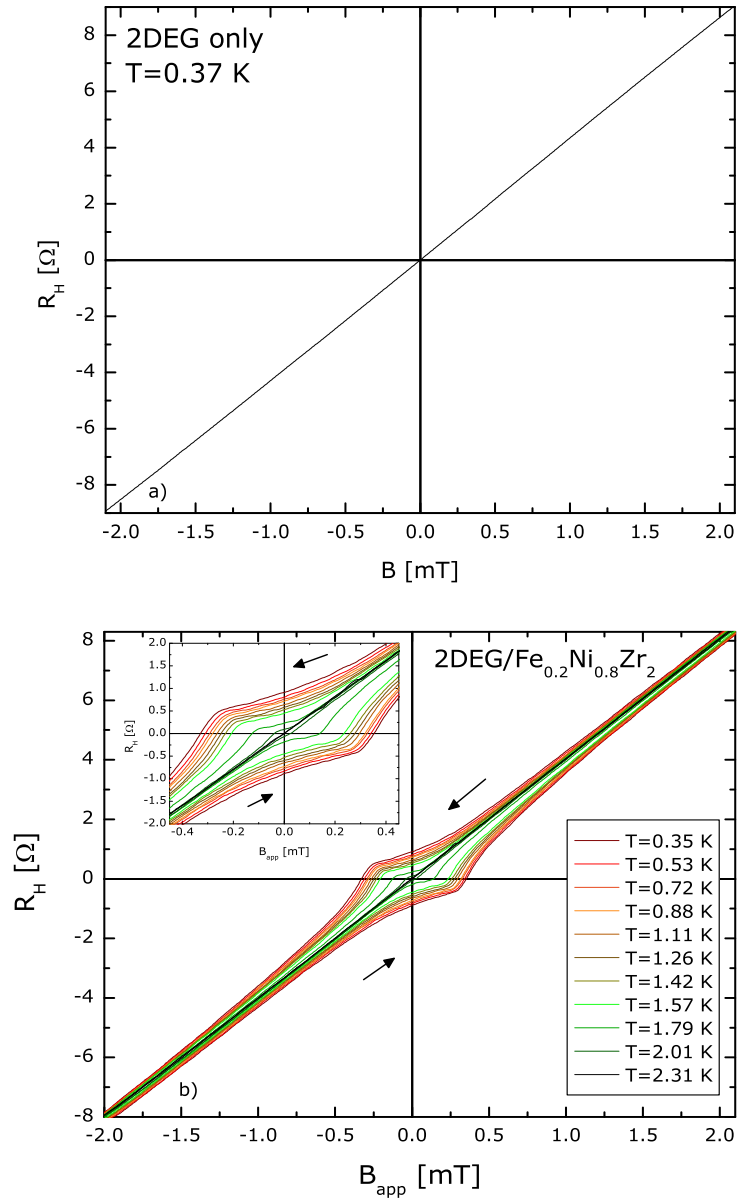


Figure 3.13: Hall resistance vs applied magnetic field for a) a 2DEG only b) a 2DEG with a sample of $\text{Fe}_{0.2}\text{Ni}_{0.8}\text{Zr}_2$ on top, for different temperatures below T_c .

Superconducting properties of the amorphous Fe-Ni-Zr alloys

Superconducting amorphous alloys were first synthesized by vapor deposition in 1954 by Bückel and Hilsch [64]; soon after that, in the second half of the 1950s and early 1960s, numerous theoretical studies were performed on the subject of their superconducting properties [29, 65, 66, 67, 68, 69, 70, 71]. Renewed interest in these material from an experimental standpoint awaited until the mid-1970s when amorphous films of 4d and 5d-transition metal alloys were fabricated by electron beam evaporation and their T_c was systematically studied by Collver and Hammond [72]. These first attempts at the synthesis of amorphous alloys were marked by the inconvenient instability of these alloys at room temperature. Indeed, they were fabricated at liquid helium temperature and had to be kept at this low temperature because they crystallized if allowed to warm up to room temperature. These first studies revealed that the critical temperature of amorphous alloys is larger than that of their crystalline counterparts, which has now been demonstrated to arise from the softening of phonon modes in amorphous materials.

The principal physical characteristic that dictates the superconducting properties of amorphous alloys is their dirtiness, defined by a large ratio of the BCS coherence length to the mean free path ($\xi/l \gg 1$); this results in a large ratio of the Ginzburg-Landau parameter ($\kappa \gtrsim 10$ for the very dirty limit). This dirty character of amorphous alloys is one of the reasons for the added impetus to their study. Indeed, Anderson [71] has argued that the interaction potential of Cooper pairs and the size of the energy gap are more constant for dirty limit superconductors than for some pure crystalline

superconductors in which the energy gap depends strongly on the momentum vector at the Fermi surface, often very complicated in such superconductors. Properties of dirty limit superconductors in a magnetic field are also particularly interesting to study experimentally because numerous theories predicting for instance the lower critical field B_{c1} [28, 73] and upper critical field B_{c2} [26, 28, 29, 65, 66, 67, 69, 74] exist; the reasons for the existence of these numerous predictions is related to the simplification brought by the high- κ limit. For instance, determination of B_{c1} entails finding self-consistent solutions to the GL equations which for arbitrary κ can only be solved numerically. However, analytical solutions can be obtained from consideration of certain limiting cases such as the high- κ limit characteristic of amorphous superconductors. The temperature dependence of B_{c2} in dirty superconductors is also especially intriguing because it differs from the BCS predictions [27] and exhibits enhanced values as well as a linear behavior over a wide range of temperatures [75, 76, 77, 78, 79, 80, 81].

Among the first theories of superconductivity in high- κ superconductors stands the work of Ginzburg, Landau, Abrikosov and Gor'kov, later referred to as the GLAG theory [26, 28, 29, 65, 66], which describes the behavior of B_{c2} as a function of temperature in the vicinity of T_c , and as a function of the electronic mean free path l for the complete temperature range in bulk type-II superconductor. They predict a very linear behavior of B_{c2} vs T yielding very large values of B_{c2} at low temperature which are usually not observed in dirty superconductors.

More realistic values of the upper critical field in dirty superconductors are obtained from consideration of the normal state paramagnetic energy, as suggested independently by Clogston [74] and Chandrasekhar [82] and ignored in the GLAG theory. These early suggestions of paramagnetic limiting of B_{c2} were verified by Berlincourt and Hake [83, 84] in different transition metal alloys and were found to agree well with experimental data for alloys of Ti-V. It is to be noted that the Clogston predictions only impose an upper limit on the upper critical field, and do not predict the temperature dependence of this parameter.

Later, Werthamer, Helfand and Hohenberg [68, 69], and Maki [67] (WHHM) proposed an extension to the Gor'kov equations which includes the effects of spin-orbit interaction, Pauli spin-paramagnetism and electron-phonon coupling to predict the temperature-dependent behavior of B_{c2} over the whole temperature range between $T = 0$ and T_c for high- κ superconductors. They predict a negative curvature of $B_{c2}(T)$ at low T and a fairly linear behavior close to T_c . Although their predictions make assumption of a high- κ , they do not account well for the extended range of linearity and dramatically enhanced values of $B_{c2}(T)$ often observed in amorphous superconductors [75, 76, 77]. However, good agreement between the predictions of the WHHM theory and experimental observations on high- κ superconductors has also been reached [85, 86]; in these same studies, the large enhancement of B_{c2} particularly observed at low temperature for instance in Ref.[75, 76, 77] is suggested to arise due to the presence of inhomogeneities in the superconductors.

As made obvious by the disagreement between the various aforementioned predictions and experimental observations of the temperature dependence of B_{c2} , a good understanding of the expected behavior of $B_{c2}(T)$ in dirty limit superconductors has yet to be reached. The same is true for the theoretical predictions of the lower critical field which have not been subjected to numerous experimental verification before [80, 87]. This is because accurate experimental determination of B_{c1} is difficult to attain since it involves numerous uncertainties mainly related to pinning properties of the superconductor which greatly affect the field of flux entry and exit. However, the weak-pinning properties characterizing our amorphous Fe-Ni-Zr alloys constitute enviable qualities for such a study. These concerns provide the motivation for the studies of the temperature dependence of the lower and upper critical fields in the amorphous Fe-Ni-Zr alloys that will be presented in this chapter. In general, this chapter will provide fundamental information regarding the superconducting state of the $\text{Fe}_x\text{Ni}_{1-x}\text{Zr}_2$ metallic glasses series: We will commence this chapter by introducing the expressions derived by Gor'kov [29, 66] for weak-coupling amorphous superconductors in the dirty limit and determine the superconducting parameters describing

our amorphous Fe-Ni-Zr alloys from these expressions. Then, we will proceed with the presentation of the low-field magnetization data which were used to determine B_{c1} ; this will be followed by an overview of the theories predicting the lower critical field and the experimental results. A presentation of the WHHM theory for the B_{c2} dependence on temperature will conclude the chapter with the corresponding experimental results.

4.1 Expressions for superconductors in the dirty limit

4.1.1 What is the dirty limit?

Superconductors in the dirty limit were initially investigated by Anderson [71] who developed a BCS-like theory to account for their properties. This theory, instead of considering electron pairs of opposite momentum and spin, is based on the pairing of time-reversed states which is independent of the reduced electronic mean free path of this type of material. Indeed, the dirty limit pertains to superconductors relatively homogeneous on a scale of ξ_0 , whilst containing an enormous amount of physical and chemical impurities acting as scattering centers. As a result of this, elastic scattering with energy larger than the gap energy is important in these materials [71]. From this, it is determined that the superconducting state is insensitive to large amounts of impurities as long as they are non-magnetic and of size $< \xi_0$: Indeed, it has been found that a small amount of such impurities causes a sharp depression of superconducting properties such as T_c , H_c , and Δ , but no significant further degradation is observed for more impurities. At this point it is important to note that despite the presence of a large amount of scattering in dirty superconductors, they can be very homogeneous on the scale of ξ_0 which is the important length scale for superconductivity-related phenomena, while inhomogeneities of size ξ_0 or larger really affect the quality of the superconducting state. However, the presence of impurities of size $< \xi_0$ only changes the density of states by adding or removing electrons from bands and gradually mod-

ifying the free-electron parameters.

4.1.2 Dirty limit expressions

Various parameters describing superconductivity in amorphous (dirty) alloys can be obtained from simple experimental quantities and expressions derived by Gor'kov [29, 66]. For instance, the slope of the upper critical field as a function of temperature close to T_c , $\left. \frac{dB_{c2}}{dT} \right|_{T_c}$, is related to the electron diffusion coefficient D through the relation

$$-\left. \frac{dB_{c2}}{dT} \right|_{T_c} = \frac{8k_B}{2\pi eD}, \quad (4.1)$$

which is in turn related to the Fermi velocity v_F , the electron mean free path l and the density of states per spin at the Fermi level $N(E_F)$ by

$$D = \frac{v_F l}{3} = \frac{1}{2e^2 \rho_n N(E_F)}, \quad (4.2)$$

where ρ_n is the normal state resistivity. Then we introduce relations derived by Bardeen, Cooper and Schrieffer (BCS) [1] which relate the thermodynamic critical field $B_c(0)$ to the energy gap $\Delta(0)$ at zero temperature

$$B_c^2 = \mu_0 N(E_F) \Delta^2(0), \quad (4.3)$$

and

$$-\left. \frac{dB_c}{dT} \right|_{T_c} = 1.73 \frac{B_c(0)}{T_c}, \quad (4.4)$$

and finally the Ginzburg-Landau (GL) parameter

$$\kappa = \frac{1}{\sqrt{2}} \left| \frac{dB_{c2}/dT}{dB_c/dT} \right|_{T_c}. \quad (4.5)$$

Gathering these expressions and substituting for the energy gap $\Delta(0) = 1.746k_B T_c$, one obtains

$$\kappa = 3.54 \times 10^4 \left[-\rho_n \left. \frac{dB_{c2}}{dT} \right|_{T_c} \right]^{1/2} \quad (4.6)$$

and a useful expression for evaluation of the thermodynamic critical field from T_c and the slope of the upper critical field at T_c

$$B_c(0) = \frac{-T_c}{2.45\kappa} \left. \frac{dB_{c2}}{dT} \right|_{T_c}. \quad (4.7)$$

Also, the temperature dependence of the coherence length

$$\xi_G(T) = 0.85 (\xi_0 l)^{1/2} \left(\frac{T_c}{T_c - T} \right)^{1/2} \quad (4.8)$$

can be derived from the BCS coherence length (equation (2.18)) and reduces to

$$\xi_G(0) = 1.81 \times 10^{-8} \left[-T_c \frac{dB_{c2}}{dT} \Big|_{T_c} \right]^{-1/2} \quad (4.9)$$

at zero temperature. We will refer to $\xi_G(0)$ as the Gor'kov coherence length, as it differs from the GL coherence length given by

$$\xi_{GL}(0) = \left[\frac{\Phi_0}{2\pi B_{c2}(0)} \right]^{1/2} \quad (4.10)$$

at $T = 0$. ξ_G resembles the BCS coherence length ξ_0 in that it also expresses the distance over which the electrons composing a Cooper pair are correlated, but it accounts for the reduced mean free path found in dirty superconductors which diminishes the coherence length. ξ_0 can differ greatly from the GL coherence length which expresses the distance over which the average Cooper pair density changes and which is thus larger since it encloses many Cooper pairs.

Finally, the penetration depth is obtained from

$$\lambda(0) = 1.63\kappa\xi(0) = 1.05 \times 10^{-3} \left(\frac{\rho_n}{T_c} \right)^{1/2}. \quad (4.11)$$

4.1.3 Calculated dirty limit parameters

The results obtained for these different parameters for our series of alloys are presented in Tables (4.2) and (4.3). Unless specified otherwise, $\frac{dB_{c2}}{dT} \Big|_{T_c}$ is obtained from resistance measurements as a function of magnetic field at different temperatures. B_{c2} is determined from the value of B at $0.5R_n$. In the same manner, T_c is determined at $0.5R_n$ from resistance vs temperature measurements. This criterion is chosen because in some alloys the transitions are slightly wide and in such cases, the $0.5R_n$ criterion represents better the average T_c or B_{c2} of the alloy than the 10 % or 90 % of R_n criteria for instance. The T_c values given in Table (4.2) are averages over several

| Alloy | Number of measurements | Number of samples | T_c variation [K] (same sample) | T_c range [K] for alloy |
|--------|------------------------|-------------------|--------------------------------------|------------------------------|
| x=0 | 32 | 11 | 0.01 | 2.40 - 2.48 |
| x=0.1 | 15 | 8 | 0.005 | 2.63 - 2.69 |
| x=0.15 | 9 | 6 | 0.007 | 2.28 - 2.31 |
| x=0.2 | 2 | 2 | N. A. | 2.12 - 2.17 |
| x=0.3 | 13 | 7 | 0.02 | 1.99 - 2.21 |
| x=0.33 | 2 | 2 | N. A. | 2.09 - 2.18 |
| x=0.36 | 12 | 6 | 0.02 | 2.02 - 2.05 |
| x=0.4 | 19 | 8 | 0.01 | 1.70 - 1.91 |
| x=0.5 | 41 | 15 | 0.02 | 1.21 - 1.31 |

Table 4.1: Details on the number of measurements of T_c performed for each alloy

measurements of different samples, and the errors stated are statistical (standard error on the mean = $\frac{\text{standard deviation}}{\sqrt{N}}$, where N is the number of measurements). Details on the total number of T_c measurements performed and the number of different samples measured for each alloy appear in Table (4.1), along with typical variations in the T_c measured on the same sample, and the range of T_c values obtained for each alloy. Variations in T_c measured on a unique sample are due to the measurement process, whereas variations among samples of the same alloy are attributable to the fabrication technique. Indeed, as the melted alloy is projected onto the spinning copper wheel, it heats it such that the material at the end of the ribbon is not cooled exactly at the same rate as the beginning of the ribbon, and this produces variations in the glass structure for different parts on the ribbon. $\left. \frac{dB_{c2}}{dT} \right|_{T_c}$ is determined from a single set of measurements for each sample. Resistivities were computed from resistance and sample dimensions measurements on long ribbons (~ 80 cm) such that sample dependent errors are intrinsically averaged; thus the errors stated are experimental and come from the resistance and lengths measurements. From the experimental measurements we find the largest T_c of the series of alloys for $\text{Fe}_x\text{Ni}_{1-x}\text{Zr}_2$ with $x = 0.1$ at 2.65 K. T_c for the other alloys then decreases with increasing Fe content as expected from

the increase of spin fluctuations with Fe content. However, the fact that $\text{Fe}_{0.1}\text{Ni}_{0.9}\text{Zr}_2$ has a higher T_c than NiZr_2 was not expected; this unforeseen result will be discussed later. These T_c values are generally slightly lower than those reported on some of the same alloys in Ref.[53] which we attribute to increased structural relaxation of the samples. Also from experimental measurements, the slope of the upper critical field as a function of temperature at T_c is found to be about $-2.4 \frac{\text{T}}{\text{K}}$ which is typical for amorphous alloys (see for instance [88, 80, 85]). A large amount of scatter in the data for $\left. \frac{dB_{c2}}{dT} \right|_{T_c}$ can be seen, for instance the value determined for the alloy $\text{Fe}_{0.4}\text{Ni}_{0.6}\text{Zr}_2$ (2) is much larger than what is expected for these alloys. But, as mentioned above, these values come from a single measurement and were not subjected to averaging over many measurements as the values for T_c were such that these discrepancies can arise. Moreover, it can be presumed that not enough data points for $B_{c2}(T)$ in the vicinity of T_c were acquired to determine $\left. \frac{dB_{c2}}{dT} \right|_{T_c}$ with best certainty. From the expressions for superconductors in the dirty limit introduced above, the typical coherence lengths $\xi_G(0) \simeq 7$ nm and $\xi_{GL}(0) \simeq 9$ nm and penetration depth $\lambda(0) \simeq 0.9$ μm are determined. Similarly, the GL parameter κ is determined from equation (4.6) to be about 80 across the series of alloys, which confirms that they are hard type II superconductors. Moreover, as reported in Table (4.3) the mean free path for these alloys is about 3 Å which is about the size of the inter-atomic spacing and confirms that they are in the dirty limit.

Table 4.2: Experimental superconducting parameters.

| Alloy specimen | T_c [K] | ρ_n [$\mu\Omega$ m] | $\frac{dB_{c2}}{dT} _{T_c}$ [T / K] |
|---|------------------------------|---------------------------|-------------------------------------|
| NiZr ₂ (1) | 2.45 ± 0.01 | 1.82 ± 0.09 | -2.98 ± 0.03 ^a |
| NiZr ₂ (2) | | | -4.4 ± 0.4 |
| Fe _{0.1} Ni _{0.9} Zr ₂ (1) | 2.65 ± 0.02 | 1.61 ± 0.09 | -2.20 ± 0.04 ^a |
| Fe _{0.1} Ni _{0.9} Zr ₂ (2) | | | -4.9 ± 0.4 |
| Fe _{0.15} Ni _{0.85} Zr ₂ | 2.31 ± 0.01 | 1.62 ± 0.08 | -5.25 ± 0.04 ^a |
| Fe _{0.2} Ni _{0.8} Zr ₂ (1) | 2.15 ± 0.03 | 1.61 ± 0.07 | -2.37 ± 0.04 ^a |
| Fe _{0.2} Ni _{0.8} Zr ₂ (2) | | | -4.64 ± 0.02 |
| Fe _{0.3} Ni _{0.7} Zr ₂ (1) | 2.02 ± 0.07 | 1.98 ± 0.08 | -2.81 ± 0.05 ^a |
| Fe _{0.3} Ni _{0.7} Zr ₂ (2) | | | -4.8 ± 0.2 |
| Fe _{0.33} Ni _{0.67} Zr ₂ | 2.13 ± 0.06 | 1.84 ± 0.08 | -3.18 ± 0.03 |
| Fe _{0.36} Ni _{0.64} Zr ₂ | 2.04 ± 0.01 | 1.74 ± 0.08 | -3.18 ± 0.04 ^a |
| Fe _{0.4} Ni _{0.6} Zr ₂ (1) | 1.79 ± 0.03 | 1.85 ± 0.1 | -2.57 ± 0.05 ^a |
| Fe _{0.4} Ni _{0.6} Zr ₂ (2) | | | -8.10 ± 0.08 |
| Fe _{0.5} Ni _{0.5} Zr ₂ (1) | 1.26 ± 0.01 | 1.61 ± 0.08 | -2.36 ± 0.01 |
| Fe _{0.5} Ni _{0.5} Zr ₂ (2) | | | -2.28 ± 0.03 |
| Fe _{0.6} Ni _{0.4} Zr ₂ | 0.28 ± 0.02 ^b | 1.10 ± 0.05 | N. A. |

^aDetermined from resistance measurements as a function of temperature for different external fields.

^bThe T_c value for this alloy is estimated. Only the onset of the superconducting transition was observed at $T \approx 0.3$ K.

Table 4.3: Some superconducting properties derived from experimental measurements.

| Alloy specimen | $\lambda(0)$ [μm] | ξ_0 [nm] ^a | $\xi_G(0)$ [nm] | $\xi_{GL}(0)$ [nm] | κ | D [$10^{-5} \text{ m}^2 / \text{s}$] | $N(0)$ [$10^{47} \frac{\text{states}}{\text{J m}^3}$] | l [\AA] |
|---|--------------------------------|---------------------------|-----------------|--------------------|--------------|--|---|----------------------|
| NiZr ₂ (1) | $0.91 \pm 5\%$ | 248 | $6.7 \pm 3\%$ | $8.6 \pm 0.4\%$ | $83 \pm 5\%$ | $3.7 \pm 3\%$ | $2.9 \pm 5\%$ | 2.5 |
| NiZr ₂ (2) | | 169 | 5.5 | | 100 | 2.5 | 4.3 | |
| Fe _{0.1} Ni _{0.9} Zr ₂ (1) | 0.82 | 273 | 7.5 | 8.3 | 67 | 5.0 | 2.4 | 2.9 |
| Fe _{0.1} Ni _{0.9} Zr ₂ (2) | | 123 | 5.0 | | 99 | 2.3 | 5.4 | |
| Fe _{0.15} Ni _{0.85} Zr ₂ | 0.88 | 131 | 5.2 | 8.4 | 103 | 2.1 | 5.8 | 2.9 |
| Fe _{0.2} Ni _{0.8} Zr ₂ (1) | 0.92 | 315 | 8.1 | 8.4 | 69 | 4.6 | 2.6 | 2.9 |
| Fe _{0.2} Ni _{0.8} Zr ₂ (2) | | 161 | 5.8 | | 97 | 2.4 | 5.1 | |
| Fe _{0.3} Ni _{0.7} Zr ₂ (1) | 1.04 | 338 | 7.6 | 9.3 | 83 | 3.9 | 2.5 | 2.4 |
| Fe _{0.3} Ni _{0.7} Zr ₂ (2) | | 197 | 5.8 | | 109 | 2.3 | 4.3 | |
| Fe _{0.33} Ni _{0.67} Zr ₂ | 0.96 | 252 | 6.8 | 9.3 | 86 | 3.5 | 3.1 | 2.6 |
| Fe _{0.36} Ni _{0.64} Zr ₂ | 0.96 | 254 | 7.1 | N. A. | 83 | 3.5 | 3.3 | 2.7 |
| Fe _{0.4} Ni _{0.6} Zr ₂ (1) | 1.07 | 387 | 8.4 | 10.0 | 77 | 4.3 | 2.5 | 2.6 |
| Fe _{0.4} Ni _{0.6} Zr ₂ (2) | | 123 | 4.8 | | 137 | 1.4 | 7.8 | |
| Fe _{0.5} Ni _{0.5} Zr ₂ (1) | 1.19 | 517 | 10.5 | 14.5 | 69 | 4.7 | 2.6 | 3.0 |
| Fe _{0.5} Ni _{0.5} Zr ₂ (2) | | 535 | 10.7 | 13.3 | 68 | 4.8 | 2.5 | |
| Fe _{0.6} Ni _{0.4} Zr ₂ | 2.08 | N. A. | N. A. | 16.4 | N. A. | N. A. | N. A. | 4.4 |

^aExperimental uncertainty not determined because ξ_0 is computed from the electronic mean free path, which was computed, as will be explained later in the text, from assumptions of electronic density and Fermi surface area. Therefore, it is expected that experimental uncertainties are much smaller than those related to the assumptions.

4.2 Magnetization results

As discussed in section (3.4.2), we have measured the low-field magnetization of some of our $\text{Fe}_x\text{Ni}_{1-x}\text{Zr}_2$ using a 2DEG Hall probe as a detector of magnetic flux. Knowledge of the magnetization of type II superconductors will permit the determination of the lower critical field B_{c1} of our alloys. In this section, we present these experimental magnetization data.

4.2.1 Experimental determination of the magnetization

The total magnetic field (B_{tot}) threading the 2DEG (applied field plus demagnetizing field) is proportional to the Hall resistance of the 2DEG according to

$$B_{tot} = \frac{R_H}{dR_H/dB|_{T>T_c}}, \quad (4.12)$$

where $\frac{dR_H}{dB}|_{T>T_c}$ is the slope of R_H vs B for $T > T_c$ of the superconducting sample. Then, the superconductor's magnetization is determined from

$$\mu_0 M = B_{tot} - B_{app}. \quad (4.13)$$

B_{app} is determined from the linear fit of the R_H vs B_{app} results obtained for $T > T_c$.

Demagnetization correction

In magnetization measurements on superconductors, one often needs to consider a correction for demagnetization effects due to the geometry of the superconductor. This correction, called demagnetization factor, accounts for the fact that due to the Meissner effect, the magnetic field experienced by the superconductor at its surface is not equal to the applied field but is larger. For superconductors of elongated shapes with a field applied in the direction parallel to the long dimension of the sample this correction is unimportant, but it becomes very significant when the field is applied perpendicular to a long dimension. In thin film superconductors, this correction is very large and this is also true for our metallic glass ribbons with the magnetic field perpendicular to the plane of the sample. In our geometry, the demagnetization factor D is approximated from $D \simeq 1 - \frac{\pi W}{2L}$, which gives $D \simeq 0.9$ depending on

the sample. This is however good only for global magnetization measurements, and defining a demagnetization factor for our local magnetization measurements becomes dubious since demagnetization effects are more important at the sample edges and our 2DEG probe is located in the middle of the superconductor [89]. Therefore, instead of defining a lower demagnetization factor based on assumptions, we have not included a correction for demagnetization effects. As a result, B_{c1} values that will be reported later are probably slightly lower than they should be.

Results

The results of the magnetization measurements of different samples of our series of Fe-Ni-Zr-based alloys are shown in Fig.(4.1). The typical characteristics of type II superconductors' magnetization curves are all observable in these results: hysteresis, a quasi linear increase of M for $B < B_{c1}$, and the sharp and sudden drop in magnetization at a field just larger than B_{c1} . Moreover, the magnitude of $\mu_0 M$ close to B_{c1} is of the same order as initially crudely estimated for the field produced by a circular ring of current (0.16 mT). An estimate of the superconducting fraction can also be obtained from these results: Indeed, for an ideal superconductor in the Meissner state, the magnetic susceptibility $\chi = \mu_0 M / B = -1$, but we obtain $\chi \approx -0.6$ for all the alloys in this series, except for $\text{Fe}_{0.5}\text{Ni}_{0.5}\text{Zr}_2$ for which $\chi \approx -0.55$, and for $\text{Fe}_{0.3}\text{Ni}_{0.7}\text{Zr}_2$ for which $\chi \approx -0.65$. Accordingly, the superconducting fraction is estimated to be about 55 % for $\text{Fe}_{0.5}\text{Ni}_{0.5}\text{Zr}_2$, 65 % for $\text{Fe}_{0.3}\text{Ni}_{0.7}\text{Zr}_2$, and 60 % for the other alloys.

A more peculiar and unexpected characteristic which emerges across the measurements for the whole series of alloys is the apparent increase of noise as x increases in $\text{Fe}_x\text{Ni}_{1-x}\text{Zr}_2$. As these measurements were performed under similar conditions using the same apparatus, it would be utterly surprising that the noise originates from an external source and must therefore arise from the samples themselves. In addition, our instrumental resolution is 5 m Ω , but some of these features have an amplitude of 100 m Ω , which is much larger than our resolution and thus also indicates that these features are not actual instrumental noise. Moreover, these fluctuations are not observed above T_c , which confirms that they originate from properties of the super-

conducting state. These fluctuations will be analyzed and discussed in more detail in chapter 4.4.

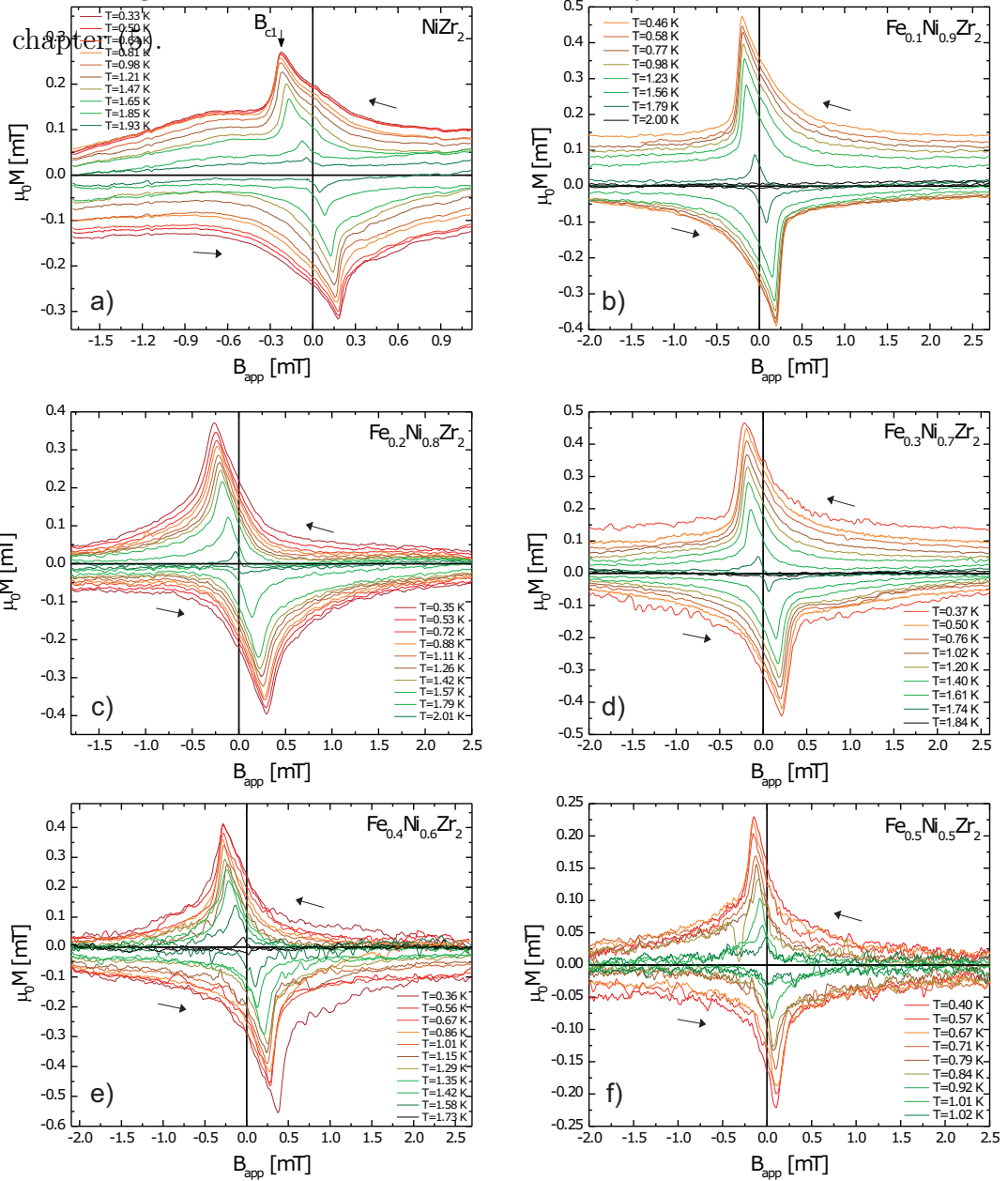


Figure 4.1: Magnetization vs applied field at different temperatures below T_c for different alloys of $\text{Fe}_x\text{Ni}_{1-x}\text{Zr}_2$. The $M = 0$ line represents data above T_c .

4.3 The lower critical field

The lower critical field in type II superconductors refers to the field of flux entry, i.e. the field at which the first vortices penetrate into the superconductor. The

experimental determination of B_{c1} and its comparison with theoretically predicted values is generally very problematic because experimental results are greatly affected by sample-dependent properties. For instance, edge pinning, important in crystalline materials, is known to delay flux entry, and thus yields enhanced values of B_{c1} ; this effect is expected to be strongly reduced in amorphous samples due to their weak flux-pinning properties [63, 90]. Sample inhomogeneity has also been pointed out as a source of uncertainty in the experimental determination of B_{c1} because it induces flux trapping which results in hysteretic magnetization curves [87]. Fortunately, the weak-pinning properties characteristic of amorphous superconductors has allowed us to determine the temperature dependence of B_{c1} in the $\text{Fe}_x\text{Ni}_{1-x}\text{Zr}_2$ alloys. The experimental results will be compared to theoretical predictions of B_{c1} in high- κ superconductors in the $T \rightarrow 0$ and $T \rightarrow T_c$ limits.

4.3.1 Theoretical predictions of B_{c1}

At B_{c1} , the flux lines penetrate the superconductor in a continuous transition in the form of a sparse array of vortices. In this field regime, the distance separating vortices is much larger than λ and interactions between flux lines is very negligible. Theories developed to predict B_{c1} make good use of this fact by considering only the free energy involved in the addition of a single isolated vortex line to a vortex-free system. The problem then involves finding self-consistent solutions to the Ginzburg-Landau equations to calculate this extra free energy. Unfortunately, as discussed in section (2.3), for arbitrary κ , only numerical solution to the GL equations exist. However, analytical solutions can be determined for certain limiting cases, namely, the high- κ limit (which describes our alloys), and the two temperature limits: $T \rightarrow 0$, and $T \rightarrow T_c$. Theoretical predictions for these three limiting cases will be discussed here.

The high- κ approximation

Vortices in superconductors in the high- κ limit ($\kappa = \lambda/\xi \gg 1$) are characterized by a very small core region of size $\sim \xi$, while the size of the vortex itself is much larger (radius $\sim \lambda$). A simplified solution to the GL equations exists in this approximation

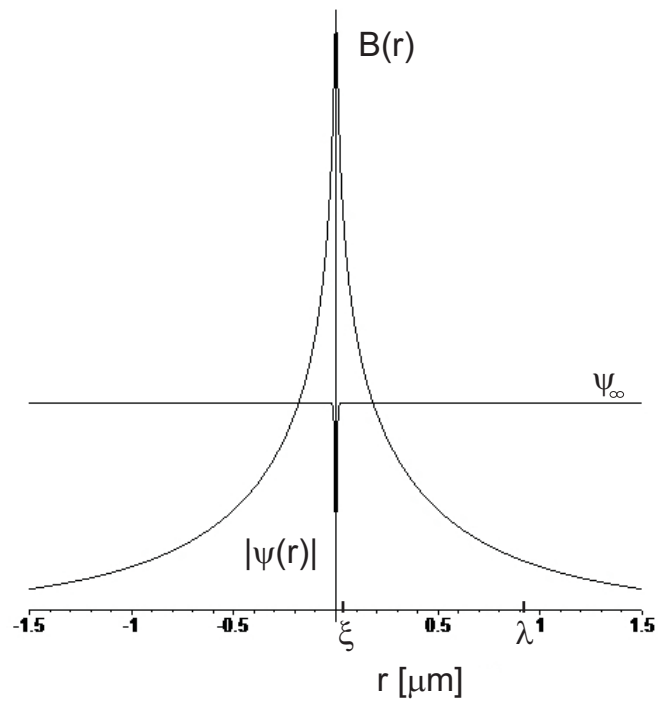


Figure 4.2: Representation of an isolated vortex using superconducting parameters for NiZr₂, with $\kappa = 83$. $B(r)$ is the spatial dependence of the magnetic flux density of the vortex, and $\psi(r)$ is the superconducting order parameter.

because of the fact that the order parameter of the GL theory ψ rises from zero to a limiting value ψ_∞ over the narrow core region, such that most of the vortex can be treated as a regular London superconductor with constant free energy [1]. A representation of this situation is shown in Fig.(4.2), in which the smallness of the core region compared to the vortex size is obvious for a superconductor with $\kappa = 83$. In this manner, the core can be neglected in calculations of the flux line energy to yield

$$\varepsilon_1 \approx \left(\frac{\Phi_0}{4\pi\lambda} \right)^2 \ln \kappa \quad (4.14)$$

and one obtains for the lower critical field

$$B_{c1}(T_c) = \frac{4\pi\varepsilon_1}{\Phi_0} = \frac{\Phi_0}{4\pi\lambda^2} \ln \kappa = \frac{B_c}{\sqrt{2}\kappa} \ln \kappa \quad (4.15)$$

close to T_c . Since superconductors in our series have $\kappa \approx 80$, computation of B_{c1} in this approximation is definitely justified; the results thus obtained in the limit $T \rightarrow T_c$ are listed in the fourth column of Table (4.4). We note that the core contribution to the energy is about $\frac{B_c^2}{2\mu_0} \xi^2$ such that the vortex line energy given in equation (4.14) is $4\pi \ln \kappa$ times larger than the core contribution, which confirms that the core contribution is indeed negligible for $\kappa \gg 1$.

Theoretical predictions for the temperature dependence of B_{c1}

A simplified description for the temperature dependence of B_{c1} is given by the empirical formula [1]

$$B_{c1}(T) = B_{c1}(0) \left(1 - (T/T_c)^2 \right). \quad (4.16)$$

The temperature dependence of B_{c1} can also be approximated by assuming that the ratio λ/ξ is independent of temperature and that $B_{c1}(T)$ assumes the dependence shown in equation (4.15) with $\lambda \rightarrow \lambda(T) = \lambda(0) \left(1 - (T/T_c)^4 \right)^{-1/2}$ as described by Gorter and Casimir [91] in the two-fluid model of superconductivity. This yields the relation

$$B_{c1} = B_{c1}(0) \left(1 - (T/T_c)^4 \right). \quad (4.17)$$

More specifically, for superconductors in the high- κ limit, Maki [73] developed a microscopic theory for the temperature dependence of B_{c1} . His work follows Abrikosov's

[28] early treatment in his predictions of the vortex line structure in type II superconductors. Maki shows that the vortex line structure in the vicinity of B_{c1} can be described by a parameter $\kappa_3(T)$, analogous to the GL parameter κ , and which incidentally reduces to κ at T_c . Also, in the limit $T = 0$, $\kappa_3(0) = 1.53\kappa$. The complete temperature dependence of $\kappa_3(T)$ was numerically computed by Maki, and tabulated values can be found in Ref.[92]. Considering this new parameter $\kappa_3(T)$ the temperature dependent B_{c1} is then given by the analogous to equation (4.15)

$$\frac{B_{c1}(T)}{B_c(T)} = \frac{1}{\sqrt{2}\kappa_3(T)} \ln \kappa_3(T), \quad (4.18)$$

while the temperature dependence of the thermodynamic critical field $\frac{B_c(T)}{B_c(0)}$ was computed by Mühlischlegel [93]. Note that in the limit $T \rightarrow T_c$, equation (4.18) reduces to equation (4.15). We will consider here only the simpler asymptotic forms of $\kappa_3(T)$ given by

$$\kappa_3(T) = \kappa_3(0) \left(1 - \frac{2}{3} \left(\frac{\pi T}{\Delta(0)} \right)^2 \right)^{1/2}, \quad \text{for } T \ll T_c, \quad (4.19)$$

and

$$\kappa_3(T) = \kappa \left(1 + 0.32 \left(1 - \frac{T}{T_c} \right) \right), \quad \text{for } T \approx T_c. \quad (4.20)$$

Combining this with the predictions for the temperature dependence of $B_c(T)$ [†] in the same limit

$$B_c(T) = 1.73B_c(0) \left(1 - \frac{T}{T_c} \right), \quad \text{for } T \approx T_c \quad \text{Ref.}[93] \quad (4.21)$$

in which we use $B_c(0)$ as given by equation (4.7), we obtain $B_{c1}(T=0)$ given in Table (4.4).

[†]The temperature dependence of $B_c(T)$ is often given by $B_c(T) = B_c(0) (1 - t^2)$ which is an approximation according to the two-fluid model developed by Gorter and Casimir [91] in an early treatment of the thermodynamics of superconductors. In this model, the superconducting state was depicted as being composed of two coexisting fluids: one made up of normal electrons, and the other made up of the superconducting electrons.

4.3.2 Experimental determination of B_{c1}

We experimentally determined B_{c1} as a function of temperature for different superconductors in our series of Fe-Ni-Zr amorphous alloys. Again, we expect that the weak-pinning character of these alloys should minimize uncertainties inherent to the experimental determination of B_{c1} caused by pinning effects and yield a reliable value of B_{c1} which could be compared to the above-mentioned theoretical predictions. The value of B_{c1} is determined at the peak position in the magnetization curves as shown in Fig.(4.1a). Fig.(4.3) shows the experimental B_{c1} as a function of temperature for different alloys in our series. In Table (4.4), we also report the values of the slope of the temperature dependence of B_{c1} close to T_c ($\left. \frac{dB_{c1}}{dT} \right|_{T_c}$). This quantity is used to determine the GL parameter κ (also reported in Table (4.4) from the following definition: Combining equation (4.5) and [1]

$$\left. \frac{dB_{c1}}{dT} \right|_{T_c} = \frac{\ln \kappa}{\sqrt{2}\kappa} \left. \frac{dB_c}{dT} \right|_{T_c}, \quad (4.22)$$

we obtain

$$\frac{\left. \frac{dB_{c2}}{dT} \right|_{T_c}}{\left. \frac{dB_{c1}}{dT} \right|_{T_c}} = \frac{2\kappa^2}{\ln \kappa}, \quad (4.23)$$

in which we input our experimental values of $\left. \frac{dB_{c1}}{dT} \right|_{T_c}$ and $\left. \frac{dB_{c2}}{dT} \right|_{T_c}$ and numerically solve for κ . We choose to use values of κ determined from this expression instead of those reported in Table (4.3) obtained from equation (4.6) because we note that calculations for the prediction of B_{c1} strongly depend on the GL parameter κ which in turn depends on the slope of B_{c2} at T_c . However, as described in section (4.1.3), this parameter is found to be strongly sample-dependent and because we are not using the same samples for measurements of B_{c1} as those which were used in measurements of $B_{c2}(T)$, we expect an important disagreement between experimental values and values computed from theoretical predictions. So, we hope that the use of $\left. \frac{dB_{c1}}{dT} \right|_{T_c}$ proper to these particular samples in the computation for κ will reflect more the particular properties of the measured samples in subsequent calculations of B_{c1} from theoretical predictions. Indeed, the values of κ reported in Table (4.4) are larger than those reported in Table (4.3) and should therefore yield lower values of B_{c1} from the

Maki equation (4.18).

The experimental B_{c1} values at $T \simeq 0.35$ K (B_{c1}^{exp}) determined from hysteretic and virgin magnetization curves are also reported in Table (4.4) for comparison with B_{c1} values determined from the Maki theory. The virgin curves are obtained from the first magnetic field sweep after the sample is cooled below T_c and are thus free of trapped flux. The errors on B_{c1} are determined from consideration of uncertainties in reporting the magnetization peak positions; these are not very large since the peaks are so sharp¹. Errors on temperature are determined from temperature variations during data acquisition. As readily seen from the data in Table (4.4) our experimental B_{c1} s determined from virgin magnetization curves are larger than those obtained from the subsequent hysteretic curves. This is expected because the virgin curves do not suffer from any bulk pinning effects which retain vortices in the sample, but delayed flux entry due to edge pinning might take place. In this manner, our experimental B_{c1} s determined from the virgin magnetization curves are very close to the theoretical predictions or larger. The B_{c1} s determined from the hysteretic curves are however lower than the Maki predictions, as expected in the presence of flux pinning. These results show that even in weak pinning superconductors, flux trapping is sufficient to significantly affect values of B_{c1} , even if the measurements are performed only over very small applied magnetic field (here $B_{\text{app}} \lesssim 0.25$ mT).

¹Sharp magnetization peaks reflect the weak-pinning character of our samples; samples with high-pinning properties generally exhibit a broad and shallow peak in magnetization which makes determination of the exact value of B_{c1} very difficult [94].

Table 4.4: Theoretical and experimental values of B_{c1} .

| Alloy | $\frac{dB_{c1}}{dT} _{T_c}$ [$m\Omega/K$] | κ | $B_{c1}(T_c)$ [mT] ^a | $B_{c1}(0)$ [mT] | virgin B_{c1}^{exp} [mT] ^b | B_{c1}^{exp} [mT] ^b |
|---|---|----------|-------------------------------------|----------------------|--|---|
| NiZr ₂ | -0.4 ± 0.1 ^c | 131 | 0.24 | 0.43 | N. A. | 0.175 ± 0.005 |
| Fe _{0.1} Ni _{0.9} Zr ₂ | -0.36 ± 0.04 | 121 | 0.29 | 0.39 | 0.678 ± 0.005 | 0.197 |
| Fe _{0.2} Ni _{0.8} Zr ₂ | -0.43 ± 0.05 | 114 | 0.32 | 0.37 | 0.736 | 0.295 |
| Fe _{0.3} Ni _{0.7} Zr ₂ | -0.64 ± 0.07 | 125 | 0.22 | 0.36 | N. A. | 0.210 |
| Fe _{0.4} Ni _{0.6} Zr ₂ | -0.63 ± 0.06 | 97 | 0.33 | 0.46 | 0.418 | 0.279 |
| Fe _{0.5} Ni _{0.5} Zr ₂ | -0.6 ± 0.1 | 91 | 0.19 | 0.32 | 0.280 | 0.101 |

^aComputed using $\lambda = \lambda_{GL}(0)$ reported in Table (4.2).

^bAt $T \simeq 0.35$ K.

^cErrors on $\frac{dB_{c1}}{dT}|_{T_c}$ are determined from consideration of the maximum and minimum possible slope of B_{c1} vs T close to T_c according to the errors reported on B_{c1} .

In addition to edge and bulk pinning, and sample inhomogeneity, other physical phenomena have been found to alter the value of B_{c1} . For instance, consideration of strong electron-phonon coupling effects in the prediction of B_{c1} has been shown [95] to yield slightly lower values of B_{c1} than those obtained from the weak-coupling theory developed by Maki. Indeed, the values of B_{c1} reported in Ref.[95] including strong-coupling considerations are lower than those for weak-coupling only by at most 10%. However, as described in section (4.4.3), our samples are weak-to-intermediate coupling superconductors such that strong-coupling corrections should be extremely small. However, it is interesting to point out that the strong coupling theory also predicts a flattening of $B_{c1}(T)$ at low temperature [95], much like the ones we observe in the measurements reported in Fig.(4.3). In any case, the values of B_{c1} obtained here are very close to the theoretically determined values considering the significant dependence of B_{c1} on particular sample characteristics, such as its geometry and homogeneity, and so this approach leads to an agreement between the theoretical and experimental values. Good agreement between values of B_{c1} obtained from ac susceptibility measurements on homogeneous amorphous alloys of Zr-Ni, Zr-Pd, and Zr-Rh, and theoretical predictions of B_{c1} according to the Maki theory are also reported in Ref.[87]. This agreement is however found to degrade for inhomogeneous samples. On the other hand, Ref.[80] also reports values of B_{c1} from ac susceptibility measurements on amorphous alloys of Zr-Rh for which the experimental values are always lower than the Maki predictions, and which are found to be highly sample dependent.

4.4 Upper critical field

In type II superconductors, the number density of vortices is dictated uniquely by the externally applied magnetic field through the relation $n_\varphi = B_{app}/\Phi_0$ at high field above B_{c1} , i.e. for any such superconductor, the number of vortices is the same for some applied field B_{app} . Also, the simplest manner in which the upper critical magnetic field can be defined can be visualised in Fig.(4.4): it is the field at which the whole superconducting sample is filled with vortices; this field changes from sample

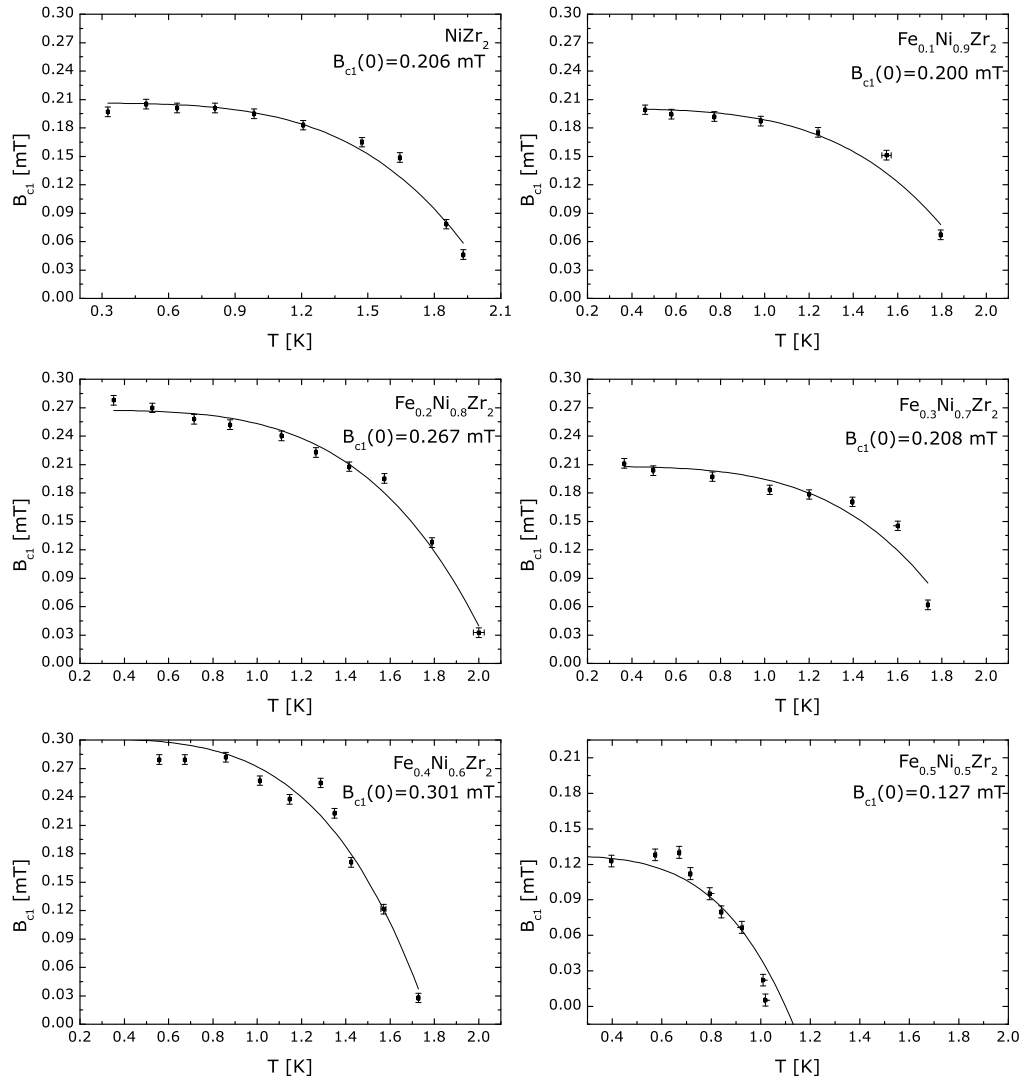


Figure 4.3: B_{c1} vs T for $\text{Fe}_x\text{Ni}_{1-x}\text{Zr}_2$ alloys with $x = 0, 0.1, 0.2, 0.3, 0.4,$ and 0.5 . The data points represent experimental data while the lines are fits to equation (4.17) performed using T_c and $B_{c1}(0)$ as fit parameters. The $B_{c1}(0)$ values shown in the graphs are the best-fit values obtained for B_{c1} at $T = 0$.

to sample depending on the size of vortices in the material, the number density being the same for identical B_{c2} . From this simple picture, the upper critical field is given by [14]

$$B_{c2} = \frac{\Phi_0}{\pi\xi_{GL}^2}. \quad (4.24)$$

This picture is really the most naive definition of the upper critical field and many physical processes have been shown to alter it. For instance, B_{c2} can be limited by spin-orbit coupling scattering processes which induce spin flips and causes pair-breaking [1]. Even in the absence of significant spin-orbit coupling, B_{c2} has been shown to be depressed by Pauli paramagnetic effects [69, 74, 82, 96].

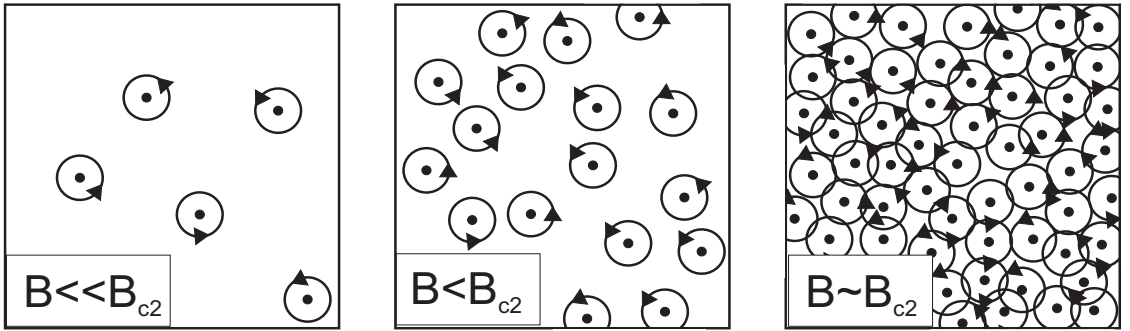


Figure 4.4: Representation of the density of vortices for different magnetic fields.

Various predictions for the upper critical field of dirty superconductors have been made by different authors: Helfand and Werthamer [97] give the orbital critical field from a microscopic theory

$$B_{c2}^*(0) = -0.693T_c \left[\frac{dB_{c2}}{dT} \Big|_{T_c} \right] \quad (4.25)$$

which does not include effects due to spin-orbit coupling nor spin-paramagnetism. Clogston [74] (see section (4.4.1)) predicts an upper limit to the critical field from consideration of normal state paramagnetic effects

$$B_p(0) = \frac{\Delta(0)}{\sqrt{2}\mu_B}, \quad (4.26)$$

Maki [67] also predicts a paramagnetically limited upper critical field given by

$$B_{c2}^{**}(0) = \frac{B_p(0)}{\sqrt{2}} \frac{\alpha}{\sqrt{1 + \alpha^2}} \quad (4.27)$$

where

$$\alpha = \sqrt{2} \frac{B_{c2}^*(0)}{B_p(0)} \quad (4.28)$$

is the Maki parameter; finally, Werthamer, Helfand and Hohenberg [69] derive a maximum value for the upper critical field given by

$$B_{c2\max}^{**}(0) = \frac{B_p(0)}{\sqrt{2}}. \quad (4.29)$$

In Table (4.5) we summarize the results obtained for these critical fields using our experimentally determined T_c and $\left. \frac{dB_{c2}}{dT} \right|_{T_c}$.

Table 4.5: Maki parameter and various critical fields

| Alloy specimen | α | $B_p(0)$ [T] ^a | $B_{c2}^*(0)$ [T] | $B_{c2}^{**}(0)$ [T] | $B_{c2\max}^{**}(0)$ [T] | $B_{c2}^{\text{exp}}(T \simeq 0.4 \text{ K})$ [T] | $B_c(0)$ [<i>m</i> T] ^b |
|---|-----------|---------------------------|-------------------|----------------------|--------------------------|---|-------------------------------------|
| NiZr ₂ | 1.58 ± 4% | 4.55 ± 2% | 5.06 ± 3% | 2.95 ± 6% | 3.21 ± 2% | 4.41 ± 0.01 | 43.8 ± 5% |
| Fe _{0.1} Ni _{0.9} Zr ₂ (2) | 1.16 | 4.92 | 4.04 | 3.24 | 3.48 | 4.78 | 53.1 |
| Fe _{0.15} Ni _{0.85} Zr ₂ | 2.77 | 4.29 | 8.40 | 2.87 | 3.03 | 4.63 | 49.7 |
| Fe _{0.2} Ni _{0.8} Zr ₂ (2) | 1.25 | 3.91 | 3.45 | 2.56 | 2.76 | 4.67 | 41.2 |
| Fe _{0.3} Ni _{0.7} Zr ₂ (2) | 1.48 | 3.75 | 3.92 | 2.47 | 2.65 | 3.85 | 36.3 |
| Fe _{0.33} Ni _{0.67} Zr ₂ | 1.68 | 4.13 | 4.89 | 2.51 | 2.92 | 3.78 | 33.7 |
| Fe _{0.36} Ni _{0.64} Zr ₂ | 1.68 | 3.85 | 4.57 | 2.34 | 2.72 | N. A. | 32.3 |
| Fe _{0.4} Ni _{0.6} Zr ₂ (2) | 1.36 | 3.32 | 3.18 | 2.28 | 2.35 | 3.30 | 43.1 |
| Fe _{0.5} Ni _{0.5} Zr ₂ (2) | 1.20 | 2.33 | 1.99 | 1.27 | 1.65 | 1.86 | 17.2 |
| Fe _{0.6} Ni _{0.4} Zr ₂ | N. A. | 0.52 | N. A. | N. A. | 0.37 | 1.23 | N. A. |

^aObtained using BCS energy gap.^b $B_c(0)$ obtained from equation (4.7).

4.4.1 Origin of limiting effects on B_{c2}

The Clogston limit and paramagnetic limiting effects

Clogston [74] derived an upper limit to the value of the upper critical field of superconductors at $T = 0$ from simple free energy and normal state paramagnetism considerations. This limiting of the upper critical field arises from consideration of the Zeeman splitting experienced by the pair of electrons composing the Cooper pair in a high magnetic field. Indeed, in a magnetic field, the energy of one of the electrons of the pair is increased by an amount $\mu \cdot B$ while the energy of the other electron is lowered by this same amount (μ is the magnetic dipole moment of the electron). At sufficiently high magnetic field, this energy becomes so large that it becomes energetically more favorable for the electrons to orient their spins with the externally applied field and to abandon superconductivity. A resulting upper limit to the value of the critical field can be deduced from these considerations and is expressed by equation (4.26) [14]. $B_p(0)$ is generally found to be much larger than the experimentally observed B_{c2} .

Spin-orbit coupling effects

In superconductors, spin-orbit coupling effects lead to a depression of B_{c2} which becomes more important at low temperature, or large B_{c2} . Spin-orbit interaction in superconductors is more problematic in small samples with size less than the penetration depth. This is because in such a case, a relatively small magnetic field can polarize enough of the paired electrons composing the superconducting state to lead to a finite and significant internal magnetic field in the superconductor. In contrast, in large samples, the paired-arrangement of Cooper pairs with electrons of opposite spins would necessitate a large external field to polarize the system such that spin-orbit coupling effects become less influential on the superconducting state. [98].

Spin fluctuations

Spin fluctuations have been mentioned a few times so far in this work, but no details about their origin has been discussed except for the fact that they become more im-

portant with increasing concentration of magnetic ions in the superconductor. We bring remedy to this situation here with a short physical description of spin fluctuations. We have said that they are principally due to the presence of the Fe magnetic ions; this is true, but they can also be caused by any other paramagnetic ion with a magnetic moment. Indeed, in a systematic study of lanthanum alloys containing rare-earth elements, Matthias *et al.* [99] have shown that, for instance, Gd impurities caused the largest depression in T_c ; while Gd has the largest spin of the impurity ions investigated, it does not have the largest magnetic moment. That being said, spin fluctuations arise in superconductors due to the presence of magnetic ions having a spin because in conventional superconductors, the correlated electrons forming a Cooper pair have antiparallel spin orientations, but as the Cooper pair approaches a paramagnetic ion it interacts with it and no matter what the orientation of the spin of the magnetic ion is, the electrons forming the Cooper pair tend to align their spins with that of the magnetic ion. In this manner, pair correlations are destroyed and the Cooper pair is broken apart. This breaking of Cooper pairs can strongly suppress superconductivity, especially if the amount of magnetic ions in the superconductor is important, and thus leads to a depression of superconducting parameters such as T_c and B_{c2} .

4.4.2 Discussion on critical fields results

All the formulations for the upper critical field presented in section (4.4), except $B_{c2}^*(0)$, contain a consideration of paramagnetic limitation which decreases the predicted upper critical field, while $B_{c2}^*(0)$ only depends on orbital limitation. And, as apparent from the data in Table (4.5), the experimentally determined critical fields $B_{c2}^{\text{exp}}(T \simeq 0.4 \text{ K})$ for the whole series of alloys are lower than the predicted $B_{c2}^*(0)$, thus indicating that paramagnetic limitation takes place in our samples. It is however not too strong because the experimental B_{c2}^{exp} are fairly larger than the paramagnetically limited fields $B_{c2}^{**}(0)$ and $B_{c2\text{max}}^{**}(0)$. In fact, the experimental upper critical fields generally follow the predictions of the Clogston limit field $B_p(0)$ which we recall is an upper limit on the critical field in the presence of paramagnetic effects.

Therefore, we conclude that paramagnetic effects are present, but not very strong in these alloys. The values obtained experimentally for the upper critical field can be compared with values obtained on similar alloys of $\text{Zr}_{0.73}\text{Ni}_{0.27}$ in Ref.[85] and of $\text{Zr}_{0.75}(\text{Ni}_{0.5}\text{Fe}_{0.5})$ in Ref.[100] in which B_{c2} is expected to be slightly larger than in our alloys because of the more important Zr content than in our alloys; as expected, values of B_{c2} about 4.8 T at $T = 1.1$ K and 2.6 T at $T = 2$ K are observed in the former and latter case respectively.

A more interesting phenomena transpires from critical field results: a significantly larger upper critical field for alloys containing a small concentration ($0.1 \leq x \leq 0.2$) of iron compared to none in the alloy NiZr_2 . We recall that T_c is also larger for $\text{Fe}_{0.1}\text{Ni}_{0.9}\text{Zr}_2$ than for NiZr_2 . From this, it appears that the introduction of a small amount of Fe improves the superconducting properties of NiZr_2 . This is contrary to what is expected from the introduction of a magnetic element which induces spin fluctuations which act as pair breakers [53]. This oddity cannot result from a structural change in the sample due to the addition of Fe because as we have discussed already in section (3.1.2) the sizes of the Fe and Ni atoms are identical and the alloy structure is thus expected to be identical². In addition, the resistivities for the whole series should be approximately the same: Ref.[53] reports $\rho_n = 167.7 \mu\Omega \text{ cm}$ for FeZr_2 and $\rho_n = 168.2 \mu\Omega \text{ cm}$ for NiZr_2 . We obtain more scattered values for ρ_n of $\text{Fe}_x\text{Ni}_{1-x}\text{Zr}_2$ with $0 \leq x \leq 0.6$ as reported in Table (4.2), probably due to uncertainties in the measurements of the geometrical factors used in the calculations of the resistivities.

A plausible explanation for the enhancement of T_c with the introduction of a small amount of Fe to NiZr_2 results from consideration of the position of the d band for both Fe and Ni. Indeed, results from ultraviolet photoemission spectroscopy (UPS) on binary alloys of Fe-Zr and Ni-Zr have revealed that the maximum of the Fe d band lies closer to the Fermi level than the maximum of the Ni d band [101], such that the density of states at the Fermi level $N(E_F)$ for Fe is larger than for Ni.

²We will show in chapter (5) that this is not necessarily the case, especially for those alloys containing a large amount of Fe. However, this is still expected to be true for NiZr_2 and $\text{Fe}_{0.1}\text{Ni}_{0.9}\text{Zr}_2$.

But, according to the predictions of the BCS theory, T_c depends exponentially on the inverse of $N(E_F)$ as given by equation (2.25). Therefore, as can be deduced from this equation, an increase of $N(E_F)$ translates into an increase of T_c . So it seems plausible that substitution of a small amount of Ni for Fe in our alloys results in a sufficient increase of the density of state at the Fermi level to yield an increase of T_c , and that even if the introduction of Fe should increase spin fluctuations which tend to lower T_c .

This can also explain the observed increase of B_{c2} . Indeed, in equations (4.25, 4.26, 4.27 and 4.29) B_{c2} is expressed in a proportional relation to T_c , such that a larger T_c should thus result in a larger B_{c2} , as observed here.

4.4.3 The WHHM theory

As briefly mentioned in the introductory section of this chapter, the WHHM theory takes into account the effects of Pauli spin-paramagnetism and spin-orbit coupling to predict the temperature dependence of the upper critical field. It typically yields enhanced values of B_{c2} compared to the BCS theory, as is required for high- κ superconductors; considerations of spin-paramagnetism however limits B_{c2} such that one obtains a negative curvature of $B_{c2}(T)$ at low T . Before getting into the details of the WHHM theory, we will describe the conditions for its applicability and verify that it indeed applies to our series of Fe-Ni-Zr superconducting alloys.

Applicability criteria

The WHHM theory applies to superconductors exhibiting the following characteristics [85]:

1. Superconductors in the dirty limit, with dirtiness parameter $\frac{\xi}{l} \gg 1$.
2. A large ratio of the spin-orbit-coupling induced electron-spin-flip scattering time to the transport scattering time, $\frac{\tau_{so}}{\tau_{tr}}$.
3. A BCS weak-coupling electron-phonon interaction parameter of the order $\lambda_{e-ph} \lesssim 1$.

4. Sample spatial homogeneity down to the scale of the GL coherence length $\xi_{GL}(0)$.
5. Isotropic electronic structure
6. Sample is 3D (i.e. $d \gg \xi_{GL}(0)$).

The last three criteria are expected to be true for our series of alloys. Indeed, sample homogeneity is expected for such rapidly cooled alloys prepared by the melt-spinning technique. Also, the amorphous nature of our samples ensures isotropic electronic structure, and all three dimensions are larger than superconducting parameters, such that they are effectively 3D. The calculated values of the parameters pertaining to the first three conditions can be found in Table (4.6).

We obtain the dirtiness parameter from the ratio of the Gor'kov coherence length ξ_G^\dagger (equation (4.9)) to the electronic mean free path l , which is in turn obtained from

$$l = (3\pi^2)^{1/3} \left[e^2 \rho_n \left(n_e^{2/3} \frac{S}{S_F} \right) \right]^{-1}, \quad (4.30)$$

where n_e is the free electron density and S/S_F is the ratio of the area of the free Fermi surface to that of a free-electron gas of density n_e . We estimate both of these quantities as follows: We take for n_e the ratio of the average number of electrons per atom outside closed shells to the atomic volume $n_e = \langle \frac{e}{a} \rangle V_0^{-1}$. This is a somewhat unphysical assumption but it should not be too far off from reality. To confirm in passing, we also obtained a lower limit to the electron density of $n_e \geq 1.4 \times 10^{28}$ electrons/m³ in Ref.[8]. Also, we use $\frac{S}{S_F} = 0.6$ as in Ref.[85]. If we were to use $\frac{S}{S_F} = 1$ as for a free electron-like Fermi surface the value of l would not change by an order of magnitude. In this manner, we obtain a mean free path of the order of the inter-atomic distance, and thus a very large dirtiness parameter $\frac{\xi_G}{l} \gtrsim 20$ classifying

[†]The dirtiness parameter is usually computed from the ratio of the BCS coherence length ξ_0 to the mean free path. However, we use the experimentally determined ξ_G because it represents the real coherence length in our samples, whereas ξ_0 merely relies on theoretical predictions which are not necessarily true in the dirty limit.

these alloys in the very dirty limit. Knowledge of the mean free path allows us to determine the transport scattering time τ_{tr} from

$$\tau_{tr} = \frac{l}{v_F}, \quad (4.31)$$

while the spin-orbit scattering time τ_{so} can be obtained from equation (4.36) for the spin-orbit-coupling parameter λ_{so} which is obtained as the best-fit parameter of equation (4.32) of the WHHM theory, as will be described in section (4.4.3). From these, we determine a ratio of the scattering times $\frac{\tau_{so}}{\tau_{tr}}$ often much larger than 100. Finally, the electron-phonon coupling constant is determined from the McMillan predictions (equation (2.29)) as $\lambda_{e-ph} \sim 0.5$, thus classifying these alloys as weak-to-intermediate-coupling superconductors. These parameters confirm the applicability of the WHHM theory to our series of alloys.

Table 4.6: Some superconducting and electronic properties

| Alloy specimen | $\langle \frac{e}{a} \rangle^a$ | V_0 [$\text{\AA}^3/\text{atom}$] ^b | n_e [10^{29} m^{-3}] | τ_{tr} [10^{-16} s] | λ_{so} | τ_{so} [10^{-14} s] | $\frac{\xi_G}{l}$ | $\frac{\tau_{so}}{\tau_{tr}}$ | λ_{e-ph} ^c |
|---|---------------------------------|---|------------------------------------|--------------------------------------|----------------|--------------------------------------|-------------------|-------------------------------|-------------------------------|
| NiZr ₂ | 6.00 | 18.96 | 3.2 | 8 | 2.88 | 11.5 | 22 | 202 | 0.59 |
| Fe _{0.1} Ni _{0.9} Zr ₂ (2) | 5.93 | 19.00 | 3.1 | 12 | 2.89 | 10.6 | 18 | 194 | 0.61 |
| Fe _{0.15} Ni _{0.85} Zr ₂ | 5.90 | 19.02 | 3.1 | 14 | 0.27 | 129.8 | 18 | 991 | 0.58 |
| Fe _{0.2} Ni _{0.8} Zr ₂ (2) | 5.87 | 19.04 | 3.1 | 12 | 4.43 | 8.69 | 20 | 144 | 0.57 |
| Fe _{0.3} Ni _{0.7} Zr ₂ (2) | 5.80 | 19.07 | 3.0 | 8 | 1.81 | 22.2 | 25 | 462 | 0.56 |
| Fe _{0.33} Ni _{0.67} Zr ₂ | 5.78 | 19.09 | 3.0 | 6 | 7.91 | 4.61 | 27 | 73 | 0.58 |
| Fe _{0.36} Ni _{0.64} Zr ₂ | 5.76 | 19.10 | 3.0 | 7 | 7.40 | 5.29 | 26 | 74 | 0.57 |
| Fe _{0.4} Ni _{0.6} Zr ₂ (2) | 5.73 | 19.11 | 3.0 | 16 | 0.52 | 86.9 | 19 | 1704 | 0.55 |
| Fe _{0.5} Ni _{0.5} Zr ₂ (2) | 5.67 | 19.15 | 3.0 | 6 | 2.15 | 30.1 | 36 | 494 | 0.51 |
| Fe _{0.6} Ni _{0.4} Zr ₂ | 5.60 | 19.19 | 2.9 | N. A. | N. A. | N. A. | N. A. | N. A. | 0.40 |

Uncertainties are not computed for quantities that depend on n_e and S/S_F because those quantities come from assumptions of the electronic structure of the material. Experimental uncertainties are expected to be much smaller than uncertainties related to these assumptions. Moreover, these quantities are computed only to provide a fair idea of their order of magnitude, and should not be taken as absolute values for these alloys.

^aElectron to atom ratio (average group number).

^bAtomic volume. For Zr, the atomic volume is obtained from Ref.[85]. For Ni and Fe, the atomic volume is computed from empirical values of the atomic radii obtained from Ref.[56].

^cExperimental uncertainty ~ 4 %

The WHHM equations

The WHHM equations which include the effects of Pauli-spin paramagnetism and spin-orbit interaction are obtained from Ref.[69]:

$$\ln\left(\frac{1}{t}\right) = \left(\frac{1}{2} + \frac{i\lambda_{so}}{4\gamma}\right) \psi\left(\frac{1}{2} + \frac{\bar{b} + 0.5\lambda_{so} + i\gamma}{2t}\right) + \left(\frac{1}{2} - \frac{i\lambda_{so}}{4\gamma}\right) \psi\left(\frac{1}{2} + \frac{\bar{b} + 0.5\lambda_{so} - i\gamma}{2t}\right) - \psi\left(\frac{1}{2}\right) \quad (4.32)$$

in terms of the reduced temperature

$$t = \frac{T}{T_c}, \quad (4.33)$$

scaled upper critical magnetic field

$$\bar{b} = \frac{2eB_{c2}v_F^2\tau_{tr}}{6\pi k_B T_c}, \quad (4.34)$$

Maki parameter

$$\alpha = \frac{3\hbar}{2mv_F^2\tau_{tr}}, \quad (4.35)$$

spin-orbit-coupling induced spin-flip scattering parameter

$$\lambda_{so} = \frac{\hbar}{3\pi k_B T_c \tau_{so}}, \quad (4.36)$$

and

$$\gamma = \left[(\alpha\bar{b})^2 - (0.5\lambda_{so})^2 \right]^{\frac{1}{2}}, \quad (4.37)$$

and where ψ is the digamma function . We numerically solve equation (4.32) and use a nonlinear fit routine to obtain the least-squares best fit values for λ_{so} for our data and to determine B_{c2} at arbitrary temperatures. The values for λ_{so} thus obtained are shown in Table (4.6) while the best-fit curves for B_{c2} vs T are represented by the blue curves in Figs.(4.5) and (4.6).

In the absence of spin-paramagnetic effects and spin-orbit interactions, $\alpha = 0$ and $\lambda_{so} = 0$, equation (4.32) reduces to the simpler

$$\ln\left(\frac{1}{t}\right) = \psi\left(\frac{1}{2} + \frac{\bar{b}}{2t}\right) - \psi\left(\frac{1}{2}\right) \quad (4.38)$$

from which one obtains results for $B_{c2}(T)$ only due to orbital pair-breaking. We also numerically solved this equation inputting our experimental T_c results and obtained the black curves shown in Figs.(4.5) and (4.6). It is apparent that the relationship between B_{c2} and T resulting from this equation generally represents our data better, close to T_c , than the full WHHM theory does, but this is not true at high field. Taking into account spin-paramagnetism α , but leaving out spin-orbit interactions i.e. $\lambda_{so} = 0$, one obtains in place of equation (4.32)

$$\ln\left(\frac{1}{t}\right) = \frac{1}{2}\psi\left(\frac{1}{2} + \frac{\bar{b} + i\alpha\bar{b}}{2t}\right) + \frac{1}{2}\psi\left(\frac{1}{2} + \frac{\bar{b} - i\alpha\bar{b}}{2t}\right) - \psi\left(\frac{1}{2}\right), \quad (4.39)$$

shown by the red curves in Figs.(4.5) and (4.6). These curves reveal the importance of taking into account both paramagnetic effects and spin-orbit interactions for our series of alloys. Indeed, it appears that including the effects of spin-paramagnetism and leaving out spin-orbit coupling limits B_{c2} too much over the whole temperature range, thus yielding $B_{c2}(T)$ values much lower than determined experimentally. This confirms the results obtained in section (4.4) that B_{c2} in these alloys is limited by paramagnetic effects, but not very strongly.

Further modifications: effect of electron-phonon coupling strength

At this point we can conclude that our experimental $B_{c2}(T)$ are reasonably well-represented by the predictions of the WHHM theory including spin-paramagnetism and spin-orbit interactions, although for many of the samples ($\text{Fe}_x\text{Ni}_{1-x}\text{Zr}_2$ with $0 \leq x \leq 0.3$) the predictions yield an enhanced $B_{c2}(T)$ in the low- T regime compared to the experimentally determined values. Also, for most of the samples, the predictions are lower than the experimentally determined values for intermediate temperatures. In order to obtain better agreement between theory and experiments in the intermediate temperature range, we proceed by including a correction due to electron-phonon coupling in the WHHM theory. Strong coupling effects have been shown to enhance $B_{c2}(T)$ [41].

As described briefly in section (2.8.2), one obtains the electron-phonon coupling parameter λ_{e-ph} from the McMillan equation (2.29) simply from an experimentally

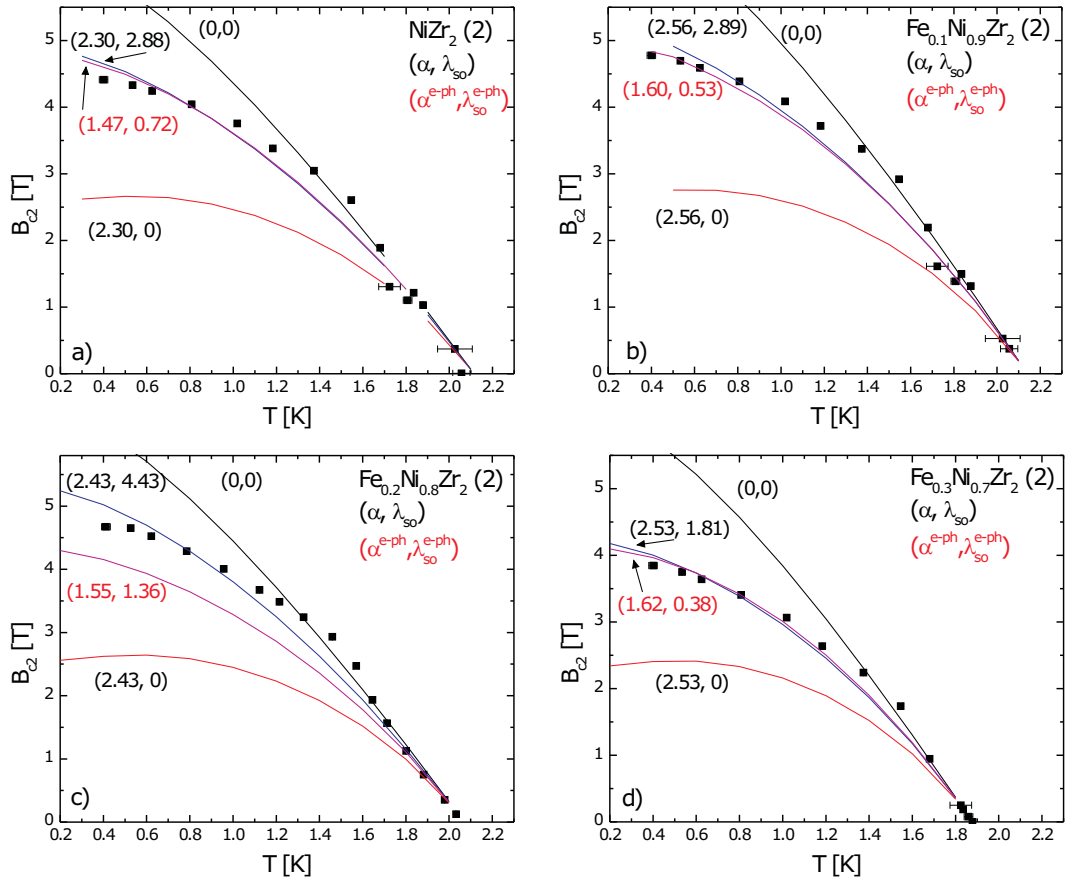


Figure 4.5: B_{c2} vs T for our different alloys. The data points represent experimental data, with error bars on T determined from temperature fluctuations during data acquisition, and experimental errors on B_{c2} smaller than the size of the dot. Blue curves: Fits to the full WHHM theory (equation (4.32)). Black curves: Plot of equation (4.38) including our experimental T_c and $\frac{dB_{c2}}{dT}|_{T_c}$. Red curves: Plot of equation (4.39) using our experimental T_c and $\frac{dB_{c2}}{dT}|_{T_c}$. Magenta curves: Fit to equation (4.32) using α^{e-ph} which includes a correction to account for electron-phonon coupling.

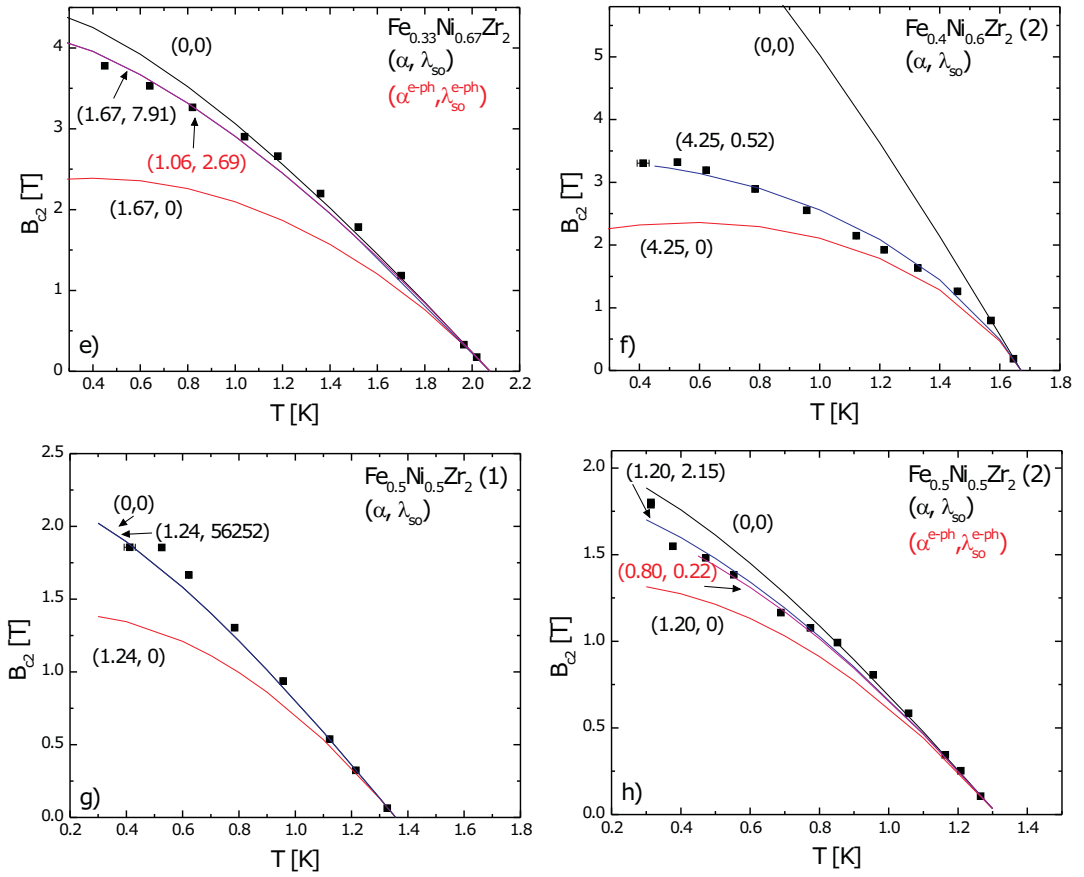


Figure 4.6: B_{c2} vs T for our different alloys. The data points represent experimental data, with error bars on T determined from temperature fluctuations during data acquisition, and experimental errors on B_{c2} smaller than the size of the dot. Blue curves: Fits to the full WHHM theory (equation (4.32)). Black curves: Plot of equation (4.38) including our experimental T_c and $\frac{dB_{c2}}{dT}|_{T_c}$. Red curves: Plot of equation (4.39) using our experimental T_c and $\frac{dB_{c2}}{dT}|_{T_c}$. Magenta curves: Fit to equation (4.32) using α^{e-ph} which includes a correction to account for electron-phonon coupling.

determined T_c . The λ_{e-ph} 's determined for our series of alloys (Table (4.6)) make them rather weak to intermediate-coupling superconductors such that strong coupling corrections should have very little effect on $B_{c2}(T)$. At this points, we could also consider including a correction due to spin fluctuations through a spin-fluctuation parameter λ_{sf} . Spin fluctuations are predicted to be important in this series of alloys because of the presence of the magnetic Fe atoms [53]. Therefore, we could to include effects of electron-phonon coupling and spin fluctuations through a renormalization of B_p as discussed in Ref.[88] such that

$$B_p^{e-ph} = \frac{1 + \lambda_{e-ph} + \lambda_{sf}}{S} B_p, \quad (4.40)$$

where S is the Stoner factor which comes in the early treatment of spin fluctuations as an enhancement factor in the valence magnetic susceptibility at low temperature [55]. Unfortunately, in the absence of magnetic susceptibility data, treatment of the spin-fluctuation correction is not possible, and so we proceed by considering only effects due to electron-phonon coupling, in which case, the renormalized and enhanced upper critical field becomes

$$B_p^{e-ph} = (1 + \lambda_{e-ph}) B_p. \quad (4.41)$$

We include the correction in the WHHM theory by fitting equation (4.32) as before, but using

$$\alpha^{e-ph} = \frac{1}{1 + \lambda_{e-ph}} \alpha \quad (4.42)$$

in place of α as given by equation (4.35). As shown by the magenta curves in Figs.(4.5) and (4.6), the reduced values of α^{e-ph} compared to α used here also yield fairly lower values of the fitting parameter λ_{so}^{e-ph} compared to λ_{so} . Even though we obtain lower values for the fitting parameters, the theoretical curves do not seem to agree significantly better with the experimental data. Some of the predictions are improved in the low temperature regime by a reduction of B_{c2} , but no changes are observable in the intermediate temperature regime where the predictions are lower than the experimental values of B_{c2} . Therefore, we conclude this section by predicting that including the effects of spin fluctuations might improve slightly the agreement between these

experimental results and the predictions of the WHHM theory, but that this is rather uncertain. Indeed, best agreement between the WHHM theory and experimental data is obtained for $\text{Fe}_x\text{Ni}_{1-x}\text{Zr}_2$ with $x \geq 0.33$, which are specifically those alloys in which spin fluctuations should be the most important because of the larger iron content. Nevertheless, the WHHM theory models fairly well the linearity of $B_{c2}(T)$ in the high temperature regime and its negative curvature at low temperature. Good agreement between experimental $B_{c2}(T)$ and the predictions of the WHHM theory have also been reported in Refs.[85, 86]. Although the values obtained here for the Maki parameter α and the spin-orbit coupling parameter λ_{so} are generally physically reasonable because they imply spin-orbit coupling induced spin-flip scattering times τ_{so} much longer than the transport scattering time τ_{tr} and agree well with the values for these same parameters obtained in Refs.[85, 86], an unphysically large value of $\lambda_{so} \rightarrow \infty$ is obtained for the alloy $\text{Fe}_{0.5}\text{Ni}_{0.5}\text{Zr}_2$ (1) (Fig.(4.6g)). In Ref.[85, 102, 86], the obtaining of such large values of λ_{so} was attributed to inhomogeneities in the alloy which have been shown to increase $B_{c2}(T)$ at low temperature [103]. As far as we know, samples $\text{Fe}_{0.5}\text{Ni}_{0.5}\text{Zr}_2$ (1) and $\text{Fe}_{0.5}\text{Ni}_{0.5}\text{Zr}_2$ (2) come from the same batch and were thus prepared in the same conditions such that we cannot explain why the first sample yields an unphysically large λ_{so} while the second one yields a reasonable value of λ_{so} .

4.5 Summary

In summary, the series of $\text{Fe}_x\text{Ni}_{1-x}\text{Zr}_2$ metal glasses was shown to exhibit superconducting properties which classifies them in the category of weak-to-intermediate coupling superconductors in the very dirty limit. Low-field magnetization loops were shown from which the temperature of the lower critical field could be extracted. Thus deduced values of B_{c1} were shown to be of the same order of magnitude as the Maki predictions, but still differed due to a small amount of flux pinning. Superconducting parameters such as T_c and B_{c2} were found to vary as expected across this series of alloys in which spin fluctuations are expected to be important. Even though the actual

strength of spin fluctuations was not determined from experimental measurements, it is known to increase with iron content, and T_c was generally found to decrease accordingly. The only inconsistency to this trend was found for the alloy with the lowest iron content for which T_c is enhanced compared to the alloy not containing Fe. This was explained from the fact that the Fe d-band lies closer to the Fermi level than the Ni d-band which increases the density of states at the Fermi level for alloys containing Fe. Moreover, the variation of the upper critical field with temperature was shown to be reasonably well-fitted by equations of the WHHM theory including corrections due to spin-orbit coupling, Pauli paramagnetism, and electron-phonon coupling. Unfortunately, corrections due to spin fluctuations could not be integrated to this model, but we suggest that they be in future work.

Local structure dependence on x in the a -Fe $_x$ Ni $_{1-x}$ Zr $_2$ alloys

The local structure of superconducting materials greatly affects their superconducting properties; be it induced by defects in the form of structural perturbations or chemical impurities, disorder has an important influence on parameters such as the critical temperature and fields. Local structural perturbations can originate from the presence of voids or dislocations in the lattice of crystalline or glassy materials, but can also arise from the presence of foreign atoms having a different volume than the host material atoms. Such impurities will generate mechanical strain fields in their environment and disturb the local structural order of the host material. While impurity atoms with a differing number of valence electrons than the host material will change the concentration of charge carriers in the material and thus the density of states at the Fermi level $N(E_F)$ such that T_c will also be affected, plain structural defects (i.e. not arising from the presence of impurity atoms) do not change the number of charge carrier but still affect $N(E_F)$ because they change the states of electrons in their local environment [14].

In a number of studies on pseudo-binary series of metallic glasses composed of early transition metals (ET) (e.g. Ti, Zr, Hf) and late transition metal (LT) (e.g. Fe, Co, Ni, Cu) in the form $(LT_x^a LT_{1-x}^b)_y ET_{1-y}$, a constant glass structure was assumed for varying relative content of the LT metal x and constant amount of the ET metal y [104, 105, 106, 53, 7] in order to study different dependences due to chemical composition across the series of alloys whilst excluding effects due to structure. Indeed, because the LT metal atoms Fe, Co, Ni and Cu all have similar volumes, it is rea-

reasonable to assume that changing their relative amounts x while keeping the content of ET metal y constant does not change the structure of the glass and only leads to changes in the physical properties attributable to changes in the density of states [7]. However, this assumption may overlook possible influence of the density of states on the structure of such pseudo-binary metallic glasses. The question whether the glass structure varies across the series of metal glasses $\text{Fe}_x\text{Ni}_{1-x}\text{Zr}_2$ studied in this thesis is particularly justified because it is generally assumed that the local short range order (SRO) in metallic glasses is intimately related to that of the first crystallization products¹ [7], and while these present a body-centered-tetragonal (bct) structure of the CuAl_2 -type in the NiZr_2 alloy, they are face-centered-cubic (fcc) of the NiTi_2 -type in the FeZr_2 alloy, such that across the series of amorphous alloys $\text{Fe}_x\text{Ni}_{1-x}\text{Zr}_2$, a transition in the short range order as a function of x is consequently expected. Therefore, in the series of alloys $\text{Fe}_x\text{Ni}_{1-x}\text{Zr}_2$, superconductivity is expected to be influenced by the increasing presence of spin fluctuations related to the Fe content, but also by a possible change in the local short range order at some critical value of x . In chapter (4), the increase of Fe content x in the alloys was observed to lead to a depression of T_c and B_{c2} as expected from the increase of spin fluctuations with related destruction of Cooper pairs. In this chapter, we will demonstrate that a structural transition arises in the series of alloys for x between 0.4 and 0.5.

5.1 Fluctuations in magnetization

In chapter (4), low-field magnetization curves were presented for different alloys with $0 \leq x \leq 0.5$ in which increasing fluctuations in magnetization with Fe content could be observed. In this section, we present a more careful investigation of these fluctuations and relate their appearance to a structural evolution of the short range order (SRO) characterizing the metallic glasses with x .

¹The assumption that the SRO in metallic glasses is similar to that of the crystalline counterpart comes from the fact that in metal-metal glasses, diffusion lengths are short such that upon crystallization, the atoms do not move far away from their initial positions in the glass.

Fig.(5.1) shows an analysis of the noise level in the magnetization curves of Fig.(4.1) as a function of the Fe content in the samples: the data is obtained from fitting parts of the magnetization curves for $B > B_{c1}$ with a polynomial of order 4, then subtracting the fit ($\langle M(B) \rangle$) from the data to obtain the fluctuations around the mean² ($M(B) - \langle M(B) \rangle$). The ratio of the fluctuations around the mean to the mean is then computed to obtain the relative fluctuations (Fig.(5.1)). In this manner, the dramatic increase of magnetization fluctuations with Fe content in the magnetization data becomes evident.

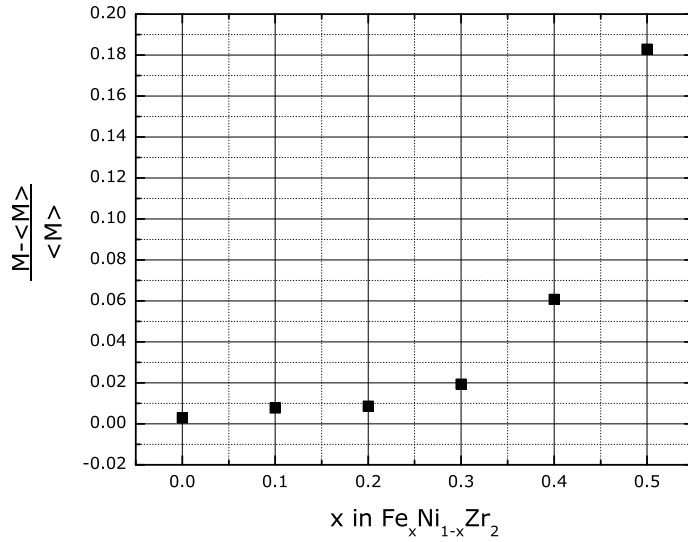


Figure 5.1: Standard error on the mean of the statistical distribution of the ratio of the fluctuations in magnetization to the mean magnetization for different $\text{Fe}_x\text{Ni}_{1-x}\text{Zr}_2$ alloys.

The magnetization basically represents the sum over the magnetic moments in the sample, i.e. $M = \sum_i^N m_i$; accordingly, M depends on both the total number $N = V/a^3$ of these magnetic moments, and on their magnitude (V is the volume of the superconducting sample and a^3 is the characteristic size of grains). For a homogeneous

²An order 4 polynomial was chosen to fit the data for no other particular reason than the fact that it followed the data well; this fit technique has to be used here to determine the noise level because our signal is not constant.

superconductor with equal magnitude magnetic moments, the global sample magnetization does not fluctuate significantly because self-averaging over all the moments in the sample takes place. However, if the sample contains large size inhomogeneities, or regions with a much larger magnetic moment than the average, then fluctuations in the global magnetization arise because, even upon self-averaging, the signal from these regions stands out from the average. The size of relative fluctuations gives an estimate for the number of grains N , and can thus be used to obtain an approximate value for the size of grains. Indeed, for systems with a large number of independent parts, the size of relative fluctuations is of order $1/\sqrt{N}$, and since $N = V/a^3$, the approximate size of grains is thus

$$a \sim \left(\frac{V}{N}\right)^{1/3} = \left(\frac{\langle M - \langle M \rangle \rangle^2}{\langle M \rangle^2} V\right)^{1/3}. \quad (5.1)$$

Using this expression with the data shown in Fig.(5.1) and the volume of the superconducting sample determined from the active area of the 2DEG probe and the thickness of the superconductor $V = 20 \mu\text{m} \times 750 \mu\text{m} \times 100 \mu\text{m}$, we obtain $a \sim 37 \mu\text{m}$ for the $\text{Fe}_x\text{Ni}_{1-x}\text{Zr}_2$ sample with $x = 0.5$. The size of a then decreases with decreasing Fe content just like the relative size of fluctuations.

Analysis of the magnetization fluctuations can be further developed to evaluate the characteristic magnitude of the fluctuations in magnetic field. To a first approximation, determination of the characteristic field of fluctuations B_0 is performed from evaluation of the standard deviation of the magnetization as a function of magnetic field increment ε , i.e. $f(\varepsilon) = \langle m(B) m(B + \varepsilon) \rangle - \langle m(B) \rangle^2$, at $\delta^2/2$ where $\delta = \sqrt{f(0)} = \sqrt{\langle m(B)^2 \rangle - \langle m(B) \rangle^2}$ is the usual standard deviation expression. A plot of $f(\varepsilon)$ as obtained from data on a sample of the alloy $\text{Fe}_{0.4}\text{Ni}_{0.6}\text{Zr}_2$ is shown in Fig.(5.2); as expected, $f(\varepsilon)$ decreases with increasing ε as correlations diminish.

Fig.(5.3) shows the values for the characteristic field of fluctuations B_0 thus obtained for each alloy studied. The magnitude of B_0 generally increases with Fe content as expected from the data of Fig.(5.1). Fig.(5.3) also displays the magnetic flux Φ related to the field fluctuations B_0 . We believe that the fluctuations in magnetiza-

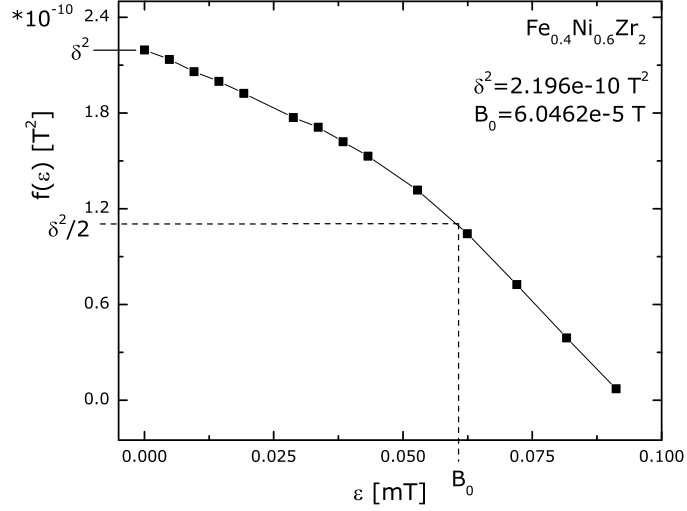


Figure 5.2: Standard deviation as a function of magnetic field increment $f(\varepsilon)$ used to determine the characteristic field of fluctuations B_0 at $\delta^2/2$. (The line is just a guide for the eye.)

tion originate from entry and exit of clusters of vortices in the sample taking place inhomogeneously in the sample due to an inhomogeneous distribution of grains with differing superconducting properties due to their different SRO. From the data for Φ of Fig.(5.3), it can be deduced that the clusters in the $x = 0.5$ sample contain about 1000 vortices; the number of vortices in the clusters generally decreases with decreasing Fe content. This clustering of vortices most likely comes from the presence of inhomogeneities in the samples which could originate from structural instability as x approaches the structural transition expected across the series of alloys. From the dramatic increase in the size of grains a and characteristic magnetic flux of fluctuations, it appears that the structural transition occurs very close to the $\text{Fe}_x\text{Ni}_{1-x}\text{Zr}_2$ alloy with composition $x = 0.5$. We will show in section (5.2.1) more evidence for the existence of a structural transition close to alloy composition with $x = 0.5$ and also discuss this problem in more detail.

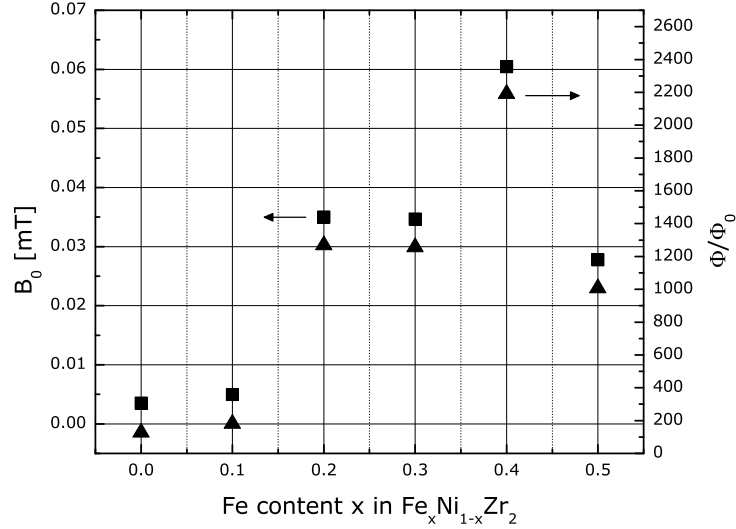


Figure 5.3: Characteristic field of fluctuations B_0 and characteristic magnetic flux Φ threading grains in units of Φ_0 as a function of the Fe content x in the $\text{Fe}_x\text{Ni}_{1-x}\text{Zr}_2$ metallic glasses.

5.2 Anomalous hysteresis loops in $x = 0.5$ and $x = 0.6$

Due to flux pinning, the transition at B_{c2} in superconductors often exhibits hysteresis. These hysteresis loops are counterclockwise, i.e. B_{c2} is larger on the up-going field sweep than on the down-going field sweep, as strong pinning centers tend to trap the magnetic flux in the superconductor as the field is decreased from the field-induced normal state. Surprisingly, all the samples of the alloys $\text{Fe}_x\text{Ni}_{1-x}\text{Zr}_2$ with $x = 0.5$ (about 10 samples) and $x = 0.6$ (only one sample) we have measured exhibit clockwise hysteresis loops at B_{c2} , while all the samples of the other alloys ($x \leq 0.4$) show the usual counterclockwise hysteresis loops characteristic of superconductors, or no visible hysteresis. A specimen resistance vs applied magnetic field curve showing this phenomenon for each alloy is shown in Fig.(5.4). Compared to the very narrow, or even absent, counterclockwise hysteresis loops found in alloys with $x \leq 0.4$, the clockwise hysteresis loops for the alloys with $x = 0.5$ and $x = 0.6$ are very large and

definite. For $\text{Fe}_{0.6}\text{Ni}_{0.4}\text{Zr}_2$, the transition is observed to proceed in two well-defined steps of which the uppermost is very broad and with a hysteresis loop in the opposite direction (counterclockwise). This type of transition will be discussed later. We now introduce the peculiar results obtained on these two alloys with a large iron content, and will complete the chapter with a proposition for a model to explain these results which will confirm the existence of a structural transition with x across the series of alloys; this model will be shown to also accommodate the findings presented in the previous section from the fluctuations in magnetization.

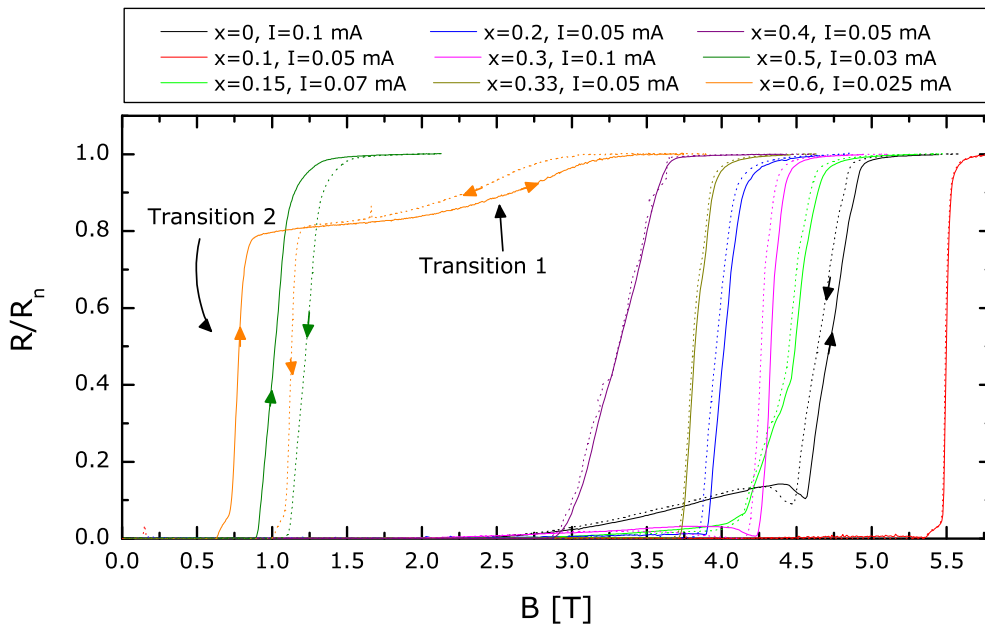


Figure 5.4: Normalized resistance vs applied magnetic field for different samples of the alloys $\text{Fe}_x\text{Ni}_{1-x}\text{Zr}_2$. Solid lines are for increasing B sweeps and dotted lines are for decreasing B sweeps. $T \simeq 0.35$ K

5.2.1 Experimental results: Evidence for a dynamical effect

We present in this section a gathering of the various anomalous results obtained from measurements of the $\text{Fe}_x\text{Ni}_{1-x}\text{Zr}_2$ alloys with $x = 0.5$ and $x = 0.6$. Various dependences such as the evolution of the size of hysteresis loops with magnetic field

sweep rate, as well as different history-dependent observations will be shown. The dependence of the width of the hysteresis loops at the B_{c2} transition determined from resistance measurements as a function of magnetic field on the magnetic field sweep rate yields important information about the origin of the anomalous clockwise hysteresis loops. Namely, a dependence on sweep rate is an indication that a dynamical process is taking place such as flux motion or creep. In Fig.(5.5a), we present the dependence of the width of the hysteresis loop ΔB as a function of the B -sweep rate for a sample of $\text{Fe}_{0.5}\text{Ni}_{0.5}\text{Zr}_2$. The width of the hysteresis loop is taken as the difference between the magnetic field at $R_n/2$ on the decreasing and increasing field sweep. Data for two different driving currents are presented; in both cases the size of the hysteresis loop increases with increasing field sweep rate, and while the loops are thinner for the larger driving current, the increase in loop size is faster for this larger current.

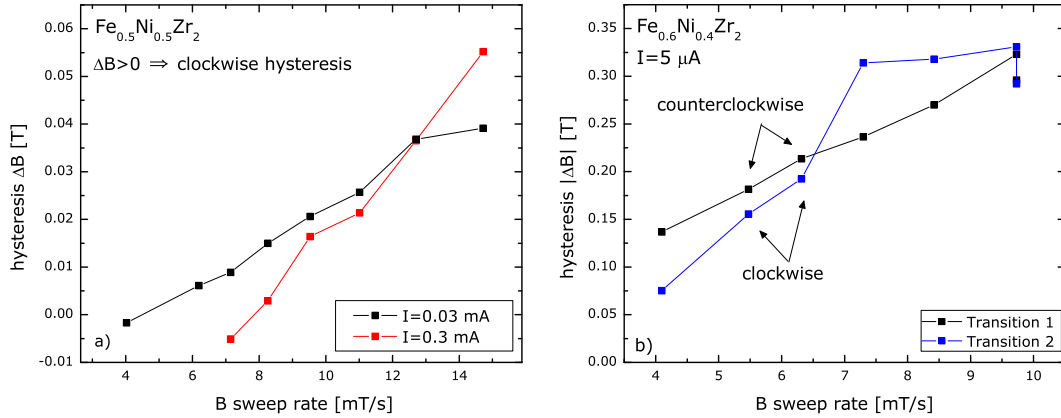


Figure 5.5: Width of hysteresis loop as a function of magnetic field sweep rate for a) $\text{Fe}_{0.5}\text{Ni}_{0.5}\text{Zr}_2$ at $T = 0.34$ K and b) $\text{Fe}_{0.6}\text{Ni}_{0.4}\text{Zr}_2$ at $T \simeq 50$ mK. The lines are guides to the eye.

Similar results were obtained on a sample of $\text{Fe}_{0.6}\text{Ni}_{0.4}\text{Zr}_2$ as shown in Fig.(5.5b). The situation is slightly more complicated in this case because the transition to the superconducting state proceeds in two steps. Therefore, we report the results for the size of the hysteresis loops separately: we will refer to the uppermost transition

as transition 1 and the lower one as transition 2, as can be seen in Fig.(5.4). Also observe in this figure that the direction of the hysteresis loops of these two transition is not the same: transition 1 exhibits an anti-clockwise loop as often observed in superconductors and the final transition to the superconducting state exhibits the anomalous clockwise loop. The counterclockwise hysteresis observed at transition 1 in $\text{Fe}_{0.6}\text{Ni}_{0.4}\text{Zr}_2$ results from usual vortex pinning behavior in superconductors according to which the strong pinning properties trap and delay flux exit at B_{c2} upon decreasing the external field, resulting in an apparently lower B_{c2} . The width of the hysteresis loop for transition 1 is taken as the field difference at $\frac{R_m - R_c}{2}$ and at $\frac{R_c}{2}$ for transition 2. R_c is determined as the resistance at which the curves for increasing and decreasing field intersect between the two transitions. These criteria are used for all the ΔB data on the $x = 0.6$ alloy presented in this chapter. As observed in the alloy with $x = 0.5$, the size of the hysteresis loops (for both transitions) of Fig.(5.5b) increases with field sweep rate.

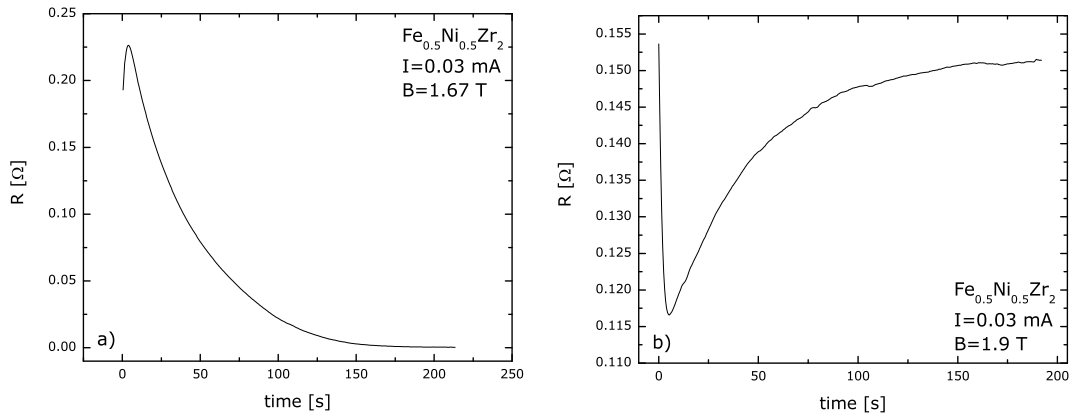


Figure 5.6: Resistance as a function of time after pausing the external magnetic field in the B_{c2} transition during a) an increasing B sweep and b) a decreasing B sweep.

Additional evidence for the dynamical origin of the clockwise hysteresis loops is brought by the data shown in Fig.(5.6) which was acquired by measuring a $x = 0.5$ sample resistance as a function of time immediately after pausing the external magnetic field sweep in the middle of the B_{c2} transition. In the figure, time $t = 0$

represents the moment at which the field was paused. In this manner, it is observed that upon pausing the field in an up-going field sweep (Fig.(5.6a) the resistance initially keeps increasing, but turns around after a few seconds to finally decrease back to zero. A similar phenomenon is observed upon pausing the field in a decreasing field sweep: as shown in Fig.(5.6b), after an initial sharp decrease, the resistance turns around and increases back to a value close to the initial value it had when the field was paused.

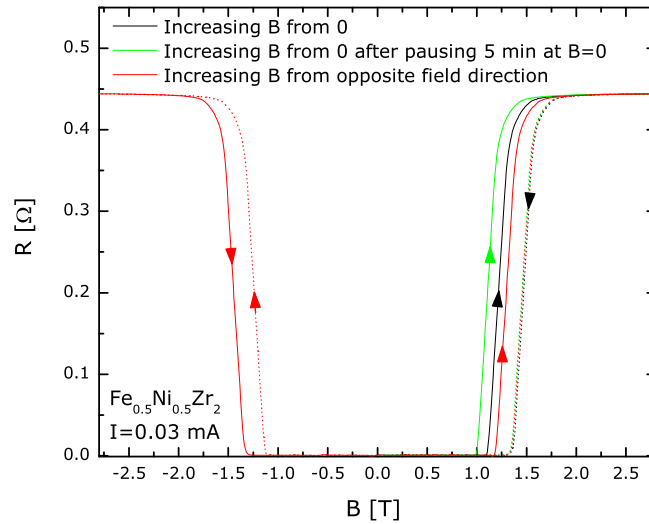


Figure 5.7: Resistance vs magnetic field from sweeping the magnetic field at 11 mT/s over a single field polarity without pausing at $B = 0$ (black curves), pausing at $B = 0$ for 5 min, and from sweeping over the two field polarities (green curves).

The data shown in this section up to now were acquired by sweeping the magnetic field between zero and a value above B_{c2} of the same field polarity. Interestingly, slightly different results are obtained when the field is swept across $B = 0$ from negative field polarity to positive field polarity. As shown in Fig.(5.7), in this case (red curves), the width of the hysteresis loop diminishes with respect to its size when the field sweep is only performed over the same field polarity (black and green curves). Moreover, even larger hysteresis loops are observed if after decreasing the field, we pause at $B = 0$ for some time before bringing the field back up again

above B_{c2} (of the same polarity), as shown by the green curves in Fig.(5.7). This observation also confirms the dynamical origin of the clockwise hysteresis loops. Also, it can be observed that no matter the preparation history, the B_{c2} transition upon decreasing field sweep is always the same (overlapping dotted lines on the positive B field side). Therefore, because this transition shows no history dependence, it appears that applying a magnetic field larger than B_{c2} resets the system, which can hence be attributed to the fact that no field is expelled in this regime since $B > B_{c2}$.

5.2.2 Effect of driving current

Important information on the superconducting state can be learned from measurements of the resistance with different driving currents. For instance, in superconductors, unlike in normal metals, the current-voltage characteristics are non-linear as a result of vortex motion, such that using different driving currents to measure the superconducting properties can reveal a variety of vortex phases. Incidentally, vortex phases will be discussed in chapter (6). In our alloys, analysis of the dependence of the width of the hysteresis loops on driving current has to be performed carefully because of the appearance of the peak effect (PE) and other vortex phases at large driving current close to the transition (see section (6)) which can tangle the effects of inhomogeneities and vortex phases³.

Figs. (5.8a) and (5.9a) show resistance curves as a function of magnetic field for different driving currents on the $x = 0.5$ and $x = 0.6$ alloys respectively. The appearance of the peak effect at large driving current in $\text{Fe}_{0.5}\text{Ni}_{0.5}\text{Zr}_2$ is obvious, as well as the emergence of a depinned vortex phase between the PE and the normal state for decreasing B field. Related to the advent of this phase is an apparent large broadening of the transition with reversal of the direction of hysteresis which is not related to the effect resulting in the clockwise hysteresis loops. For the alloy with $x = 0.6$, no PE nor depinned vortex phase is apparent (except for a small shoulder on

³The PE is seen as a drop in resistance as a functions of magnetic field close to the B_{c2} transition which results from the sudden re-pinning of the vortex lattice attributed to its softening. See for instance Refs.[107, 108].

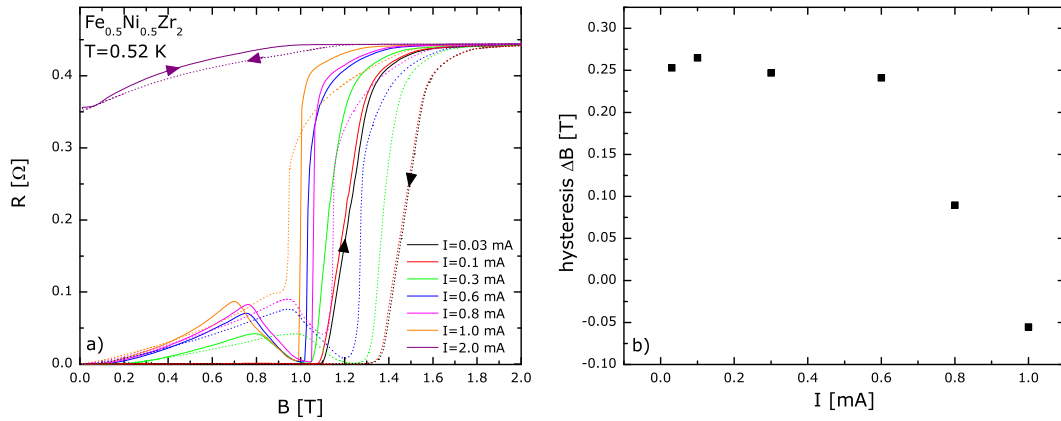


Figure 5.8: a) Resistance vs magnetic field for different driving currents for an alloy of $\text{Fe}_{0.5}\text{Ni}_{0.5}\text{Zr}_2$. Solid lines are for increasing magnetic field and dotted lines are for decreasing magnetic field. The B sweep rate is 15 mT/s. b) Width of the hysteresis loops observed in a).

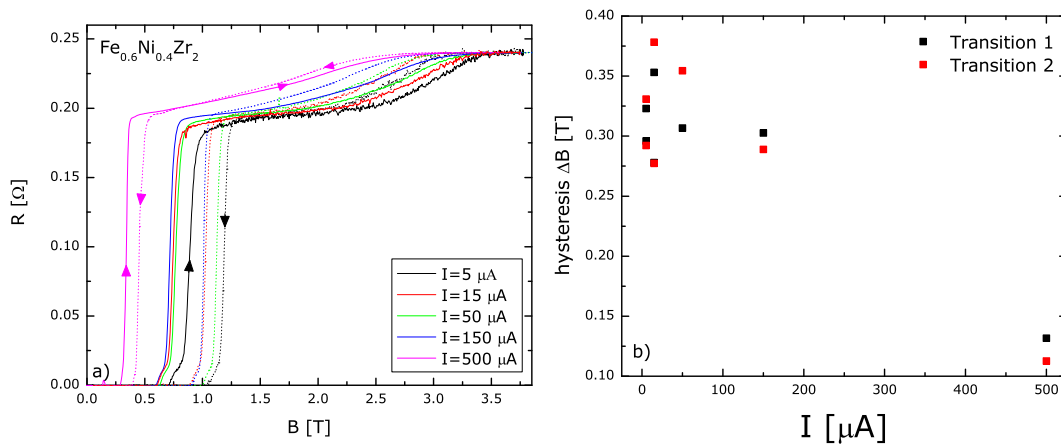


Figure 5.9: a) Resistance vs magnetic field for different driving currents for an alloy of $\text{Fe}_{0.6}\text{Ni}_{0.4}\text{Zr}_2$. Solid lines are for increasing magnetic field and dotted lines are for decreasing magnetic field. The B sweep rate is 10 mT/s. b) Width of the hysteresis loops observed in a).

the low field side of the transition) such that this data can be considered more reliably for a dependence of hysteresis on driving current. The width of the hysteresis loops for the $x = 0.5$ and $x = 0.6$ alloys are shown in Figs. (5.8b) and (5.9b) respectively. The observed decrease in the size of the hysteresis loops for $x = 0.5$ is unreliable, but a similar decrease is clearly observed in $x = 0.6$, such that we can assert that this is the true hysteresis dependence on the driving current.

5.2.3 Temperature dependence of hysteresis

Measurements of the resistance as a function of magnetic field were performed at different temperatures on a sample of $\text{Fe}_{0.5}\text{Ni}_{0.5}\text{Zr}_2$; the results are shown in Fig.(5.10a), while the temperature dependence of B_{c2} extracted from these curves appeared in Fig.(4.6h). $B_{c2}(T)$ was found to be well-described by the WHHM theory. The clockwise hysteresis loops are observed for all temperatures up to T_c . A steady increase of the width of hysteresis loops relative to the mean value of B_{c2} ($B_{c2}^{mean} = (B_{c2}^{down} - B_{c2}^{up})/2$) is witnessed (see Fig.(5.10a)). The width of the B_{c2} transition ΔB_{c2} determined from the magnetic field difference at 90 % of R_n and 10 % of R_n is also shown in Fig.(5.10c). An increase in the width of the B_{c2} transition with decreasing temperature is a feature predicted by Zwicknagl and Wilkins [103] from consideration of conductivity fluctuations in inhomogeneous superconductors. It results from the fact that close to T_c , the coherence length $\xi(T)$ is very large such that superconducting properties are determined by their spatially-averaged values and the effect of inhomogeneities of size ξ_0 is smeared out. However, as the temperature is decreased, $\xi(T)$ decreases and the spatial resolution of inhomogeneities is thereby increased; in this manner the measurements reflect deviations from the average value. Therefore, seeing that the width of the transition is determined by conductivity fluctuations, increased deviation from averaged values broadens the width of the transition.

5.2.4 Magnetic field dependence of hysteresis

Measurements of the critical temperature dependence upon applied magnetic field were performed on the same sample of $\text{Fe}_{0.5}\text{Ni}_{0.5}\text{Zr}_2$ as used to measure the $B_{c2}(T)$

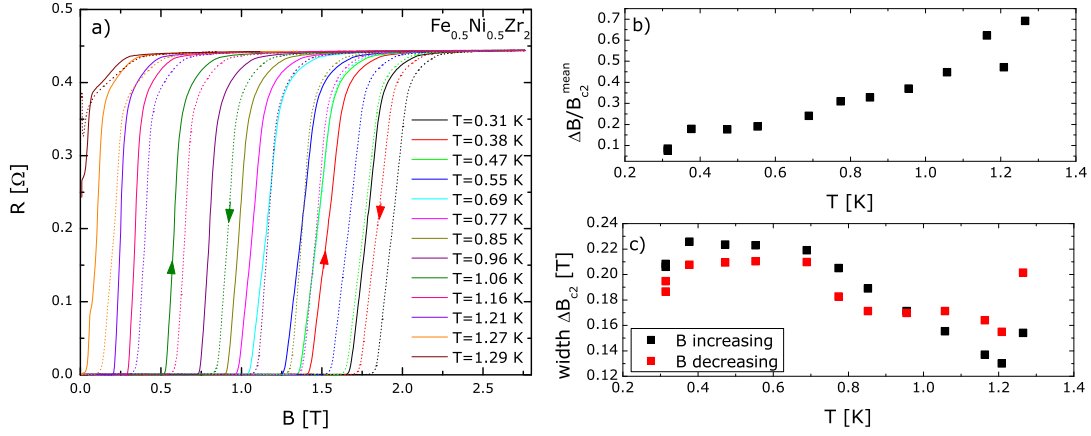


Figure 5.10: a) Resistance vs magnetic field at different temperatures for $\text{Fe}_{0.5}\text{Ni}_{0.5}\text{Zr}_2$. The B sweep rate is 15 mT/s. b) Width of the hysteresis loops normalized by the mean value of B_{c2} for increasing and decreasing B sweeps vs temperature. c) Width of the B_{c2} transition for increasing and decreasing magnetic field sweeps as a function of temperature.

data presented in Fig.(5.10). The measurements were performed by applying the external field when the temperature is above T_c , then sweeping the temperature down to below T_c , and finally sweeping the temperature back up to above T_c to complete the loop. The external magnetic field remains fixed during this whole process. The results are shown in Fig.(5.11) in which a striking observation comes into view: the hysteresis loops are now counter-clockwise and much thinner. The mere existence of hysteresis loops at this transition in zero field is uncanny because superconductors do not generally show history effects at T_c ; such behavior has been observed in materials in which superconductivity has been found to coexist with long-range magnetic order (see for instance Refs. ([109])). In our case, even if this sample contains a fairly large amount of iron (16.7 %), no long-range magnetic order is expected to exist, as it has been shown that long range ferromagnetic order appears in similar alloys for Fe content over 35 % [110]. In addition, if the hysteresis were due to some magnetic transition with the hysteretic region being the metastable phase, we would expect the direction of both the thermal and magnetic hysteresis loops to be the same. Therefore, it is most probable that these counterclockwise hysteresis loops in temperature arise

because of a slight delay between the temperature at the thermometer and that at the sample. This can easily occur in a temperature sweep since the thermometer is not located next to the sample. However, this delay would not be large enough to transform clockwise hysteresis loops into counterclockwise loops since the temperature sweep rate was only 0.02 K/min and we estimate the time delay in temperature reading and actual sample temperature to be 8 seconds which would yield a hysteresis of 5 mK; this is smaller than the typical ΔT (counterclockwise) we observe from 8 mK to 40 mK. These loops cannot originate from pinning effects since the magnetic field was maintained at a constant value during the whole sweeps. An increase in the width ΔT_c with increasing magnetic field as observed in Fig.(5.11c) is expected in inhomogeneous superconductors (see for instance Ref. [103]).

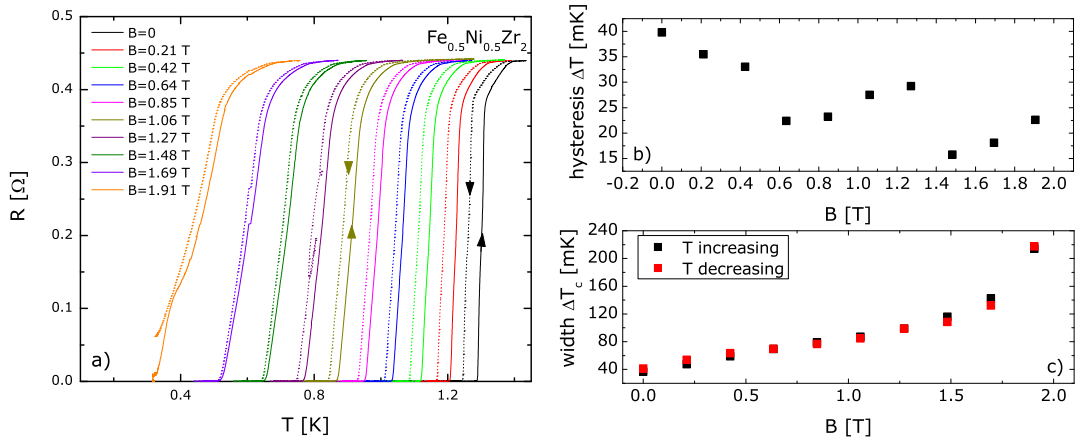


Figure 5.11: a) Resistance vs temperature data at different magnetic fields for a sample of $\text{Fe}_{0.5}\text{Ni}_{0.5}\text{Zr}_2$. b) Width of hysteresis loops extracted from the data in a). c) Width of the transitions shown in a) determined from the temperature difference between the 90 % and 10 % of R_n criteria.

5.3 Analysis of results

In this section, we will present an explanation for the origin of the peculiar hysteresis loops presented above and the information that can be extracted about the $x = 0.5$ and $x = 0.6$ alloys from these results. To this end, we will first introduce a model

describing the physical structure of these two sets of alloys and then describe how it explains the results presented above. Finally, we will argue that these results prove the existence of a structural transition in the series of metallic glasses $\text{Fe}_x\text{Ni}_{1-x}\text{Zr}_2$ with critical point between $x = 0.4$ and $x = 0.5$.

5.3.1 Proposed model

We propose that the anomalous clockwise hysteresis loops observed at B_{c2} in resistance measurements shown above arise because of the presence of structural inhomogeneities having different flux pinning properties in the $x = 0.5$ and $x = 0.6$ alloys. Indeed, as we have argued in the introductory section to this chapter, the structural order of superconductors strongly influences superconducting properties such as T_c and B_{c2} , but also pinning properties. So we propose that these alloys are composed of a main phase characterized by weak pinning properties and low critical current J_c , but also comprise inclusions of superconducting material having stronger pinning properties characterized by a larger J_c . Clockwise hysteresis loops appear in the magnetic field dependence of superconducting properties of such inhomogeneous material as a result of an inhomogeneous distribution of magnetic flux in the sample due to inhomogeneous pinning properties. According to this model, the flux distribution upon sweeping the magnetic field up and down is schematically depicted in Fig.(5.12), in which we refer to the strong pinning inclusions as phase B and to the main weakly-pinned phase as A. Phase A also assumes the connected superconducting path across the sample; it is thus the superconducting properties of this phase which are measured in resistance measurements. In such a sample, flux entry and exit proceeds in the following manner: Starting with the sample in the Meissner state at $B = 0$, upon application of a magnetic field, vortices first penetrate into phase A because flux entry is facilitated there because of its weaker pinning properties. As the external magnetic field is further increased, some vortices can penetrate in the strong-pinning inclusions, but they tend to stay in the weakly-pinned phase A and bend around the inclusions because their elasticity makes this energetically more favorable [3]. This results in an inhomogeneous distribution of the applied field in the

sample according to which the effective field in phase A is larger than it would be if the magnetic fluxes were homogeneously distributed among the two phases. As the magnetic field increases, the elasticity of the flux line lattice (FLL) diminishes and the flux lines cannot bend around the inclusions as easily; they become straighter and have to go through some high-pinning inclusions, thus forming large clusters around the inclusions. These clusters are characterized by a critical current lower than that of the initial inclusions alone, but larger than that of the weakly-pinned phase [3]. As the field is increased further passed the respective (true) upper critical field of phase A and B, the field-induced normal state is reached in the whole sample and a homogeneous flux distribution results in the sample. However, as the field is decreased back to below B_{c2} , the fluxes tend to stay trapped within the strong-pinning inclusions, while they easily leave phase A because of its weak-pinning properties. Again, the flux distribution between phase A and B becomes unbalanced as the flux density in the inclusions is now larger than it would be if the flux distribution was homogeneous. Accordingly, the effective field in the connected phase A is lower, resulting in a higher apparent B_{c2} . In this manner, the apparent B_{c2} transition is higher on the down-going field sweep than on the up-going field sweep, which results in clockwise hysteresis loops.

Clockwise hysteresis loops and double resistive transitions to the superconducting state have often been reported on inhomogeneous superconductors and granular superconductors [111, 112, 113, 3]. In granular superconductors, the grains exhibit good superconducting properties with larger T_c and J_c than the grain boundaries. These regions in between the grains are called weak links (WL); they ensure the (weak) coupling between the grains as Cooper pairs can tunnel through them, and they exhibit superconducting properties as found in Josephson junctions. A similar phenomenon takes place in inhomogeneous superconductors simply composed of regions with better superconducting properties than others [111], although the overall superconducting state in such material is not established via Josephson coupling.

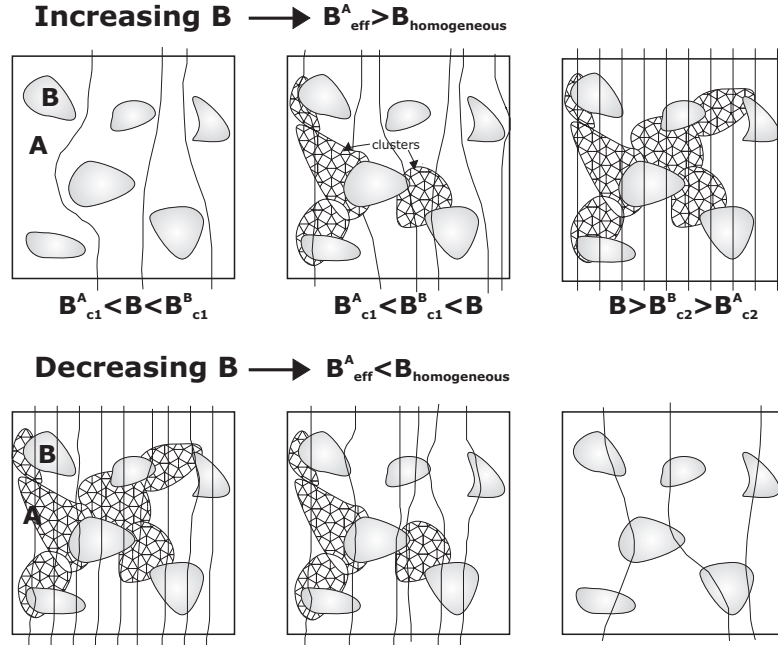


Figure 5.12: Schematic representation of the flux distribution upon increasing and decreasing the external magnetic field in inhomogeneous superconductors. The gray areas represent the inclusions with strong pinning properties.

5.3.2 The experimental results explained

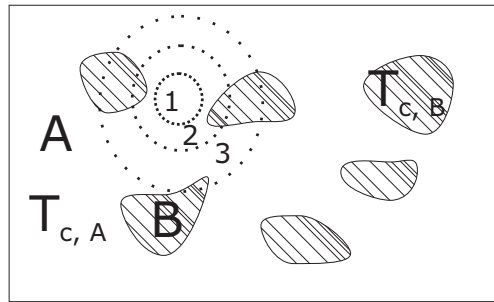


Figure 5.13: Schematic representation of an inhomogeneous superconductor composed of inclusions with transition temperature $T_{c, B}$ and a majority phase with transition temperature $T_{c, A}$.

A broadening of the transition to the superconducting state at T_c and B_{c2} , or more critically a double transition such as that observed in the $x = 0.6$ alloy studied here, are often observed in inhomogeneous superconductors [85, 114, 87, 115, 113, 116]. In order to picture how the presence of inhomogeneities in a superconductor leads to transition broadening, we consider the simple model depicted in Fig.(5.13), in which

the hatched regions (B) represent inhomogeneities with transition temperature $T_{c, B}$ and the rest (A) is the main phase of the sample with $T_{c, A}$. We will consider here that $T_{c, A} > T_{c, B}$ but the opposite could also arise and lead to similar results. As the temperature is lowered from above T_c , defined as the average transition temperature of the sample determined at $R_n/2$, and approaches $T_{c, A}$ ($T_{c, A} > T_c$), pockets of superconductivity appear in the sample which are small enough to fit between the lower T_c regions B; this is depicted by the region delimited by the heavy dotted line denoted by the number 1 in the figure. As the temperature is lowered further, the size of the superconducting regions increases, as shown by regions 2 and 3, and starts to enclose parts of the lower T_c regions B. While doing so, the pockets of superconductivity lower their own T_c since they are now composed of parts of superconductor with $T_{c, A}$ and $T_{c, B}$. Calling the transition temperature of the pocket of superconductivity which encloses parts of regions A and B $T_c(B)$, the width of the transition is given approximately by $\Delta T_c \approx T_{c, A} - T_c(B)$ [115]. Obviously, the larger the difference between $T_{c, A}$ and $T_{c, B}$ is, or the more of the B phase there is, the larger ΔT_c will be. From the very broad double resistive transition at B_{c2} observed in the $x = 0.6$ alloy, it can be assumed that the difference in T_c or B_{c2} between the two phases composing the alloy is very large; however, the observation of a single and sharp transition in the $x = 0.5$ alloy reveals that the superconducting properties, except the pinning properties, of the two phases in this alloy are very similar.

According to this model with inhomogeneous pinning properties in the sample, a variation of the size of the hysteresis loops with magnetic field sweep rate is expected because flux pinning and diffusion are dynamical processes. Moreover, an increase of the size of hysteresis loops with increasing magnetic field sweep rate such as that observed in Fig.(5.5) is expected because for slower $\frac{dB}{dt}$ the fluxes have more time to diffuse into the inclusions upon increasing the field, and similarly have more time to move into phase A as the field is decreased, such that the resulting flux distribution in phases A and B is more homogeneous. A similar observation was made by Liu *et al.* [111] from numerical simulations and experimental measurements of flux creep in a

superconductor with inhomogeneous pinning properties in which the size of hysteresis loops was observed to increase with increasing current sweep rate. In this case, increasing $\frac{dI}{dt}$ also increases the rate at which the vortices can enter the inclusions, thus resulting in a more inhomogeneous flux distribution. As suggested by Liu *et al.* [111], changing the sweep rate is equivalent to changing the observation time window: for a very slow sweep rate, our observation window is too late to observe a large inhomogeneity in the flux distribution which had plenty of time to move into the inclusions.

The results presented in Fig.(5.6) for the time dependence of the resistance when the magnetic field sweep is paused in the middle of the B_{c2} transition can be explained from similar arguments. Upon pausing the field in an increasing (decreasing) B sweep, the resistance initially keeps increasing (decreasing) because the magnetic fluxes easily and rapidly enter (exit) the weakly-pinned phase, but it takes a finite time for the resistance value to catch up with the field. Then, when the field is paused in the up-going field sweep, the resistance decreases back to zero because the excess flux present in the main (weakly-pinned) phase diffuses into the grains, thereby decreasing the magnetic field present in phase A. At some point, the magnetic field present in phase A has decreased below the value of the effective B_{c2} and the resistance reaches zero. A similar phenomenon is observed upon pausing the field in a decreasing field sweep: as shown in Fig.(5.6b), after an initial sharp decrease, the resistance turns around and increases back to a value close to the initial value it had when the field was paused as the excess flux in the inclusions slowly diffuses into the weakly-pinned phase A. Indeed, the velocity of flux diffusion obeys the relation $v \propto (J/J_c)^{U_0/k_B T}$, where U_0 represents an energy barrier to flux motion, such that for the same applied current J , the velocity of flux diffusion is larger in the region with smaller critical current J_c (more weakly-pinned) [111]. As an experimental observation of this effect, note the difference in the resistance scale difference between Figs.(5.6a) and (5.6b): Over about the same period of time, the resistance drops by more than 0.2Ω in Fig.(5.6a) while it increases back by only about 0.035Ω in Fig.(5.6b), which shows that significantly

more flux diffuses from the weakly-pinned phase into the inclusions after increasing the field than from the strongly-pinned inclusions into the main phase after decreasing the field over the same period of time. This confirms the slower diffusion of flux in the strongly-pinned inclusions, but also shows that the flux distribution upon decreasing the magnetic field is more homogeneous than upon increasing the field, as application of a magnetic field larger than B_{c2} resets the flux distribution and makes it homogeneous.

For temperatures close to T_c , or lower B , the size of the clockwise hysteresis loops at B_{c2} increases, as seen in Fig.(5.10b). This is because the excess flux in the weakly-pinned phase for increasing B field, and in the inclusions for decreasing B field becomes larger since the elasticity of the FLL is greater at lower B , which allows it to bend more easily around less desirable pinning regions.

The results presented in Fig.(5.11a) showing the absence of the clockwise hysteresis loops in temperature sweeps at fixed values of the magnetic field can also be explained according to this model with inhomogeneously-pinned regions in the sample. Indeed, in the context of a sample with inhomogeneous pinning properties, clockwise hysteresis loops in R vs T are not expected [3], in opposition to what is observed in R vs B measurements, because when a magnetic field is applied to the sample in the normal state, the flux lines are straight and penetrate the sample uniformly. Then as the temperature is decreased in the presence of an external field the flux lines are expected to stay straight and not to wander around trying to find better pinning sites to lower their energy. Moreover, because the field is fixed for this type of measurement, the flux density does not change, such that the interaction between the flux lines does not change either and they must then remain homogeneously distributed throughout the sample, as they were prepared in the normal state. Because the field remains fixed, as the temperature is swept back up above T_c , the flux distribution has not changed and no hysteresis is expected.

Therefore, all the experimental observations on the $x = 0.5$ and $x = 0.6$ presented above can be explained if these alloys are composed of different superconducting

phases characterized by different pinning properties. In granular superconductors in which similar results are obtained, superconductivity has been described according to a two-level critical state model [3]; in this model, the flux distribution within the weakly-pinned phase is homogeneous, while it is described by a local critical state within the inclusions. We will now present the details of this two-level critical state model and show that it leads to clockwise hysteresis loops.

5.3.3 The two-level critical state model

The observation of clockwise hysteretic resistance curves in superconductors resulting from inhomogeneous pinning properties can be interpreted according to a two-level critical state model, analogous to the Bean critical state model introduced in section (2.7). While in the Bean state the critical current is assumed to be constant over the whole sample in regions where a magnetic field is present, and with the superconducting properties determined by the macroscopic state, in the two-level critical state description, two different critical currents, related to the different pinning strength of different regions, exist in the sample: one in the main connected phase and one in the inclusions. Anomalous hysteresis loops arise according to this model as the critical state on the local level becomes dominant. Following the work of Ji *et al.* [3], we introduce the details of the two-level critical state model and show how it leads to the prediction of clockwise hysteresis loops and how it depends on various parameters pertaining to the two phases.

As before, we assume that the superconductor is composed of two main phases with a connected phase (phase A) having weak-pinning properties and a low critical current density J_c^A , and non-percolating strongly-pinned inclusions (phase B) with larger critical current density J_c^B . Evidently, this is a simplified model and a real inhomogeneous superconductor most likely exhibits more than two distinct phases, in which case a similar model with more levels can be applied, but with ensuing complications. As a further simplification, it is assumed that the inhomogeneous superconductor is an infinite flat slab in a perpendicular magnetic field with an ordered lattice of high- J_c inclusions, as shown in Fig.(5.14). As shown, the length L_B

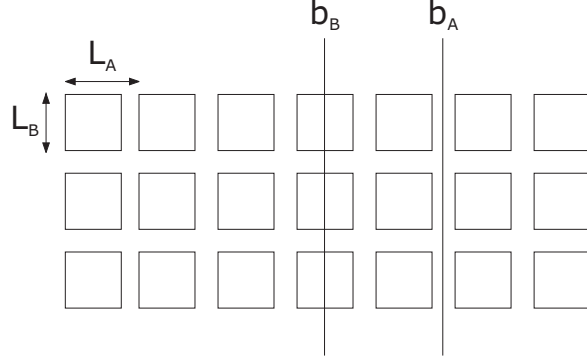


Figure 5.14: Side view of a superconducting flat slab in a perpendicular magnetic field with regions of large pinning properties represented by a lattice of squares. (Inspired from Ref. [3].)

represents the width of the inclusions and L_A is the lattice parameter such that the cross-sectional area of the weakly-pinned phase per lattice site is $(L_A^2 - L_B^2)$. Also introducing the cross-sectional fraction of the strongly-pinned area s_p (this is also the local critical state region), and the notation b_B and b_A which denotes the microscopic magnetic flux density pinned in the inclusions and free in the percolating phase A respectively, the externally applied magnetic field is given by [3]

$$(1 - s_p) b_A + s_p \langle b_B \rangle = B_{app} \quad (5.2)$$

where $\langle b_B \rangle$ represents the averaged flux density in the inclusions. The average of the magnetic flux density in the inclusions has to be considered because according to the model, the local flux density in the inclusions is not constant; however, it is considered almost constant in the weakly-pinned phase A such that the average of b_A needs not to be taken. The local and averaged flux profile in phases A and B are as depicted in Fig.(5.15). Then, because of the simplification of the ordered case,

$$s_p = \frac{L_B^2}{L_A^2}. \quad (5.3)$$

Defining the parameter

$$y = \frac{L_A - L_B}{L_A} \quad (5.4)$$

which represents the length over which pinned-fluxes in phase B pass through phase A between inclusions, the total magnetic flux present in phase A can be obtained

from [3]

$$B_A = [(1 - s_p) b_A + s_p x \langle b_B \rangle]. \quad (5.5)$$

In this last expression, the first term represents the free flux present in phase A and the second term represents the pinned flux in phase B which passes through phase A between inclusions. Determining $\langle b_B \rangle$ from the two-level critical state model as will be shown, and using b_A as a free parameter, equations (5.2) to (5.5) can be solved parametrically to obtain the total magnetic flux in phase A B_A as a function of the applied field. Because in the flux flow regime the resistivity is directly related to the magnetic field according to

$$\rho = \rho_n \frac{B}{B_{c2}}, \quad (5.6)$$

the behavior of B_A as a function of B_{app} is directly related to the resistance measured as a function of an external magnetic field (for depinned vortices).

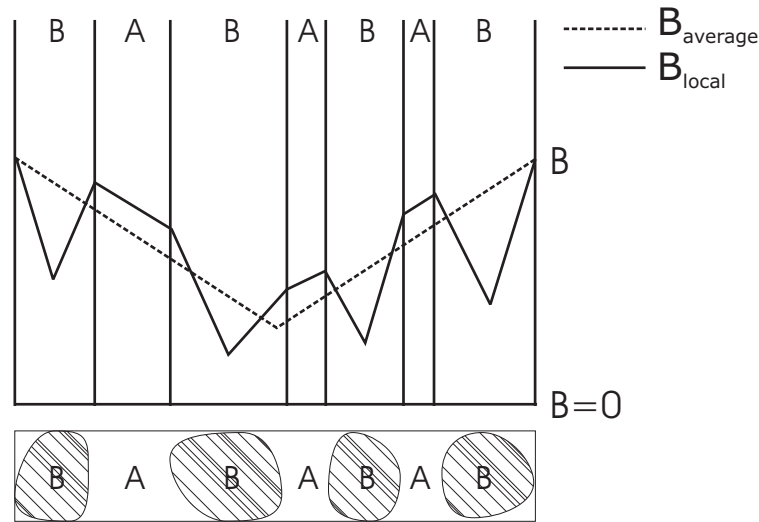


Figure 5.15: Schematic representation of the average flux profile (dotted line) and local flux profile (solid line) in an inhomogeneous superconductor containing strongly-pinned regions (denoted by B) and weak pinning regions (A). Picture inspired by Fig.3 of Ref.[3].

Bean critical state with hysteresis

Recall that according to the Bean critical state model (section (2.7)), the penetration of magnetic flux in a superconducting sample proceeds in two different regimes, a low and a high field regime, with the characteristic field $B^* = \mu_0 J_c a$ defining the

limit between the two regimes and also representing the field at which flux penetration reaches the middle of the superconductor. In the two-level critical state model considered here, the characteristic field of the strongly-pinned inclusions is [3]

$$B^* = \mu_0 J_c^B \frac{L_B}{2}. \quad (5.7)$$

Then, for a zero-field-cooled infinitely wide superconducting flat slab in a perpendicular magnetic field with maximum applied field $B_{\max} > B^*$, the hysteresis curves describing the averaged flux within the inclusions are determined as a function of the free flux in the percolating phase according to the Bean critical model [30, 31, 3]:

1. For increasing field,

$$\begin{aligned} \langle b_B \rangle &= b_A - \frac{B^*}{2} + \frac{(b_A + B_{\max} - 2B^*)^2}{4B^*} & \text{for } -B_{\max} < b_A < -B_{\max} + 2B^* \\ \langle b_B \rangle &= b_A - \frac{B^*}{2} & \text{for } -B_{\max} + 2B^* < b_A < B_{\max} \end{aligned} \quad (5.8)$$

2. For decreasing field,

$$\begin{aligned} \langle b_B \rangle &= b_A + \frac{B^*}{2} - \frac{(b_A - B_{\max} + 2B^*)^2}{4B^*} & \text{for } B_{\max} > b_A > B_{\max} - 2B^* \\ \langle b_B \rangle &= b_A + \frac{B^*}{2} & \text{for } B_{\max} - 2B^* > b_A > -B_{\max} \end{aligned} \quad (5.9)$$

Substituting these values for $\langle b_B \rangle$ in equations (5.2) to (5.5) and choosing different values for the parameters B^* , and s_p yields the B_A vs B_{app} curves shown in Figs.(5.16) and (5.17). From the R vs B data on the alloy $\text{Fe}_{0.6}\text{Ni}_{0.4}\text{Zr}_2$, experimental values for some of these parameters can be estimated and are shown in Table (5.1). For this alloy, because two major transitions to the superconducting state are easily distinguishable, the fraction of phase B in the sample is easily determined from the ratio of the resistance drop at transition 1 to the normal state resistance, i.e. $s_p = (R_n - R_c)/R_n = 0.19$. Also, from the widths of transition 1 $\Delta T_c = 1.07$ K and $\Delta B_{c2} = 1.06$ T, the size of inhomogeneities is estimated to be of the order of several $\lambda(0)$, such that we arbitrarily use $L_B = 20 \mu\text{m}$. J_c^A and J_c^B are determined from extrapolation of the B_{c2} vs I dependence to $B_{c2} = 0$ extracted from the data shown in Fig.(5.9) for transition 2 and 1 respectively. Take note that using this value of J_c^B

| | |
|------------------|-----------------------------------|
| s_p | 0.19 |
| L_B | 20 μm |
| L_A | 46 μm |
| y | 0.57 |
| B_{max} | 4 T |
| J_c^A | $3.3 \times 10^4 \text{ A / m}^2$ |
| J_c^B | $6.4 \times 10^4 \text{ A / m}^2$ |

Table 5.1: Some parameters pertaining to phases A and B of the alloy $\text{Fe}_{0.6}\text{Ni}_{0.4}\text{Zr}_2$.

in equation (5.7) yields a very small value of $B^* = 80 \mu\text{T}$ which probably does not represent the field at which the flux reaches the middle of the inclusions because this cannot depend solely on the properties of the flux pinned in phase B, but must also depend on the elasticity of the free fluxes in phase A and their ability to bend around the inclusions. This is why we have used different larger values of B^* in the plots of Fig.(5.16) to determine which would yield B_A vs B_{app} curves with hysteresis loops that best represent the hysteretic curves obtained from R vs B measurements of this alloy.

From the plots of Figs.(5.16) for which B_{max} , s_p and L_B are as given in Table (5.1), it is evident that a large B^* is necessary for the development of a large (clockwise) hysteresis loop, although the width of the widest loop obtained here is only about $\Delta B_{app} = 0.15 \text{ T}$ while wider loops with ΔB_{app} between about 0.2 and 0.3 T are obtained experimentally. Considering the crudeness of the model, the agreement with experimental data is significant. The dependence of the width of the hysteresis loop on B^* can be understood considering that once the flux has penetrated to the middle on the inclusions at $B_{app} = B^*$ the local flux in the inclusions and in phase A is no longer as inhomogeneous as it is at low field and the size of the hysteresis loop diminishes and eventually closes as B_{app} is increased. Moreover, as B^* is a direct measure of trapped flux, it is elementary that the size of the hysteresis loops increases as B^* increases. These results also show that the size of the hysteresis loops increases

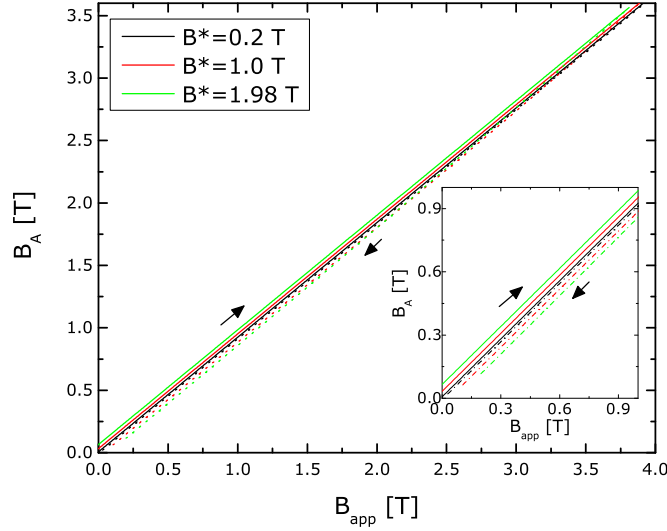


Figure 5.16: Total magnetic flux in percolating phase A as a function of the applied magnetic field determined according to the 2-level critical state model. The results are calculated for different characteristic fields B^* , with $s_p = 0.19$, $B_{\max} = 4$ T and $L_B = 20$ μm . Inset: Enlargement of the low field region.

with decreasing applied field; a similar result is obtained experimentally as the width of the hysteresis loops increases with increasing temperature (or decreasing B_{c2}) in the alloy with $x = 0.5$ (Fig.(5.10)). This result is expected because as the magnetic field increases, the vortex lattice loses some of its elasticity such that it becomes more difficult to bend around the inclusions; the fluxes become straighter and have to pass through more inclusions which homogenizes the flux distribution between the inclusions and the connected phase such that the size of the hysteresis loops decreases.

The dependence of the size of hysteresis loops in B_A vs B_{app} on the fraction of phase B s_p is much more obvious than the dependence on the characteristic field B^* . As shown in Fig.(5.17), the size of the loop becomes very narrow as the amount of the strongly-pinned phase diminishes, and becomes much broader as the fraction of the strongly-pinned phase increases. This is as expected since these hysteresis loops should not exist for a homogeneous sample. Although the results are not shown, we mention that keeping s_p constant and varying the size of the inhomogeneities L_B ,

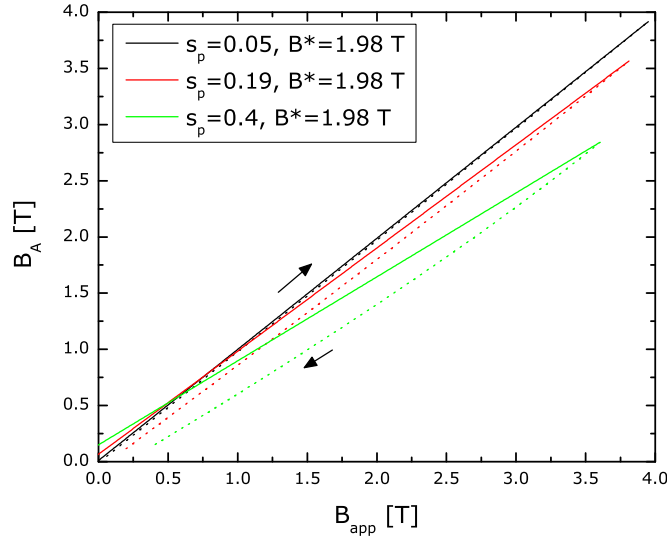


Figure 5.17: Total magnetic flux in percolating phase A as a function of the applied magnetic field determined according to the 2-level critical state model. The results are calculated for different cross-sectional fractions of the strongly-pinned phase B s_p , with $B^* = 1.98$, $B_{\max} = 4$ T and $L_B = 20$ μm .

and L_A accordingly (from equation (5.3)), should also have a significant influence on the hysteresis. Indeed, it is expected that larger inhomogeneities have a larger characteristic field B^* (from equation (5.7)) and should thus contribute much more to the hysteresis than smaller inhomogeneities. We do not show these results since we have used arbitrary values of B^* in these plots, and varying L_B is equivalent to varying B^* . However, the real situation is significantly more complicated than this: Considering the elasticity of the vortex lattice in phase A, one can argue that it should be easier (less costly in energy) for the vortices to bend around smaller inclusions and that for a significantly stiff lattice flux entry in larger inclusions should be preferred. However, it is believed that as stiff fluxes become pinned by the inclusions, they form clusters; larger than the original L_B and with a larger critical current than that of the weakly-pinned regions J_c^A but smaller than J_c^B , these large clusters could contribute significantly to the hysteresis [3].

In the light of these results, we conclude that the observation of clockwise hysteresis loops in the R vs B_{app} measurements in the $x = 0.5$ and $x = 0.6$ alloys of the series $\text{Fe}_x\text{Ni}_{1-x}\text{Zr}_2$ is well-explained by a model which considers the presence of inhomogeneously-pinned regions and which can be analyzed according to a two-level critical state model analogous to the Bean critical state model. The presence of a visible double transition in the $x = 0.6$ alloy permits the estimation of the volume fraction of each phase as well as the size of the inhomogeneities. Unfortunately, in the $x = 0.5$ alloy, no double transition can be distinguished, most likely because the connected phase and the strongly-pinned inclusions have very similar critical temperatures and fields. Nevertheless, we expect that the very similar behavior at B_{c2} obtained for this alloy can also be explained according to a two-level critical state model with inhomogeneous pinning. In any case, the two-level model considered here is without doubt much simpler than the real problem for which randomly located inhomogeneities of different sizes should be regarded and for which more than two levels should probably be considered in addition to the variations in the elasticity of the vortex lattice as the magnetic field is changed, but nevertheless yields meaningful results.

5.3.4 Origin of inhomogeneities in the $x = 0.5$ and $x = 0.6$ alloys

In the discussion above, we have argued that it is the presence of inhomogeneities presenting different pinning properties in the $x = 0.5$ and $x = 0.6$ alloys which is responsible for the appearance of clockwise hysteresis loops. Throughout the discussion however, it was never explicitly mentioned why such inhomogeneities would be present in these particular alloys and not in the other alloys of the series, nor what is the exact nature of these inhomogeneities. In this section, we argue that these inhomogeneities are structural and arise because of a change in the short range order across the series of alloys. Indeed, we have already discussed that in metallic glasses, the SRO is assumed to be very similar to that of the first crystallization products

since diffusion lengths are short, typically of a few atomic distances. The first crystallization products of the NiZr_2 alloy is a bct structure resulting in a smaller SRO with a nearest neighbour distance of 2.746 \AA [7], while the crystal structure of FeZr_2 is the larger fcc structure which has correspondingly larger SRO in its amorphous counterpart and in which the nearest neighbour distance is 2.816 \AA [7]. Most importantly, SRO is also determined from the coordination number N , i.e. the number of Zr nearest neighbour atoms surrounding the LT atoms Ni or Fe. The coordination number is the factor which will have the most influence on the density of states, and thus on superconducting properties. In particular, in the fcc-like structure characteristic of FeZr_2 , each Fe or Ni atom is surrounded by 6 Zr nearest neighbour atoms, whereas in the bct structure of the NiZr_2 crystalline products, each Ni or Fe atom has 2 Ni or Fe nearest neighbours in addition to 8 Zr nearest neighbour atoms [7]. According to these observations, a transition in the SRO in the series of amorphous alloys $\text{Fe}_x\text{Ni}_{1-x}\text{Zr}_2$ should be expected at some critical value x . The evidences presented above for the presence of inhomogeneities in the $x = 0.5$ and $x = 0.6$ alloys infer that phase separation occurs in these amorphous alloys and results in the formation of quenched in Ni-rich and Fe-rich glass clusters having different SRO. The Ni-rich clusters should exhibit the better superconducting properties with higher T_c and larger pinning properties and yield to the upper transition observed in the $x = 0.6$ alloys, while the Fe-rich regions should have a lower T_c since the presence of Fe induces spin fluctuations which promote the breaking of Cooper pairs. These inhomogeneities do not result from a faulty fabrication process such as for instance a too slow cooling of the melt which might result in crystallite inclusions in the glass, but are intrinsic to this alloy composition. Accordingly, spanning the x dependence in $\text{Fe}_x\text{Ni}_{1-x}\text{Zr}_2$, for $x \leq 0.4$ no signs of large scale inhomogeneities are present in the superconducting properties and the SRO is typical of the NiZr_2 glass structure. Then, for $x \approx 0.5$, a structural transition occurs as clusters having SRO typical of the FeZr_2 glass form a separate phase in the alloy. For $x = 0.6$, the Fe-rich clusters proliferate as more important signs of inhomogeneity become visible in superconducting properties. Al-

loys with a larger Fe content than $x = 0.6$ were not tested for superconductivity, therefore it is not known if they exhibit superconductivity at all or if they do at very low temperature, but as x increases they would presumably show less signs of phase separation and a more homogeneous structure having SRO characteristic of the FeZr_2 glass.

A systematic study of the local structure of these alloys with $0 \leq x \leq 1$ from Mössbauer spectroscopy has not revealed the presence of such structural transition for some x value [7]. However, we believe that the isomer shift data as a function of x presented in Ref.[7] show a change of slope at $x = 0.4$ which was overlooked and which confirms the existence of a structural transition. Because we observe the clockwise hysteresis loops only for the $x = 0.5$ and $x = 0.6$ alloys and not for any other alloy with $x \leq 0.4$, we believe that the structural transition occurs for $0.4 \leq x \leq 0.5$; the precise value of x at which this transition occurs could vary because any small difference in the conditions during the melt-spinning process can lead to significant differences in the physical structures of the amorphous alloys.

5.4 Summary

Together with the results obtained from analysis of the fluctuations in magnetization in section (5.1), the determination that the appearance of clockwise hysteresis loops for alloys with $x = 0.5$ and $x = 0.6$ is related to the presence of structural inhomogeneities with different local SRO confirms for the first time that there exists a structural transition across the series of the pseudo-binary amorphous alloys $\text{Fe}_x\text{Ni}_{1-x}\text{Zr}_2$. From evaluation of the fluctuations in magnetization, we have determined that with increasing x , the characteristic magnitude of fluctuations in magnetization also increases, which can be related to the formation of a two-phase material with Fe content. An increase in the characteristic size of grains with x was also deduced from these measurements; the characteristic size of grains was found to reach about $40 \mu\text{m}$ for the $x = 0.4$ and $x = 0.5$ alloys. From the width of the double resistive transition to the superconducting state in the $x = 0.6$ alloy, the characteristic size of grains was

also evaluated to be about $40 \mu\text{m}$. From the appearance of clockwise hysteresis loops at B_{c2} in the $x = 0.5$ and $x = 0.6$ alloys, we also deduced that a structural transition with x across the series of alloys must exist; the critical value of x for this structural transition was determined to lie between $x = 0.4$ and $x = 0.5$. Because superconducting properties are very sensitive to the structure of the material, it is then not very surprising that fluctuations in the magnetization increase strongly as the critical point is approached, as we have observed here for the $x = 0.4$ and $x = 0.5$ alloys. As a concluding remark, we note that in addition to the fact that these results prove that the local SRO in the $\text{Fe}_x\text{Ni}_{1-x}\text{Zr}_2$ alloys changes across the series, these also show how superconducting properties constitute a sensitive probe to the structural order in amorphous alloys. This is particularly true for these alloys which were previously inspected by high resolution electron microscopy [6] from which no signs of large scale inhomogeneities were detected and by Mössbauer spectroscopy [7] from which a faint sign of a structural transition can be seen, but which was neglected in the past. As a last comment on the magnetization fluctuations measurements: Although we managed to reach a meaningful conclusion regarding their origin, it would nevertheless be interesting to repeat the measurements using different magnetic field sweep rates in order to determine the dynamics of the phenomenon, i.e. the time dependence.

6

Transverse dynamics of the vortex state

The vortex state of type II superconductors is rich in interaction phenomena: Governed by vortex-vortex repulsion, thermal fluctuations and pinning by quenched disorder, the competition between ordering and disordering gives rise to a wealth of static and dynamic phase transitions, as well as non-equilibrium phenomena. The effects of disorder on the static case have been widely studied in the past 20 years or so [4, 117, 118, 119, 120, 121], in part because of the added impetus due to the discovery of the high- T_c superconductors. More recently, the dynamic state has also been the subject of numerous studies [5, 122, 17, 18, 19, 123, 16, 124], from which an all new vortex phase diagram has emerged. Some of these studies have also unveiled theoretical predictions of interesting dynamic and pinning properties in the direction transverse to vortex motion which have been elusive to experiments so far.

Having established in the last two chapters the various properties and parameters of the superconducting state of the $\text{Fe}_x\text{Ni}_{1-x}\text{Zr}_2$ amorphous alloy series, we move on with an investigation of the vortex phases in the vortex state of some of these alloys. Indeed, we have seen that amorphous alloys are best-suited for such an inquiry since the absence of long-range order reduces vortex pinning properties and the alloys are accordingly characterized by a low critical current. Therefore, we begin this chapter with an overview of theoretical predictions about vortex phases, followed by results of two different experiments probing the transverse pinning and dynamical properties of the vortex state, both of which rely on dissipative transport measurements.

6.1 Vortex phases

6.1.1 Static phase diagram

The prediction of the existence of a vortex lattice by Abrikosov in 1957 [28] was the first step toward the development of a novel field of research: vortex phases in type II superconductors. This original prediction of the ideal vortex lattice arranged in a triangular array of vortices as dictated by the elastic repulsive interaction of the vortices is a simplistic description of the vortex state which, upon addition of disorder or increase of magnetic field and temperature, has been shown to evolve in a variety of phases [4, 120], analogous to the phases found in ordinary matter. In particular, in the absence of a driving force, and for weak disorder strength and low temperature, the vortex state has been demonstrated to evolve in a phase called the “Bragg glass” (BG) characterized by quasi-long range and topological order. With algebraic translational order, this phase shares similarities with a perfect lattice and, even though it has many metastable states like a glass, it shows Bragg peaks in neutron diffraction experiments, which in passing explains its name. As schematically depicted in Fig.(6.1), upon increase of the magnetic field, the BG transforms into a phase named the “vortex glass” (VG). This phase arises as the increase of the magnetic field is equivalent to the augmentation of effective disorder which causes a proliferation of topological defects, injects dislocation and ultimately destroys the Bragg glass. Moreover, whereas the BG is characterized by a strong elasticity of the vortex lattice in which collective pinning takes place, thus resulting in weak barriers against depinning, the VG, with its nearly destroyed lattice and dislocations is characterized by larger barriers because it adapts better to the larger pinning potential. Still referring to Fig.(6.1), upon increase of temperature the vortex state evolves in a vortex liquid-like phase which is nearly insensitive to disorder. This phase is poorly understood, but shows no topological order [4].

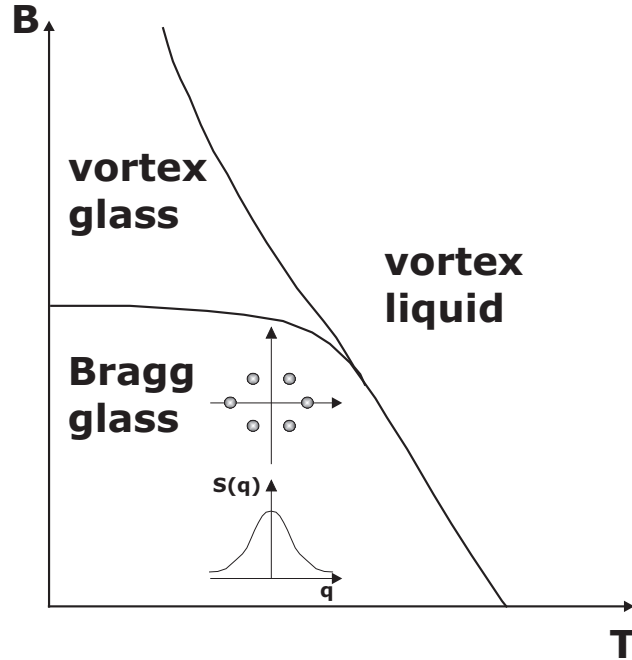


Figure 6.1: Representation of the magnetic field-temperature vortex phase diagram in the absence of a driving force. The peaks in structure factor $S(q)$ as a function of reciprocal lattice vector q (Bragg peaks) are also depicted in the Bragg phase. (Inspired from Ref.[4]).

6.1.2 Dynamic phase diagram

For driven vortex lattices, the phase diagram appears to evolve quite nicely as an extension of the static phase diagram, though its determination and implications are much more difficult to attain, which probably explains why it has remained an open question for a long time. Indeed, because of the need to consider many sources of anisotropy and nonlinear elasticity, and an out-of-equilibrium system, even the usually simpler elastic case becomes very difficult to solve in the dynamic regime. Pioneers and authors of extensive work on this subject, T. Giamarchi and P. Le Doussal [5, 16] have demonstrated that the Bragg glass survives motion by becoming the moving Bragg glass (MBG): A topologically ordered phase with a persistent translational quasi-long range order for large velocities or weak disorder. The MBG phase is characterized by the flow of vortices along static channels determined by the static disorder and correlated along the direction transverse to motion by elastic modes. As a results of the existence of these channels which provide strong barriers against

transverse motion, the existence of a transverse critical force is predicted [5, 17, 18, 19, 16, 20, 21]. At intermediate disorder strength, a slightly different moving glass phase is predicted to exist: the moving transverse glass (MTG). With smectic order in the transverse direction, this phase is also characterized by channels, but whereas the position of particles in different channels in the MBG is coupled, they are not coupled in the MTG. These vortex channels have been observed experimentally in magnetic decoration experiments [125, 126] and scanning tunneling microscopy (STM) images [127]. We show, in Fig.(6.2) a schematic depiction of these vortex flow patterns along with the dynamic phase diagram depending on temperature, disorder and driving force, as predicted by Le Doussal and Giamarchi [5]. As visible in the phase diagram, for large disorder strength, the flow of vortices is described by a highly defective plastic flow, with depinning proceeding via plastic channels between pinned regions.

More on the moving glass phases

In both the MBG and the MTG, the system is essentially described by the component of motion perpendicular to the driving force, because as the structure moves through the disorder potential, the component of disorder along the direction of motion is averaged out, but the transverse component remains essentially unaffected. As a result of this averaging and for large driving forces, the disorder potential along the direction of motion appears weaker, which literally leads to a dynamic ordering of the vortex lattice. This phenomenon has been observed in numerous theoretical and experimental studies [5, 122, 17, 18, 19, 123, 16, 124, 20, 125, 126, 128, 129, 130, 131, 132, 133]. Experimentally, the crossover to a more ordered vortex phase at large driving force appears in transport measurements as a peak in the differential resistance [128, 130] as the rate of dissipation suddenly decreases as the driving current is increased. A decrease in the low frequency broadband noise [133], and an increase of the longitudinal correlation length in neutron diffraction experiments [129] have also revealed the presence of this dynamical ordering phenomenon. Direct observations of this phenomenon also exist from magnetic decoration experiments [125, 126].

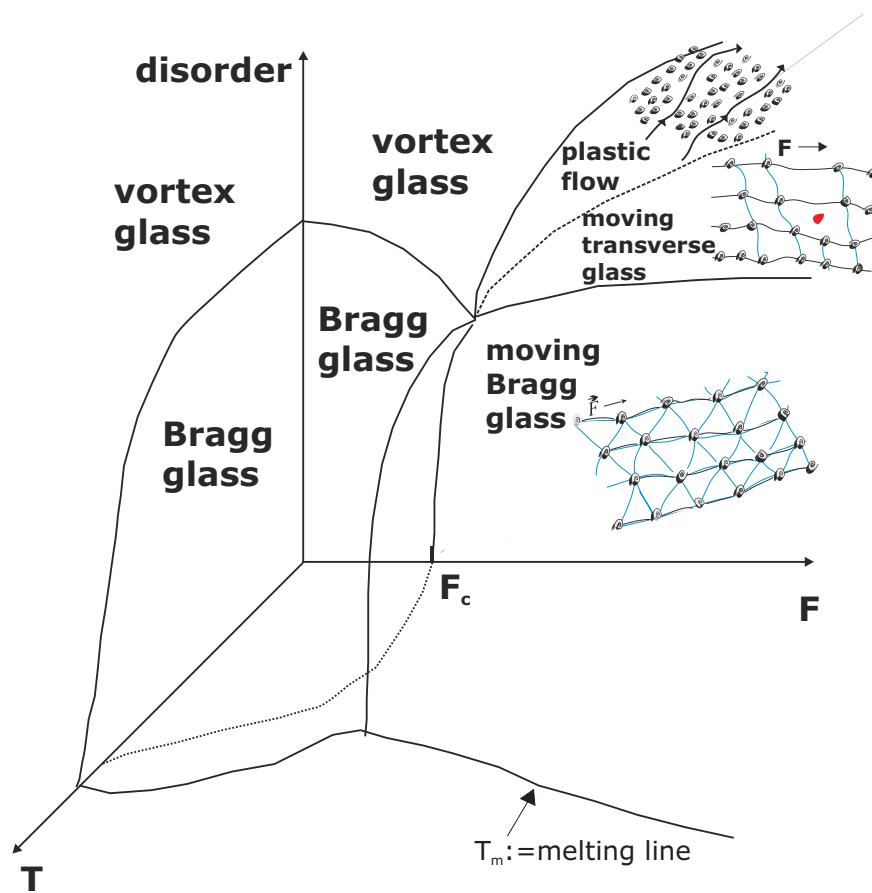


Figure 6.2: Representation of the dynamic vortex phase diagram in temperature, disorder and driving force. Schematic vortex flow patterns are also shown for the moving phases. (Inspired from Ref.[5]).

6.2 Experimental measurements of vortex phases

Many phenomena related to vortex phases such as the existence of a transverse critical depinning force have not, or rarely been observed experimentally. Some imaging techniques such as magnetic decoration or STM have succeeded at providing tangible evidence of the existence of some vortex phases, but such techniques are only effective at low vortex density and velocity. Therefore, for many phases of vortex motion, the only experimental evidence that can be provided are from transport measurements. This provides the motivation for the transport measurements we performed to probe the transverse dynamics of the vortex state and which we introduce below. The first experiment consists in the measurement of the Hall resistance of the Fe-Ni-Zr amorphous alloys; the results thus obtained yield the first experimental evidence for the existence of a vortex phase characterized by smectic order, analogous to the MTG introduced above, at very low driving forces.

6.2.1 Hall effect in type II superconductors

The study of Hall effects in type II superconductors started over 40 years ago, but the number of research on the subject remains slim and the problem still eludes the scientific community. While some have predicted a Hall sign reversal below T_c caused by pinning effects [134, 135], others reject pinning as the source of the phenomenon [136, 137, 138, 139], and others even predict no sign reversal at all [140, 141]. A few studies report measurements of the Hall effect on superconductors which also exhibit the peak effect, like our amorphous alloys, but their measurements do not show any correlation to the different vortex phases [139, 142, 143, 144].

Resistance in superconductors

In a normal metal carrying a current density \vec{J} and in a magnetic field \vec{B} , a Hall voltage can be measured in the direction $\vec{J} \times \vec{B}$ as a result of the deflection of charge carriers by the magnetic field. In type II superconductors, a Hall resistance arises because of a similar phenomenon, but in this case, it is not the transverse motion of charge carriers which induces the Hall signal but rather the transverse motion of the

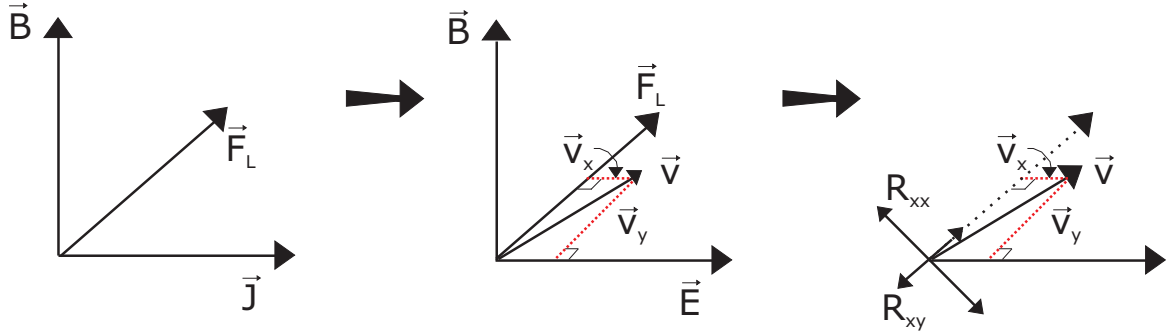


Figure 6.3: Schematic representation of the direction of vortex motion due to the Lorentz force resulting from the action of the applied current and magnetic field.

vortices. Indeed, in the vortex state of type II superconductors, the appearance of a resistance is attributed to the motion of vortices which, as a result of the application of a current and magnetic field, will move in the direction of the Lorentz force per unit length $\vec{f}_L = -\vec{J} \times \vec{B}$, thereby inducing a measurable voltage in the direction perpendicular to \vec{f}_L according to $\vec{E} = \vec{v} \times \vec{B}$, where \vec{v} is the vortex velocity. A schematic drawing of the spatial orientation of these various quantities is presented in Fig.(6.3). As shown, if the vortices move precisely in the direction of the Lorentz force, no Hall resistance will be measured because all electric dissipation will take place in the longitudinal direction (direction of \vec{J}). However, if the vortices travel at some angle to the Lorentz force, then the component of motion parallel to \vec{J} will induce a voltage in the direction of the Lorentz force, which is measured as the Hall voltage.

Complications in the measurement of the Hall resistance in superconductors

The measurement and analysis of experimental Hall resistance data on type II superconductors is not trivial. The presence of normal electrons in vortex cores and in possible pockets of normal phase in an inhomogeneous superconductor induces a Hall voltage which competes with the Hall voltage produced by the moving vortices. In the Hall resistance measurements on our metallic glasses, this problem is circumvented because the Hall contribution due to the moving vortices is mainly symmetric in B ,

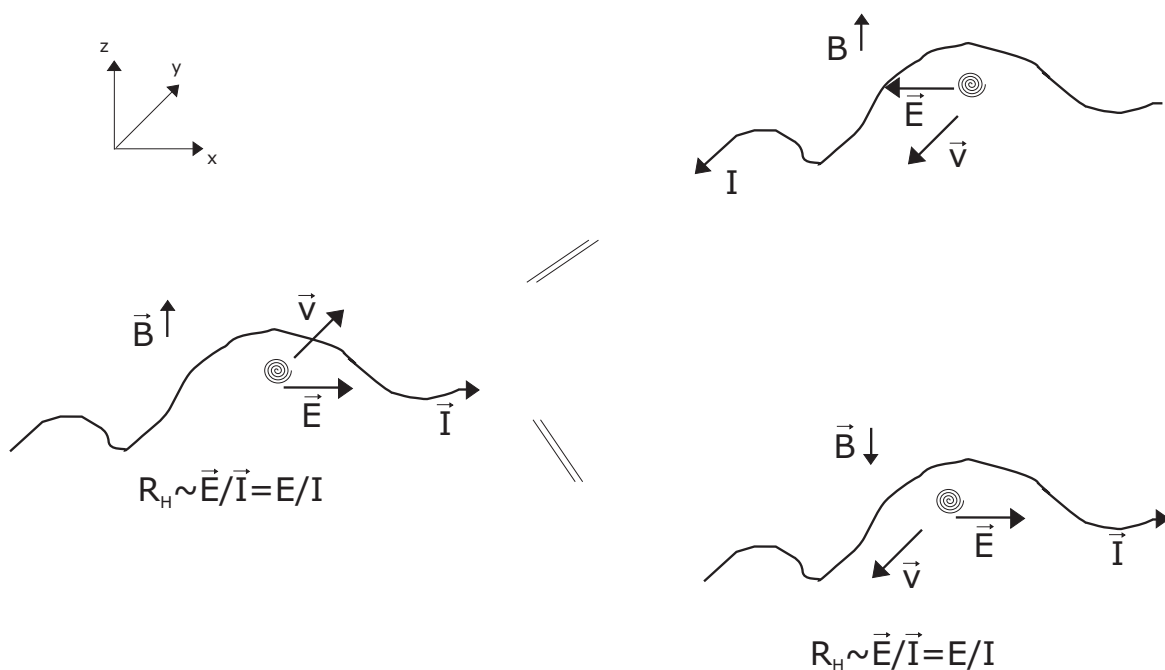
while the Hall contribution of the normal electrons is antisymmetric. We obtain the asymmetric contribution to the Hall resistance $R_H^{asy} \simeq B/ne < 10 \mu\Omega/T$, which is always negligible compared to all other contributions, with $n > 1.4 \times 10^{22} \text{ cm}^{-3}$ a lower bound for the electron density [8]. This normal electron density can be evaluated from the value of the Hall resistance just above B_{c2} , or from its value measured using a low driving current before vortex depinning. Such density values are consistent with those found for melt-spun NiZr₂ ribbons [145].

ac versus dc driving current: Consequence on R_H

Before presenting the results, take note that the Hall resistance results presented in this chapter have also been published in *Phys. Rev. B* [8], and some were also part of this author's Masters thesis [107]. Also, unless specified otherwise, all the R_{xy} data presented were acquired using an ac driving current¹. In such a case, both the positive and negative current directions ($\pm I$) are probed and one obtains $R_H(I, B) \simeq R_H(I, -B)$, since the Hall resistance contribution due to the normal carriers is negligible and the Hall resistance due to vortex motion is symmetric in B . However, one could argue that the results we obtain are due to a long range inhomogeneous current flow, as discussed in Ref.[146], rather than to the true Hall signal due to vortex motion. Such current distribution could result from parts of the sample becoming normal at a slightly lower magnetic field, as can be expected if the distribution of the iron content in the sample is inhomogeneous. In order to confirm that this is not the case and that the Hall resistance measured with the ac current is indeed the true Hall signal, we also performed Hall resistance measurements using a dc current which allows the two current directions to be probed independently. In this case, if the current flow path were to solely determine the Hall voltage, one would

¹In this chapter, we will use interchangeably the notation R_H and R_{xy} to denote the Hall resistance, whereas the longitudinal resistance will be denoted by R_{xx} . The notation R_{xx} and R_{xy} for the longitudinal and Hall resistance indicate that the current is applied in the x direction and the resistance is measured in the x direction as well for R_{xx} , while I is applied in the x direction and R measured in the y direction (transverse) for R_{xy} .

Current flow path determines the Hall voltage



Intrinsic vortex channels determine the Hall voltage

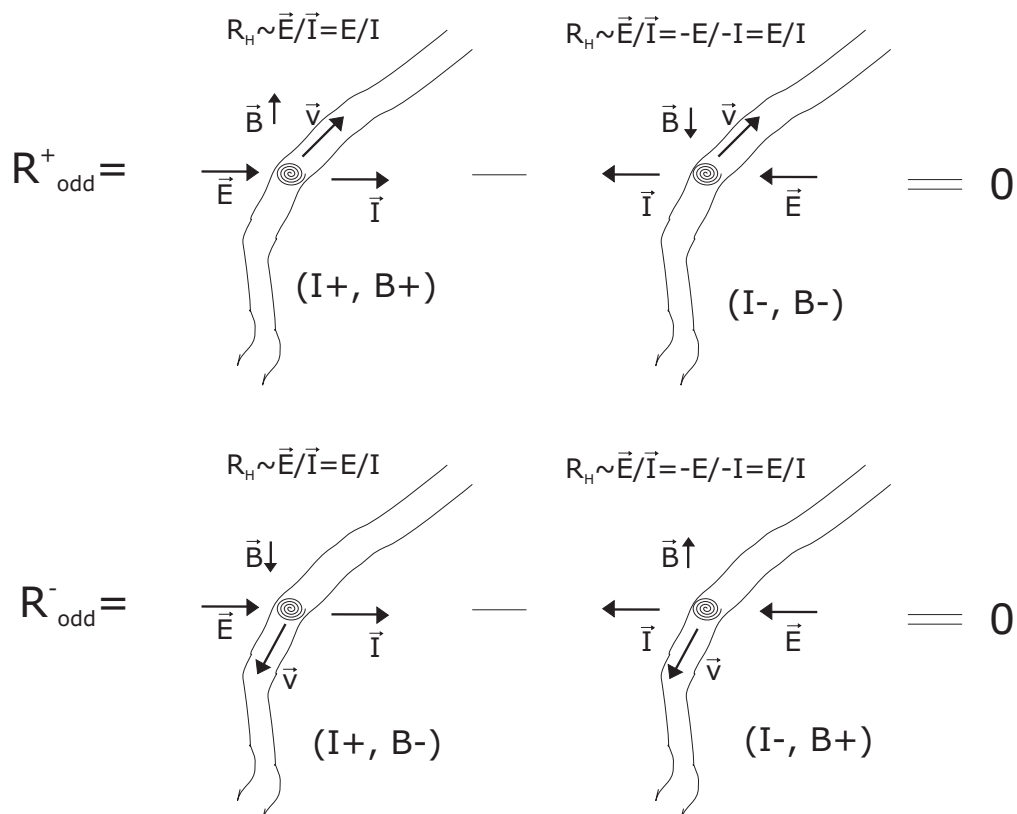


Figure 6.4: Schematic drawing representing the direction of vortex flow and resulting Hall voltage from different combinations of driving current and magnetic field.

have $R_H(I, B) \simeq R_H(-I, B)$ and $R_H(I, B) \simeq R_H(I, -B)$. However, we find differences which are almost as large as the values themselves, thus excluding a large scale inhomogeneous current flow as the main source for the Hall resistance. Similarly, we prove that the Hall resistance measured is not the result of intrinsic vortex channels, for which $2R_{odd}^\pm = R_H(I, \pm B) - R_H(-I, \mp B)$ would have to be zero because the electric field due to the vortex flow would be opposite for the paired variables $(I, \pm B)$ and $(-I, \mp B)$ but with the same vortex flow direction. This results from the fact that the vortex flow direction is antisymmetric in I and B , but the electric field produced by the vortex motion is symmetric in B and antisymmetric in I . This is depicted in Fig.(6.4), where it can also be seen that generally, R_{odd}^+ represents the vortex flow contributions originating from one edge and R_{odd}^- contributions originating from the other edge, and a nonzero value of R_{odd} implies that the vortex motion cannot be solely described by pure vortex channeling. This is consistent with our results that R_{odd} is of the same order as R_H , as shown in Fig.(6.5). The figure also shows that $R_H^{ac} \simeq R_{even}^\pm = [R_H(I, \pm B) + R_H(-I, \mp B)]/2$, thereby confirming that R_H^{ac} corresponds to the even contribution of the Hall resistance and represents an average over vortices flowing in opposite directions, hence avoiding intrinsic edge effects. Finally, this provides the confirmation that the measured R_H^{ac} is intrinsically due to lateral vortex motion, which cannot come from pure vortex channeling nor inhomogeneous current flow.

In addition, measurements of the Hall resistance using a dc current in the positive and negative directions and in opposite magnetic field polarities can be used to remove the longitudinal contribution in the Hall signal due to the small contact misalignment. Since the Hall resistance measured in this manner is very similar to that measured using an ac current, it is concluded that the contact misalignment is small.

Hall resistance experimental results

It is impossible to interpret the Hall resistance results without considering as well the results of longitudinal resistance measurements; these results were previously published in Refs.[107, 108]. The longitudinal resistance measurements in our Fe-Ni-Zr

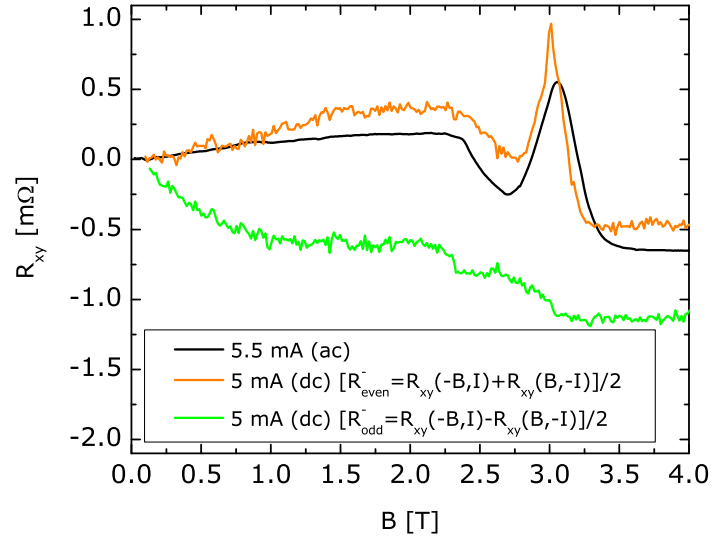


Figure 6.5: Comparison between the Hall resistance obtained using an AC current and $R_{odd}^- = [R_{xy}(-B, I) - R_{xy}(B, -I)]/2$ and $R_{even}^- = [R_{xy}(-B, I) + R_{xy}(B, -I)]/2$ obtained with a DC current.

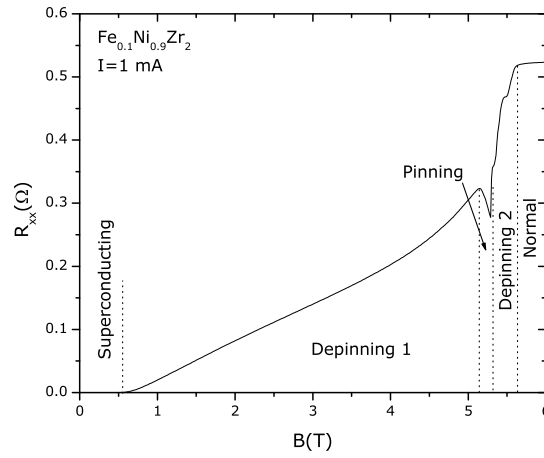


Figure 6.6: Sample longitudinal resistance curve as a function of magnetic field showing the boundaries of the different vortex phases.

alloys have revealed the presence of the peak effect: A widely observed anomaly in the transport properties of type II superconductors which was proposed to originate from a softening of the vortex lattice which causes it to adapt better to the pinning potential [147], or from the destruction of long range order by the field-induced disorder increase, as described in the collective pinning theory of Larkin and Ovchinnikov [148] and which results in the observation of a peak in the critical current measured as a function of magnetic field, or, as observed here, as a dip in resistance as a function of magnetic field. In addition to the peak effect, different phases of vortex motion have been observed in these measurements: Following the labeling scheme of Ref.[108] also presented in Fig.(6.6), the phase diagram obtained from longitudinal resistance measurements of different driving currents I on a sample of $\text{Fe}_{0.1}\text{Ni}_{0.9}\text{Zr}_2$ is shown in the upper panel of Fig.(6.7). The first depinned vortex state, labeled depinning 1, is characterized by collectively moving vortices and was identified as the moving Bragg glass discussed in section (6.1.2). Then, at larger B , one encounters the peak effect, with its increased pinning properties; the onset of the pinning phase was defined as the point just before the resistance drop of the peak effect where the derivative of R_{xx} vs B is zero. The end of this phase was determined from the point in B after the peak effect where R_{xx} is the same as at the onset of the phase. Finally, just below B_{c2} and for larger driving currents, an additional depinned vortex phase is observed: named depinning 2, this phase results from a sudden depinning of the vortex lattice before the transition to the normal state and is characterized by a smectic (reminiscent of the MTG phase (section 6.1.2)) or plastic flow of vortices [5, 19, 132]. The onset of this phase is easily distinguished as the abrupt increase in resistance in R_{xx} vs B data which follows the depinning 1 phase for high driving currents (see the dark green curve in Fig.(6.8)). For low driving currents, the exact nature of the transition between the pinned phase and the normal state for low driving current was never established before, but we have determined that it is separated by a depinned phase, as evidenced by the observation of a pronounced peak in the Hall resistance.

The upper panel of Fig.(6.7) also shows the Hall resistance as a colour map as a

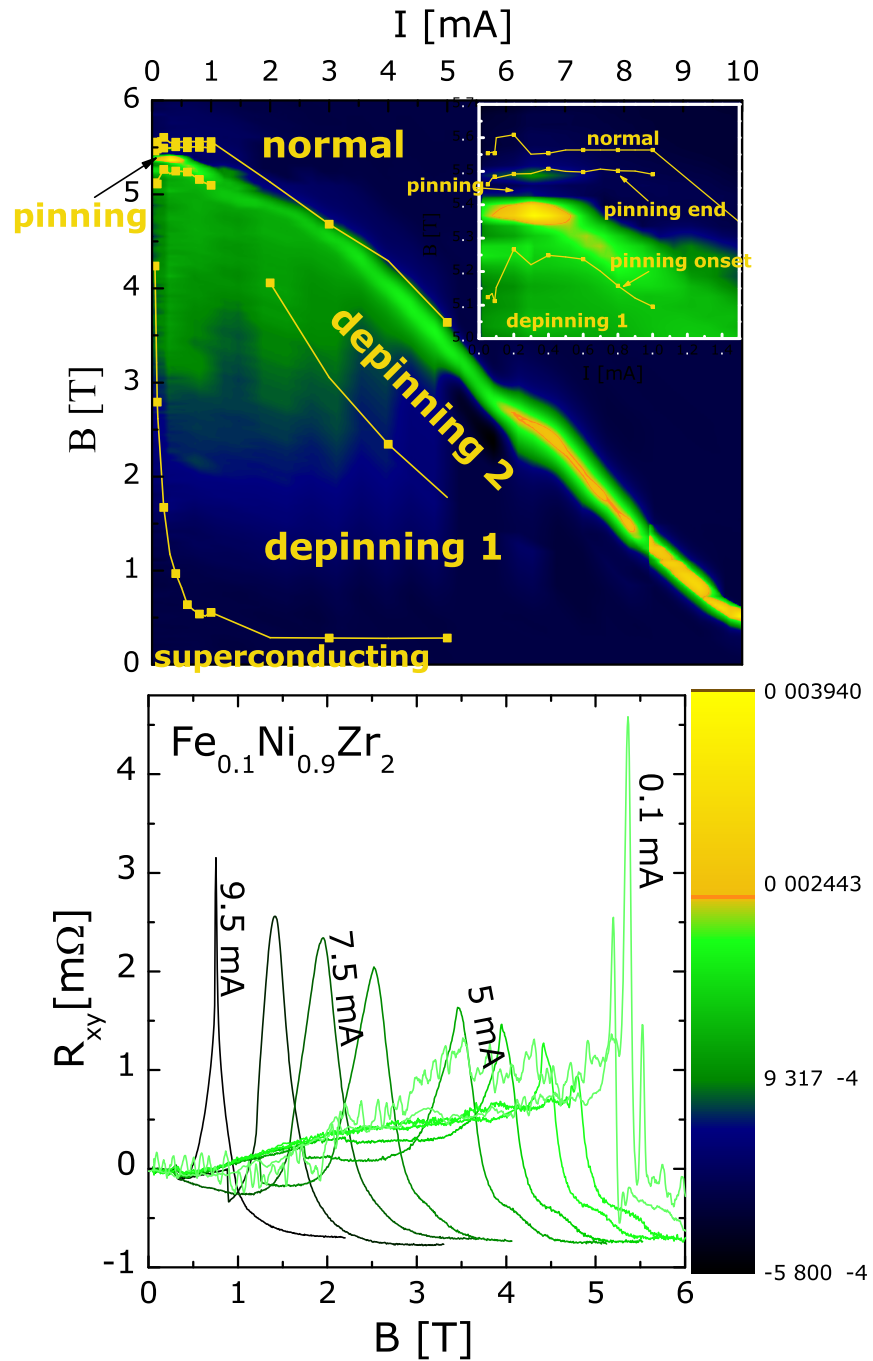


Figure 6.7: Upper panel: The lines represent the phase diagram obtained from the longitudinal resistance. The colour map as a function of B and I represents the value of the Hall resistance according to the colour scale shown in the lower panel. It is important to note that a line accounting for the contact misalignment was subtracted from the Hall curves in the graph. Lower panel: Hall resistance as a function of magnetic field for the following driving currents: 0.1, 1, 2.5, 3.33, 4.16, 5, 6.66, 7.5, 8.3, 9.5, and 10 mA.

function of magnetic field and driving current. The colour scale appears in the lower panel of Fig.(6.7) next to the Hall resistance curves at different driving currents to ease comparison between the magnitude of R_{xy} and the corresponding colour in the colour map. The colour map highlights the correspondence of different features of the Hall resistance with the vortex phases established from the R_{xx} measurements. In this manner, the sharp peaks observed in the Hall resistance are seen to correspond with the termination of the depinning 2 phase close to the transition to the normal state. This can be observed more easily in Fig.(6.8) in which both R_{xx} and R_{xy} are plotted against corresponding field. Also apparent in this figure is the presence of a second peak in the Hall resistance of the low driving current curves, corresponding with the onset of the pinning phase in the R_{xx} measurements.

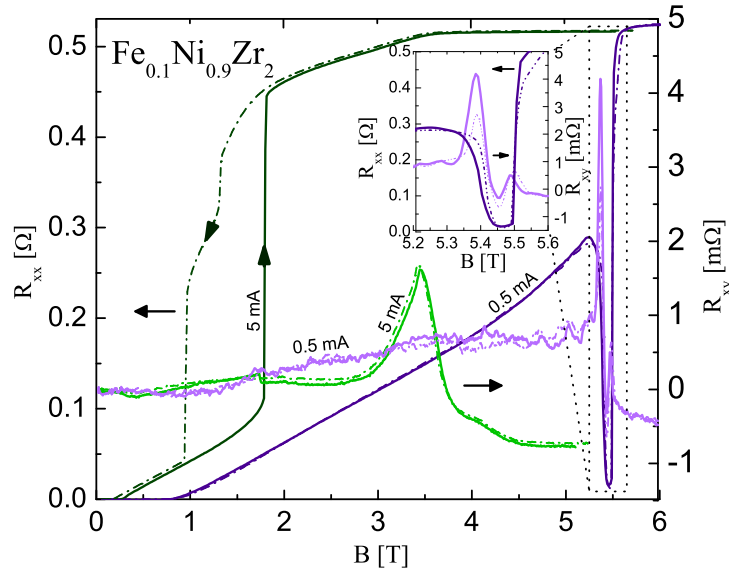


Figure 6.8: Longitudinal resistance and Hall resistance as a function of magnetic field for up (solid lines) and down (dotted lines) B sweeps with $I = 0.5$ mA (purple curves) and $I = 5$ mA (green curves). Inset: Enlargement of the peak effect region. The nonzero Hall resistance above the critical field is due to the small unavoidable misalignment of the Hall contacts.

The results explained

The results presented above are representative of all the Hall resistance results we have obtained from about half a dozen samples of varying iron content with $0 \leq x \leq 0.4$. All R_{xy} results exhibit no clear distinction between the depinning 1 and depinning 2 transition, where a sharp and sudden jump in resistance is observed in longitudinal resistance data and which serves to determine the phase boundary. On the contrary, the features observed in the Hall resistance always become very pronounced in the depinning 2 phase, where no important features are present in the longitudinal resistance. Small features are observed in R_{xy} in the depinning 1 phase which vary from sweep to sweep and are indicative of a noisy history dependent behaviour. This noisy B -dependent Hall resistance stems from the very nature of the depinning 1 phase which, like the MBG phase, shows a small lateral movement of the vortices along channels depending on the vortex density [5], and which, analogous to fluctuations, is not reproducible. This stands in contrast to the sharp peaks observed in R_{xy} in the depinning 2 phase and which are found to be highly reproducible for different B sweeps; this phenomenon can also be understood from consideration of the nature of the depinning 2 phase. Indeed, the depinning 2 phase is characterized by the long range inhomogeneous flow of vortices in smectic channels, with an orientation which can change very suddenly depending on the local disorder configuration and vortex density. This smectic phase is less ordered in the longitudinal direction than the MBG phase, but long range translational order in the transverse direction is preserved despite the dislocations generated by the increased disorder provided by the B field which induce a decoupling of the channels. Generically, a peak in the Hall signal is a measure of a long-ranged moving vortex structure, because a short-ranged order would be averaged out over the sample width. Therefrom, we expect that the peak observed in the Hall resistance is an indication of a transition to a smectic phase with a reorientation of the vortex flow direction.

Origin of the Hall resistance peak

We proceed to analyze the high-field region of the phase diagram comprised between the pinning phase and the normal state. We show that there must exist a moving vortex phase at fields just below the transition to the normal state since a sharp Hall resistance peak is observed in this region of the phase diagram. As shown in Fig.(6.9), the Hall resistance peak is even present at very low driving current, which suggests that a vortex phase with long range inhomogeneous vortex flow such as a smectic phase exists between the peak effect and the normal state all the way down to vanishingly small driving currents. Such a strong peak in R_{xy} at very low driving current is observed in all the samples we have measured; to the best of our knowledge, this is the first reported evidence for the existence of a smectic-like phase in such a low driving regime, and comes in contradiction to the predictions of Ref.[5], as depicted in Fig.(6.2). Also note that the Hall resistance peak becomes smaller with increasing temperature and only vanishes at T_c , which brings a further confirmation that it is not due to an inhomogeneous current flow close to the superconducting to normal transition, but rather a consequence of a long-ranged transverse vortex flow just below the upper critical field transition.

To summarize the results exposed in this section, measurements of the Hall resistance have brought evidence that the first depinned vortex phase encountered as the magnetic field is increased is consistent with the moving Bragg glass. For larger magnetic field, the reentrant pinning phase known as the peak effect and characterized by a vanishing longitudinal resistance also leads to a zero Hall resistance. For still larger magnetic fields and for all driving currents, large peaks are observed in the Hall resistance which correspond with the termination of the second depinned vortex phase close to the normal state. These important features are manifestations of the long range inhomogeneous vortex flow characterizing this phase, which has smectic order and undergoes orientational changes. The observation of a large Hall resistance peak at very low driving current demonstrates for the first time that this phase also extends to the low driving force region of the phase diagram.

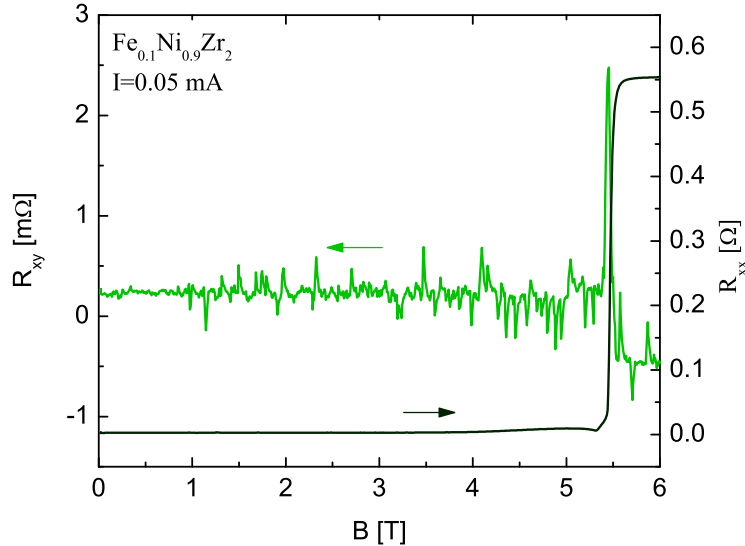


Figure 6.9: Longitudinal resistance and Hall resistance as a function of magnetic field for B sweeps with $I = 0.05$ mA.

6.2.2 Critical transverse depinning

While the Hall resistance measurements presented in section (6.2.1) have enlightened some of the high magnetic field vortex phases in our alloys, the transverse dynamics of the low field phase, the MBG, will be probed in the experiment to be described in this section. More precisely, using crossed ac and dc driving currents, the transverse depinning force due to the transverse ac drive for different longitudinal dc drive will be determined. The use of the ac/dc combination permits the separation of the transverse and longitudinal components of vortex drive and motion. The experiments show that the force required for depinning in the transverse direction in the presence of a longitudinal drive is enhanced; the results also confirm the existence of a large transverse critical force, as predicted theoretically in Ref.[5, 17, 18, 19, 16, 20, 21]. This is the first experimental evidence for the existence of a critical transverse depinning force on a system of vortices, while a transverse depinning force roughly one tenth the magnitude of the parallel depinning force was observed previously in a magnetically-induced Wigner solid in a GaAs/GaAlAs heterojunction [149].

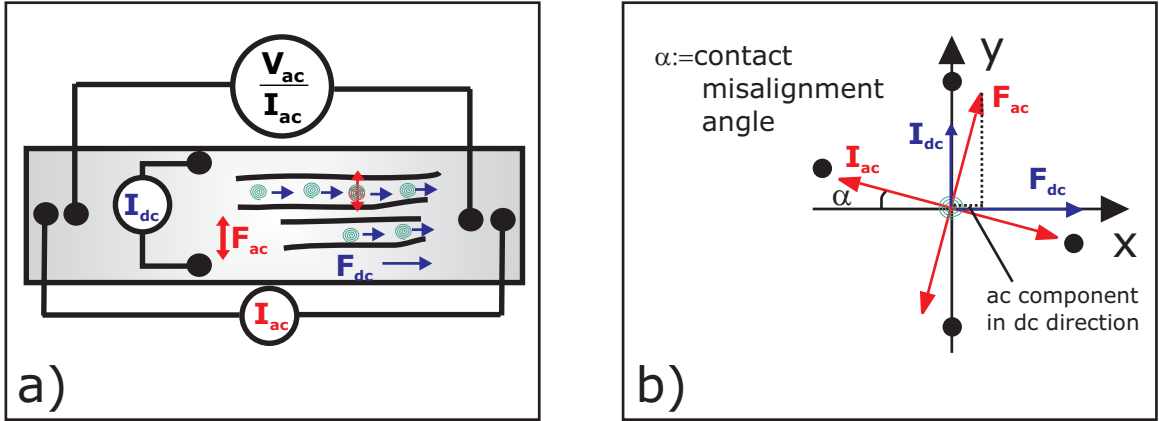


Figure 6.10: a) Drawing showing the contact configuration and resulting directions of vortex motion due to the combination of ac and dc currents. b) Representation of the directions of applied currents and resulting forces with the contact misalignment as discussed in the text.

Experimental configuration

As was the case for the description of the configuration used for the Hall resistance measurements, we provide again in Fig.(6.10a) a schematic drawing of our experimental configuration, because with two different driving currents and vortices moving in the direction perpendicular to the current and magnetic field, things can get confusing! Indium contacts are soldered to the sample as shown in the figure, and the magnetic field is applied perpendicular to the sample plane, i.e. perpendicular to the page here. The dc current is applied along the short edge of the sample such that, from the combination of magnetic field and dc driving, the vortices move under the action of the Lorentz force along the long edge of the sample. Similarly, the ac driving current applied along the long edge of the sample induces a force which results in an oscillatory movement of the vortices parallel to the short edge of the sample. In this manner, the dc driving current is used to set the vortices in motion in the longitudinal direction, along the characteristic channels of the MBG phase. We recall that these channels are predicted to provide strong barriers against transverse vortex motion [5, 16]. This is precisely the property of the MBG that we propose to challenge using the ac driving current to set up a small force on the vortices in the direction transverse to the channels. Evidently, the two sets of contacts used for dc and ac driving cannot

be made perfectly perpendicular to each other, and the transverse voltage measured (from the ac driving) also contains a component resulting from the ac component along the dc longitudinally driven motion, as shown in Fig.(6.10b). This contact misalignment α can be estimated, and is of the order of 2° for the sample used to measure the data that will be presented in the next section; we discuss below how this component can be excluded from the data.

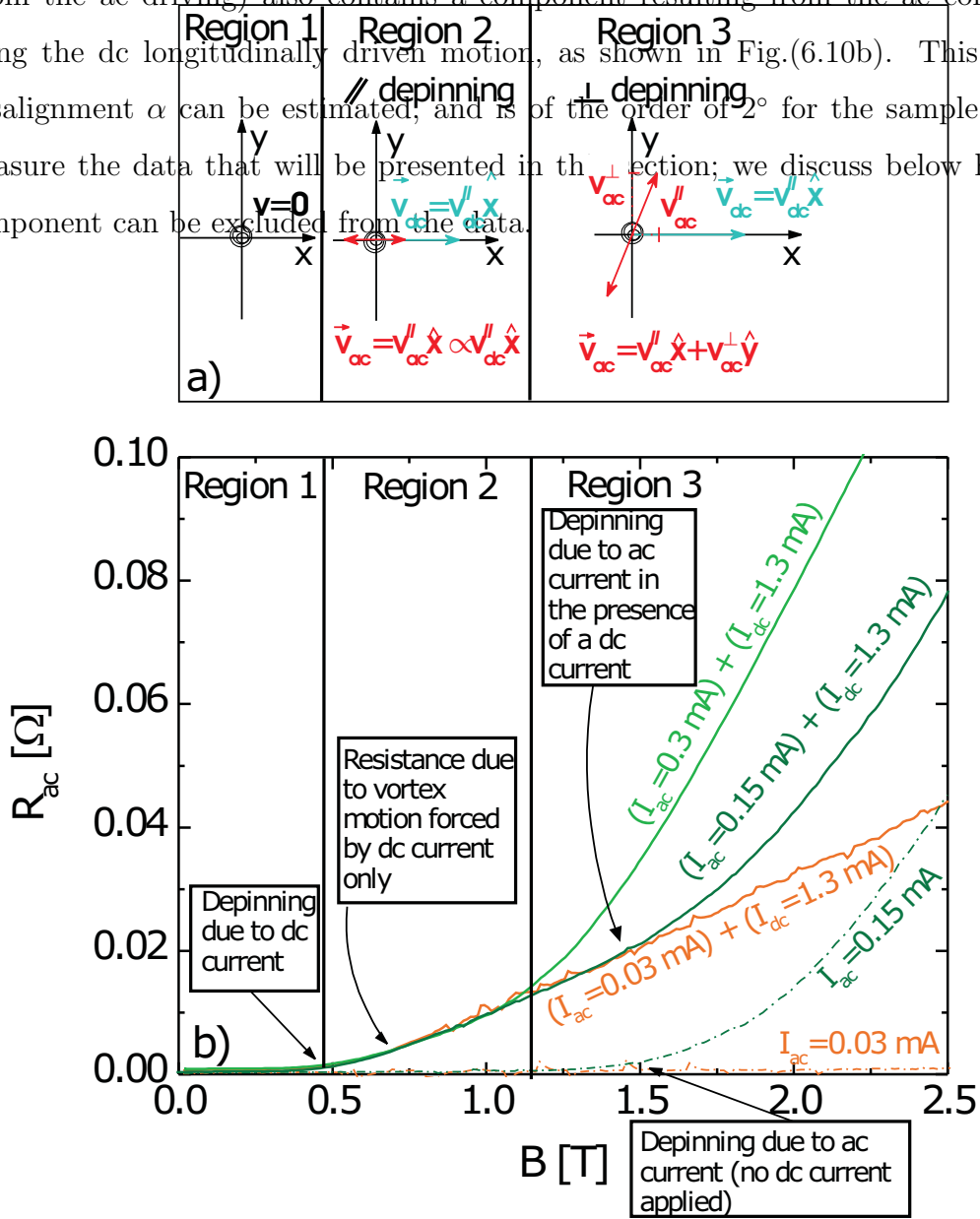


Figure 6.11: a) Schematic representation of the trajectory followed by vortices in the three regimes of vortex motion described in the text. b) Resistance vs magnetic field measured with different ac and dc currents.

Results of the ac resistance as a function of magnetic field

Fig.(6.11b) shows measurements of the transverse ac resistance for different ac driving currents as a function of magnetic field for zero and non-zero dc driving currents. The dc driving current used is $I_{dc} = 1.3$ mA which is larger than the longitudinal depinning current of 0.55 mA at $B=0.95$ T. Three distinct regions can be defined corresponding to three different regimes of vortex motion: Region 1 is characterized by vortices pinned in both directions, because no matter the combination of ac and dc current used, none of the currents is large enough to depin the vortices, and the resistance remains zero. In region 2, the resistance measured using solely ac currents $I_{ac} = 0.03$ mA and $I_{ac} = 0.15$ mA remains zero because these currents are not large enough to depin the vortices. However, the data acquired using a dc current in addition to these ac currents show an ac resistance, which is the same for both ac drives; this ac resistance must therefore result from the small component of vortex motion proportional to $\sin(\alpha)$ along the longitudinal (dc) direction since we have seen that none of the ac currents alone is strong enough to depin the vortices. Indeed, it appears from the data in this region that the ac resistance is independent of the ac current, thus clearly demonstrating that the depinning is only longitudinal and that vortices remain pinned in the transverse direction, since depinning is associated with strong non-linearities of the $V - I$ characteristics. This is in stark contrast to the behaviour visible in region 3 where the ac transverse resistance depends on the transverse ac current and indicates the region where the vortices also start moving in the transverse direction. The direction of vortex motion in these 3 regimes is shown schematically in Fig.(6.11a) The transverse depinning current can then easily be identified as the point in field and ac current where the ac resistance starts to depend on the ac current. Hence, for a given longitudinal dc drive, the pure transverse dynamics can be obtained by subtracting from $R_{ac}(I_{dc} + I_{ac})$ the resistance measured from the combination of the same I_{dc} and a very small transverse ac current which alone does not depin the vortices ($I_{ac} = 0.03$ mA in Fig.(6.11b)). Or, still referring to the data in Fig.(6.11b), this means computing $R_{ac}[(I_{ac} = 0.3 \text{ mA}) + (I_{dc} = 1.3 \text{ mA})] -$

$$R_{ac}[(I_{ac} = 0.03 \text{ mA}) + (I_{dc} = 1.3 \text{ mA})].$$

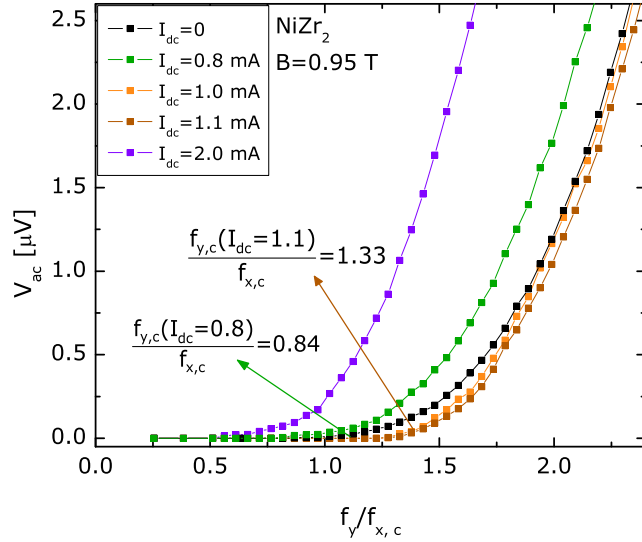


Figure 6.12: Transverse ac voltage as a function of the applied ac force normalized by the critical force in the static case. The data for different longitudinal driving currents is shown.

Voltage-transverse force characteristics

Using the methodology described above to remove the component of the measured ac signal attributable to the contact misalignment, we show in Fig.(6.12) the corrected transverse voltage V_{ac} vs the transverse driving force normalized by the critical longitudinal force for different longitudinal drives and at $B = 0.95$ T. Take note that we will use the terms “critical force” and “depinning force” interchangeably throughout the text because both are equivalent experimentally. However, we will establish later in the text a definition for a “true” critical force. The force is calculated according to the Lorentz force equation (see equation (2.15)) from the combination of the current density and magnetic flux threading the sample. A 10 nV voltage criteria was used to determine the transverse depinning force ($f_{y,c}/f_{x,c}$) indicated for two different longitudinal drives in the figure. The critical longitudinal force $f_{x,c}$ is obtained from the ac (transverse) depinning current determined in the absence of

a longitudinal drive; as our system is isotropic and transport properties measured using ac or dc currents are equivalent (as argued in section (6.2.1)), this approach is valid. The results show that for $I_{dc} = 0.8$ mA, the transverse depinning force is slightly decreased compared to the longitudinal depinning force i.e. $f_{y,c}/f_{x,c} < 1$. In contrast, for $1.0 \text{ mA} \leq I_{dc} \leq 1.1 \text{ mA}$, the transverse depinning force is increased by the presence of the longitudinal drive, with $f_{y,c}/f_{x,c}$ reaching 1.33. This result demonstrates that strong barriers against transverse motion are established for these longitudinal driving forces. The complete dependence of the transverse dynamics on the longitudinal driving force can be described as follows: for $I_{dc} = 0.8$ mA, the longitudinal force is just strong enough to depin the vortex lattice in the longitudinal direction, but the strength of the barriers established by the channel motion is still too weak to cause a strong pinning action in the transverse direction and strongly delay transverse depinning. On the contrary, for $0.9 \text{ mA} \leq I_{dc} \leq 1.1 \text{ mA}$, the longitudinal force appears very effective at restraining transverse vortex motion as the force required to induce transverse depinning becomes larger than the depinning force in the absence of longitudinal driving. Moreover, the transverse depinning force even grows with increasing longitudinal driving force. For $I_{dc} = 1.3$ mA, a decay of the critical forces ratio is visible, which becomes still lower for $I_{dc} = 1.5$ mA. This decay is likely due to a weakening of the barriers against transverse vortex motion due to the additional dynamic disorder induced by the strong longitudinal driving force, as proposed in Ref.[20].

Defining critical behaviour

Choosing different cutoff voltage criteria, the evolution of $f_y/f_{x,c}$ is extracted from the V_{ac} vs $f_y/f_{x,c}$ data and the results are presented in Fig.(6.13). For all longitudinal driving forces, one observes that $f_y/f_{x,c}$ approaches unity for large voltage cutoff; as the voltage is a measure of vortex velocity according to $v = (V_{ac}/W)/B$, where W is the distance traveled (or the width of the sample here), it appears that $f_y/f_{x,c}$ approaches unity for transverse vortex velocities exceeding the longitudinal vortex velocity. In other words, for a large transverse force, corresponding to large

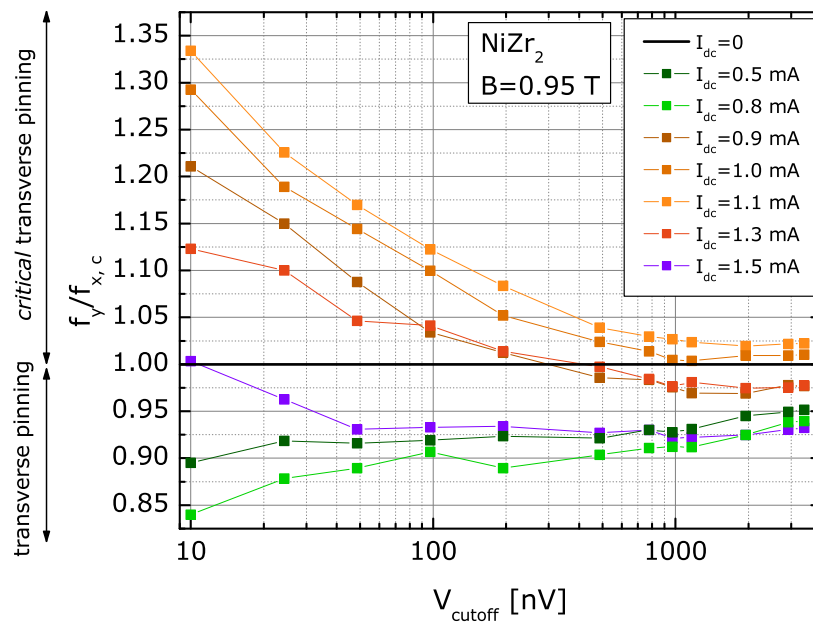


Figure 6.13: Ratio of the critical force in the transverse case to that in the static case as a function of the choice of transverse voltage cutoff criteria.

transverse vortex velocities, one recovers the normal longitudinal dynamics. It was experimentally determined that $f_y/f_{x,c}$ becomes very close to 1 when the transverse force equals approximately five times the longitudinal force. The fact that $f_y/f_{x,c}$ does not reach unity right after transverse depinning occurs implies that the barriers against transverse vortex motion not only delay transverse depinning, but also constrain transverse vortex motion at larger velocities as well. This effect was also observed numerically in Ref.[20].

More importantly, we also show in Fig.(6.13) how the criticality of the transverse depinning transition is determined and confirmed for longitudinal driving currents between 0.9 mA and 1.5 mA. Indeed, in this regime, extrapolation of $f_y/f_{x,c}$ to $V_{cutoff} = 0$ determines the true critical transverse force ratio $f_{y,c}/f_{x,c}$ which, according to the slope of $f_y/f_{x,c}$ vs V_{cutoff} close to zero, will clearly remain larger than zero. In opposition, this cannot be asserted for the data with $I_{dc} = 0.5$ mA and 0.8 mA for which $f_y/f_{x,c}$ decreases with decreasing V_{cutoff} , and which indicates that in this regime of longitudinal driving current, transverse depinning is not critical.

In order to further illustrate this critical behaviour, we show in Fig.(6.14a) and (6.14b) the dependence of the transverse depinning force $f_y/f_{x,c}$ on the longitudinal force for different cutoff voltages for two different samples. The longitudinal force is presented in units of f_0 , the interaction force between two vortices separated by a distance λ^\dagger because we will use this data later to compare our results to results from numerical studies expressed in such units. The general behaviour observed with increasing dc driving force mentioned previously is obvious in these graphs: an initial slight decrease of $f_y/f_{x,c}$ followed by a strong increase, reaching a maximum at $f_x = 0.2 \times 10^{-3} f_0$ (for the NiZr₂ sample). In the region below $f_x = 0.16 \times 10^{-3} f_0$, the longitudinal force is smaller than the longitudinal depinning force so the

[†]The interaction force between two vortices is obtained from Clem [62] as $f_0 = \frac{\Phi_0^2}{8\pi\mu_0\lambda^3} K_1\left(\frac{r}{\lambda}\right)$, where K_1 is the modified Bessel function of the 2nd kind, and r is the distance from the center of the vortex; we set $r = \lambda$. This f_0 gives the force per vortex, so this is multiplied by the number of vortices in our sample, as computed from the magnetic field and the physical size of the sample to give the f_0 used in the calculations.

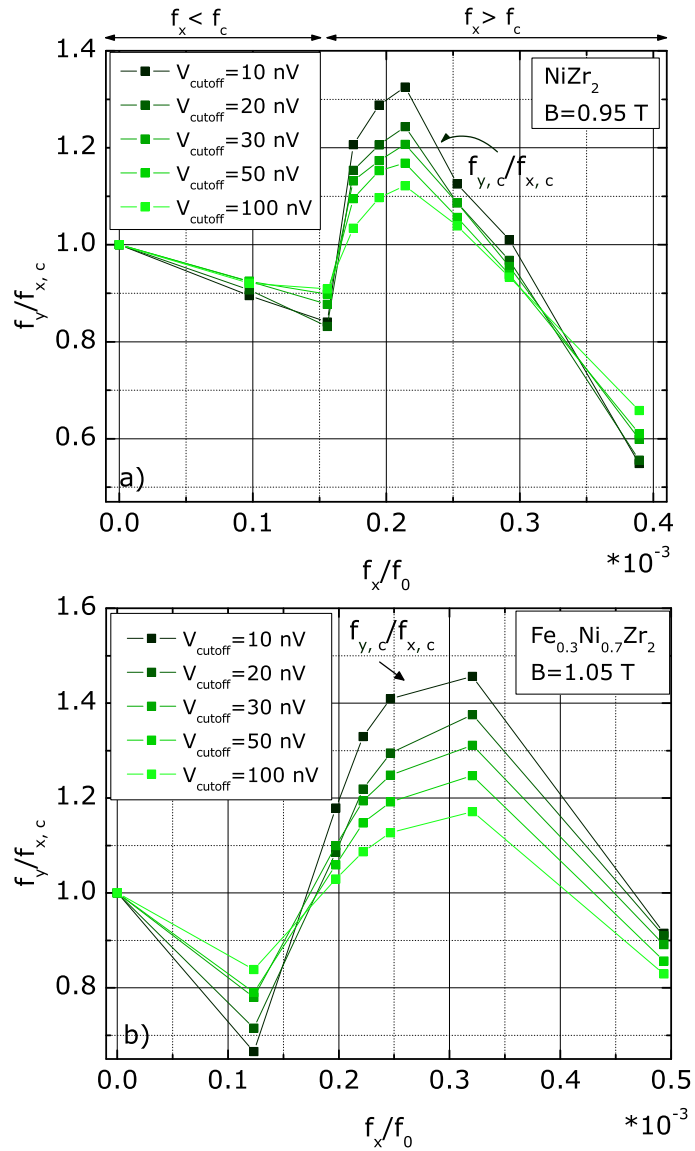


Figure 6.14: Ratio of the critical force in the driven and the static case vs the longitudinal dc force determined using different cutoff voltages for a) a sample of NiZr_2 at $B = 0.95 \text{ T}$ b) a sample of $\text{Fe}_{0.3}\text{Ni}_{0.7}\text{Zr}_2$ at $B = 1.05 \text{ T}$.

ratio $f_y/f_{x,c}$ is dominated by the transverse motion, which means that $f_y/f_{x,c}$ should approach 1. However, we observe an initial small decrease of $f_y/f_{x,c}$, attributable to the small longitudinal dc component in the transverse direction due to the contact misalignment, which now eases depinning in the transverse direction. In the peak region, i.e. for $0.16 \times 10^{-3} f_0 < f_x < 0.33 \times 10^{-3} f_0$, the longitudinal force is greater than the longitudinal depinning force and an important enhancement of the transverse depinning force is witnessed. This is also the region in which a true critical transverse force exists, as described in the previous paragraph. A strong dependence on the choice of voltage cutoff is observed, which signifies that the effect of the longitudinal dc drive is not equivalent for all transverse ac forces. We choose the curve with $V_{cutoff} = 10$ nV to determine the true critical transverse force ratio $f_{y,c}/f_{x,c}$ because, as discussed earlier, the criticality of the transverse depinning transition is determined by the behaviour in the limit where V_{cutoff} approaches zero.

Comparison to numerical studies

A striking result obtained in this study is the huge magnitude of $f_{y,c}/f_{x,c}$, between 0.55 and 1.33, compared to between 0.01 and 0.1 obtained in numerical studies [17, 18, 20, 21]. This much larger magnitude of $f_{y,c}/f_{x,c}$ obtained in our experimental study on a very weakly-pinned vortex system is consistent with results obtained numerically in Ref.[20], which have demonstrated that $f_{y,c}/f_{x,c}$ becomes larger for more weakly-pinned simulated samples. This increase in transverse to longitudinal critical force ratio with decreasing degree of longitudinal pinning is explainable from the fact that the transverse depinning is largely independent of the longitudinal depinning. So, for weak longitudinal pinning potential, $f_{x,c}$ is very small, but $f_{y,c}$ remains essentially unaffected by the degree of longitudinal pinning since the moving system is topologically ordered. For a quantitative comparison with numerical studies, we use $f_p = A \left| \vec{J}_c \times \vec{B} \right|$, where A is the area of the sample perpendicular to the magnetic field, to obtain the pinning force per unit length for our sample and we obtain $f_p = 0.02 f_0$, which is 6 times smaller than the pinning force of the most weakly-pinned sample in Ref.[20]. In addition, we obtain the longitudinal critical force for

our sample $f_c = 1 \times 10^{-4} f_0$, which is more than 200 times smaller than the longitudinal critical force simulated in Ref.[20]. These quantities confirm the weak-pinning nature of our samples, which leads to the very large observed critical transverse to longitudinal force ratio observed here.

Another particularity of our results compared to results from numerical studies is the increase of the transverse critical force with increasing longitudinal drive in the critical region, for instance between $f_x = 0.16 \times 10^{-3} f_0$ and $f_x = 0.22 \times 10^{-3} f_0$ in Fig.(6.14a). This result is contrary to the general observation in numerical simulations of a strong decrease of the transverse critical force with increasing longitudinal vortex velocity [5, 16, 20, 150]. Their results show that as soon as the vortex lattice is depinned in the longitudinal direction in the MBG phase, the transverse depinning force attains its maximum value and then strongly decreases with further increase of the longitudinal vortex velocity; the functional form of the decrease is not known but some estimate it as exponential, or at least nonlinear [20]. This decrease is argued to occur because for large longitudinal driving force, the channels straighten and can no longer adhere to optimal pinning sites which should weaken the strength of the barriers to transverse motion. We speculate that our contradictory results are due to the fact that our experiments are performed in the limit of very weak pinning, hence collective pinning effects become more important and depend less on the underlying optimal pinning sites.

Transverse depinning transition: Dependence on the longitudinal pinning strength

The amorphous nature of our Fe-Ni-Zr alloys provides them with their weak collective-pinning properties caused by the absence of long-range order in such systems. In an increasing magnetic field, the pinning properties are expected to increase due to the effective increase of disorder it generates from the proliferation of dislocations in the vortex lattice. As a result, the force required to depin the vortex lattice (in the longitudinal direction) increases with magnetic field (J_c decreases, but the force is provided by $F_c \sim J_c \times B$). Of course, the pinning force is also influenced by interactions between

the vortices, elasticity of the vortex lattice, and vortex ordering in phases such as the moving Bragg glass, which we showed improves transverse pinning properties, but weakens the longitudinal pinning potential from the averaging of disorder along the direction of motion. According to this, studying the transverse depinning transition as a function of magnetic field is equivalent to investigating its dependence on longitudinal pinning properties. Therefore, with the aim of examining the dependence of the transverse depinning transition on longitudinal pinning strength, we present in this section the results from measurements of the transverse depinning force for different external magnetic fields. The results reveal that a large critical transverse depinning

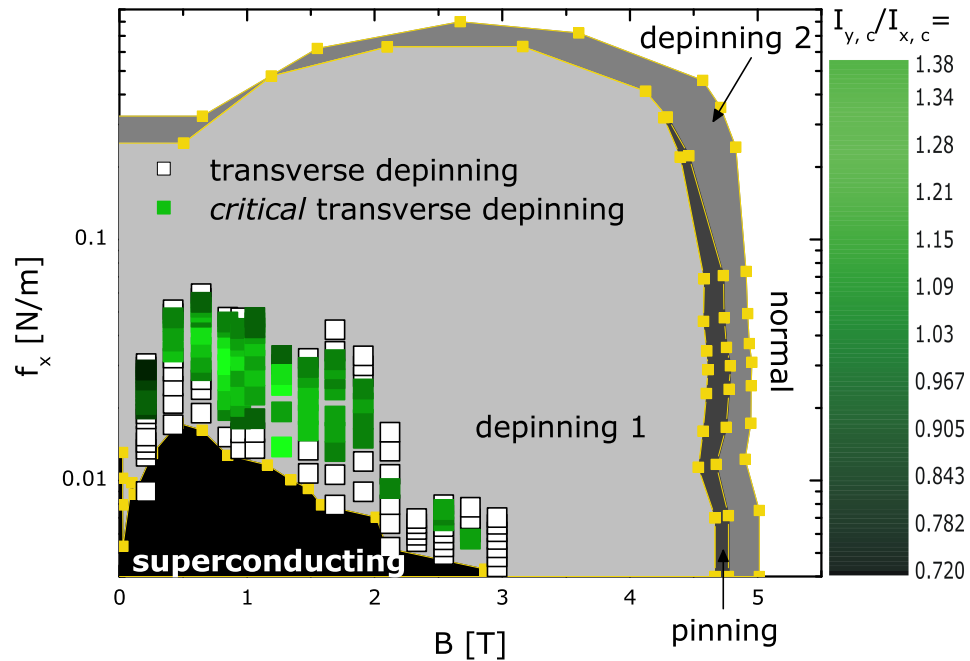


Figure 6.15: Longitudinal driving force vs magnetic field phase diagram showing the different vortex phases observed in the weakly-pinned amorphous metallic glass NiZr₂ and determined from longitudinal resistance measurements performed using an ac driving current. Also shown are regions for which a critical transverse depinning force was found (filled squares) with the magnitude $I_{y,c}/I_{x,c}$ given according to the colour scale on the right. Open squares represent regions for which transverse depinning was investigated but was not found to be critical.

force exists in regions of the phase diagram where a large longitudinal pinning force

also exists. This is emphasized in Fig.(6.15) which shows the complete longitudinal driving force f_x -magnetic field phase diagram for the NiZr₂ sample; the graph also displays data points showing regions where transverse depinning was investigated and found to be critical (green squares with the magnitude of $I_{y,c}/I_{x,c}$ represented by the colour scale on the right), and not critical (open squares). The longitudinal depinning force, represented in this graph by the yellow line delimiting the superconducting and depinning 1 phases, is found to increase for low magnetic field ($B \leq 0.5$) as disorder proliferates, but decreases again for larger fields as dynamic ordering in the direction of motion due to the motion of vortices in channels takes place. It can also be seen that while the transverse depinning transition could only be investigated in the region $0 \leq B \leq 3$ T because the depinning current becomes too low for larger fields and noise dominates the signal, a transverse depinning current with $I_{y,c}/I_{x,c}$ significantly larger than 1 is only found in the region $0.4 \leq B \leq 1.6$ T where the longitudinal depinning force is also largest. This can be understood considering the fact that the larger the longitudinal depinning force is (or equivalently the longitudinal pinning potential), the stronger the channels must be due to the proliferation of pinning sites; the stronger channels must then also constitute a stronger barrier against transverse depinning and lead to the large transverse critical force. A similar increase of the transverse critical force with increasing longitudinal pinning strength for a simulated vortex lattice in the elastic flow regime has also been observed by Fangohr *et al.* [20]. In section (6.2.2), we argued that the ratio of the transverse to longitudinal depinning force $f_{y,c}/f_{x,c}$ is expected to be larger for samples exhibiting a weak longitudinal pinning potential because the longitudinal depinning force is very sensitive to pinning, whereas the transverse depinning force depends less drastically on longitudinal pinning because the moving system is topologically ordered for any pinning strength. This is particularly true when comparing longitudinal pinning forces which lead vortex flow in the elastic regime (weak pinning) and flow in the plastic regime (large pinning): As plastic deformations proliferate, a weakening (not necessarily a breakdown) of the MBG phase is witnessed [20] with accompanying decrease in strength

of barriers against transverse motion. However, for two systems well in the elastic flow regime but with different longitudinal pinning strengths, such as created here from varying the external magnetic field, increased longitudinal pinning leads to a strengthening of the barriers against transverse motion which yield the larger values of the transverse critical force obtained.

The data presented in Fig.(6.15) data does not necessarily represent the boundary of the phase in which critical transverse depinning exists: For instance, large ratios of $I_{y,c}/I_{x,c} \approx 0.75$ were still obtained for the largest dc currents used around $B = 1$ T, but the values of $I_{y,c}/I_{x,c}$ obtained on the boundary are considerably lower than the maximum of $I_y/I_{x,c}$ close to 1.3 obtained here. Moreover, for $B = 2.96$ T which is the largest field probed, no region with $I_y/I_{x,c}$ increasing with decreasing V_{cutoff} (this was argued to define critical behaviour, as in Fig.(6.13)) was observed from measurements using several different dc currents in increments of 0.01 mA, such that if a *critical* transverse depinning region suiting our definition exists at these high fields, it must be very narrow.

A note on our definition of criticality At this point, we would like to comment on our definition of “true” critical transverse force: As described in section (6.2.2), we have defined the criticality of the transverse depinning transition as apparent from the asymptotic behaviour of $f_y/f_{x,c}$ vs V_{cutoff} for V_{cutoff} close to 0, according to which an increasing slope indicates “true” critical behaviour while a decreasing slope simply indicates the existence of barriers against transverse depinning. In this view, a finite value of $f_y/f_{x,c}$ is not sufficient to define the criticality of the transition, which appears as a contradiction to the proposition by Le Doussal and Giamarchi [5] that the transverse critical force is the order parameter of the moving glass phases at $T = 0$. The problem lies in the difficulty in determining criticality experimentally as the limited resolution of our detectors, and impurity and finite size effects cause a rounding of the divergence [151]. Therefore, experimentally the relevant questions become “What is the asymptotic behaviour of the system as it approaches the critical point ?” and “How close is the system to criticality ?”. In this perspective, we find

that our definition of criticality addresses the relevant issues, and that the mere determination of a finite transverse depinning force does not infer the criticality of the transition; the important observation rather becomes that of the behaviour of the transverse depinning force as one approaches the critical point.

Temperature dependence of the transverse depinning force

The “true” critical transverse force refers to the value of this force at $T = 0$ and thus cannot be evaluated in experiments nor in theoretical simulations which are limited by finite size effects. Therefore, prediction of the behaviour at finite temperature is of prime importance to render possible comparisons with experiments. In this perspective, Le Doussal and Giamarchi [5] have predicted that the MBG phase survives at finite temperature, but exhibits a broadening of the vortex channels due to thermal displacements about their average position with a weakening of the transverse barriers. The strong non-linearities of transverse motion still exist, but whereas transverse displacements at $T = 0$ were predicted to grow logarithmically, at finite temperature the asymptotic behaviour is found to be linear. With increasing temperature, critical transverse depinning is predicted to be destroyed at the melting line, when the MBG transforms into the highly disordered vortex liquid phase and the channels no longer exist.

Just like transverse depinning, longitudinal depinning is also expected to be eased by the increase of temperature, simply because the particles have more energy to overcome the pinning potential. This is observed in Fig.(6.16) as a decrease in the driving current necessary to produce a particular dissipation voltage with increasing temperature for fixed magnetic field $B = 0.95$ T. In the figure, the data for longitudinal depinning only ($I_{dc} = 0$) is represented by the dotted lines with triangular data points while the solid lines with round data points represent transverse depinning data with a $I_{dc} = 1$ mA longitudinal driving current. While the need to supply a larger force for depinning in the transverse direction than in the longitudinal direction was expected in the light of the results obtained previously, the increase of the transverse depinning force observed with increasing temperature from $T = 0.41$ K

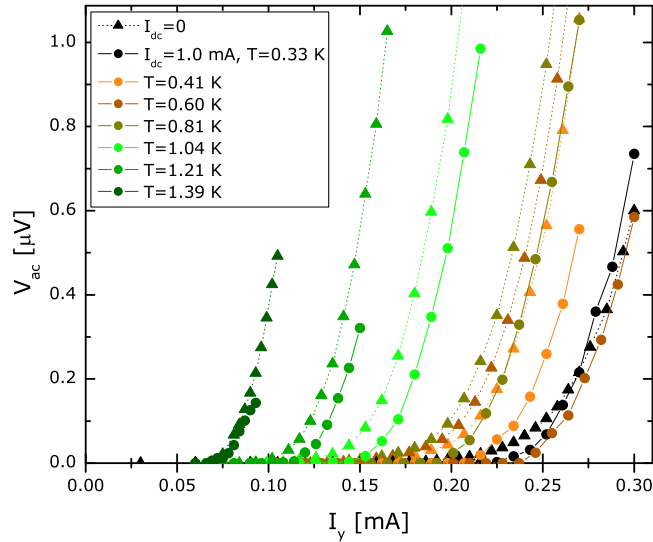


Figure 6.16: Transverse voltage vs transverse driving force for $B = 0.95$ T for longitudinal driving current $I_{dc} = 0$ (dotted lines with triangular data points) and $I_{dc} = 1.0$ mA (solid lines with round data points). The lines are guides to the eye. The colours correspond to different temperatures.

to 0.60 K was certainly not expected. Indeed, from simulations of vortex lattices, Fangohr *et al.* [20] have obtained a decrease of the transverse depinning force with increasing temperature. However, our observation signifies that for the same longitudinal force applied on the vortices, the barriers against transverse motion have strengthened with the increase of temperature whereas they are predicted to weaken. This behaviour is particularly obvious in Fig.(6.17a) in which the values of $I_y/I_{x,c}$ for several longitudinal driving currents at $T = 0.60$ K well surpass those at lower temperatures. A plausible explanation for this effect comes from consideration of the longitudinal vortex velocity induced for the same driving current and magnetic field but for different temperatures: For the same external driving force the velocity of vortices becomes larger with increasing temperature (see Fig.(6.16), recalling that voltage is proportional to vortex velocity), hence resulting in a strengthening of the barriers against transverse motion just like the one observed for increasing longitudinal drive in the results of Fig.(6.14) for instance. Therefore, it appears that for T

between 0.4 K and 0.6 K increased transverse pinning due to increased longitudinal vortex velocity is stronger than the temperature-induced weakening of the channel barriers.

We show in Fig.(6.17b) the magnitude of $I_{y,c}/I_{x,c}$ represented as a colour map as a function of longitudinal current and temperature for data showing critical transverse depinning according to the definition discussed above. Cases where the transverse depinning is not found to be critical are represented by open squares. The solid line is the longitudinal depinning line acquired from measurements in the absence of a longitudinal driving current. T_c for this sample is 2.4 K but the largest temperature investigated is 1.56 K, well below T_c . Higher temperatures could not be investigated because at such temperatures the depinning current becomes too low and noise dominates the signal from the resistance bridge. Therefore, the region of the $I - T$ phase diagram shown to exhibit critical transverse depinning is not bounded and a region exhibiting critical transverse depinning probably does exist for higher temperatures below T_c .

We feel it is noteworthy to mention that the evolution of the magnitude of $I_{y,c}/I_{x,c}$ with temperature in Fig.(6.17b) probably appears more continuous than the evolution with magnetic field shown in Fig.(6.15) because the temperature dependence data was acquired consecutively without letting the system warm up above T_c , whereas the magnetic field dependence was acquired over three days, letting the system warm up above T_c overnight. Data acquired on different cool downs are always less comparable because slight differences in the superconducting system result from different cool down conditions. For instance, during the first cool down of a series (from room temperature), we are assured that the sample is really cooled in a zero magnetic field. However, for subsequent cool downs in the series and if the magnet was used to supply a large magnetic field on previous days, a significant field remains from persistent currents trapped in the magnet which was not warmed to above its own T_c . We have observed this remaining field to be as large as 0.3 T, meaning that on all but the first cool down, the superconducting sample is cooled to below T_c in

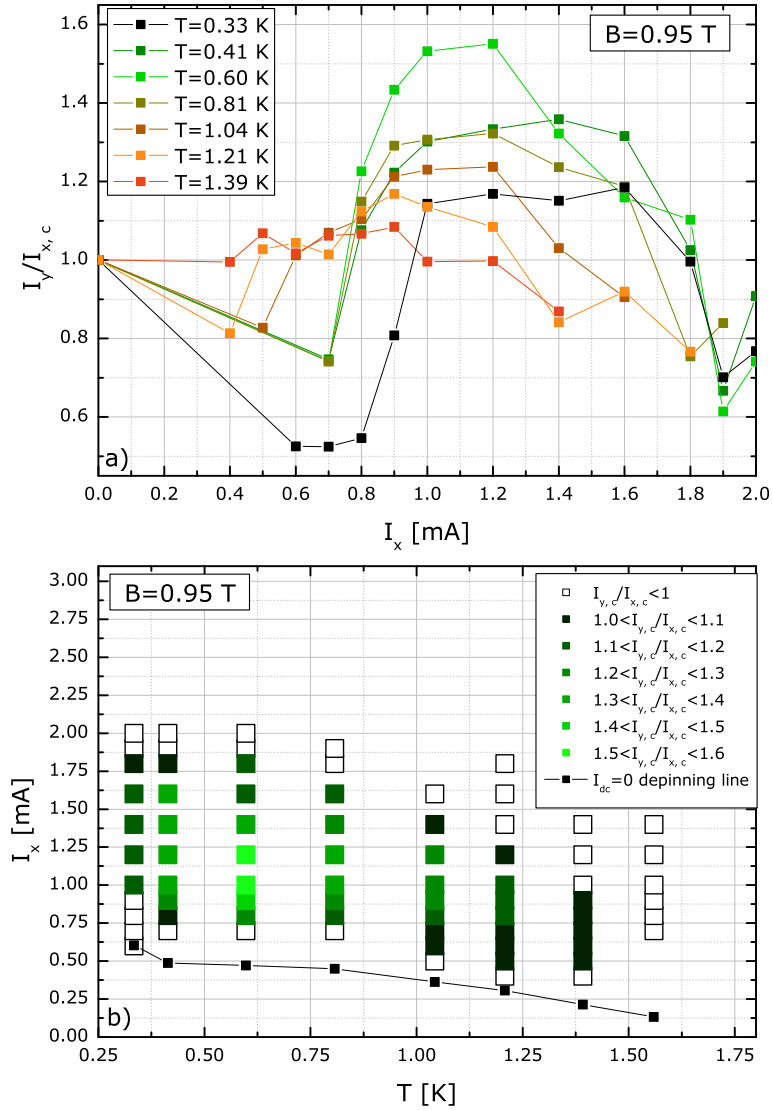


Figure 6.17: a) Ratio of the critical transverse current determined with a 10 nV criterion in the driven and the static case vs the longitudinal current for a sample of NiZr₂ at $B = 0.95$ T and for different temperatures. b) Map of the critical current ratio in the driven and static case according to the colour scale shown, as a function of longitudinal drive and magnetic field. The open squares represent data which do not exhibit *critical* transverse depinning. The solid line represents the longitudinal depinning line.

a magnetic field which can differ on different days, thus preparing the sample in a slightly different superconducting state everyday.

History effects

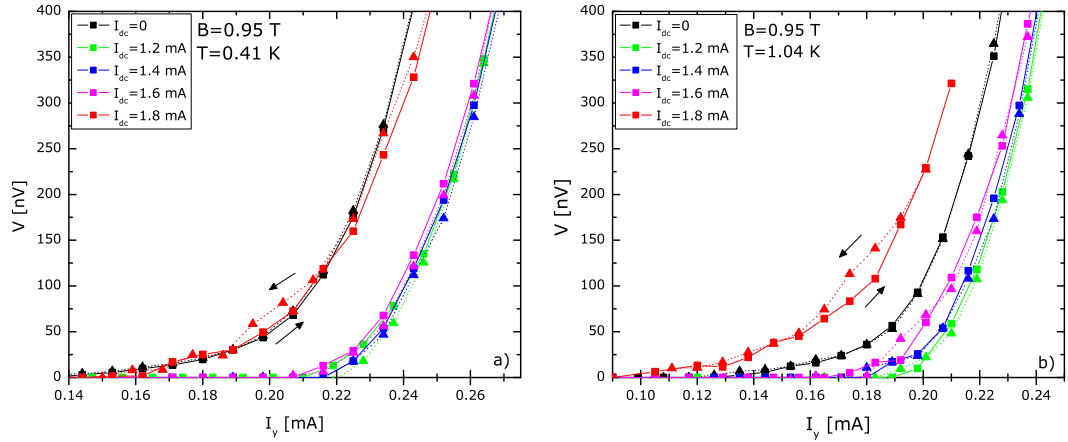


Figure 6.18: Transverse voltage as a function of transverse current at $B = 0.95$ T for different longitudinal driving currents at a) $T = 0.41$ K b) $T = 1.04$ K. The solid lines with square data points were acquired for increasing I_y , while the dotted lines with triangular data points were acquired from decreasing I_y .

The experiment described above raises interesting issues about history effects. For instance, one can wonder if the effect of applying a force in perpendicular directions simultaneously (i.e. $F = f_x \hat{x} + f_y \hat{y}$) is the same as first applying the longitudinal force $f_x \hat{x}$, then waiting for steady state before applying the transverse force $f_y \hat{y}$ [5] as we have done in this experiment. As discussed in Ref.[5], if the vortex state were liquid-like, the result of both these experiments would be the same, but for the moving vortex glass, the answer is not trivial and it could bear important information about the glassy state. In a numerical study of transverse dynamics of elastic strings, Reichhardt and Olson [150] have obtained hysteretic transverse depinning transitions for strings also driven in the parallel direction. With the aim of verifying experimentally the existence of history effects in transverse depinning, we have performed some measurements of V_{ac} vs I_y for both increasing and decreasing I_y for the same

longitudinal current. The data was obtained in the following manner: First the longitudinal current is applied, and only when the measured voltage is stable is the small transverse current applied. I_y is then increased in small steps and the resulting V_{ac} recorded. When V_{ac} is large and we are certain that the vortex lattice is well depinned in the transverse direction, we start decreasing I_y , still in small steps, and recording V_{ac} when steady-state is established after each change of I_y . A sample of this data is shown in Fig.(6.18a) at $T = 0.41$ K and in Fig.(6.18b) at $T = 1.04$ K for different longitudinal dc currents including $I_{dc} = 0$. The solid lines in the figure are for data acquired from increasing I_y while the dotted lines are for decreasing I_y . A small hysteric region can be observed close to depinning in the cases which were also driven longitudinally with a large current ($I_{dc} = 1.8$ mA). The size of the hysteresis loop also seems to increase with increasing temperature. In opposition, the case $I_{dc} = 0$ which represents longitudinal depinning is definitely free of hysteresis. Moreover the counterclockwise direction of the hysteresis loops in the $V - I_y$ characteristics observed in this data is the same as that observed in Ref.[150]. Unfortunately, the data for the complete temperature dependence is not available. This observation of the presence of hysteresis at the transverse depinning transition brings the first experimental confirmation that the transition is first order, and not a mere crossover.

6.3 Summary

In summary, the results obtained in this study bring the first experimental evidence for the existence of a critical transverse depinning transition of first-order nature in a vortex lattice. More specifically, the results have shown that for a system driven longitudinally, application of a small transverse force does not result in immediate transverse depinning. Moreover, in some regimes of longitudinal motion, the transverse force required for depinning the vortices in the transverse direction is even increased by more than 30 % with respect to the force required in the longitudinal case, thus implying the appearance of very strong barriers against transverse motion. Numerical studies have found a transverse to longitudinal critical force ratio of 1 %

[17, 18, 21] to 10 % [20]; a ratio which is larger for more weakly-pinned samples. Unfortunately, finite size effects in numerical simulations make studies in the very weakly-pinned regime of our experiment very difficult to realize because they are computationally expensive. The transverse critical force has been observed in a large portion of the MBG phase in the $B - F$ and $T - F$ phase diagrams. Hysteresis close to depinning in the $V - I_y$ characteristics for large longitudinal driving currents has also been observed, thus confirming the first-order nature of the transverse depinning transition in the glass state.

Therefore, both the Hall resistance measurements and the transverse depinning measurements have shed light on the nature of the moving vortex phases in weakly-pinned superconductors. While the smectic order of the second depinned phase was evidenced by the large features observed in the Hall resistance measurements, the channeled vortex flow characteristic of the moving Bragg glass phase was confirmed in the first depinned phase right after depinning. A very limited number of experiments on the transverse dynamics of the vortex state have been performed before, although theoretical predictions resulting from numerical simulations are numerous. Many of the features observed in these measurements were predicted in numerical simulations, but some new phenomena were also uncovered by the experiments, such as the large critical depinning force.

Conclusions

Superconducting properties of metallic glasses of the series $\text{Fe}_x\text{Ni}_{1-x}\text{Zr}_2$ with $0 \leq x \leq 0.6$ were systematically studied from longitudinal and transverse (Hall) resistance measurements using ac and dc driving currents and from magnetization measurements at different temperatures below T_c . From these measurements, conclusions can be drawn about the nature of the superconducting state in these amorphous alloys, and also about variations in superconducting properties across the $\text{Fe}_x\text{Ni}_{1-x}\text{Zr}_2$ series. Furthermore, the weak pinning character of the alloys has permitted the exposition of utterly interesting characteristics of transverse dynamics of the moving vortex state. More precisely, the results for the critical temperature and upper critical field obtained from resistance measurements as a function of temperature and magnetic field have permitted the computation of various superconducting parameters and length scale such as ξ_G , λ and κ whose values have demonstrated, among other things, that these superconductors are hard type II superconductors in the very dirty limit with weak to intermediate electron-phonon coupling strengths.

The strength of spin-orbit coupling and paramagnetic limiting in these alloys was also determined from fits to the B_{c2} dependence on temperature according to equations from the WHHM theory and was found to generally agree with results from other research groups on similar alloys. Indeed, it was found that both spin-orbit coupling and paramagnetic effects lower the value of B_{c2} as low temperature in these alloys, but not too significantly as the values of B_{c2} remained quite large. The expected decrease of T_c and B_{c2} across the series of alloys with increasing x has also been observed; such a decrease was expected on the basis of increasing spin fluctuations

with Fe concentration which tends to break Cooper pair. Interestingly however, both superconducting parameters T_c and B_{c2} were found to increase when going from the alloy NiZr_2 to $\text{Fe}_{0.1}\text{Ni}_{0.9}\text{Zr}_2$ which is thought to originate from an increase of the density of states at the Fermi level with the addition of Fe to the compound. In the future, it would be interesting to measure the normal state magnetic susceptibility of these alloys, simply to confirm how important spin fluctuations really are in the alloys based on quantities rather than only on the known fact that they increase with Fe concentration.

The low magnetic field magnetization measurements performed using a 2-dimensional electron gas as a detector of magnetic flux have permitted the evaluation of B_{c1} in these alloys. Determination of this parameter cannot be attained from transport measurements as no signs of vortex entry can be seen for a static vortex lattice in such type of measurements. Considering how B_{c1} is highly sample dependent and easily affected by edge pinning, the magnitude of the values of B_{c1} thus determined are found to agree with the Maki predictions for this parameter for hard type II superconductors. The use of a 2DEG probe for the observation of superconducting magnetic properties in the low field regime has proved to be advantageous because the technique offers great sensitivity and is relatively easy to realize since for magnetization measurements we have demonstrated that a reduced distance of the order of hundreds of nanometers between the 2DEG and superconductor is not mandatory. The great sensitivity of the 2DEG probe was further exposed by the observation of fluctuations in the magnetization. Analysis of these magnetization fluctuations has revealed their correlation to the Fe content of the superconducting alloy. For instance, the magnitude of the fluctuations and the size of grains having correlated magnetic moment were found to increase with Fe content.

Resistance measurements as a function of magnetic field for different driving currents and field sweep rates on samples of $\text{Fe}_x\text{Ni}_{1-x}\text{Zr}_2$ with $x = 0.5$ and $x = 0.6$ have uncovered large anomalous hysteresis loops with a clockwise direction; this is opposite to the counterclockwise hysteresis loops generally observed in superconduct-

tors and which result from flux pinning. Moreover, it was shown that the transition from the normal to the superconducting state in the $x = 0.6$ alloy proceeds in two well-defined steps, as often observed in very inhomogeneous superconductors. It was thus demonstrated that these peculiar loops most likely result from an inhomogeneous distribution of vortex pinning properties in these alloys resulting from the presence of two different phases in the material. It was described that the two phases result from the existence of a transition in the amorphous structure with x in the $\text{Fe}_x\text{Ni}_{1-x}\text{Zr}_2$ alloys. Indeed, as the structure of amorphous alloys is very similar to that of the first crystallization products, which assumes a bct structure for $x = 0$ and a fcc structure for $x = 1$ in $\text{Fe}_x\text{Ni}_{1-x}\text{Zr}_2$, one expects that for some x in between 0 and 1 a structural transition occurs. We have determined that this transition occurs for x between 0.4 and 0.5 and that alloys with $x = 0.5$ and $x = 0.6$ show a phase-separated structure with regions showing a NiZr_2 -like structure and other regions showing a FeZr_2 -like structure. These regions exhibit different pinning properties from which the large clockwise hysteresis loops observed result.

Both the results from the analysis of fluctuations in magnetization and the clockwise hysteresis loops indicate the evolution of the amorphous structure of the $\text{Fe}_x\text{Ni}_{1-x}\text{Zr}_2$ alloys with x . As x increases, the augmentation in concentration of Fe in the alloys leads to the formation of regions with more and more Fe near-neighbours. This results in the formation of grains having SRO characteristic of the FeZr_2 metallic glass. From analysis of the magnetization fluctuation, we have determined that the presence of these structural inhomogeneities results in the formation of large vortex clusters; the entry and exit out of the sample of these clusters of vortices yields the fluctuations in magnetization. Similarly, it was determined from the magnetization fluctuations data that the size of these correlated regions reaches about $40 \mu\text{m}$ for the alloys with largest iron content studied. A comparable value was determined from consideration of the superconducting-to-normal transition width in the $x = 0.6$ alloy. As it appears from the drastic change in hysteretic behavior at the B_{c2} that the structural transition across x occurs between $x = 0.4$ and $x = 0.5$, it is not very surprising that

fluctuations in magnetization, reflecting fluctuations in superconducting properties, become more important with increasing x as the transition is approached. It is then expected that for further increase of x above 0.6, fluctuations diminish as one moves away from the transition and the structural order resembles more and more that of FeZr_2 . As a confirmation of this, it would be very insightful in future work to measure alloys with $x > 0.6$ at very low temperature ($T \lesssim 0.3$ K) simply to check if they become superconducting, but also to verify if they show clockwise hysteresis loops at B_{c2} and increased fluctuations in magnetization.

Finally, Hall resistance measurements in the superconducting state performed using ac and dc currents have revealed properties pertaining to the transverse dynamics of the vortex state. Indeed, the large sharp peaks observed in the Hall resistance at high magnetic field close to the superconducting to normal state transition have uncovered the existence of a transversely-ordered vortex state reminiscent of the moving transverse glass in which long range order exists and which is characterized by vortex motion in decoupled channels. As a result of this decoupling, the orientation of the channels can change very suddenly; the observation of large Hall resistance peaks results from this re-orientation of channels. In opposition, the Hall resistance measured in the low field range shows smaller features resulting from single vortex slips out of channels, but no large scale features such as those observed for large magnetic fields, which is more analogous to the behavior expected from a vortex phase such as the moving Bragg glass; also characterized by vortex motion in channels, the positions of vortices in different channels in this phase are coupled. Other measurements of the transverse dynamics of the vortex state were performed using crossed ac and dc currents, but this time in the regime close to the depinning transition. The combination of ac and dc currents has shown to be successful in allowing the signal from the longitudinal and transverse vortex motion to be untangled. Moreover, the results have provided the first experimental proof of the existence of a huge critical transverse force in a weakly-pinned vortex system. It was also indicated that the ratio of the transverse critical force to that of the longitudinal depinning force is

strongly dependent on the degree of pinning, and that we obtain such a large transverse critical force in this study because of the very weak-pinning nature of our alloys. Hysteresis has also been observed at the depinning transition which confirms that it is first order. These results were obtained for various magnetic fields and temperatures such that a good portion of the phase diagram was mapped out, and a large part of these results have been shown to exhibit transverse critical depinning. For further investigations of transverse dynamic vortex phases, it would be interesting to apply the same technique of using crossed ac and dc currents to investigate the transverse depinning transition on a series of superconductors with different degrees of quenched in pinning sites in order to confirm that the huge critical transverse depinning force we obtained compared to that predicted in theoretical simulations is indeed due to the extremely weak pinning character of our samples.

Despite a few gaps that require some more investigation, the work presented in this thesis has exposed a significant amount of information about the nature of the superconducting state in the $\text{Fe}_x\text{Ni}_{1-x}\text{Zr}_2$ alloy series, and has yielded important experimental confirmation of some theoretical predictions about dynamic vortex phases. Moreover, it has uncovered a few creative techniques for the measurement of superconducting properties, such as the use of 2DEG Hall probes sufficiently sensitive to permit the measurement of magnetization fluctuations stemming from vortex clusters.

A

Estimation of the magnetization

For a sample with thickness $d > \lambda$ and $B_{app} < B_{c1}$, we model the superconductor by a thin ring of circulating current. In our case, this current is the shielding current which ensures the Meissner state of the superconductor. Letting a be the radius of the circular loop, I the circulating current and the set of coordinates (r, z) the position of observation with r being along the radius and z being the perpendicular distance away from the ring (i.e. the distance away from the sample), we obtain [152] for the magnetic field perpendicular to the ring of current (superconducting sample)

$$B_z = \frac{2\mu_0 I}{\sqrt{(a+r)^2 + z^2}} \left[K(k) + \frac{a^2 - r^2 - z^2}{(a-r)^2 + z^2} E(k) \right] \quad (\text{A.1})$$

where $K(k)$ and $E(k)$ are complete elliptic integrals of the first and second kind respectively. k is given by

$$k^2 = \frac{4ar}{(a+r)^2 + z^2}. \quad (\text{A.2})$$

Setting $r = 0$, this reduces to

$$B_z = \frac{2\pi\mu_0 a^2 I}{(a^2 + z^2)^{\frac{3}{2}}}. \quad (\text{A.3})$$

According to the Bean critical state model [1], for $B_{app} < B_{c1}$, as the external magnetic field is applied and increased, the shielding current progressively penetrates deeper into the sample so as not to exceed I_c , while still shielding the magnetic field. So we assume that below B_{c1} , the current flowing in the sample is I_c . From the geometry of the samples, we also have $a \simeq 0.5$ mm, $d \simeq 20$ μm , and from experimental results $J_c \simeq 1 \times 10^6$ A/m², such that we obtain $I_c = J_c a d = 10$ mA. Using these values in equation (A.3), we obtain the dependence of the magnetic field induced by the superconductor's shielding current on the distance from the superconductor shown in Fig.(A.1). Right at the surface, $B_z = 0.158$ mT and does not decrease significantly over a distance of several microns.

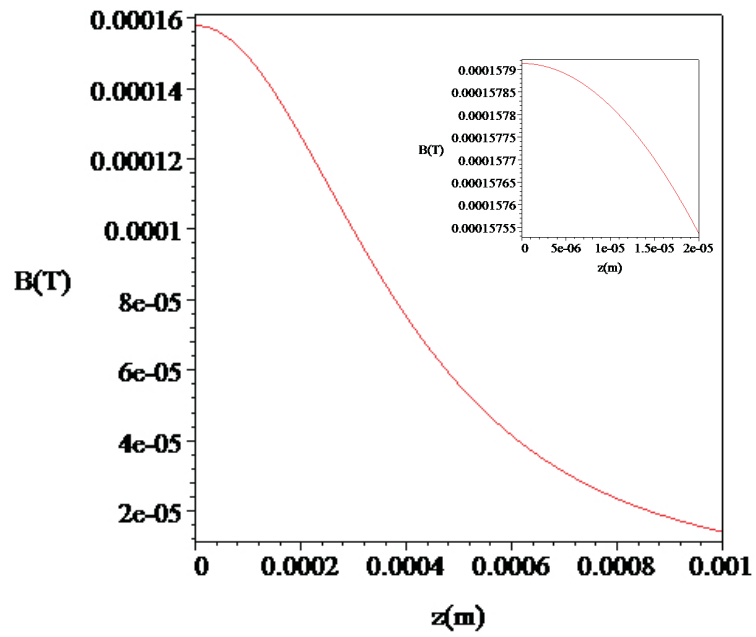


Figure A.1: B_z as a function of the distance away from the sample for $a = 0.5$ mm, $r = 0$, and $I = 10$ mA. Inset: Enlargement of the low z region.

B

Magnetoresistance results

Magnetoresistance measurements were performed simultaneously with the Hall resistance measurements using two synchronous lock-in amplifiers. We do not expect to see any macroscopic effect of the superconductor in the magnetoresistance (R_{xx}) signal; only effects due to vortices are usually observed in this type of measurement [153, 154, 155, 60, 156]. But, we do not expect to see any of those either because our 2DEG-superconductor separation is too large to provide single-vortex resolution at the 2DEG. Nevertheless, we describe in a few words the consequences that the presence of vortices in the 2DEG would have on R_{xx} . The Hall resistance and the magnetoresistance yield complimentary information about the number of positive and negative vortices in the superconductor. Indeed, the Hall resistance is proportional to the difference between the number of positive and negative vortices (or the net number of vortices), while the magnetoresistance is proportional to the absolute number of vortices, positive and negative together [60, 154]. This is because the Hall resistance is antisymmetric with magnetic field while the magnetoresistance is symmetric, i.e. R_{xx} does not change sign upon reversal of the field polarity. However, an inhomogeneous vortex distribution in which positive and negative vortices overlap is not reflected in the magnetoresistance because of field cancellation.

Fig.(B.1) shows magnetoresistance and Hall resistance data for temperatures below and above T_c . Below T_c , R_{xx} exhibits peaks, whose tips coincide with the applied field at which $R_H = 0$, or the point where there is an equal number of up and down vortices in the sample. These peaks disappear for $T > T_c$, as can be seen in Fig.(B.1b). This behaviour of R_{xx} below T_c is different from the behaviour observed in Ref.[60, 154] in similar measurements, and in which no such strong peaks with differing concavity on up and down field sweep are observed. Recalling that R_{xx} is symmetric with magnetic field, this switching of the peak direction with field direction is very puzzling. We hypothesize that these peaks result from the existence of a magnetic field component parallel to the 2DEG. Indeed as the magnetic field induced by the superconductor changes from positive to negative, it does not switch instantaneously; its direction rather turns in a circle as depicted in the inset of Fig.(B.1a), such that the total magnetic field direction is effectively parallel to the 2DEG for some short moment. This can result in a Hall component for fields parallel to the 2DEG in the R_{xx} signal because the contacts on the 2DEG are not perfectly plane.

B.1 Weak localisation

While no significant information about the superconductor can be learned from the magnetoresistance results, interesting information about the low-field transport prop-

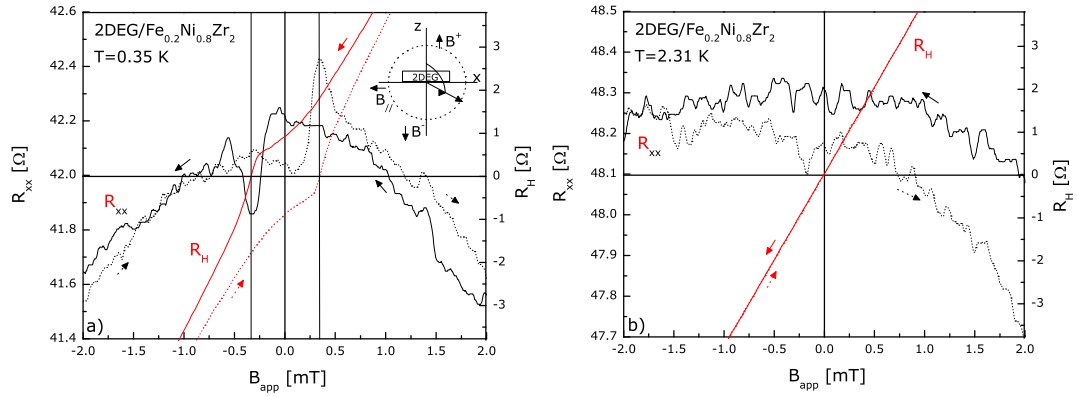


Figure B.1: R_{xx} and R_H vs B_{app} for a) $T = 0.35$ K. Inset: schematic representation of the evolution of the magnetic field direction as it flips from positive to negative. b) $T = 2.31$ K, which is above T_C .

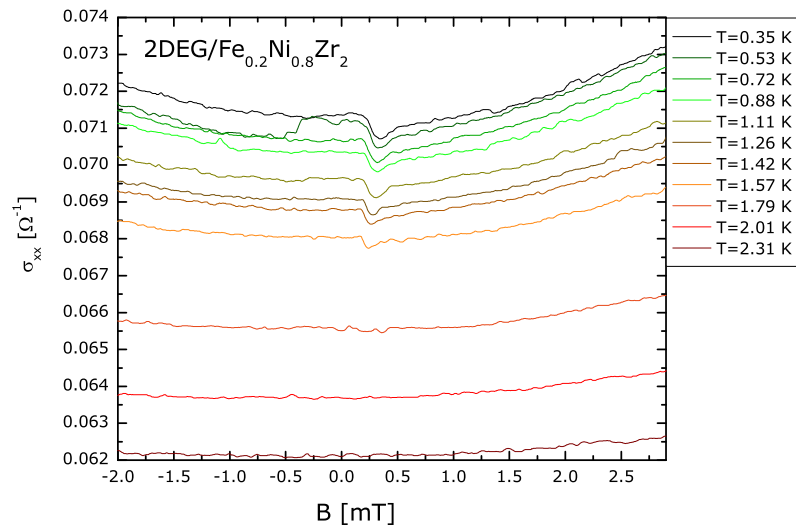


Figure B.2: Magnetoconductivity at different temperatures obtained for our 2DEG sample with a Fe_{0.2}Ni_{0.8}Zr₂ on top.

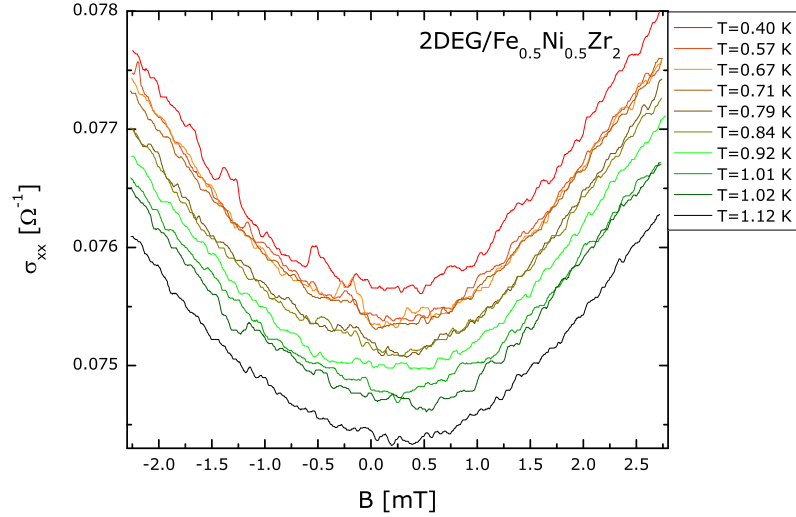


Figure B.3: Magnetoconductivity at different temperatures obtained for our 2DEG sample with a $\text{Fe}_{0.5}\text{Ni}_{0.5}\text{Zr}_2$ on top.

erties of the 2DEG can be extracted from these results. Figs.(B.2) and (B.3) displays the magnetoconductivity ($\sigma_{xx} = \rho_{xx}^{-1} = L/W R_{xx}$, where L and W are respectively the length and width of the active area of the 2DEG) results at different temperatures for two different runs of data with the same 2DEG, but different superconducting samples¹. The curvy shape of σ_{xx} results from weak localisation effects: a quantum correction to the Drude conductivity resulting from the constructive interference of time-reversed electronic paths and which results in a reduction of the low-temperature conductivity [157]. In a homogeneous magnetic field and for a doubly spin-degenerate system, the weak localisation correction to the conductivity is given by [156]

$$\sigma_{xx}(B, T) - \sigma_{xx}(0, T) = \alpha \frac{e^2}{2\pi^2 \hbar} \left[\psi \left(a_i + \frac{1}{2} \right) - \psi \left(a_e + \frac{1}{2} \right) + \ln \left(\frac{\tau_i}{\tau_e} \right) \right], \quad (\text{B.1})$$

where $a_{i,e} = \hbar/4eBD\tau_{i,e}$, ψ is the digamma function, and α is a constant of order 1 which depends on which scattering process dominates: inelastic, spin-orbit, or magnetic. In this last expression, D is the electron diffusion coefficient proportional to the elastic scattering time τ_e , $D = \frac{v_F^2 \tau_e}{2}$, which is more easily determined experimentally

¹The presence of the nearby superconductor is not expected to affect these measurements because vortex resolution is not achieved. We simply mention which superconductor was present with the 2DEG during these measurements for transparency. In the same order of idea, we confirm the presence of the weak localisation weak in the R_{xx} measurements of this 2DEG alone, i.e. in the absence of a nearby superconductor.

from the mobility μ according to the expression

$$D = \frac{k_B T \mu}{|e|}, \quad (\text{B.2})$$

while the mobility is obtained from

$$\mu = \frac{L}{n_e R_x W |e|} \quad (\text{B.3})$$

in which R_x represents the value of R_{xx} at zero magnetic field. The expression for the Fermi velocity

$$v_F = \frac{\hbar}{m_e} \sqrt{2\pi n_e} \quad (\text{B.4})$$

is also used to determine the electron elastic scattering time τ_e [158]. For low magnetic fields (less than $B_i = \hbar/4eD\tau_i$), equation (B.1) can be approximated by

$$\sigma_{xx}(B, T) - \sigma_{xx}(0, T) \approx \frac{1}{24} \alpha \frac{e^2}{2\pi^2 \hbar} \left(\frac{B}{B_i} \right)^2, \quad (\text{B.5})$$

in which the low field dependence of the weak localisation correction on the square of the magnetic field is very clear. Note that this dependence is predicted to be linear in the presence of an inhomogeneous magnetic field, such as that created by a superconductor's vortex lattice [59]. We fit equation (B.5) to our $\sigma_{xx}(B, T)$ data and obtain α and τ_i as fit parameters. The inelastic scattering times τ_i thus obtained for the σ_{xx} curves of Figs.(B.2) and (B.3) are plotted as a function of temperature in Fig.(B.4). The power-law behavior of τ_i found here is: $\tau_i \sim T^{-(0.57 \pm 0.02)}$ and $\tau_i \sim T^{-(0.56 \pm 0.01)}$ for the data reported in Figs.(B.2) and (B.3) respectively. These results differ from those of Ref.[159] who find $\tau_i \sim T^{-1}$, and from those of Ref.[156] who find $\tau_i \sim T^{-1.6}$. Best-fit values of α are: for the data of Fig.(B.2) at $T = 0.35$ K, 0.24, and 0.44 for the data of Fig.(B.3) at $T = 0.40$ K.

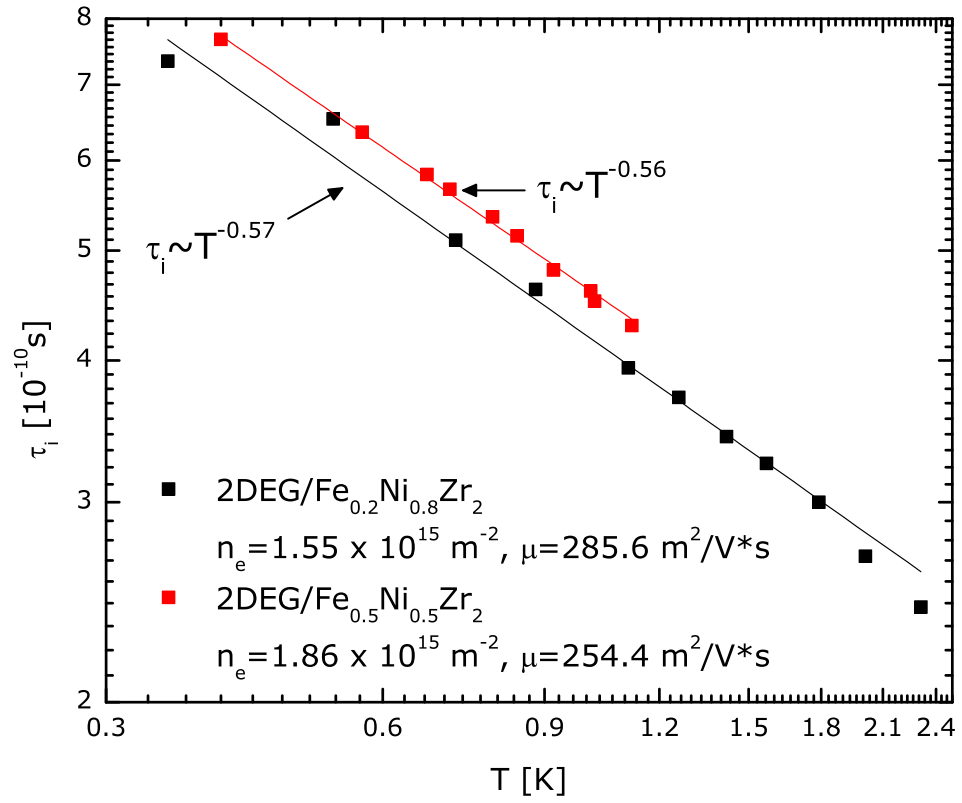


Figure B.4: Log-log plot of the inelastic electron scattering time τ_i vs temperature obtained from a unique 2DEG, but with different superconductors on top. The difference between the results obtained is not attributed to the superconductor which is expected to have no effect here, but rather to the rate of cooldown of the sample which has a marked effect on the electron density.

C

Hall resistance results

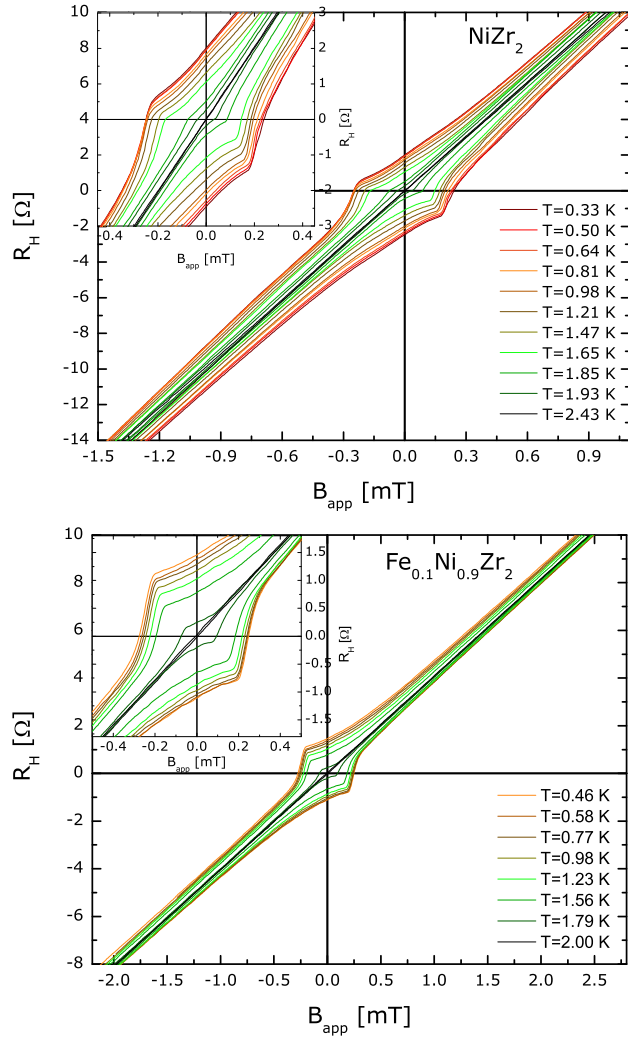


Figure C.1: Hall resistance vs applied magnetic field for $\text{Fe}_x\text{Ni}_{1-x}\text{Zr}_2$ with $x = 0$ and $x = 0.1$.

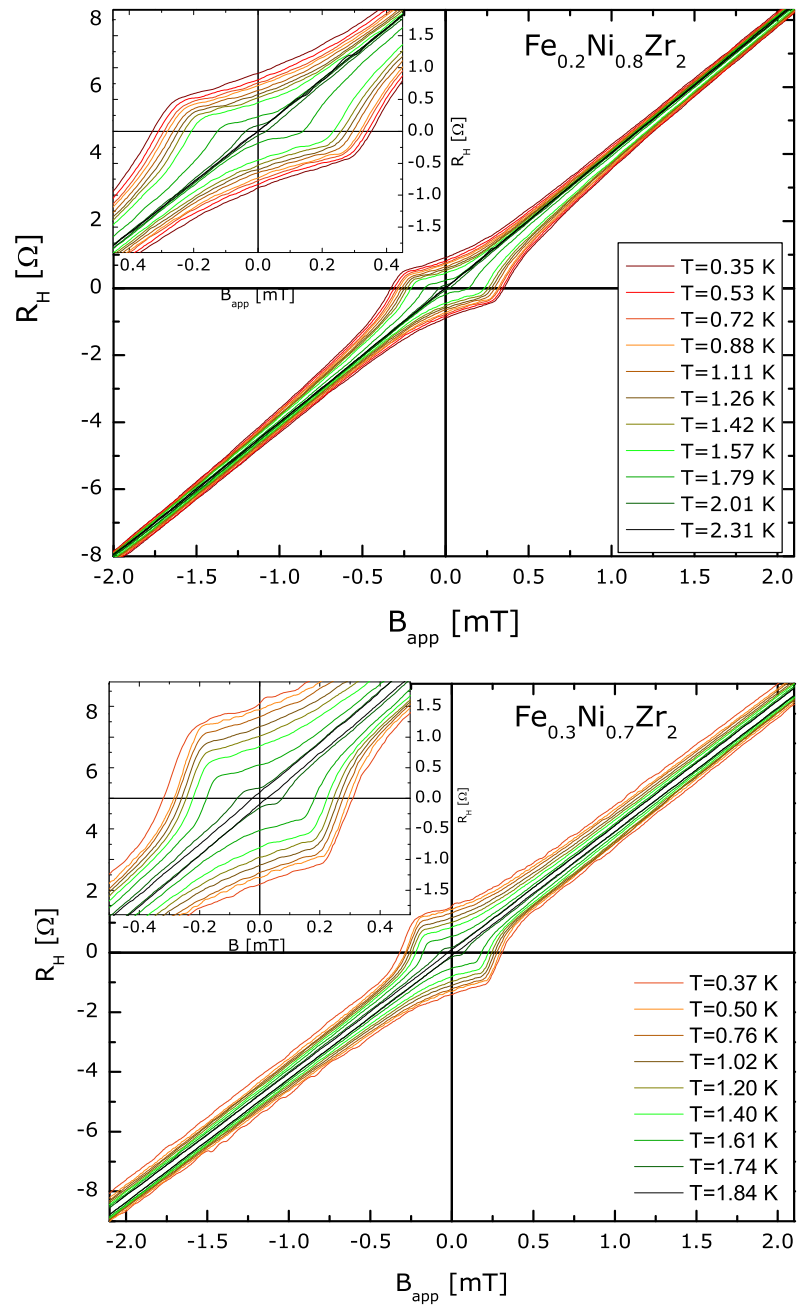


Figure C.2: Hall resistance vs applied magnetic field for $\text{Fe}_x\text{Ni}_{1-x}\text{Zr}_2$ with $x = 0.2$ and $x = 0.3$.

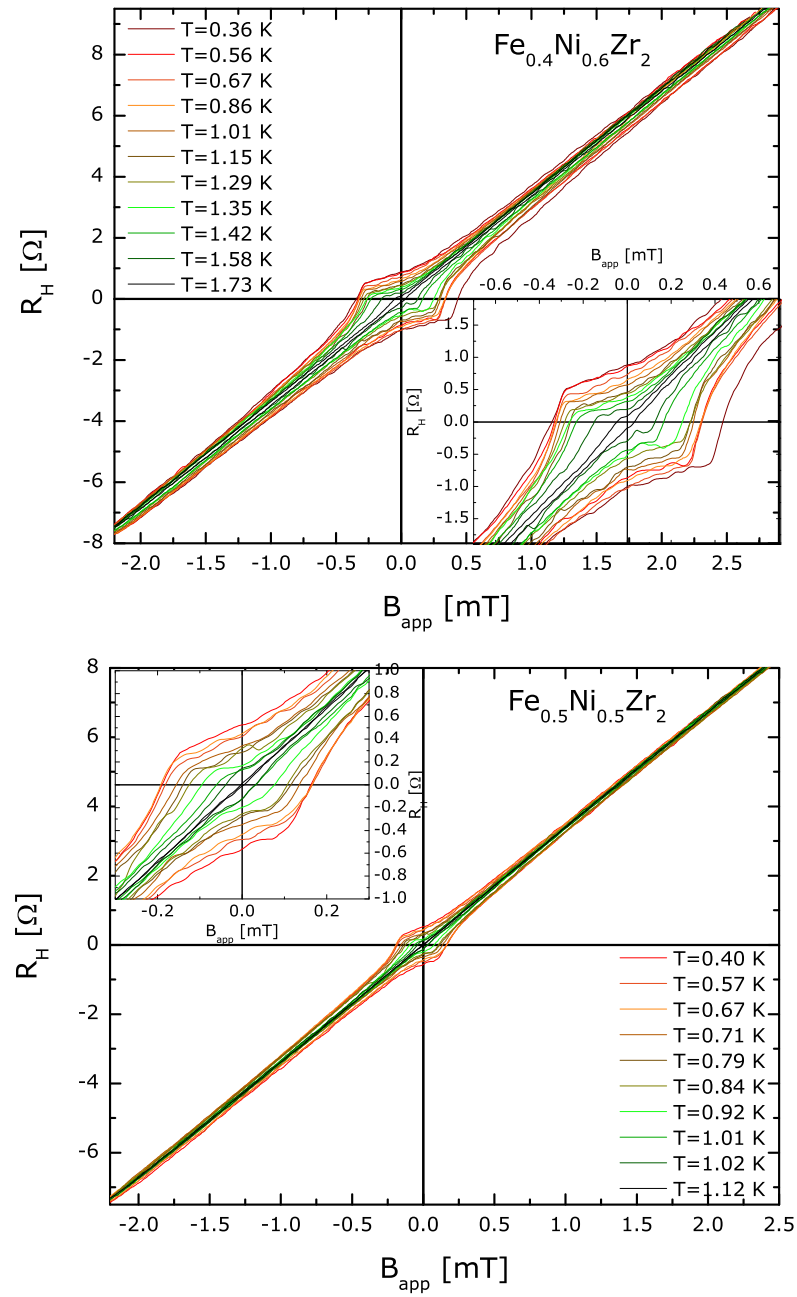


Figure C.3: Hall resistance vs applied magnetic field for $Fe_xNi_{1-x}Zr_2$ with $x = 0.4$ and $x = 0.5$.

BIBLIOGRAPHY

- [1] M. Tinkham, *Introduction to Superconductivity* (McGraw-Hill, 1996).
- [2] C. P. Poole Jr., H. A. Farach, and R. J. Creswick, *Superconductivity* (Academic Press, Inc., 1995).
- [3] L. Ji, M. S. Rzchowski, N. Anand, and M. Tinkham, *Phys. Rev. B* **47**, 470 (1993).
- [4] T. Giamarchi and P. Le Doussal, *Phys. Rev. B* **55**, 6577 (1997).
- [5] P. Le Doussal and T. Giamarchi, *Phys. Rev. B* **57**, 11356 (1998).
- [6] Z. Altounian, private communication, 2008.
- [7] M. Dikeakos, Z. Altounian, D. H. Ryan, and S. J. Kwon, *J. Non-Cryst. Solids* **250-252**, 637 (1999).
- [8] J. Lefebvre, M. Hilke, R. Gagnon, and Z. Altounian, *Phys. Rev. B* **74**, 174509 (2006).
- [9] J. G. Bednorz and K. A. Müller, *Z. Phys.* **B64**, 189 (1986).
- [10] P. J. Ford and G. A. Saunders, *The rise of superconductors* (CRC press, 2005).
- [11] www.superconductors.org.
- [12] P. F. Dahl, *Superconductivity: its historical roots and development from mercury to the ceramic oxides* (American Institute of Physics, 1992).
- [13] J. Oestergaard, J. Okholm, K. Lomholt, and O. Toennesen, *Applied Superconductivity*, *IEEE Transactions on* **11**, 2375 (Mar 2001).
- [14] W. Buckel and R. Kleiner, *Superconductivity. Fundamentals and Applications* (Wiley-VCH Verlag, 2004).
- [15] H.-W. Lee, K.-C. Kim, and J. Lee, *Magnetics*, *IEEE Transactions on* **42**, 1917 (July 2006).
- [16] T. Giamarchi and P. Le Doussal, *Phys. Rev. Lett.* **76**, 3408 (1996).
- [17] K. Moon, R. T. Scalettar, and G. T. Zimányi, *Phys. Rev. Lett.* **77**, 2778 (1996).
- [18] S. Ryu, M. Hellerqvist, S. Doniach, A. Kapitulnik, and D. Stroud, *Phys. Rev. Lett.* **77**, 5114 (1996).

- [19] C. Olson, C. Reichhardt, and F. Nori, *Phys. Rev. Lett.* **81**, 3757 (1998).
- [20] H. Fangohr, P. A. J. de Groot, and S. J. Cox, *Phys. Rev. B* **63**, 064501 (2001).
- [21] C. J. Olson and C. Reichhardt, *Phys. Rev. B* **61**, R3811 (2000).
- [22] S. Scheidl and V. M. Vinokur, *Phys. Rev. E* **57**, 2574 (1998).
- [23] H. K. Onnes, *Leiden Comm.* **120b**, **122b**, **124c** (1911).
- [24] W. Meissner and R. Ochsenfeld, *Naturwissenschaften* **21**, 787 (1933).
- [25] F. London and H. London, *Proc. Roy. Soc. (London)* , 71 (1935).
- [26] V. L. Ginzburg and L. D. Landau, *Zh. Eksperim. i Teor. Fiz.* **20**, 1064 (1950).
- [27] J. Bardeen, L. N. Cooper, and J. R. Schrieffer, *Phys. Rev.* **108**, 1175 (1957).
- [28] A. A. Abrikosov, *Sov. Phys. JETP* **5**, 1174 (1957).
- [29] L. P. Gor'kov, *Sov. Phys. JETP* **9**, 1364 (1959).
- [30] C. P. Bean, *Phys. Rev. Lett.* **8**, 250 (1962).
- [31] C. P. Bean, *Rev. Mod. Phys.* **36**, 31 (1964).
- [32] Y. B. Kim, C. F. Hempstead, and A. R. Strnad, *Phys. Rev. Lett.* **9**, 306 (1962).
- [33] Y. B. Kim, C. F. Hempstead, and A. R. Strnad, *Phys. Rev.* **129**, 528 (1963).
- [34] L. Ji, R. H. Sohn, G. C. Spalding, C. J. Lobb, and M. Tinkham, *Phys. Rev. B* **40**, 10936 (1989).
- [35] D. LeBlanc and M. A. R. LeBlanc, *Phys. Rev. B* **45**, 5443 (1992).
- [36] S. Elliott, *Physics of amorphous materials* (Longman scientific and technical, 1990).
- [37] R. Zallen, *The physics of amorphous solids* (John Wiley and Sons, 1983).
- [38] N. P. Kovalenko, Y. P. Krasny, and U. Krey, *Physics of amorphous metals* (Wiley-VCH Verlag GmbH, Weinheim, 2001).
- [39] J. M. Eliashberg, *Zh. Eksp. Teor. Fiz.* **38**, 366 (1960).
- [40] J. M. Eliashberg, *Zh. Eksp. Teor. Fiz.* **39**, 1437 (1960).
- [41] W. L. McMillan, *Phys. Rev.* **167**, 331 (1968).
- [42] M. A. Jensen and K. Andres, *Phys. Rev.* **165**, 545 (1968).
- [43] J. M. Daams, B. Mitrović, and J. P. Carbotte, *Phys. Rev. Lett.* **46**, 65 (1981).

- [44] E. S. Rosenblum, S. H. Autler, and K. H. Goen, *Rev. Mod. Phys.* **36**, 77 (1964).
- [45] W. K. Kwok, J. A. Fendrich, C. J. van der Beek, and G. W. Crabtree, *Phys. Rev. Lett.* **73**, 2614 (1994).
- [46] A. M. Troyanovski, M. van Hecke, N. Saha, J. Aarts, and P. H. Kes, *Phys. Rev. Lett.* **89**, 147006 (2002).
- [47] P. L. Gammel *et al.*, *Phys. Rev. Lett.* **80**, 833 (1998).
- [48] Y. Fasano *et al.*, *Phys. Rev. B* **66**, 020512 (2002).
- [49] R. Wördenweber and P. H. Kes, *Phys. Rev. B* **33**, 3172 (1986).
- [50] T. G. Berlincourt, R. R. Hake, and D. H. Leslie, *Phys. Rev. Lett.* **6**, 671 (1961).
- [51] P. H. Kes and C. C. Tsuei, *Phys. Rev. B* **28**, 5126 (1983).
- [52] J. M. E. Geers, C. Attanasio, M. B. S. Hesselberth, J. Aarts, and P. H. Kes, *Phys. Rev. B* **63**, 094511 (2001).
- [53] Z. Altounian, S. V. Dantu, and M. Dikeakos, *Phys. Rev. B* **49**, 8621 (1994).
- [54] M. Dikeakos, *Fe-TM-Zr alloys: from glass to big cube crystal*, PhD thesis, McGill University, Montréal, Canada, 2001.
- [55] Z. Altounian and J. O. Strom-Olson, *Phys. Rev. B* **27**, 4149 (1983).
- [56] www.webelements.com.
- [57] M. P. Marder, *Condensed Matter Physics* (John Wiley and Sons, 2000).
- [58] K. v. Klitzing, G. Dorda, and M. Pepper, *Phys. Rev. Lett.* **45**, 494 (1980).
- [59] J. Rammer and A. L. Shelankov, *Phys. Rev. B* **36**, 3135 (1987).
- [60] S. J. Bending, K. v. Klitzing, and K. Ploog, *Phys. Rev. B* **42**, 9859 (1990).
- [61] M. Danckwerts, A. R. Goñi, C. Thomsen, K. Eberl, and A. G. Rojo, *Phys. Rev. Lett.* **84**, 3702 (2000).
- [62] J. R. Clem, *J. Low Temp. Phys.* **18**, 427 (1975).
- [63] D. Saint-James, G. Sarma, and E. J. Thomas, *Type II Superconductivity* (Pergamon, Oxford, 1969).
- [64] W. Bückel and R. Hilsch, *Z. Phys.* **138**, 109 (1954).
- [65] L. P. Gor'kov, *Sov. Phys. JETP* **10**, 593 (1960).
- [66] L. P. Gor'kov, *Sov. Phys. JETP* **10**, 998 (1960).

- [67] K. Maki, *Physics* **1**, 21 (1964).
- [68] E. Helfand and N. R. Werthamer, *Phys. Rev. Lett.* **13**, 686 (1964).
- [69] N. R. Werthamer, E. Helfand, and P. C. Hohenberg, *Phys. Rev.* **147**, 295 (1966).
- [70] P.-G. de Gennes, *Superconductivity of metals and alloys* (W. A. Benjamin, Inc., New York, 1966).
- [71] P. W. Anderson, *J. Phys. Chem. Sol.* **11**, 26 (1959).
- [72] M. M. Collver and R. H. Hammond, *Phys. Rev. Lett.* **30**, 92 (1973).
- [73] K. Maki, *Physics* **1**, 127 (1964).
- [74] A. M. Clogston, *Phys. Rev. Lett.* **9**, 266 (1962).
- [75] M. Tenhover, W. L. Johnson, and C. C. Tsuei, *Solid State Commun.* **38**, 53 (1981).
- [76] M. Tenhover and W. L. Johnson, *Physica* **108B**, 1221 (1981).
- [77] C. H. Strudthoff, J. Reichelt, and H. C. Freyhardt, *Physica* **107B**, 393 (1981).
- [78] W. L. Johnson, S. J. Poon, and P. Duwez, *Phys. Rev. B* **11**, 150 (1975).
- [79] W. L. Johnson, S. J. Poon, J. Durand, and P. Duwez, *Phys. Rev. B* **18**, 206 (1978).
- [80] E. R. Domb and W. L. Johnson, *J. Low Temp. Phys.* **33**, 29 (1978).
- [81] C. C. Koch, D. M. Kroeger, J. O. Scarbrough, and B. C. Giessen, *Phys. Rev. B* **22**, 5213 (1980).
- [82] B. S. Chandrasekhar, *Applied Physics Letters* **1**, 7 (1962).
- [83] T. G. Berlincourt and R. R. Hake, *Phys. Rev. Lett.* **9**, 293 (1962).
- [84] T. G. Berlincourt and R. R. Hake, *Phys. Rev.* **131**, 140 (1963).
- [85] M. G. Karkut and R. R. Hake, *Phys. Rev. B* **28**, 1396 (1983).
- [86] K. M. Wong, E. J. Cotts, and S. J. Poon, *Phys. Rev. B* **30**, 1253 (1984).
- [87] S. J. Poon and P. L. Dunn, *J. Low Temp. Phys.* **54**, 81 (1984).
- [88] N. Toyota, A. Inoue, T. Fukase, and T. Masumoto, *J. Low Temp. Phys.* **55**, 393 (1984).
- [89] C. Ren *et al.*, Linear temperature dependence of the lower critical field H_{c1} in F-doped LaOFeAs superconductors, 2008, cond-mat/0804.1726.

- [90] R. P. Huebener, *Magnetic flux structures in superconductors* (Springer-Verlag, New York, 1979).
- [91] C. J. Gorter and H. B. G. Casimir, *Phys. Z.* **35**, 963 (1934).
- [92] K. Maki, *Physics* **1**, 201 (1964).
- [93] B. Mühlshlegel, *Z. Phys.* **155**, 313 (1959).
- [94] T. H. Shen *et al.*, *Superconductor Science and Technology* **4**, 232 (1991).
- [95] J. Rammer, *J. Low Temp. Phys.* **71**, 323 (1988).
- [96] K. Maki, *Phys. Rev.* **148**, 362 (1966).
- [97] E. Helfand and N. R. Werthamer, *Phys. Rev.* **147**, 288 (1966).
- [98] V. Z. Kresin and S. A. Wolf, *Fundamentals of superconductivity* (Plenum press, New York, 1990).
- [99] B. T. Matthias, H. Suhl, and E. Corenzwit, *Phys. Rev. Lett.* **1**, 92 (1958).
- [100] F. Hamed, F. S. Razavi, S. K. Bose, and T. Startseva, *Phys. Rev. B* **52**, 9674 (1995).
- [101] P. Oelhafen, E. Hauser, and H.-J. Güntherodt, *Solid State Commun.* **35**, 1017 (1980).
- [102] A. Nordström, U. Dahlborg, and O. Rapp, *Phys. Rev. B* **48**, 12866 (1993).
- [103] G. E. Zwicknagl and J. W. Wilkins, *Phys. Rev. Lett.* **53**, 1276 (1984).
- [104] R. Brüning, Z. Altounian, and J. O. Ström-Olsen, *Journal of Applied Physics* **62**, 3633 (1987).
- [105] M. Mao and Z. Altounian, *J. Non-Cryst. Solids* **205-207**, 633 (1987).
- [106] Y. Yamada, Y. Itoh, and U. Mizutani, *Mater. Sci. Eng.* **99**, 289 (1988).
- [107] J. Lefebvre, Peak effect, Hall effect and vortex phases in $Fe_xNi_{1-x}Zr_2$ superconducting glasses, Master's thesis, McGill University, Montréal, Canada, 2004.
- [108] M. Hilke, S. Reid, R. Gagnon, and Z. Altounian, *Phys. Rev. Lett.* **91**, 127004 (2003).
- [109] W. A. Fertig *et al.*, *Phys. Rev. Lett.* **38**, 987 (1977).
- [110] M. Trudeau, *Étude de l'effect Hall et de la magnetoresistivité dans les alliages métalliques amorphes de M-Zr (M=Ni, Co et Fe)*, PhD thesis, Université de Montréal, Montréal, Canada, 1986.

- [111] Y. Liu *et al.*, Phys. Rev. B **66**, 144510 (2002).
- [112] A. Kiliç, K. Kiliç, H. Yetis, and O. Çetin, New Journal of Physics **7**, 212 (2005).
- [113] C. A. M. dos Santos, M. S. da Luz, B. Ferreira, and A. J. S. Machado, Physica C **391**, 345 (2003).
- [114] S. J. Poon, Phys. Rev. B **25**, 1977 (1982).
- [115] S. J. Poon, Phys. Rev. B **27**, 5519 (1983).
- [116] I. Felner *et al.*, Phys. Rev. B **67**, 134506 (2003).
- [117] J.-P. Bouchaud, M. Mézard, and J. S. Yedidia, Phys. Rev. B **46**, 14686 (1992).
- [118] G. Blatter, M. V. Feigel'man, V. B. Geshkenbein, A. I. Larkin, and V. M. Vinokur, Rev. Mod. Phys. **66**, 1125 (1994).
- [119] T. Giamarchi and P. Le Doussal, Phys. Rev. Lett. **72**, 1530 (1994).
- [120] T. Giamarchi and P. Le Doussal, Phys. Rev. B **52**, 1242 (1995).
- [121] D. S. Fisher, M. P. A. Fisher, and D. A. Huse, Phys. Rev. B **43**, 130 (1991).
- [122] A.-C. Shi and A. J. Berlinsky, Phys. Rev. Lett. **67**, 1926 (1991).
- [123] A. E. Koshelev and V. M. Vinokur, Phys. Rev. Lett. **73**, 3580 (1994).
- [124] L. Balents, M. C. Marchetti, and L. Radzihovsky, Phys. Rev. B **57**, 7705 (1998).
- [125] M. Marchevsky, J. Aarts, P. H. Kes, and M. V. Indenbom, Phys. Rev. Lett. **78**, 531 (1997).
- [126] F. Pardo, F. De La Cruz, P. L. Gammel, E. Bucher, and D. J. Bishop, Nature **396**, 348 (1998).
- [127] A. M. Troyanovski, J. Aarts, and P. H. Kes, Nature **399**, 665 (1999).
- [128] S. Bhattacharya and M. J. Higgins, Phys. Rev. Lett. **70**, 2617 (1993).
- [129] U. Yaron *et al.*, Phys. Rev. Lett. **73**, 2748 (1994).
- [130] M. C. Hellerqvist, D. Ephron, W. R. White, M. R. Beasley, and A. Kapitulnik, Phys. Rev. Lett. **76**, 4022 (1996).
- [131] S. Spencer and H. J. Jensen, Phys. Rev. B **55**, 8473 (1997).
- [132] H. Fangohr, S. J. Cox, and P. A. J. de Groot, Phys. Rev. B **64**, 064505 (2001).
- [133] A. C. Marley, M. J. Higgins, and S. Bhattacharya, Phys. Rev. Lett. **74**, 3029 (1995).
- [134] Z. D. Wang and C. S. Ting, Phys. Rev. Lett. **67**, 3618 (1991).

- [135] B. Y. Zhu, D. Y. Xing, Z. D. Wang, B. R. Zhao, and Z. X. Zhao, Phys. Rev. B **60**, 3080 (1999).
- [136] V. Vinokur, V. Geshkenbein, M. Feigel'man, and G. Blatter, Phys. Rev. Lett. **71**, 1242 (1993).
- [137] S. J. Hagen, C. J. Lobb, and R. L. Greene, Phys. Rev. B **41**, 11630 (1990).
- [138] C. J. Lobb *et al.*, Appl. Sup. **2**, 631 (1994).
- [139] S. Bhattacharya, M. J. Higgins, and T. V. Ramakrishnan, Phys. Rev. Lett. **73**, 1699 (1994).
- [140] J. Bardeen and M. Stephen, Phys. Rev. **140** (1964).
- [141] A. I. Schindler and D. J. Gillespie, Phys. Rev. **130**, 953 (1963).
- [142] T. W. Jing and N. P. Ong, Phys. Rev. B **42**, 10781 (1990).
- [143] A. K. Niessen and F. A. Staas, Phys. Lett. **15**, 26 (1965).
- [144] A. Niessen and C. Weijnsfeld, J. Appl. Phys. **40**, 384 (1969).
- [145] R. W. Cochrane, J. Destry, and M. Trudeau, Phys. Rev. B **27**, 5955 (1983).
- [146] G. Doornbos, R. Wijngaarden, and R. Griessen, Physica C **235–240**, 1371 (1994).
- [147] A. B. Pippard, Proc. Roy. Soc. (London) , 547 (1953).
- [148] A. I. Larkin and Y. N. Ovchinnikov, Sov. Phys. JETP **41**, 960 (1976).
- [149] F. Perruchot *et al.*, Physica B **284–288**, 1984 (2000).
- [150] C. Reichhardt and C. J. Olson, Phys. Rev. B **65**, 094301 (2002).
- [151] N. Goldenfeld, *Lectures on phase transitions and the renormalization group* (Perseus Publishing, 1992).
- [152] W. R. Smythe, *Static and dynamic electricity* (McGraw-Hill, New York, 1939).
- [153] A. K. Geim, S. J. Bending, I. V. Grigorieva, and M. G. Blamire, Phys. Rev. B **49**, 5749 (1994).
- [154] S. T. Stoddart, H. I. Mutlu, A. K. Geim, and S. J. Bending, Phys. Rev. B **47**, 5146 (1993).
- [155] S. J. Bending and A. K. Geim, Phys. Rev. B **46**, 14912 (1992).
- [156] S. J. Bending, K. von Klitzing, and K. Ploog, Phys. Rev. Lett. **65**, 1060 (1990).
- [157] D. J. Bishop, D. C. Tsui, and R. C. Dynes, Phys. Rev. Lett. **44**, 1153 (1980).

- [158] S. Datta, *Electronic transport in mesoscopic systems* (Cambridge University Press, 1995).
- [159] B. J. F. Lin, M. A. Paalanen, A. C. Gossard, and D. C. Tsui, Phys. Rev. B **29**, 927 (1984).